On the Performance of Base-Isolated Buildings: A Generic Model

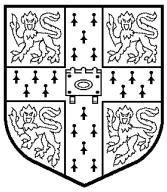

A dissertation submitted to the University of Cambridge
for the degree of Doctor of Philosophy

by

James Peter Talbot
Peterhouse

November 2001

To Mum, Dad

& Kathy

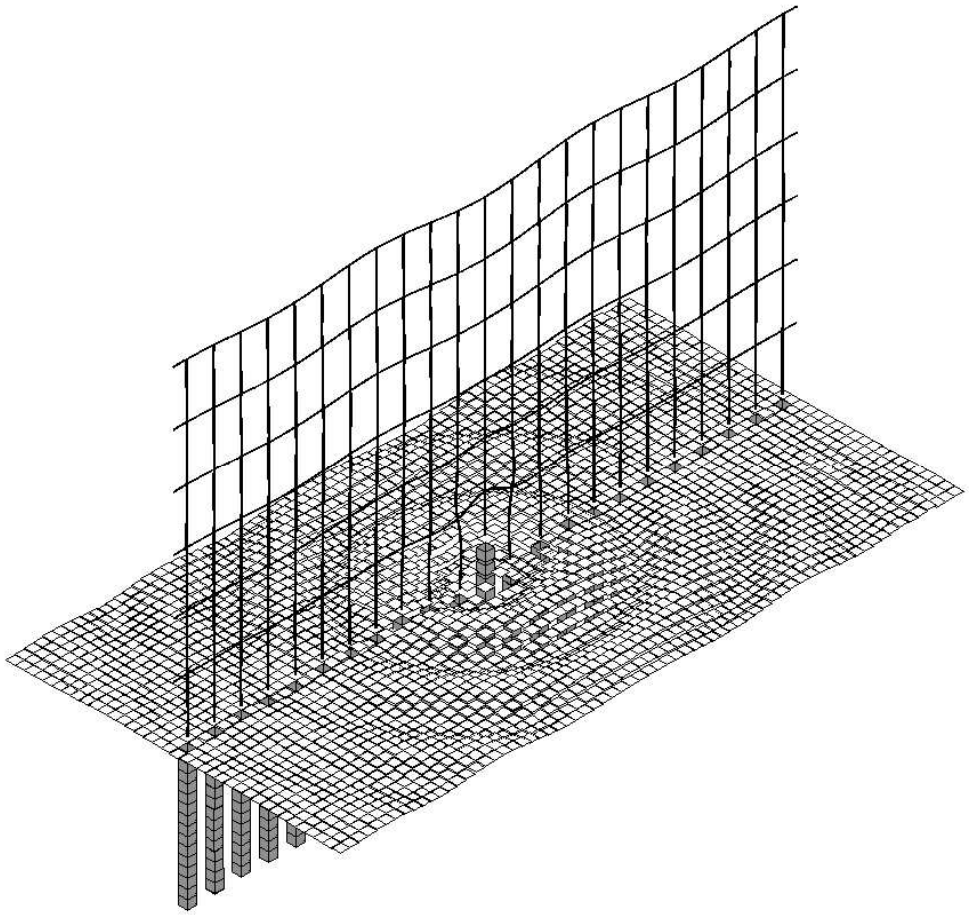

Just as in this age of mechanisation we welcome the advent of any mechanical process which makes a demand on craftsmanship and manual skill, so some of us at any rate may feel grateful that, in problems relating to vibrations, nature has provided us with a range of mysteries which for their elucidation require the exercise of a certain amount of mathematical dexterity. In many directions of engineering practice, that vague commodity known as common sense will carry one a long way, but no ordinary mortal is endowed with an inborn instinct for vibrations; mechanical vibrations in general are too rapid for the utilization of our sense of sight, and common sense applied to these phenomena is too common to be other than a source of danger.

Professor C E Inglis, OBE, MA, LLD, FRS

James Forrest Lecture, 1944

PREFACE

The work described in this dissertation was carried out at Cambridge University Engineering Department between November 1998 and October 2001. The project was suggested by Dr Hugh Hunt, who also acted as my research supervisor. I have been very fortunate in having such an enthusiastic and knowledgeable supervisor and I would like to thank him for all his help. I would also like to thank Professor David Newland, who acted as my supervisor for part of my final year and has maintained a keen interest in my work.

I am very grateful to Professor Jim Woodhouse, without whose initial encouragement I would not have returned to the Department, and to Professor Robin Langley for some helpful teatime discussions.

For help in producing my experimental apparatus, I would like to thank Mr David Miller and the staff of the Mechanics Laboratory. Thanks are also due to Dr Caroline Millar, formerly of GEC Marconi Ltd, for supplying complimentary samples of the piezoelectric materials.

This research has been funded by the Engineering and Physical Sciences Research Council, to whom I am very much indebted. I must also thank the Worshipful Company of Scientific Instrument Makers, for their award of a Scientific Instrument Makers' Scholarship, and the James Clayton fund of the Institution of Mechanical Engineers.

Finally, I would like to thank Peterhouse, for providing such a pleasant, supportive and rewarding environment in which to be a student.

I declare that, except for commonly understood and accepted ideas, or where specific reference has been made to the work of others, this dissertation is the result of my own work and includes nothing that is the outcome of collaborative work. This dissertation is approximately 56,400 words in length and contains 98 figures.

James Talbot

Cambridge, November 2001

SUMMARY

Ground-borne vibration has existed ever since the development of urban road and rail networks. Vibration generated by the moving traffic propagates through the ground and into buildings, resulting in unacceptable levels of internal noise and vibration. A common solution to this increasingly significant problem is the base-isolation of buildings by incorporating vibration isolation bearings between the buildings and their foundations. This technique has been employed for over forty years but the exact performance of base isolation remains uncertain.

This dissertation is concerned with the development of a generic computational model; generic in that it accounts for the essential dynamic behaviour of a typical base-isolated building in order to make predictions of isolation performance. The model is a linear one, formulated in the frequency domain, and consists of a two-dimensional portal-frame model of a building coupled to a three-dimensional boundary-element model of a piled-foundation. Both components of the model achieve computational efficiency by assuming they are infinitely long and using periodic structure theory.

The development of the model is described systematically, from the modelling of a building and its isolation bearings to that of its foundation. The majority of the work is concerned with the piled-foundation model, which is comprehensive in that it accounts for the vertical, horizontal and rotational motion of the pile heads due to both direct pile-head loading and interaction through wave propagation in the surrounding soil. It is shown that this level of detail is important in the prediction of base isolation efficiency.

A key question facing designers is not only how but on what basis base isolation should be assessed, since fundamental problems exist with the existing measures of isolation performance. Power flow analysis is explored and the concept of power flow insertion gain, based on the total mean vibrational power flow entering a building, is introduced as a useful measure of isolation performance. This is shown to offer clear benefits by providing a single measure of performance that is suitable for design purposes.

Finally, the development of a prototype force-sensitive vibration isolation bearing is described as a contribution to verifying base-isolation theory with experiments.

CONTENTS

Chapter 1
INTRODUCTION

If the earth moves, then head for the cinema.

The Times, 11 June 1999

On 11 June 1999, the British Film Institute's IMAX cinema was officially opened on a roundabout near the South Bank, London. Busy traffic encircles the cinema, Waterloo railway station is nearby and the building's foundations lie only a few metres above two underground railway lines: an unusual site for a cinema and not, one might think, a particularly desirable site given the level of noise and vibration. However, the cinema is one of the most recent examples of a base-isolated building, one specifically designed to minimise the effects of ground-borne vibration by incorporating vibration isolation bearings between the building and its foundation; see Figure 1.1.

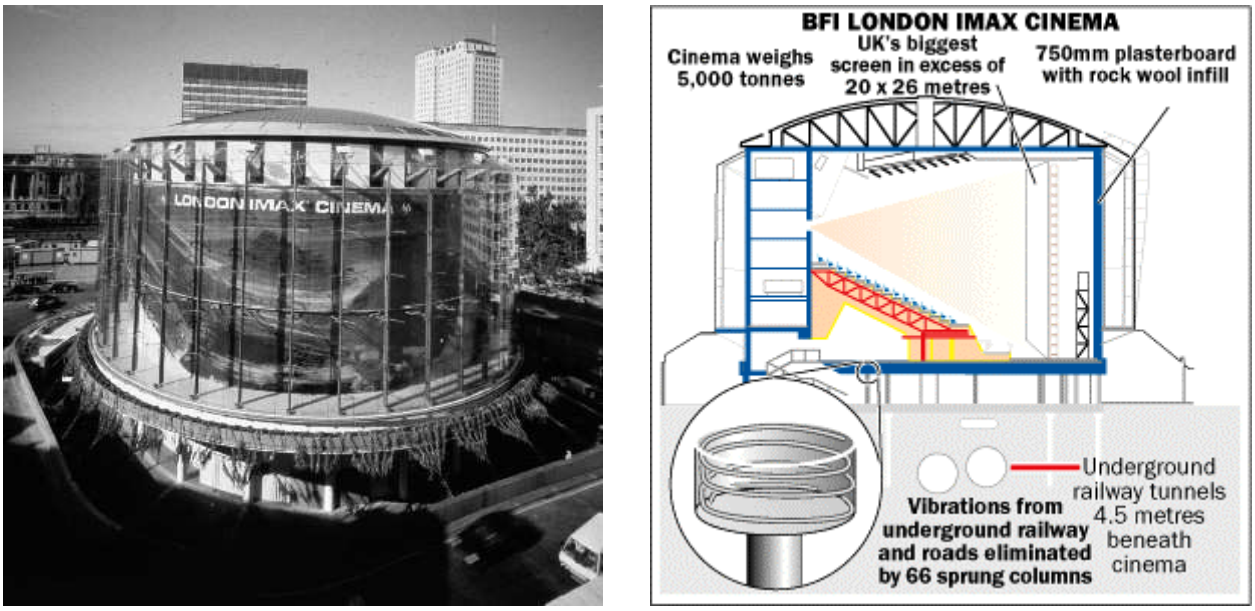

Figure 1.1: The British Film Institute's new IMAX cinema, London (courtesy of BFI and *The Times*). The building is a heavily glazed steel-framed structure and the foundation consists of a reinforced-concrete raft that distributes the weight of the building across 90 piles. Between the raft and the base of the building, mounted on top of 66 columns, lie large steel helical springs that provide the vibration isolation.

1.1. Motivation for the Research

As early as 1900, complaints were made to the Central London Railway (now the Central Line of the London Underground) concerning the excessive vibrations and their effects on buildings; see the ORE D151 report [108]. Since then, due to a number of factors, there has been an increasing need to tackle the problem of ground-borne vibration. There is generally an increasing public sensitivity to noise and vibration and this has led to more demanding legislation dictating acceptable levels within our homes and places of work. In addition, there is pressure to expand road and rail networks, and develop existing urban sites. Such sites that remain are often the undesirable ones close to railways or busy roads.

Since the 1960s base isolation has enabled the construction of buildings on sites otherwise deemed unacceptable due to high levels of ground-borne vibration. Despite many such projects, the performance of base isolation remains uncertain. The objective is to reduce vibration transmission by at least 10 dB for frequencies above approximately 10 Hz but this is difficult to verify and is not thought likely to be achieved in practice. Current practice suggests that the bearing type has a significant effect on the isolation efficiency, as well as having implications for

the design and cost of the system, but there remain unanswered questions concerning the specification and design of the bearings. For example, what is the most appropriate stiffness of the bearings for a given application and how important is the level of internal damping? The answers to these questions are important because they have significant implications for the design and cost of a base-isolated building. There is therefore a clear need for a means of determining the effectiveness of base isolation and objectively evaluating the alternative types of bearing.

1.2. Objectives of the Research

The primary aim of this research is to develop a computational model in order to make predictions of isolation performance. It is a generic model in that it accounts for the essential dynamic behaviour of a typical base-isolated building rather than a specific example. The model has three main uses:

- to determine the effectiveness of base isolation of buildings against ground-borne vibration;
- to evaluate objectively the various types of isolation bearing;
- to help establish the best design practice.

It is desirable that the model is computationally efficient and suitable for use on a standard personal computer so that, in principle, manufacturers, consultants, and designers could readily evaluate various base-isolation designs.

To achieve this aim there are specific objectives that must first be achieved:

- to develop an understanding of the soil-structure interaction associated with a base-isolated building, that is, how a building interacts with the ground and how its presence alters the ground vibration field;
- to determine an appropriate measure of isolation performance;
- to develop a comprehensive model of a typical foundation design, namely a piled foundation, and determine the significance of the interaction between neighbouring piles;

- to combine the piled-foundation model with a generic model of a building;
- to verify the model by comparison with results from more detailed models and a programme of experimental measurements.

All the numerical modelling is undertaken with programs written specifically for this dissertation using the technical computing software Matlab [87].

1.3. Outline of the Dissertation

This dissertation falls into three sections: a review of previous work and an initial theoretical study into the behaviour of base-isolated buildings; the development of a comprehensive piled-foundation model and its incorporation into a generic model of a base-isolated building; and an experimental investigation into a prototype force-sensitive isolation bearing.

An overview of previous research relevant to this dissertation is given in Chapter 2. The initial sections summarise the problem of ground-borne vibration and the various methods of reducing its effects. Later sections introduce the details of base-isolated buildings and how they may be modelled theoretically. The review highlights the limitations of existing models that are to be addressed by the current work. The importance of modelling a building's foundation is illustrated in Chapter 3 and it is concluded that a generic base-isolated building model requires a comprehensive model of a piled foundation. In addition, a new power-flow approach is introduced as a more useful means of assessing base-isolation performance than one based on vibration amplitudes.

The subject of Chapter 4 is the systematic development of a three-dimensional piled-foundation model based on a combination of the boundary-element method and periodic structure theory. The first part of the chapter deals with the modelling of a single pile, which is then developed into a model of an infinite row of piles. The result is a computationally efficient model that, as described in Chapter 5, is suitable for incorporation into a generic model of a base-isolated building.

The theoretical analysis of vibrational power introduced in Chapter 3 raises the question of whether or not the measurement of isolation performance in terms of power flow is feasible in practice. In Chapter 6 this question is addressed in part by exploring the possibility of a force-sensitive vibration isolation bearing. The concept of such a device is described, together with the design and testing of an initial prototype. Test results are presented and recommendations are made for future development work.

Overall conclusions and recommendations for further work are given in Chapter 7. In its current form the generic base-isolated building model provides a flexible and computationally efficient means of investigating base-isolation performance. It also has significant potential for further development.

The principle innovations presented in this dissertation are: the introduction of a vibrational power-flow approach to base-isolation theory; the development of a comprehensive but computationally efficient piled-foundation model for incorporation into a generic model of a base-isolated building; and the development of a force-sensitive vibration isolation bearing as a contribution to verifying base-isolation theory with experiments.

Chapter 2
LITERATURE REVIEW

Many researchers have considered various aspects of ground-borne vibration and its effects on buildings and their occupants, and several detailed studies have already been undertaken. Studies of the vibration sources include the work on vibration from surface vehicles by Hunt [57] and Ng [103], and that by Forrest [38] on underground railways. Studies of the vibration transmission path include Lo's work on the vibration of piled foundations [76], while the work of Cryer [33] and Kraemer [66] considers noise and vibration in buildings. This literature review provides an overview of previous research in this field, with particular emphasis on the work of direct relevance to base-isolated buildings. The initial sections deal with the nature of the problem and the various methods of reducing its effects. Later sections introduce the details of base-isolated buildings and how they may be modelled theoretically.

2.1. The Problem of Ground-Borne Vibration

Ground-borne vibration is essentially a man-made problem of the last 100 years or so, primarily due to the development of urban road and rail networks. Vibration generated by moving traffic propagates through the ground and into buildings, resulting in unacceptable levels of internal noise and vibration. This is illustrated in Figure 2.1, which shows a schematic diagram of Wellington Hospital in London. The building lies directly above two mainline railway tracks and within only a few metres of four underground railway tunnels and the main road. The complexity of the problem is clear: vibration from multiple sources propagates through and along

the surface of the ground, interacting with buried objects on the way, before manifesting in the building as internal noise and vibration.

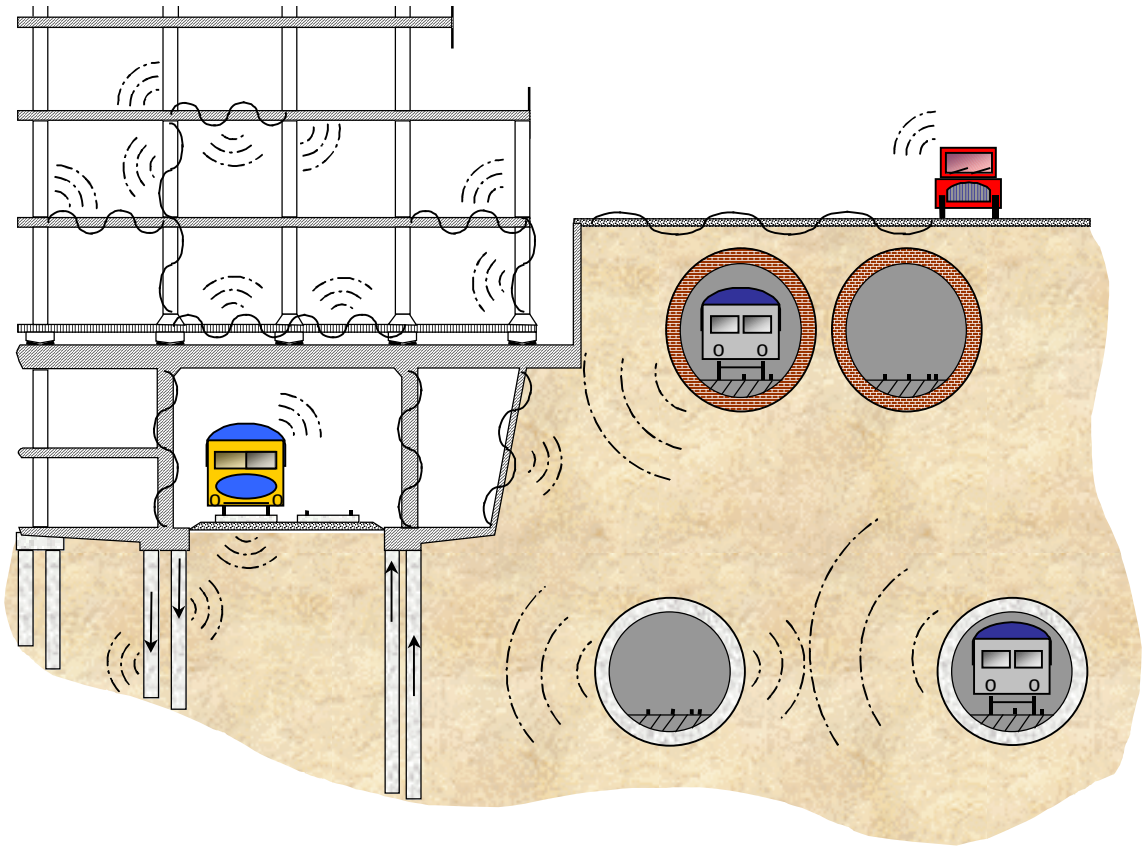

Figure 2.1: Ground-borne vibration and its effects on buildings. Based on a diagram by Grootenhuis of Wellington Hospital, London [44]. To limit the internal noise and vibration due to the moving traffic, the building is base-isolated on rubber bearings located above the basement.

2.1.1. Sources of Ground-Borne Vibration

There are many sources of noise and vibration in buildings, such as wind, building services, the closing of doors and the foot-falls of occupants. The focus in this dissertation is on the transmission of *ground-borne* vibration into buildings. Seismic tremors are a natural source of vibration but significant tremors are rare in the UK and they will not be considered in detail here. Man-made sources, on the other hand, cause daily disturbance to large numbers of people and they can have significant social and economic consequences. The three main sources are described below and typical vibration levels and frequency ranges are identified. The significance of these levels for buildings and their occupants are discussed in Sections 2.1.2 and 2.1.3.

Construction Activity

Many mechanised construction activities lead to ground-borne vibration. Examples include blasting, tunnelling, piling and vibratory compaction. Heavy industrial machines, such as drop forges, are other related sources. Hiller *et al*. [52, 28] discuss a variety of such activities and present field measurements of the resulting peak particle velocity of the ground: levels lie in the range from 6 to 160 mm/s. The frequency content depends on the particular activity but is typically below 100 Hz.

These levels of ground-borne vibration are not insignificant (see Section 2.1.2, Table 2.1) and, as reported by the ORE D151 Committee [108], construction activities can cause disturbance to building occupants and, in rare occasions, structural damage. However, the duration of the disturbance is limited, as is the number of people affected. Much more significant as sources of ground-borne vibration are roads and railways. The vibration amplitudes are comparatively small but large numbers of people are exposed to an annoyance every day of the year. Even a perfect vehicle travelling on a perfect road or railway would generate ground-borne vibration due to the movement of its weight across the elastic surface of the ground. In practice, various imperfections, in both the vehicle and the road or rail surface, lead to further vibration.

Roads

Several experimental studies have been conducted into the vibration generated by road vehicles; see for example the ORE D151 report [108] and, specifically for road tunnels, the report by Bean and Page [10]. In general, typical surface vibration levels are found to lie in the range from 0.1 to 1.0 mm/s.

Experimental work undertaken by Hunt [57] has revealed that the type of road surface has a significant effect on the surface vibration spectra measured some distance from the road. The frequencies associated with a Tarmac trunk road are largely confined to below 40 Hz, whereas a concrete motorway led to significant frequency content up to at least 100 Hz. Spectra typically contain two peaks below 20 Hz, which correspond to the body-bounce and wheel-hop frequencies of the vehicles, as can be seen in the measurements by Hao *et al*. [46].

There is evidence that the introduction of speed control measures on roads can result in additional ground-borne vibration. An experimental study by Watts [135] into the effects of road humps in residential areas concludes that perceptible levels of vibration can be experienced in nearby buildings. However, complaints are only expected in extreme circumstances.

Railways

Railways carry heavy vehicles at high speed and often pass within a few metres of buildings and their foundations. Consequently, they are generally regarded as the most significant source of ground-borne vibration. Many experimental studies have been conducted into the vibration generated by surface railways [108, 130], trams [72, 114] and underground railways [129, 91]. A review paper by Heckl *et al*. [48] presents some general conclusions applicable to all types of railway. Railway vibration is a low-frequency problem with peak vibration levels in the frequency range from 40 to 80 Hz; the lower frequencies being especially associated with heavy freight trains. A fall of 10 dB typically occurs by 100 Hz and a further 50 dB by 250 Hz. Measurements indicate vibration levels in a similar range to road-generated vibration, that is, from 0.1 to 1.0 mm/s.

The two major sources of vibration reported by the ORE D151 Committee [108] are the vertical bending of the axle and wheel-set, and the vertical bounce mode of the wheel-set on the track. In addition, speed-dependent components may be identified such as that due to the wheels passing each sleeper; typically observed by Grootenhuis [44] between 15 and 30 Hz. Vibration associated with unsteady motion of vehicles – bounce, pitch and roll – lies below 10 Hz and the energy level is usually low.

Although an increase in train speed can in fact reduce vibration levels, depending on the proximity of the wheel-passing frequency to that of the wheel-track resonance, an increase in speed generally leads to more vibration. In some cases it is possible for high-speed trains travelling on soft ground to exceed the Rayleigh (surface) wave speed of the ground, or the bending wave speed of the track. This generates unusually large vibration levels in a similar way to the sonic boom generated by supersonic aircraft, as described by Krylov [68] and Madshus and Kaynia [81].

2.1.2. The Response of Buildings to Ground-Borne Vibration

Modern construction techniques tend to exacerbate the dynamic response of buildings by using continuous light-weight structures such as steel frames and pre-stressed concrete. A prime example is the new IMAX cinema, London, presented in Chapter 1. Such buildings have inherently low damping, compared with older masonry structures, and larger span floors with lower natural frequencies. Primary structural resonances typically occur in the frequency range from 5 to 25 Hz and these can often coincide with a dominant frequency of the source, such as the wheel-passing frequency of a nearby railway. In the past it has been noted that vibration due to a passing train is of short duration and consequently any resonant response of a building is short and limited by damping. However, Grootenhuis [45] shows that, given the damping properties of modern construction materials, a typical train spends more than enough time passing a building for a full state of resonance to be established. Thus modern construction methods tend to result in buildings that are more susceptible to vibration within the frequency range of concern.

Structural vibration can be felt by a building's occupants and is known as *perceptible vibration* when the level is such that the comfort of the occupants is adversely affected. Perceptible vibration occurs mainly in the frequency range from 10 to 60 Hz, as measured by Kuppelwieser [71]. Structural vibration also radiates sound and this can be significant within the audio frequency range, approximately 25 Hz and above. *Re-radiated noise* describes vibration, originally radiated through the ground and into the building, which is then re-radiated as audible, airborne noise. It is not a precise term but it is in common use and is considered preferable to the alternatives of structure-borne or ground-borne noise.

An example of where re-radiated noise may be significant is the disturbance caused by an underground train. This causes very little airborne noise to strike the facade of a building but the ground-borne vibration it generates is transmitted through the foundation and into the building, which then radiates noise. The result is an audible low-frequency 'rumble', even when the vibration itself cannot be felt. The peak frequency-component of the noise does not necessarily coincide with that of the vibration because it depends on the radiation efficiency of the structure concerned. Kuppelwieser's measurements suggest that it is most noticeable in the frequency range from 50 to 125 Hz.

The presence of vibration in a building can often lead to concerns over the possibility of structural damage. However, there is little agreement on the vibration levels that can cause damage due to the range of construction methods and materials used in buildings of different ages. It is the inertia forces acting on a vibrating structure that have the potential to cause damage. These forces are proportional to the acceleration levels and, since most buildings respond less at higher frequencies, the potential to cause damage tends to decrease with increasing frequency. This tendency has led to the definition of *vibration intensity* as a measure of the damaging effects of structural vibration. Strictly, vibration intensity is defined for constant, simply harmonic vibration and is equal to the square of the acceleration amplitude divided by the frequency. In practice, vibration is rarely simply harmonic and the mean-square acceleration level over a narrow frequency band is used. This is expressed in non-dimensional (decibel) units as *vibrars*. Further details can be found in Mead [89].

Evidence cited by Mead suggests that the damaging effect of vibration is more dependent on the inverse-square of the frequency, rather than the simple inverse relationship of vibration intensity. This is equivalent to a dependence solely on the r.m.s. velocity, in this context referred to as the *vibration severity*. This has some physical basis given the fact that particle velocity indicates how energetic the vibration is and hence its ability to cause damage. A standard for the evaluation and measurement of vibration in buildings is under preparation by the International Standards Organisation; provisional damage criteria are given in Table 2.1. The velocity levels represent the greatest of the three orthogonal linear velocities at prescribed points on the structure. Note that Table 2.1 does not refer to the frequency of the vibration: it appears that the velocity for a certain degree of damage is independent of frequency for the normal range of ground-borne vibration and shock.

Typical ground-borne vibration levels due to road and rail traffic lie in the range from 0.1 to 1.0 mm/s, well below the criteria quoted above and even light damage, such as cracking of plaster, is rare. The ORE D151 report [108] notes that, over a period of twenty-five years, not one case of damage has been found to be directly attributable to vibration alone. It is generally concluded that adverse human reaction occurs long before any damage takes place.

Band	R.m.s. velocity [mm/s]	Effect
I	<1.75	No damage
II	2.5-5.0	Damage very improbable
III	5.0-10.0	Damage not probable
IV	>10.0	Damage possible; check the stresses!

Table 2.1: Provisional ISO building damage criteria (reproduced from Mead [89]).

An additional concern with specialist buildings, such as hospitals and research facilities, is that they contain equipment that is highly sensitive to vibration. These vary greatly depending on the equipment concerned and reference should be made to Mead [89] for criteria relating to operational efficiency of certain facilities.

2.1.3. Human Response to Vibration and Re-Radiated Noise in Buildings

The level of vibration within a building that is considered acceptable is dependent upon many factors, human nature being what it is. The threshold of perception provides the ultimate lower limit: Mead [89] reports that, in an upright seated position, the whole body can perceive vertical r.m.s. acceleration levels of the seat as low as 10 mm/s^2 over the frequency range from 1 to 100 Hz. The corresponding mid-range velocity level is of the order of 1 mm/s, which may be compared with the much higher levels in Table 2.1 that are required to cause structural damage.

In practice, the threshold of acceptability varies considerably from around the threshold of perception to several times this value. It is dependent upon factors such as the duration and nature of the vibration, the type of building and the activities of its occupants, and what the occupants feel, hear and see. More subjective factors are also involved, such as what the occupants expect to experience, concerns over structural damage, and whether they believe anything could or would be done to improve the situation, such as reducing the vibration or awarding compensation, if they were to complain.

The comprehensive book by Griffin [43] includes an assessment of building vibration together with the diagram reproduced in Figure 2.2. This figure summarises the many factors that influence human response and illustrates the difficulty in establishing criteria for acceptable levels of vibration. The annoyance simply caused by the tinkling of glasses in a cabinet or the movement

of a painting on a wall, all the more apparent due to reflections from the glass, may be the origin of a complaint.

A number of standards aim to define acceptable vibration levels for buildings. In the UK, the British Standard BS 6472 [20] and the International Standard ISO 2631-2 [59] are used extensively. Griffin presents a review of both standards, together with the German DIN 4150-2 and American ANSI S3.29 standards on vibration in buildings.

A measure deemed appropriate for assessing transient vibration, such as that from a passing train, is the vibration dose value (VDV). This is defined as the fourth root of the integral of the fourth power of the frequency-weighted acceleration a_w:

$$\mathrm{VDV} = \left[\int_{t=0}^{T} a_w^4(t)\,dt \right]^{1/4} \tag{2.1}$$

with SI units of $\mathrm{m/s}^{1.75}$. The VDV provides a cumulative measure of the exposure to both continuous and intermittent vibration, and also shocks, over the period T when vibration may be experienced. It is considered preferable to r.m.s. measures because it accounts for the duration of the vibration as well as its magnitude. Table 2.2 gives the approximate VDVs suggested in both BS 6472 and ISO 2631-2 at which adverse reactions may be expected from people living and working in buildings.

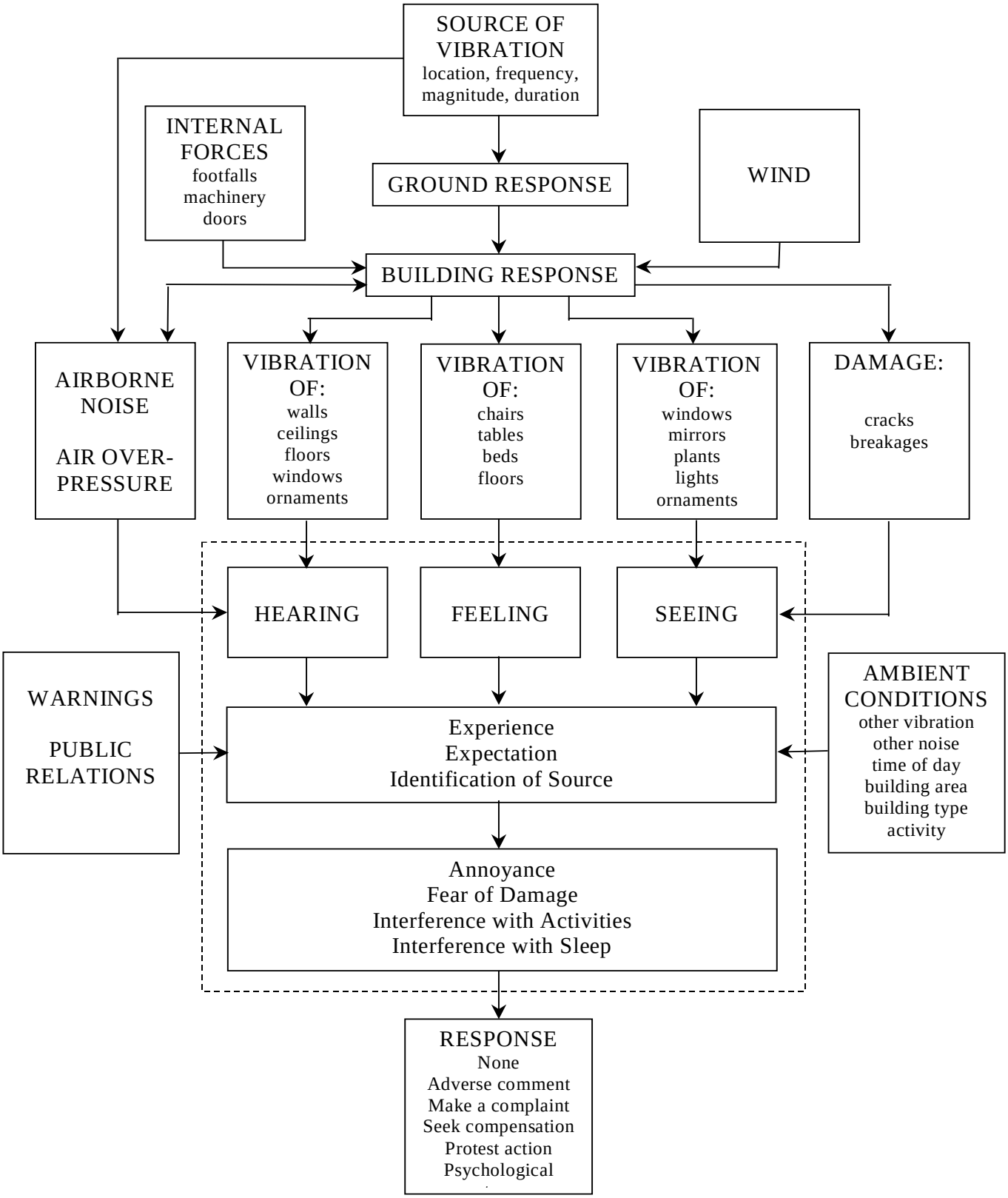

Figure 2.2: The factors influencing human response to vibration in buildings (reproduced from Griffin [43]).

Place	Low probability of adverse comment	Adverse comment possible	Adverse comment probable
Critical working areas	0.1	0.2	0.4
Residential	0.2-0.4	0.4-0.8	0.8-1.6
Office	0.4	0.8	1.6
Workshops	0.8	1.6	3.2

Table 2.2: Vibration dose values [$m/s^{1.75}$] suggested in BS 6472 and ISO 2631-2 at which adverse reactions may be expected from building occupants (reproduced from Mead [89]).

The criteria set out in Table 2.2 make no distinction between vibration exposure during the day and night. Hood *et al.* [53] present criteria, used for the assessment of the planned Channel Tunnel Rail Link, based on the VDV approach but which also account for the time of day and the presence of existing background vibration. In assessing the expected levels of re-radiated noise, they note that no appropriate British or International Standards cover this and instead derive criteria based on American guidelines, London Transport complaints history data and professional experience. Using these, noise levels in residential buildings above 35 dB are considered potentially unacceptable; for office buildings the level is 40 dB. This agrees with the generally accepted view that re-radiated noise in dwellings should not exceed approximately 35 dB, a limit which is supported by Vadillo *et al*. [129] who studied the subjective reaction of residents to nearby underground railways. It is worth noting that, since the publication of this work, DIN 4150-2 has been revised and new standards have been introduced in Norway and Austria to specifically cover both ground-borne vibration and re-radiated noise due to roads and railways. BS 6472 and ISO 2631-2 are also now under review [124] and it is hoped that similar guidance will be included in future editions.

There is evidence to suggest that it is the *combination* of simultaneous noise (airborne or re-radiated) and vibration that should be used in setting acceptability criteria. Noise may either alert the occupant to the vibration or 'mask' its effects to some degree. For example, the reduction in external airborne noise entering a room due to the installation of double windows can reveal the annoying re-radiated noise due to a passing train. Vadillo *et al*. [129] present evidence that suggests that residents in houses less exposed to road traffic noise, or those with double-glazed

windows, are more annoyed by re-radiated noise due to underground trains. Attenuation measures aimed at reducing noise may therefore increase the perception of vibration or vice versa.

Howarth and Griffin [54] describe an experimental study of the response of residents to simultaneous noise and vibration from railways. Using a laboratory representation of a sitting room mounted on a shake-table, subjects were exposed to various combinations of simulated railway noise and vibration. Summing the individual effects of the noise and vibration, in terms of the VDV and sound exposure level, was found to provide a more accurate measure of the total annoyance caused by simultaneous noise and vibration than a method based on either noise or vibration alone.

Human response to the effects of vibration in buildings is clearly a complex problem. Research on the problem and attempts to define appropriate standards are certain to continue for some time yet.

2.2. Methods of Reducing Ground-Borne Vibration

Section 2.1 has illustrated the difficulties in defining acceptable levels of noise and vibration in a building, and different construction projects will in practice set different target levels. In general, the aim must be to reduce the disturbance, whether perceptible vibration or re-radiated noise, below the background level but within economic constraints and to the satisfaction of the end user. This section reviews the various methods of achieving this.

2.2.1. Measures Taken at the Source

The most obvious action to take is to address the problem at its source and control the mechanism by which ground-borne vibration is generated. In the case of road vehicles there is little evidence of measures being implemented in practice, although work by Al-Hunaidi *et al*. [4] and Cole and Cebon [25] suggests that significant reductions can be achieved by modifying vehicle suspension systems.

The most common source of ground-borne vibration is railways and this is reflected in the extensive efforts being made at reducing railway vibration. Track maintenance is the first consideration, particularly the avoidance of track settlement and the deterioration of rail

crossings. Rail grinding and wheel truing eliminates wheel flats and rail corrugations which generate the higher frequency vibrations. More involved measures include the introduction of continuously welded track and the modification of bogie designs. Wilson *et al.* [137] report that reducing the suspension stiffness and unsprung mass significantly reduces the level of vibration generated due to the bounce and wheel-hop modes of the vehicles. Some underground railways use resilient wheels that significantly reduce vibration levels. However, this is not regarded as a general solution because it requires special track and suffers from rapid tyre wear and high power consumption. A review of special track constructions aimed at reducing vibration levels from both surface and underground railways may be found in the ORE D151 report [107].

There is a number of rubber products used to reduce noise and vibration transmission into the ground [100, 109, 110]; see Figure 2.3. These take the form of rubber pads between the rails, base plates and sleepers.

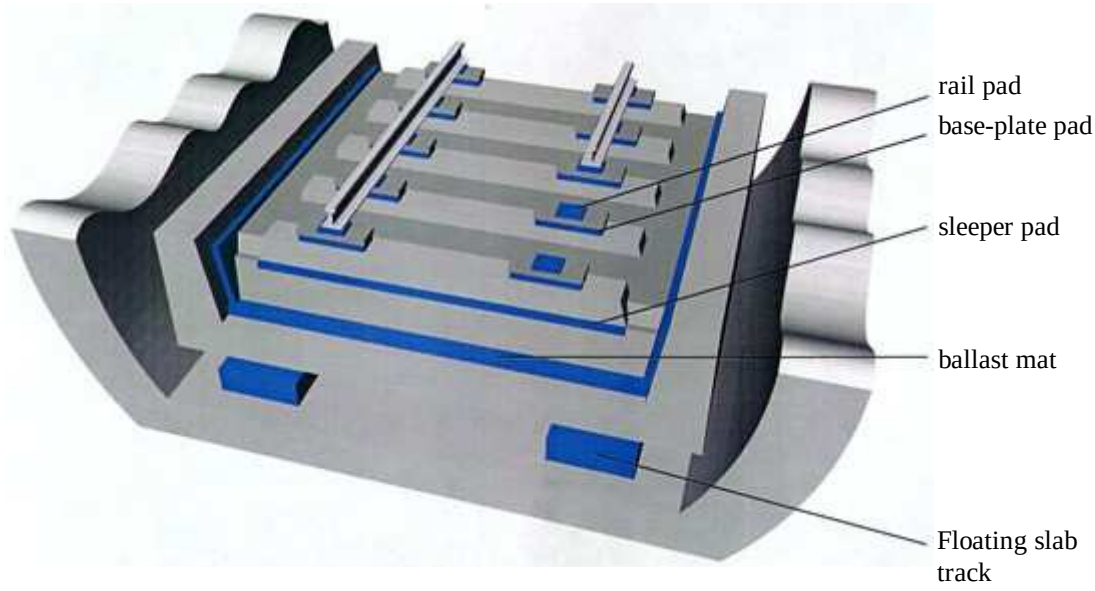

Figure 2.3: The various rubber products used to reduce noise and vibration transmission from railways (courtesy of Getzner Werkstoffe GmbH, Bludenz, Austria).

Floating slab track (FST) is often used with underground railways and is generally regarded as the most effective measure that can be taken with the track. This involves mounting the entire track on a concrete foundation slab that rests on rubber bearings or steel springs. There are numerous examples around the world [45, 137]. An equivalent to FST for conventional track is

the use of thick rubber 'ballast mats' underneath the ballast. Proponents of FST often make impressive claims regarding its performance, although recent work by Forrest [38] and Hunt [58] suggests that the performance in underground railways can be severely limited by interactions with the tunnel and the surrounding soil.

Reducing vibration transmission from the source is not always possible. For example, new buildings are often constructed near existing railways and it is difficult and expensive to take retrospective measures with either the track or the trains. In these cases measures are restricted to the transmission path and the buildings themselves.

2.2.2. Modification of the Transmission Path

Modification of the transmission path, either through or on the surface of the ground, is possible but often difficult to implement in practice. One option available is to construct deep trenches or underground 'wave barriers' to impede the transmission of surface vibration. Lang [72] describes experimental testing of trenches, filled with either ballast or mineral wool, which were found to reduce tram vibration with some success. Yang and Hung [141] consider the effectiveness of wave barriers located close to railways using a two-dimensional finite-element model representing the cross-section of the railway, barrier and soil. They conclude that the effectiveness of such barriers is largely dependent on their dimensions relative to the wavelength of the vibration. This represents the generally held view that wave barriers and trenches are only of use if they can be constructed to be at least as deep as the longest wavelength present, which is typically of the order of 10 m but can be as great as 100 m. In addition, such measures are limited to surface waves only: the ground generally becomes stiffer with depth and this can lead to diffraction of body waves around the barriers.

An alternative measure is the Wave Impedance Block (WIB), a stiff layer introduced below a surface vibration source to shield nearby buildings from the vibration. Both theoretical [123, 111, 122] and experimental [37] studies conclude that WIBs have the potential to help reduce vibration transmission, although more work is required to develop practical cost-effective designs.

A possible measure noted by Wilson *et al*. [137] for underground railways is the use of extra-heavy tunnel structures, to reduce radiated vibration levels, located at increased depth. Again, this is not straightforward to implement in practice.

2.2.3. Measures Taken at the Building

Some methods of reducing the effects of ground-borne vibration in buildings may be straightforward to implement. Examples include avoiding furniture designs that resonate at the frequencies present and moving sensitive equipment near to walls, away from the centre of the supporting floor to a region where vibration levels are likely to be lower. If the problem is one of re-radiated noise, the level of background noise may be increased to act as a mask.

More costly measures involve modifications to the building structure. Damping treatments may be applied to resonant floors or walls, or incorporated into the supporting structure. Vibration neutralizers (dynamic absorbers) may be installed at strategic points on the structure and local stiffening may be undertaken to move structural resonances away from the excitation frequency. When considering a new building, Manning [85] claims that it is invariably possible to design a structure with vibration levels within the BS 6472 Category 4 curve [20] by adjusting floor natural frequencies, using transfer structures as ‘springs’ and separating the building from adjacent ‘source structures’ such as railway structures. This usually reduces the problem to one of re-radiated noise.

In some cases, very low levels of noise and vibration may be required but only in particular areas of a building. In these cases floating floors or a ‘room within a room’ may be required. An example of the latter is a recording studio, constructed as a box mounted on isolation bearings thereby isolating it from the rest of the building structure [51].

In many cases the ground vibration levels are considered large enough to justify the base isolation of a building, that is, the building is designed with vibration isolation bearings between the building and its foundation. Base isolation is not a new concept: Waller [134] notes that lead-asbestos bearings were developed for some buildings in Manhattan in the 1930s as a means of reducing an ‘audible hum’ transmitted through the rock on which the buildings were founded. The first example of a base-isolated building in the UK is Albany Court, a block of flats

constructed on rubber bearings over St James' Park Station, London in 1965; see Figure 2.4. Since then, numerous building projects have been undertaken on sites previously deemed unacceptable due to high levels of ground-borne vibration and examples may be found in all classes of building: residential buildings, office towers, concert halls, cinemas and hospitals. Sharif [119] lists the fifty-five major base-isolated buildings in the UK.

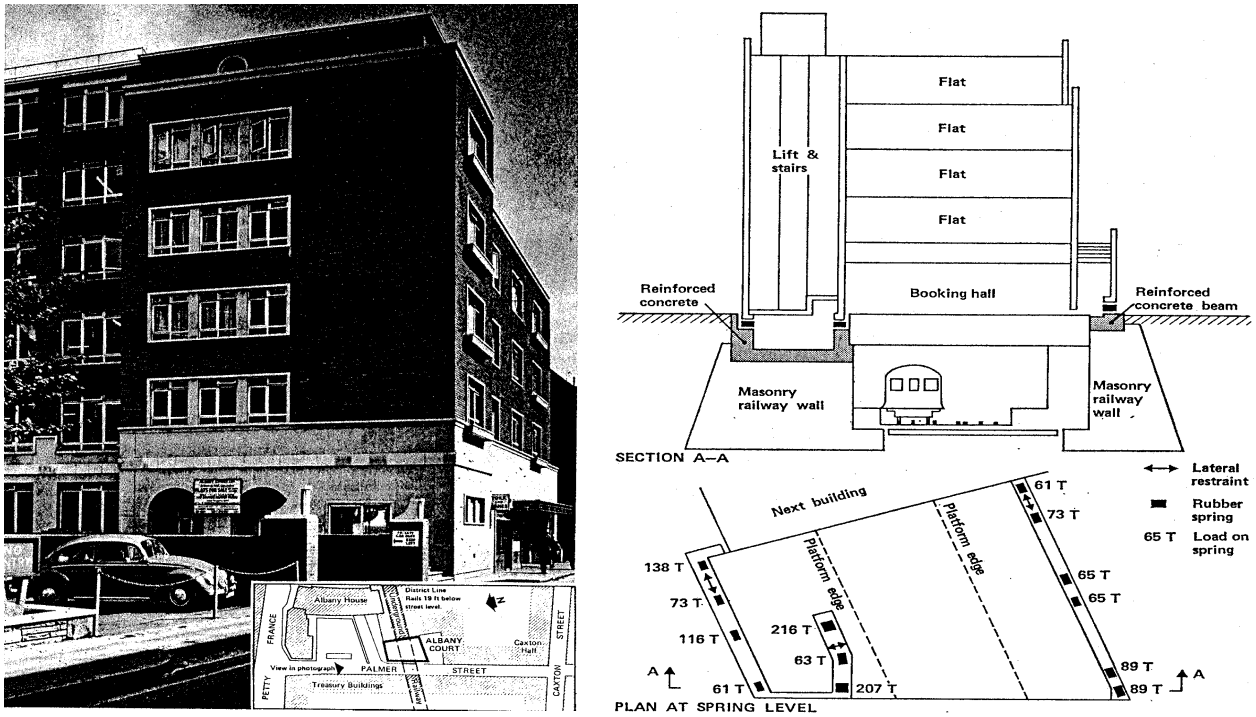

Figure 2.4: The first example of a base-isolated building in the UK is Albany Court, a block of flats constructed on rubber bearings over St James' Park Station, London in 1965 (reproduced from Waller [134]).

2.3. The Design of Base-Isolation Systems for Buildings

In the past, many different types of isolation bearing have been suggested and tried for buildings, including cork, felt, lead-asbestos and neoprene-asbestos. The choice for modern buildings essentially lies between laminated rubber bearings and steel helical springs. This section considers this choice and other design issues in more detail.

2.3.1. The Decision to Base-Isolate and its Implications

The decision on whether or not to base-isolate a building is usually based on a series of vibration measurements, usually r.m.s. velocity levels because these can be directly compared with vibration

acceptance criteria and estimates can readily be made of re-radiated noise levels; see Manning [85] and Grootenhuis [45]. Measurements may be made either at the site in question, prior to any construction work, or on a similar building to the one being designed. The data collected are then usually analysed with the help of empirical, and sometimes theoretical, models.

'Green field' measurements, made prior to any construction work, often provide the only means of assessing the viability of a building project near to an existing source of vibration. However, from these it is very difficult to predict the response of the completed building. Any site measurement is a measure of the response of the measurement point to the dynamic force input of the source and is not an absolute measure of source strength. For example, the construction of the building's foundation is likely to significantly alter the ground vibration field, even before the building itself is constructed.

Ultimately, the decision on base isolation is one of cost and perceived benefit. With the majority of the rubber-isolated buildings discussed by Crockett [32], the cost of isolation was between 2 and 2.5 % of the total cost, although the total range was between 0.75 and 4 %. The spring-isolation of the Le Corum concert hall in Montpellier, France cost 1.5 % [26] while that of an office building in Munich cost 3 % [56]. These extra costs are relatively low given that they are usually offset by the ability to build on an undesirable (due to the high levels of ground-borne vibration) and therefore low-cost site.

There are practical design implications, not normally associated with a typical building project, which must be addressed once the requirement for base isolation has been established. Some of these are discussed by Crockett [32] and Moss [97]. A major implication is the reduction in structural stiffness and overall stability due to mounting the building on isolation bearings. Many tall buildings are constructed of floor slabs supported on columns and derive their stiffness against wind excitation from a service tower or lift shaft. Once the building is mounted on isolation bearings the stiffness of the structure is often no longer adequate and additional stiffening is required. Additional horizontal stability may be provided by sets of horizontal bearings or rubber-sleeved dowel pins. The latter pass through the vertical bearings and are cast at each end into the foundation and respective building column. Alternatively, the isolation bearings may be set at an angle to provide both vertical and horizontal restraint.

Additional consideration must be given to settlement of the building on its bearings, either during construction or subsequently through creep in the bearings, fire proofing of the bearings and designing failsafe measures for the unlikely event of a collapsed bearing. Care must also be taken not to 'bridge' the isolation by, for example, staircases, building services, construction debris or acoustic coupling.

Although seismic isolation systems may be installed in existing buildings, no examples have been found of retrospective isolation against man-made vibrations. This is thought to be due to the high cost of the structural modifications involved.

2.3.2. Generic Design Principles

This dissertation is concerned with *base*-isolated buildings and usually designs do indeed locate the isolation bearings at the base of the building, such as on the pile caps or at basement level. In principle it is possible to locate the bearings higher up the structure and isolate only the upper floors. However, theoretical evidence presented by Cryer [33] indicates that this is less effective due to amplification of the ground vibration by resonances of the unisolated structure below the bearings.

It was noted in Section 2.1.1 that seismic tremors are an obvious natural source of ground-borne vibration and often, when discussing base isolation, it is assumed that isolation against earthquakes is being considered. The design of seismic isolation systems is quite different from those being considered here. Typical earthquakes cover the frequency range from 0.1 to 10 Hz, which includes the major horizontal modes of buildings. Consequently, an earthquake results primarily in low-frequency 'swaying' of buildings and the amplitudes can be large; the vertical component is potentially less damaging as structures are inherently stiff in this direction. Seismic isolation systems are therefore designed with a stiffness that is high vertically but low horizontally, thereby reducing the natural sway frequency and the seismic response of the building. The most common designs are passive and use either sliding bearings or laminated rubber bearings, often combined with some form of mechanical damper to dissipate energy. Active methods based on externally-powered actuators do exist but they are expensive and require maintenance. Seismic

isolation is now a well-developed field in itself and will not be considered further here; see Naeim and Kelly [99] for further details.

The higher frequency content and lower amplitudes of man-made vibrations require a different design approach to seismic isolation systems. Although an outline International Standard has been proposed [61], no standards currently exist specifically governing the design of base-isolated buildings. Instead, designs are based on past experience and the requirements of the particular project.

Usually only the vertical direction is explicitly considered, although ground vibration amplitudes in the horizontal and vertical directions may be found to be comparable, as reported by Waller [134]. The horizontal component of ground motion is, in general, neglected on the assumption that the building's inherent flexibility in this direction provides sufficient isolation. Whether this is a reasonable assumption or not is currently open to debate.

Base isolation systems are principally defined in terms of their *isolation frequency*. This is the frequency of vertical oscillation of the building assuming it behaves as a rigid mass on a spring; see Appendix A. Typical isolation frequencies lie in the range from 5 to 15 Hz, and the lower the frequency the more effective the isolation is expected to be. Note that isolation frequencies should be quoted with care: the stiffness used should be the dynamic stiffness of the bearings, which can depend on several factors such as excitation frequency and static load. Allowance should also be made for secondary stiffnesses. For example, Waller [134] notes that seals between Albany Court and the adjacent building, the ground, stairs, *etc*. represented 20 % of the total bearing stiffness. The mass of the building should be based on the 'unfactored' dead load of the building, including allowances for furniture, occupants and equipment.

The level of inherent damping offered by the bearings is also often quoted as an important design parameter. Base isolation relies on vibration isolation rather than energy dissipation, the basic requirement being a low dynamic stiffness. For maximum isolation, therefore, current designs are based on the inherent damping being as low as possible, provided that sufficient is present to control the rigid-body resonances of the building on the bearings and any internal resonances of the bearings themselves. Despite this, the sensitivity of the overall isolation performance to changes in bearing damping, and isolation frequency, is currently uncertain.

As mentioned in Section 2.2.3, the choice of isolation bearings for modern buildings essentially lies between laminated rubber bearings and steel helical springs. These will now be considered in more detail.

2.3.3. Rubber Bearings for Base Isolation

Bridges were one of the first types of structure to be mounted on rubber bearings. Stevenson [120] describes the use of natural rubber bearings on the Flinders Street railway viaduct in Melbourne, Australia as a means of reducing noise and vibration. The structure was completed in 1891 and, after a century's service, there is no evidence of deterioration of the bearings, the bulk rubber being protected against oxidation and ozone attack by its oxidised surface layer.

The widespread introduction of rubber bridge bearings in the 1950s provided valuable experience that eventually led to their introduction in buildings with the construction of Albany Court in 1965. Since then, rubber bearings, rather than steel springs, have been popular in the UK. Recent examples include Eland House, London [119] and Glasgow Concert Hall; see Figure 2.5. The bearings are available in two different types: either carbon-loaded natural rubber, reinforced and stiffened by laminating with steel plates, or synthetic rubber made more flexible by loading with cork particles and reinforced with layers of woven cloth.

Figure 2.5: One of the natural rubber bearings isolating Glasgow Concert Hall (courtesy of Silvertown UK Ltd, Burton-upon-Trent, UK). The bearings are located in the basement on top of concrete columns that support the building.

A major design requirement for rubber bearings is a high static load-carrying capacity in compression. This prevents excessive deflection of the building during construction, although

some flexibility is desirable to cope with construction tolerances and distribute the load between bearings. Thinner layers allow a bearing to carry a higher static load but this increases its dynamic stiffness.

Muhr [98] discusses in detail the design of rubber bearings and directly challenges the commonly held view that they are impractical for low frequency base-isolation. For a given mass of building, the lower the isolation frequency the larger must be the bearings. While this does have a cost penalty, there is no practical reason why a laminated rubber bearing cannot achieve an isolation frequency of around 4 Hz.

The level of inherent damping of rubber bearings is at least one order of magnitude greater than that of steel springs, and up to three orders greater depending on the formulation [98]. A compound may easily be formulated to have a particular level of damping and there is no need for the auxiliary damper units often used with steel springs. Synthetic rubber has a higher level of inherent damping than natural rubber, although the latter has a lower dynamic/static stiffness ratio and better creep properties [134].

Uneven or excessive creep in the rubber bearings could cause differential settlement and structural damage, and this was a major concern with the design of Albany Court. However, Stevenson [120] reports that after 15 years the amount of creep is close to that predicted and is not expected to exceed 6 mm after 100 years. It is also reported that the general condition of the bearings appears to be excellent. Despite Huffmann's claims [56] that rubber bearings tend to stiffen with age, resulting in deterioration in the isolation efficiency with time, there is little experimental evidence to support this. Measurements made by Alder and Fuller [3] on the rubber bearings of Pelham Bridge in Lincoln, UK, and those reported by the ORE D151 Committee [109] on various rubber-based anti-vibration systems for railways, show negligible deterioration in the elastic properties after decades in service.

Rubber is a highly non-linear material and the dynamic properties of rubber bearings depend on many factors: static load and frequency of dynamic loading, the stiffness increasing with both of these; strain amplitude; operating temperature; and the age and history of the bearing [75]. For most applications, Moss [96] claims that the properties are adequately described by the static load-deflection relationships in compression and shear, the long-term creep behaviour under

constant static load, and the dynamic modulus and damping factor at different frequencies and amplitudes.

The only standard of direct relevance to base isolation, the British Standard BS 6177 [19], provides guidance on the use of rubber isolation bearings for buildings. Rubber is virtually incompressible and the bearing stiffness in compression is controlled by the rubber's behaviour in shear and its ability to bulge sideways. BS 6177 defines the *shape factor* of a bearing as the ratio of the loaded area to that free to bulge. This has a large effect on the bearing's isolation frequency, with a smaller plan area giving a lower isolation frequency for the same thickness and loading. It is therefore usual to use large numbers of small bearings rather than a few large bearings.

2.3.4. Steel Springs for Base Isolation

Helical steel springs have been used extensively in continental Europe for the base isolation of buildings, including isolation against foundation subsidence such as in the German coal mining areas. Their use in the UK has not been as extensive as the rubber alternative; indeed, as recently as 1985, springs were considered too expensive, lacking in inherent damping and the number required too impractical [32]. These concerns are no longer valid, although steel springs are, in general, a more expensive option than rubber bearings. Sharif [119] gives the approximate cost of a spring isolation as £33.00 per tonne of building, compared with £10.60 and £6.70 for natural and synthetic rubber bearings respectively. Recent UK examples of spring-mounted buildings are the IMAX cinema, London [49] and the Bridgewater Concert Hall, Birmingham [5].

There are two main advantages claimed by the manufacturers of steel springs over rubber bearings: lower isolation frequencies and the benefits of pre-compression. Huffmann [56] refers to springs offering isolation frequencies as low as around 2 Hz, although the lowest quoted as being achieved in practice is a 3 Hz isolation for an office building in Munich.

Pre-compression is achieved by supplying the springs in 'spring boxes', pre-compressed between two steel plates to typically 80 % of the expected dead load [5]; see Figure 2.6. This has no effect on the isolation efficiency but it does limit the static deflection of the building during construction. It also enables post-construction adjustment of the springs, should differential

settlement be detected for example, or even removal and replacement of individual springs by jacking up the appropriate building support and re-compressing the spring. In principle, there is no reason why rubber bearings may not be supplied pre-compressed in a similar way, although none are believed to be currently available.

Figure 2.6: Steel springs for base isolation of buildings (courtesy of GERB Schwingungsisolierungen GmbH & Co, Berlin, Germany). The springs are usually supplied pre-compressed in 'spring boxes'.

Further advantages cited by manufactures [131] include a linear load-deflection characteristic, a dynamic/static stiffness ratio of one, and the ability to design for a desired horizontal stiffness avoiding the need for separate horizontal restraints. A disadvantage of steel springs is their greater active mass, leading to internal coil resonances at lower frequencies than the internal resonances of rubber bearings. This has led to concerns over poor isolation performance, particularly since the inherent damping of steel, which is significantly less than that of rubber, may be insufficient to control the resonances. As a means of limiting vibration transmission at the internal resonance frequencies, 'noise-stop pads' in the form of rubber mats may be inserted above or below the springs, or the springs may be enclosed in a cylinder containing viscous liquid. Auxiliary damper units, consisting of dashpots mounted in parallel with the springs, are also sometimes used, particularly to limit the effects of wind excitation. Such additions increase the cost of the isolation and also require long-term maintenance.

2.4. Current Measures of Isolation Performance

No standard measure exists for assessing the performance of base isolation of buildings, although three categories of measure are encountered in practice:

- green-field site predictions;
- predictions given a particular source;
- insertion gain.

The first two are measures of *absolute* performance while the third is a measure of *insertion* performance. These are now considered in more detail, along with a discussion of vibrational power flow.

2.4.1. Green-Field Site Predictions

The future occupants of a new building are interested in the absolute performance of the isolation, that is, what they will experience in the completed building. Engineers may satisfy this by predicting vibration levels within the isolated building given vibration data measured on the 'green-field' site prior to any construction work. This approach often forms the basis of a decision on whether or not base-isolation is necessary, as in the case of the IMAX cinema, London [49].

As discussed by Cryer [33], green-field site predictions require knowledge of the effects of the building and its foundation on the ground vibration-field, as well as an understanding of the dynamic behaviour of the building itself.

2.4.2. Predictions Given a Particular Source

Alternatively, occupants of an existing building may be interested in the vibration levels due to a particular vibration source, such as a new railway. In this case the prediction is particularly difficult to make because a detailed understanding of the entire vibration transmission path is required. Examples of where this has been attempted include the empirical predictions by Hood *et al*. [53], for the assessment of the planned Channel Tunnel Rail Link, and the theoretical

predictions by Chua *et al*. [24] of vibration levels in an office block above an underground railway. In the latter, the frequency range was limited to below 50 Hz and errors of up to 14 dB were encountered when the predictions were compared with experimental measurements.

2.4.3. Insertion Performance

The client who pays for the additional cost of base isolation is interested in the insertion performance, that is, the benefit of inserting isolation bearings beneath a building. It is also of interest to the Engineer who wishes to evaluate alternative types of isolation bearing.

A common measure of insertion performance is *insertion gain* (IG), as investigated experimentally by Sharif [119]; see Section 2.5. This is the ratio, usually expressed in decibels, of the vibration response of the building with the isolation bearings in position to that with no bearings at all. It is impractical to measure IG because the response of a given building cannot easily be measured both with and without the isolation bearings in position. When IG is calculated, it is usual to take the response of the building at its base, directly above the isolation bearings themselves:

$$\mathrm{IG} = 20\log_{10}\left(\frac{x_{isol}}{x_{unisol}}\right) \tag{2.2}$$

Where x_{isol} and x_{unisol} are the responses of the building in the isolated and unisolated condition respectively. Either the displacement, velocity or acceleration response may be used because it is assumed that the behaviour of the building is linear. Note that, in the case of a single-degree-of-freedom system, the IG is equivalent to the transmissibility; see Appendix A.

Insertion gain is based on vibration amplitudes alone. There are problems in using it as a single measure of isolation performance due to the fact that it only accounts for vibration occurring in one direction and varies with position in a building.

2.4.4. Power Flow

Power flow analysis is often used in acoustics. For example, Fahy [36] describes how the analysis of *sound intensity*, the instantaneous rate of work of a fluid per unit area, can be used to

investigate the characteristics of sound fields and sound sources. In a similar way, another way of assessing structures is to consider the vibrational power flows within them.

Langley [73] discusses the theoretical analysis of power flow in beams and frameworks, and illustrates how this is useful for identifying the dominant vibration transmission paths and optimising the location of a vibration neutralizer. White [136] describes experimental techniques for making measurements of power transmission in pipework and how these can be used to design effective vibration control measures. In the context of building vibration, Gibbs and Moorhouse [41, 95] discuss the importance of power flow in characterising the strength of vibration sources, such as those associated with building services machinery. In particular, it is argued that the minimisation of power flow from machines into supporting structures is the key to reducing perceptible vibration in buildings.

2.5. Experimental Investigations into Base-Isolated Buildings

There is little doubt that base isolation is effective: enough evidence is presented by Henson and Charles [49] in describing the success of the IMAX cinema, with what must be one of the most demanding specifications yet. However, the precise nature of the isolation performance and the benefits of certain design features, such as a low isolation frequency or a particular level of damping, remain uncertain. The problem is that it is difficult to measure isolation performance directly. In principle, a building may be jacked up and the bearings removed or alternatives tried but this is difficult and expensive to achieve in practice and no reports of it have been found in the literature. The closest attempt at achieving this is the recent experiment undertaken by Sharif [119] using a test structure constructed on a concrete raft foundation above one of London's underground railway tunnels. The structure, designed as one of the ground floor rooms of a residential house, was a reinforced concrete box, approximately 7 x 7 x 2 m, with openings for doors and windows. Acceleration levels were measured on the floor of the structure in its unisolated condition, resting on concrete blocks, and when isolated on three types of bearing: steel springs, natural and synthetic rubber. In this way the IG of the bearings could be determined. Five main conclusions may be drawn from the investigation:

- for all three bearing types, the vertical rigid-body mode of the structure on the bearings is clearly evident at the isolation frequencies;
- the resonant responses at the three isolation frequencies are similar, within 2 dB, despite different levels of inherent damping in the bearings;
- the lower isolation frequency offered by the steel springs provides better isolation than the rubber bearings – up to 20 dB based on the vibration measurements made;
- vibration modes of the structure significantly reduce the efficiency of the isolation – something not predicted by simple theoretical models;
- inserting isolation bearings decouples the structure from its foundation and results in greater foundation vibration than in the unisolated case due to the reduced constraint – the vibration modes of the foundation then reduce the isolation efficiency.

These are important conclusions, although care must be taken when generalising to practical base-isolated buildings given the small, relatively rigid test structure. Of immediate interest is the final conclusion that highlights the inadequacy of one technique used to indicate isolation performance. Measurements, such as those by Wagner [131] and Anderson [5], are often made above and below the isolation bearings of a completed building to demonstrate lower vibration levels above the bearings. This is not indicative of isolation performance because the measurements concentrate on the forced response of only a small part of a complex structure. In addition, as Sharif's measurements show, the performance may be exaggerated by greater vibration of the foundation than would otherwise exist beneath an unisolated building.

Cryer [33] describes a programme of measurements on a 12-storey rubber-isolated apartment building at Gloucester Park, London. This is a large development close to several underground railway lines and with parts directly above station platforms. Of particular interest are Cryer's measurements of total and direct *transmissibility* between the basement (below the isolation bearings) and various floors within the completed building. The total transmissibility is the ratio of the vibration amplitudes at the two measurement points and does not distinguish between

vibration arriving at the upper measurement point via different paths (it is of interest to the occupants who are not interested in where the vibration comes from). Direct transmissibility is the same ratio but considers only vibration at the two points that is correlated, thereby giving a measure of the importance of the particular input or transmission path.

If the isolated building behaved as a single-degree of freedom system, both transmissibilities would be equal. The measurements clearly show that this is not the case and the building behaves as a multiple-input flexible structure with a series of resonance frequencies. The 9 Hz isolation frequency of the bearings is evident but the level of transmissibility is much less than that predicted by simple theoretical models (see Section 2.6); at frequencies close to structural resonances the transmissibility is large and sometimes greater than unity. It is worth noting that these transmissibility measurements do not indicate isolation performance as no account is taken of vibration levels in the building's unisolated state.

Claims of impressive isolation performance should be viewed with caution. Commins *et al*. [26] describe the design of the Le Corum concert hall in Montpellier, France, which is located close to a surface railway. The difference, of up to 50 dB, between third-octave band vibration levels measured in the nearly completed hall and an unisolated conference hall on the same site is cited as evidence of effective isolation. However, when the details of the site are considered, it is evident that the conference hall is smaller and much closer to the railway than the new concert hall.

The use of scale models in a laboratory centrifuge, to simulate correctly the effects of gravity, is a common technique for investigating the geotechnical and seismic behaviour of structures; see for example the work of Madabhushi [79] and Cheney *et al*. [23]. Investigations into the behaviour of model footings have also been conducted by Nii [104] using a model half-space. No reports of experiments using physical models of base-isolated buildings have been have been found in the literature. It is believed that this is largely due to the frequency range of interest, which, for man-made ground-borne vibration would need to extend up to at least 100 Hz. This corresponds to 1 kHz in a 1:10 scale model and good models of a building, its foundation and isolation bearings would be difficult to produce.

2.6. Modelling Base-Isolated Buildings

Since the construction of the first base-isolated buildings, various attempts have been made at modelling their behaviour. This section reviews the two different available approaches, empirical and theoretical, that have been used to model base-isolated buildings and those subject to ground-borne vibration from roads and railways.

Models may be formulated in either the time or frequency domains. The former is often used for the seismic analysis of structures where peak vibration levels due to a transient event are of interest. Non-linear behaviour can also be treated in the time domain. When dealing with man-made ground-borne vibration the problem may be treated as linear, given the low strain amplitudes involved, and the response, particularly that due to railways, is of sufficient duration that the frequency domain is the most appropriate. This and the next section therefore concentrate on frequency-domain models. The range of models discussed is similar to that currently being considered for incorporation into a proposed International Standard on predicting ground-borne vibration due to railways in tunnels [61].

2.6.1. Empirical Models

Empirical models are usually based on octave or one-third octave band vibration measurements made at existing sites. Statistical analysis is carried out on the data and a database compiled which may then be used to make predictions for similar sites. Such models are widely used for the prediction of noise and vibration levels in buildings.

Hood *et al.* [53] present two empirical models specifically for the assessment of trains in bored tunnels, one for the prediction of vibration in buildings and the other for re-radiated noise. The calculation procedures for both models are similar in that they each consist of three stages, considering the source, propagation path and building response, and combine track-side data with a series of factors or transfer functions derived from statistical analysis of a database of measurements.

Kuppelwieser [71] presents a semi-empirical prediction model developed for the Swiss Federal Railways. This is based on a step-by-step multiplication of track-side vibration data with a series of transfer functions to obtain predictions of noise and vibration levels in buildings. The transfer

functions account for the various stages in the propagation path from the rail to the building, as in the models of Hood *et al.*, but they may be determined from theoretical models chosen by the user as well as by analysis of a database. Two further examples of semi-empirical models, based on a combination of analytical techniques, laboratory tests and *in-situ* measurements, are due to Melke [91] and Madshus *et al*. [80].

While empirical models can provide useful, as well as reasonably rapid, estimates of noise and vibration levels once a database has been compiled, they do have significant limitations. It is very difficult to compile a sufficiently comprehensive database, with a statistically significant set of data, to cover all the possible combinations of source, transmission path, type of building, *etc*. Databases are therefore rarely large enough to enable underlying physical behaviour to be identified. In fact, 'modular' models, such as those reviewed, treat each part of the transmission path separately and the various factors and transfer functions are assumed to be independent. This approach does not represent the physical situation and cannot account for coupling between various parts of the system, such as that due to interaction between the building and the ground. In addition, the databases often remain commercially confidential to the organisations that prepared them and two databases rarely share the same data structure.

2.6.2. Theoretical Models

Theoretical models rely on fundamental physical laws and some simplifying assumptions to produce a series of equations. These are then solved either analytically or numerically.

Analytical Models

The simplest model of a base-isolated building is the standard single-degree-of-freedom (SDOF) oscillator; see Appendix A. This represents the isolated building as a rigid mass supported on a spring and some form of damping element to represent the isolation bearings. The model was originally used by Waller [134] when describing Albany Court and is used extensively in the design of isolation bearings for machines. This, together with its inherent simplicity, has probably resulted in the model's popularity: it is often used to illustrate the principle of base isolation by

bearing manufactures [126] and is sometimes used to promote one bearing design over another [56, 131].

Despite its popularity, the value of the SDOF model is extremely limited because it fails to describe some of the major features of a building's dynamic behaviour, in particular the flexibility and damping properties of the building and the effects of its foundation. Even the relatively rigid test structure investigated by Sharif (see Section 2.5) suffered from structural resonances and foundation behaviour that significantly reduced the performance of its isolation.

The SDOF model may be improved by replacing the rigid mass with a flexible column. Newland and Hunt [102] and Grootenhuis [44] use the analytical solutions for an elastic bar to demonstrate that a typical building column has several natural frequencies below 200 Hz at which the predicted level of isolation is significantly reduced. Swallow and Sharif consider two similar models based on a lumped parameter model [121] and an elastic bar [119]. Additional masses and springs are coupled to the bar to represent the connected floors and it is shown that this reproduces some of the low-frequency behaviour observed with real building columns. Column models may also be coupled to a simple foundation model to account for vibration radiation into the ground [102].

The column model is still limited by its one-dimensional nature. It does not account for flexural vibration and the fact that, in practice, buildings have multiple inputs at which the vibration may or may not be correlated. The work of Cryer [33] takes the analytical models one stage further by using the dynamic-stiffness method to model a two-dimensional portal-framed building resting on a three-dimensional piled foundation. The dynamic-stiffness method accounts for both the longitudinal and transverse behaviour of the columns and floors of the building, and the foundation model, based on a series of Novak piles (see Section 2.7.2), accounts for the interaction between the building and the ground. The computation time is minimised by treating the building as infinitely long and using periodic structure theory [88]. Cryer's model clearly demonstrates the importance of including a representation of the foundation: a significant amount of vibrational energy is radiated into the ground when the building is subject to a point excitation at one of the pile caps. While the model goes some way to accounting for the behaviour of a

piled foundation, only the vertical pile behaviour is accounted for and no attempt is made to model interaction between neighbouring piles through wave propagation in the surrounding soil.

Balendra *et al*. [7] use a semi-analytical model to predict the response of buildings to underground railways. The two-dimensional plain-strain model comprises a rigid tunnel in an elastic half-space with a rigid embedded footing coupled to a lumped mass to represent the building. The rigid-body representations of the tunnel and the building are considered major limitations of this model.

Numerical Models

The finite-element method (FEM) [142, 143] is now the most widely used numerical technique for engineering analysis and it has naturally been used to model vibration of buildings. Manning [85] describes how, for design purposes, building vibration levels are estimated using simple FEM models given a digitised copy of measured railway vibration which is applied to the base of the model. A similar approach is used by Hao *et al*. [46] to predict vibration due to road traffic. Both approaches are limited as they ignore the presence of a foundation.

Chua *et al*. [24] use a FEM model to predict vibration levels in a four-storey office block directly above four underground railway tunnels. The foundation is represented as a portion of the ground with a non-reflecting boundary to reduce unwanted wave reflections (see Section 2.7.1). The model is two-dimensional, assuming plain-strain conditions, and the building is treated as symmetrical to reduce the number if elements required. Results are compared with experimental measurements over the frequency range from 6 to 50 Hz and, although the trend with frequency is correct, errors of up to 14 dB exist above 15 Hz.

It is fair to conclude that the FEM requires considerable computing power to achieve reasonable results, even with relatively simple two-dimensional models. Results are usually obtained using modal analysis and are therefore inaccurate at higher frequencies unless large numbers of elements are used.

Thornely-Taylor [125] uses the finite-difference method (FDM) [132] to model the tunnel-soil-building system in the time-domain based on the equations governing Euler beams, thin plates and elastic solids. Again the model is computationally expensive despite being two-dimensional.

Statistical energy analysis (SEA) [140] is another major numerical technique for analysing structural vibration. Craik [29] describes in detail how the method may be effectively applied, within the audio frequency range, to modelling noise and vibration transmission through buildings. Trochides [128] uses a SEA approach to model building vibration from an underground tunnel. Reasonable agreement is achieved between predicted levels and those of a simple 1:10 scale model over the frequency range from 250 to 4000 Hz. As these examples demonstrate, the success of SEA relies on a structure having sufficient modal density such that individual modes are unimportant and vibration levels in various parts of the structure may be described in terms of the average vibrational energy. The problem with applying SEA to ground-borne vibration is that the frequency range of interest extends down to only a few hertz where modal behaviour is important. Despite its computational efficiency, SEA is therefore considered inappropriate for studying base-isolated buildings.

It is clear from the literature that, where the ground has been included in building models, a three-dimensional representation is rare. Two-dimensional models are preferred for their simplicity and the need, especially when using the FEM, to restrict computation times. The disadvantage of this is that such models assume the system to be invariant in the anti-plane direction and this significantly limits the ability to correctly model wave propagation. For example, vibration that in practice may propagate on spherical wavefronts is constrained to cylindrical wavefronts and therefore attenuates less rapidly with distance, foundations such as piles are represented as infinitely long barriers around which waves can no longer diffract and point excitation becomes a coherent line source. It is therefore considered important to investigate further the methods available for modelling the three-dimensional nature of wave propagation in the ground.

2.7. Modelling the Ground and Foundations

This section summarises the nature of wave propagation in the ground and reviews the methods available for modelling this and the dynamic behaviour of foundations.

2.7.1. Wave Propagation

The fundamental behaviour of the ground may be modelled by a homogeneous isotropic linear-elastic half-space, that is, a solid bounded only by the plane formed by its free surface. Such a solid can support two types of body wave: primary and secondary waves [42, 12]. Primary or P-waves, also known as dilatational, compression or irrotational waves, result in particle motion parallel to the direction of propagation; secondary or S-waves, also known as distortional, shear or equivoluminal waves, result in particle motion perpendicular to the direction of propagation and may be polarised in a particular direction.

A third wave-type exists due to the presence of the free surface. This is known as the Rayleigh wave, after Lord Rayleigh who first discovered them [116]. Rayleigh waves are essentially surface waves, with the majority of the motion lying within one wavelength of the free surface and describing a retrograde ellipse in the vertical plane.

All three wave-types are non-dispersive and propagate at speeds dependent solely on the elastic properties of the half-space. P-waves travel the fastest, followed by S-waves and then Rayleigh waves. In general, body waves are generated by both buried and surface vibration sources, while Rayleigh waves are generated by surface sources or whenever P-waves or vertically polarised S-waves occur in the neighbourhood of the free surface. The partition of energy between the three wave-types depends strongly on the size of the source relative to the wavelengths generated. Wolf [138] shows that, for a surface source, if it is localised to an area with dimensions small compared to the S-wavelength, Rayleigh waves transmit approximately half of the energy with the remainder going largely into S-waves. If, on the other hand, the source is large, the majority of the energy is transmitted by body waves. In practice, a notable source of body waves is an underground railway whereas notable sources of Rayleigh waves are surface vehicles or piling operations.

Waves are attenuated by two mechanisms: *radiation damping* and *material damping*. The former is sometimes referred to as geometric damping and is due to the geometric spreading of wavefronts as they propagate away from a source, thereby dispersing energy over an increasing area. This attenuation is independent of frequency but affects Rayleigh waves the least because they are essentially confined to the surface. Material damping describes the frictional energy

dissipation that occurs during the passage of a wave when the ground undergoes cyclic shear or compression, and higher frequencies are attenuated the most over a given distance. The behaviour of foundations is generally dominated by radiation damping and, as reported by Prange [113], foundation models are often found to be insensitive to the level of material damping.

A uniform half-space is an idealisation and, in practice, the ground is often much more complex. In particular, soil density often increases with depth, leading to refraction of waves, and different soil strata may be present that result in multiple reflections and refractions of waves at their interfaces. The latter has a dispersing effect and wave speeds no longer depend solely on the elastic properties of the soil but also on frequency. Further complications arise due to inhomogeneous soils. While these are addressed in the literature, see for example Auersch [6] and Degrande *et al*. [34], they are considered beyond the scope of this review.

Closed-form analytical solutions to problems of ground-borne wave propagation are rarely possible and numerical techniques are usually used instead; in particular the FEM and the boundary-element method (BEM) [17, 35]. When modelling the semi-infinite extent of the ground, domain methods, such as the FEM, suffer from a fundamental problem. The element mesh should extend towards infinity but in practice must be curtailed at a certain distance. The resulting artificial boundary leads to spurious wave reflections that can distort the solution. Simple solutions to this problem are to use large models – which require long computation times – or specify artificially high material damping such that the waves have decayed sufficiently before reaching the boundary; see for example Mohammad and Krylov [94]. In general this is unsatisfactory and a more sophisticated approach is required in the form of non-reflecting boundaries.

A technique explained in detail by Bettess [14] and adopted by some of the commercial FEM codes, such as ABAQUS, is to use conventional finite elements in the interior of the model but form the boundary from *infinite elements*. In the frequency domain these take the form of a finite element based on a shape function that includes the outgoing waveform. Radiation to infinity is then accounted for by either multiplying the shape function by a decay function, such as a decaying exponential, or by mapping the element onto an infinite domain. However, no existing

infinite elements for elastic waves are exact, due to the difficulty of accounting for all three wave-types, and successful approximations have proved to be computationally expensive.

Wolf and Song [139] advocate two alternative approaches: the 'damping-solvent extraction method' and the 'consistent infinitesimal finite-element cell method'. The former is an approximate method that derives the behaviour of an unbounded domain from that of a conventional FEM model with artificially high material damping; the latter relates the unbounded domain to a geometrically similar finite domain bounded by an infinitesimal layer of finite elements. The second method converges to the exact solution in the finite-element sense but is mathematically complex. Neither approach appears to have been adopted by other researchers.

In contrast to the FEM, the BEM is ideally suited to problems with unbounded domains. Because the problem is formulated on the boundary, only the boundary has to be discretized rather than the full domain; the governing differential equations are automatically satisfied. The mesh generation process is simpler and the system of equations is smaller than those of an equivalent FEM model. In addition, the radiation of waves to infinity is automatically accounted for and particularly accurate results may be obtained within the interior of the domain because here the solution is fully continuous. Consequently the BEM is often used to model wave propagation in the ground and numerous examples may be found in the literature; see for example Beskos [13]. Specific examples concerning the three-dimensional modelling of foundations will be considered in the next section.

2.7.2. Foundations

The literature relating to the dynamic modelling of foundations is extensive, and largely due to research relating to machine foundations and seismic response. The first foundations to be studied were simple surface footings for which semi-analytical solutions are possible. For example, Luco and Westmann [77] present the full three-dimensional response of a rigid circular footing on the surface of an elastic half-space. Later work by Mita and Luco [93] extends this to embedded footings.

The solutions to such models are mathematically complex and this has motivated the search for discrete-model approximations. De Barros and Luco [9] present a five-parameter discrete

model that approximates the dynamic stiffness of simple rigid footings very well. It does, however, only account for vertical motion of a single footing. Further approximate models may be found in Wolf [138]. To effectively model flexible footings of arbitrary geometry, and to study the interaction between several footings, a BEM approach is required; see for example Karabalis and Rizos [63], and Qian and Tham [115].

Novak [105] was one of the first researchers to consider the dynamic behaviour of a pile, and the first to consistently account for the effects of radiation damping. The Novak model uses the solutions for an elastic bar and Euler beam to model a pile's longitudinal and transverse behaviour, while the surrounding soil is modelled as an infinite number of infinitesimally thin, independent, horizontal layers that overly either rigid bedrock or an elastic half-space. The model has the advantage of an analytical solution and experiments by Novak and Grigg [106] and Cryer [33] show that it describes the behaviour of individual piles well, given its simplicity. A limitation of Novak's model is that it is incapable of modelling the interaction between several piles. It is important to establish whether or not this is significant when modelling base-isolated buildings.

Kuhlemeyer [69, 70] is credited with one of the first rigorous analyses of a single pile. This model uses an axisymmetric FEM formulation in conjunction with non-reflecting boundaries. Again, the limitations of this method, outlined in Section 2.7.1, mean that it is unsuitable for more than one pile.

The BEM is now regarded by many researchers as the most rigorous, versatile and economical method for analysing piles and pile groups. A good example of this is the model by Sen *et al*. [118]. This model uses an elastic bar-beam – representing the pile in a similar way to Novak's model – coupled to either a uniform or layered, elastic half-space. The model by Kaynia [65] is similar but uses a different formulation of the Green's functions for a layered half-space. It is important to note that the Green's functions used in either of these models are significantly more complex than those for an elastic full-space and their calculation requires considerable computational effort in itself; see Appendix B for a note on Green's functions and further details of the BEM.

Both the Sen and the Kaynia model are capable of modelling the interaction between neighbouring piles through wave propagation in the surrounding soil, known as pile-soil-pile

interaction (PSPI). Lo [76] demonstrates that results from a simplified version of Sen's model compare well with field measurements on real piles, although only vertical motion is considered. In general, when calculating the interaction between two piles, any intermediate piles are ignored; the overall solution for several piles is then obtained by superposition. This approach is necessary due to the long computation times required by models involving large numbers of piles. This may be acceptable when dealing with low-frequency seismic waves but at the frequencies associated with ground-borne vibration the wavelengths are often comparable with the diameter of a pile and wave reflections from intermediate piles are likely to have a significant effect. This view is supported by the work of Qian and Tham [115] who note that the sub-soil coupling between two surface footings, as represented in a comprehensive BEM model, is reduced by intermediate footings. The effect is expected to be greater with piles, which may interact over a significant proportion of their length.

A number of models approximately account for PSPI; see for example Lo [76] and Wolf [138]. The most comprehensive is due to Gazetas and Makris [40, 84]. They model the piles themselves in a similar way to Novak but the soil is represented by a pile-soil interface of continuously distributed linear springs and viscous dashpots, with wave propagation accounted for by modelling the far-field as an elastic half-space. Although the results are approximate, the computation time is significantly shorter than more rigorous models.

The recent BEM model by Kattis *et al*. [64] is a rare example of a comprehensive three-dimensional model that accounts fully for the elastic behaviour of a row of piles. While useful in a research environment, such models require extensive computational effort and are unsuitable for use on a personal computer.

2.8. Conclusions

The primary sources of ground-borne vibration are roads and railways. Peak vibration levels typically occur in the range from 10 to 80 Hz and significant levels rarely exist above 200 Hz. Ground vibration levels range from 0.1 to 1 mm/s and, in the vast majority of cases, cause no damage to buildings. However, disturbance of their occupants can have significant social and economic consequences.

Modifications to the vibration source or the transmission path can help reduce building vibration, although both are often difficult to achieve and not entirely effective. Since the 1960s, base isolation of buildings has provided an alternative solution. There is little doubt that base isolation is effective but there is no standard measure of isolation performance and the level of performance is uncertain. There is a clear need for a means of determining the effectiveness of base isolation and objectively evaluating the alternative types of bearing.

Experiments with real buildings require measurements to be made with and without isolation bearings in position. Such measurements are difficult to make and specific to the building in question, making it difficult to draw general conclusions. Experiments based on physical models are difficult to produce, as well as time consuming and expensive. These conclusions suggest that a mathematical model is required.

The complexities of the vibration source, transmission path and building, together with the uncertainties in soil properties, structural damping mechanisms, *etc*., ensure that the prediction of vibration levels given a particular source is difficult. However, a mathematical model is well suited to investigating the fundamental behaviour of a base-isolated building and establishing the best design practice. Existing models generally account for a particular aspect of dynamic behaviour, such as the building's flexibility, wave propagation in the ground, or some aspect of foundation behaviour. No one model fully accounts for all of these because the complexity of the system ensures that comprehensive models rapidly become computationally expensive. A generic model is required that accounts for the essential dynamic behaviour of a base-isolated building while remaining computationally efficient such that, in principle, bearing manufacturers, consultants and designers can readily evaluate various base isolation designs. This dissertation is a contribution towards this end.

Chapter 3
AN INITIAL MODEL OF A BASE-ISOLATED BUILDING

When modelling a physical system there is always a compromise between adequately accounting for its behaviour and computational efficiency. This is particularly so with a system as complex as a base-isolated building. As well as being computationally expensive, a detailed model requires the specification of many parameters that cannot be accurately determined and, at the time of a particular design feasibility study, most parameters are unknown. A fast and convenient model will incorporate only the essential dynamic behaviour of the building and its foundation, and will involve the specification of a minimum number of parameters.

In Chapter 2 it was concluded that a theoretical, rather than empirical, model is most suitable for a base-isolated building. This chapter considers the building, its foundation and the ground as the three essential elements of a base-isolated building. The dynamic behaviour of each element is discussed and appropriate modelling techniques are identified. An initial model of a base-isolated building is then presented which is used to introduce a new measure of isolation performance based on vibrational power flow. It is argued that this new measure is more useful than one based on vibration amplitudes.

3.1. Modelling the Building

A building is a three-dimensional structure and a fully three-dimensional analysis, which must consider six degrees of freedom at any one point, is time consuming both to formulate and to solve. A two-dimensional representation of a building subject to in-plane excitation greatly simplifies the modelling process, halving the number of degrees of freedom, and is the approach

taken by many researchers (see Section 2.6.2). It may be argued that the lack of the third dimension is too great a simplification and it is necessary to consider the significance of this.

The introduction of a second dimension, when going from a one-dimensional column to a two-dimensional portal frame, significantly alters a model's behaviour. This is because a portal frame is able to account for the flexural and shear behaviour of a building's floors and walls, and the coupling between them, rather than just the longitudinal behaviour of a single column. Introducing the third dimension extends this behaviour into three dimensions and enables the modelling of torsion in the various structural elements: the result is an increase in modal density and an additional mechanism of vibration transmission. The increase in modal density is not expected to reveal significantly different base-isolation behaviour to that exhibited by a two-dimensional model. The significance of accounting for torsion depends on the nature of the excitation from the ground but, provided the excitation lies in the plane of the building, torsion does not arise. These limitations of a two-dimensional model are considered to be a price worth paying for the significant increase in computational efficiency.

It is therefore decided to represent the building as a two-dimensional portal frame and reserve the three-dimensional treatment for the modelling of the foundation. With the latter, the third dimension is particularly important because it governs wave diffraction. As discussed in Section 2.6.2, there are several methods of modelling a building. The finite-element (FEM) and finite-difference methods (FDM) require considerable computing power to achieve reasonable results, even with relatively simple models. An alternative, statistic energy analysis (SEA), is considered inappropriate given that modal behaviour is important in the frequency range associated with ground-borne vibration. The technique chosen here is the dynamic-stiffness method (DSM).

3.1.1. The Dynamic-Stiffness Method

The DSM is an alternative to the FEM for modelling the dynamic behaviour of structures, the primary advantage being improved accuracy at higher frequencies without the need for large multi-element models. The application of the DSM to building structures is supported by the work of Cryer [33] who found its predictions of transmissibility agreed well with measurements

made in the Gloucester Park building, London. This section provides a summary of the method, as well as discussing the modelling of damping and the behaviour of beams in more detail.

Summary of the Method

A typical element from a two-dimensional portal frame, illustrated in Figure 3.1, is defined by its length L, cross-sectional area A, second moment of area I, density ρ and Young's modulus E. The DSM formulation used in this dissertation describes the dynamic longitudinal and transverse behaviour of this element by the analytical solutions for an elastic bar and Euler beam, that is, one in which shear deformation and the effects of rotational inertia are assumed negligible. Given the low vibration amplitudes of interest, any coupling between the longitudinal and transverse behaviour is assumed negligible.

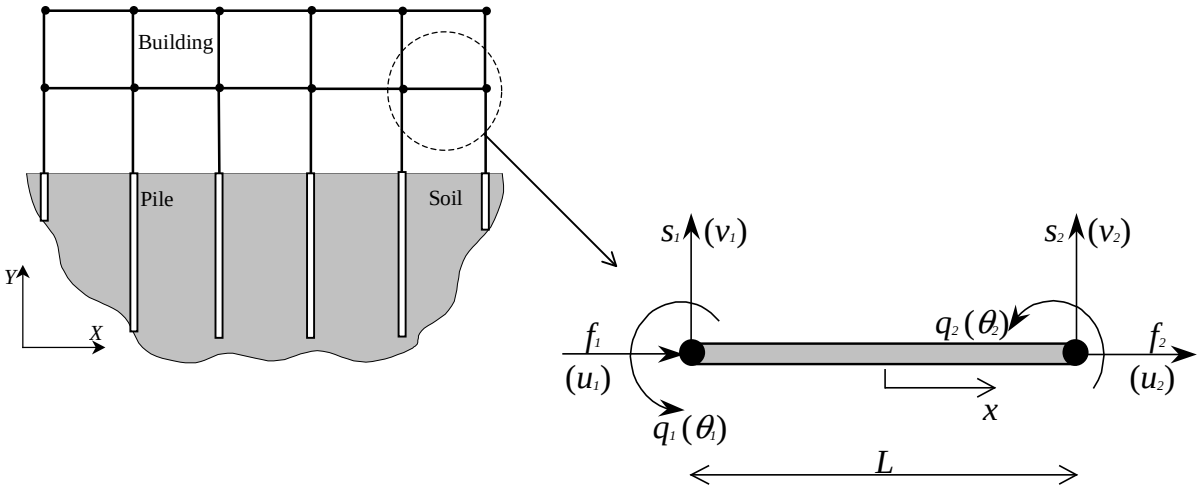

Figure 3.1: A typical bar-beam element from a two-dimensional portal frame. The generalised forces *f*, *s* and *q*, and the corresponding generalised displacements (*u*, *v* and θ) are related through the element's dynamic-stiffness matrix. Junctions between elements are known as nodes (•).

For harmonic motion, the complex amplitudes of the generalised forces and displacements associated with element '*j*' are related, in the global coordinates (*X*, *Y*), through the element's global dynamic-stiffness matrix $\mathbf{K}_{\mathbf{g}}^{j}$:

$$\mathbf{f}_{\mathbf{g}}^{j} = \mathbf{K}_{\mathbf{g}}^{j}\mathbf{u}_{\mathbf{g}}^{j} \tag{3.1}$$

where $\mathbf{K}_{\mathbf{g}}^{j}$ is a 6 x 6 frequency-dependent matrix, as derived in Appendix C.

The individual dynamic-stiffness matrices corresponding to each element of the portal frame are assembled, in a similar way to the FEM [143], to give the overall global dynamic-stiffness matrix **K** of the model. External forces and moments may only be applied at the junctions between elements, known as *nodes*, and these must be in equilibrium with the internal forces of the elements. Thus, for a model with *N* nodes:

$$\mathbf{f} = \mathbf{K}\mathbf{u} \tag{3.2}$$

where $\mathbf{u} = \begin{bmatrix} u^1 & v^1 & \theta^1 & u^2 & v^2 & \theta^2 & \ldots & u^N & v^N & \theta^N \end{bmatrix}^{\mathrm{T}}$ is a vector containing the complex amplitudes of the generalised nodal displacements due to the applied generalised forces $\mathbf{f} = \begin{bmatrix} f^1 & s^1 & q^1 & f^2 & s^2 & q^2 & \ldots & f^N & s^N & q^N \end{bmatrix}^{\mathrm{T}}$ ('T' denoting the vector transpose). Each component of **K** is the sum of the stiffnesses associated with the elements connected to the corresponding node.

Solution of the model for a given vector **f** is achieved by inverting Equation 3.2 for each frequency of interest, accounting for any constrained degrees of freedom in **u**.

Accounting for Structural Damping

Structural damping is the least well-understood aspect of structural dynamics and remains the subject of intense research; see for example Adhikari and Woodhouse [1, 2]. As in the rest of this dissertation, only linear models are considered.

The two major classes of structural damping in buildings are *material damping*, due to the frictional energy dissipation that occurs in the bulk material, and *boundary damping*, due to dissipation at structural joints. Material damping is often modelled in the frequency domain by representing the material as a viscoelastic continuum and accounting for damping by replacing the standard elastic constants with suitable complex values [15]. Thus, for example, Young's modulus *E* becomes $E(1+i\eta_E)$. In this way the primary effect of damping – the production of a phase difference between stress and strain – is accounted for. The *damping loss factor* η_E is, in general, a function of frequency – and indeed must be so to satisfy causality in the time domain

[30] – but is often found to be approximately constant in practice. Frequency independent damping is known as *hysteretic* damping and results in a structural response with modal bandwidth proportional to frequency.

A common alternative to the hysteretic model, originated by Rayleigh [117], is *viscous* damping. This is the damping associated with a classical viscous dashpot and represents energy dissipation that is directly proportional to velocity. It may be defined as proportional to mass, assuming that each elemental mass is connected to a dashpot secured to ground, or proportional to stiffness, each elemental stiffness having a dashpot in parallel with it. Either one of these definitions may be used, or a combination of both (as in commercial FEM codes such as ABAQUS). Newland [101] describes how the two definitions lead to structural responses with either constant modal bandwidth (mass proportional) or modal bandwidth proportional to frequency squared (stiffness proportional).

Laboratory experiments on various concrete columns described by Newland and Hunt [102] indicate that the variation in damping between columns with differing reinforcing configurations is small and that the loss factors are not strongly dependent on frequency, being of the order of 0.01. This supports the use of hysteretic damping to describe a single reinforced concrete column. Based on experimental data, Cremer *et al*. [31] advocate the use of a loss factor of 0.02 as representative of a wide range of construction materials. However, it is unlikely that these figures are appropriate for an entire building where damping may be an order of magnitude greater than the inherent material damping. The extra damping is believed to be due to boundary damping arising at structural joints and damping due to radiation into foundations. Such damping is less easy to model than material damping and, in practice, the model adopted for material damping is usually assumed to extend to boundary damping, assuming that the damping is 'small', that is $\eta << 1$.

Given that no precise structural damping model currently exists, the hysteretic model is adopted throughout this dissertation, primarily for its mathematical simplicity in the frequency domain. Where appropriate, a nominal loss factor of 0.1 is assigned to the building to account for both material and boundary damping.

A Note on Beam Behaviour

The DSM formulation used in this dissertation is based on Euler's model for the transverse behaviour of a bending beam. This model ignores the rotational inertia and shear deformation of the beam and it is prudent to confirm that this is acceptable for the frequency range of interest.

The validity of Euler's assumptions is discussed by Timoshenko *et al*. [127] using the example of a simply supported beam. They derive the following equation for the natural frequencies of the beam when rotational inertia and shear deformation are accounted for:

$$\omega_j = \omega_j^E \left(1 - j^2 \frac{2.1\pi^2 I}{AL^2} \right) \tag{3.3}$$

where ω_j^E is the j^{th} natural frequency predicted by Euler's theory for a beam of rectangular cross-sectional area A, length L and second moment of area I.

The frequency range of interest for ground-borne vibration extends up to 200 Hz (see Section 2.1.1). For a typical concrete beam, with a cross-section of 0.3 x 0.3 m, $L = 4$ m, $E = 10$ GPa and $\rho = 2400$ kg/m^3, the highest frequency mode in this range is the third mode (156 Hz). The corresponding error introduced by Euler's assumptions, according to Equation 3.3, is 8 %. Euler's model is therefore reasonably accurate even close to the limit of the frequency range of interest and, given that peak levels of ground-borne vibration occur significantly below 200 Hz, the use of Timoshenko's beam theory is considered unnecessary.

An additional concern is the effect of a static axial load in the beam, such as that due to pre-stressing during construction. This problem is also considered by Timoshenko *et al.*, who give the natural frequencies of a simply supported beam subject to a compressive axial force S as:

$$\omega_j = \omega_j^E \sqrt{1 - \frac{SL^2}{j^2 EI\pi^2}} \tag{3.4}$$

A typical upper design limit corresponds to an axial load of 10 % of the Euler buckling load, that is, $SL^2 / EI\pi^2 = 0.1$. According to Equation 3.4, this reduces the value of the first natural frequency by 5 %, with higher modes being affected less. It is therefore also considered unnecessary to account for static axial loads in the building model.

The above calculation also confirms the assumption that the dynamic, longitudinal and transverse behaviour of the beam are effectively uncoupled; axial loads due to longitudinal vibration are sufficiently low to have negligible effect on the transverse modes.

3.1.2. Modelling the Isolation Bearings

The dynamic behaviour of the isolation bearings themselves, particularly rubber bearings, is complex and worthy of detailed study in itself. For the purposes of this dissertation, three aspects of bearing behaviour are considered: the assumption of linearity, the specification of representative stiffnesses and the significance of internal resonances.

Linearity

The characteristics of natural rubber are discussed in detail by Lindley [75]. For many practical applications the most serious difficulty in predicting the stiffness of rubber components is the material non-linearity. This results in elastic properties that vary both with strain amplitude and frequency. However, under the conditions associated with base-isolated buildings, it is reasonable to assume that these effects are negligible. The primary reason is the very low dynamic strain amplitudes, of the order of 0.01 %, associated with a bearing subject to ground-borne vibration. At these strain levels the rubber may be assumed linear provided that an appropriate value of the dynamic elastic modulus is used, which depends on the static load applied by the building.

The variation in elastic modulus with frequency is more significant, although frequency-independence is a reasonable assumption over the frequency range of interest. Lindley states that, above 5 °C, the modulus of natural rubber does not vary strongly with frequency below 1 kHz, and with filled rubbers the variation is generally below 25 %. The variation up to 200 Hz for most rubbers is therefore expected to be small.

In the case of helical steel springs, the assumption of linearity is more easily justified given the inherent small-strain elastic behaviour of steel. The static and dynamic stiffnesses are equal and there is no significant variation in stiffness with frequency.

Bearing Stiffnesses

Assuming linear elasticity, and ignoring torsion about the vertical axis, an isolation bearing may be described by three stiffnesses associated with the three modes of deformation. This is illustrated for a rubber bearing in Figure 3.2.

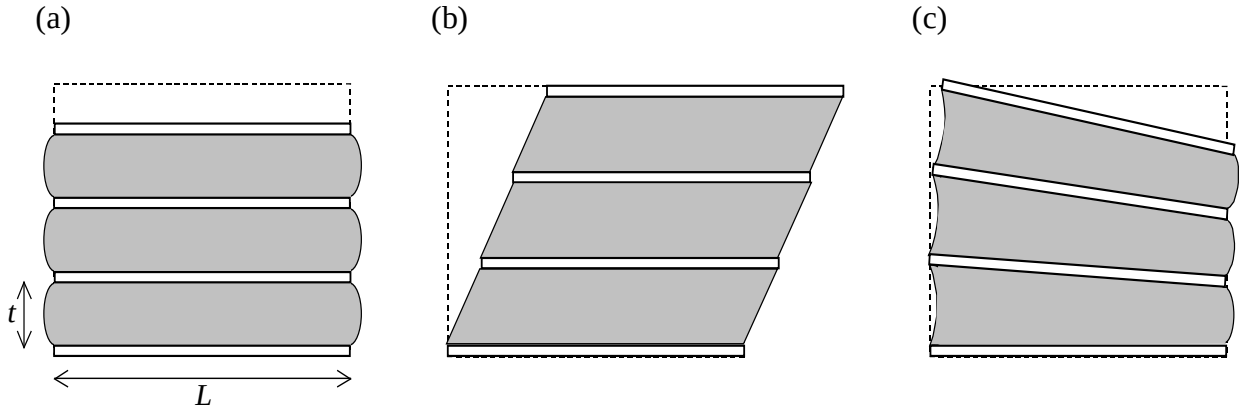

Figure 3.2: The three modes of deformation associated with a rubber isolation bearing are described by three stiffnesses: (a) k_v, vertical compression; (b) k_u, horizontal shear; and (c) k_θ, rotation.

The isolation frequency f_{isol} for a particular base-isolated building is defined (in Hz) as the frequency of vertical oscillation of the building assuming it behaves as a rigid mass on a spring; see Appendix A. As far as modelling is concerned, therefore, the isolation frequency defines the vertical stiffness of each bearing as:

$$k_v = 4\pi^2 f_{isol}^2 M \tag{3.5}$$

where *M* is the mass supported *per bearing*.

The horizontal and rotational stiffnesses are less easily specified given that no definitive relationship exists between these and the vertical stiffness, and little experimental data is available. In the case of a laminated rubber bearing the ratio k_u / k_v is primarily determined by the shape factor of the constituent pads, which is inversely proportional to the square of the pad thickness *t*; see Naeim and Kelly [99]. In the case of a helical steel spring k_u / k_v depends on its length and diameter, as given by Wahl [133].

The rotational stiffness of an individual rubber pad is very low [99] and the same is expected to be true for steel springs. However, rotational stiffness is rarely considered explicitly during the design of a building [50]. Clusters of bearings are always used in practice and the total rotational stiffness seen by a column therefore depends primarily on the vertical stiffness of a single bearing and the number used. A further consideration is that additional horizontal bearings are often used to provide extra restraint against wind loading.

In conclusion, the *in-situ* stiffnesses associated with the isolation bearings, whether rubber bearings or steel springs, depend heavily on the design details of the particular application. No general relationship exists between them, although the horizontal and rotational stiffnesses are generally less than the vertical stiffness. In this dissertation, each isolation bearing is represented by three linear massless springs, with k_v specified according to Equation 3.5 and a value of $0.5k_v$ assigned to both k_u and k_θ. This value is considered to be typical of base isolation bearings [21], although it is used on the understanding that more precise figures may easily be specified if they ever become available. Internal damping in the bearings is accounted for using the hysteretic model, as described in Section 3.1.1. Loss factors of 0.01 and 0.1 are investigated as the approximate limiting values associated with isolation bearings, the values being representative of an undamped steel spring and a high-hysteresis rubber bearing respectively.

Internal Resonances

Concern is sometimes expressed over the possibility of internal resonances in the bearings reducing their isolation performance. This is particularly so in the case of steel springs where their higher active mass leads to coil resonances at lower frequencies than the internal resonances of rubber bearings. No experimental data has been found in the literature concerning this problem, nor is it available from manufacturers. Instead the analytical expression for an undamped helical compression spring will be considered. For a spring of mean coil diameter *D* consisting of *n* turns of wire of diameter *d*, shear modulus *G* and density ρ, Wahl [133] derives the lowest longitudinal natural frequency (in Hz) as:

$$f_1 = \frac{2d}{\pi D^2 n}\sqrt{\frac{G}{32\rho}} \tag{3.6}$$

A typical base-isolation spring, designed for an isolation frequency of between 3 and 6 Hz, is described by the following parameter values [22]: $D = 80$ mm, $n = 4$, $d = 20$ mm, $G = 81$ GPa and $\rho = 7840$ kg/m^3. With these values, Equation 3.6 predicts the lowest natural frequency to be 283 Hz. Base isolation springs have low ratios of free length to coil diameter (less than 3) and therefore the lowest transverse natural frequency always exceeds the longitudinal frequency [133].

The value of 283 Hz exceeds the frequency range associated with ground-borne vibration and it is unlikely that significant energy is available in the frequency range of internal bearing resonances for these to affect isolation performance. This view is shared by at least one of the major bearing manufacturers [21]. Consequently, although internal resonances may be a concern for lightly damped bearings, they will not be considered further in this dissertation.

3.2. Modelling the Ground and Foundation

It has been argued in Section 3.1 that the essential dynamic behaviour of a building may be accounted for with a two-dimensional model. One option, followed by several researchers, is to extend this to include a two-dimensional representation of the ground and foundation. However, as discussed in Section 2.6.2, the invariance of such a model in the anti-plane direction is a major limitation. It is considered essential that the three-dimensional nature of the ground is accounted for in order to correctly model wave propagation and the behaviour of a foundation.

The model chosen to represent the ground is the homogeneous isotropic linear-elastic half-space, as reviewed in Section 2.7.1. This accounts for the essential dynamic behaviour of the soil, including the three fundamental wave types and both radiation and material damping. The soil is characterised by two elastic constants: in this dissertation these are the shear modulus μ and Poisson's ratio ν. The small-strain values are used, which are determined in practice from seismic measurements of wave speed; see for example Lavergne [74]. The assumption of linearity is again justified on the basis of the strain amplitudes associated with ground-borne vibration. These typically lie between 10^{-6} and 10^{-5}, well below the shear strain of 10^{-3} reported by Gazetas [39] as the level at which soil non-linearities become significant.

The uniform half-space is an idealisation and, in practice, the ground is often much more complex, such as comprising different soil strata. The complications involved in modelling

inhomogeneous and layered soils are considerable and, although it is recognised that their effects may be significant, they are beyond the scope of this dissertation.

3.2.1. Damping in Soils

In his study on vibration from surface vehicles, Hunt [57] presents a review of material damping in soils. From the many experimental studies, such as those of Prange [113] or Hardin and Drnevich [47], it is concluded that a hysteretic damping model is suitable for many soils over the frequency range and amplitudes typical of ground-borne vibration. More recent work by Bolton and Wilson [16] supports this conclusion.

Incorporating the hysteretic damping model into the half-space representation of the ground, in general, requires the specification of two damping loss factors, one for each of the elastic constants chosen to describe the soil. The soil damping model used throughout this dissertation is that adopted by Hunt, in which the material damping is assumed to occur entirely through shear motion. This is supported by the generally held view that damping in soils due to volumetric expansion is small. Damping is accounted for by a complex shear modulus $\mu(1+i\eta_\mu)$ and a complex Poisson's ratio $\nu - i\eta_\mu(1+\nu)(1-2\nu)/3$, where the loss factor in shear $\eta_\mu << 1$ is assumed constant. Henceforth, the soil loss factor η_μ will simply be referred to as η.

As discussed in Section 2.7.1, the behaviour of foundations is generally dominated by radiation damping, rather than material damping. When modelling foundations, therefore, representing the unbounded nature of the ground such that radiation damping is correctly accounted for is generally of more concern than the precise modelling of material damping. This is confirmed later in Section 4.1.1.

3.2.2. Soil-Structure Interaction

There is some experimental evidence that constructing a building significantly modifies the original ground vibration field. Newland and Hunt [102] present data that show that pile-cap vibration levels of the Gloucester Park building, London decreased in magnitude as construction progressed. This suggests that the building acts to constrain its foundation, thereby locally reducing its vibration levels, either by the effect of adding mass or stiffness. However, base

isolating a building decouples it from its foundation and, as noted in Section 2.5, the experimental work of Sharif [119] indicates that this results in greater foundation vibration than with an unisolated building.

A building is never coupled to the ground through a single point but rather through some form of distributed foundation, such as a series of footings or piles. It is suspected that interaction between different parts of a foundation, through wave propagation in the ground, is also an important consideration when modelling a base-isolated building.

This section aims to investigate the significance of the above behaviour with simple theoretical models.

Single-Footing Models of Soil-Structure Interaction

Consider the model shown in Figure 3.3. This represents the base-isolated building as a single-degree-of-freedom (SDOF) system, consisting of a rigid mass *M* on a spring of stiffness *k*, founded on a rigid, massless, circular footing bonded to the surface of a homogeneous isotropic linear-elastic half-space.

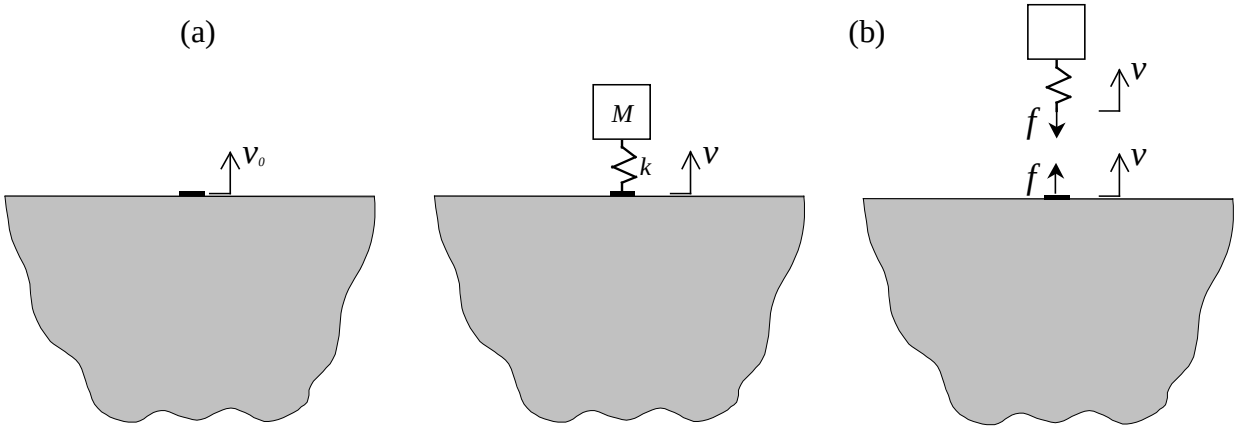

Figure 3.3: A SDOF building model of a base-isolated building. A SDOF system is founded on a rigid, massless, footing bonded to the surface of an elastic half-space. Prior to construction of the building (a) the footing moves with amplitude v_0; following construction (b) this becomes *v*.

Assume that, prior to the construction of the building, a ground vibration field exists which causes the footing to move vertically with a harmonic displacement amplitude v_0. Following the construction of the building, the footing amplitude becomes *v*, which may be expressed as the superposition of the original amplitude and that due to the force *f* applied by the SDOF system:

$$v = H_f f + v_0 \tag{3.7}$$

where H_f is the driving-point displacement frequency-response function (FRF) of the foundation.

Equilibrium of forces ensures that an equal but opposite force acts on the base of the SDOF system and compatibility of displacements ensures that this also moves with amplitude *v*. Therefore, for the building:

$$v = -H_b f \tag{3.8}$$

where H_b is the displacement FRF of the building.

Eliminating *f* from Equations 3.7 and 3.8 enables the ratio of the final footing amplitude to that prior to the construction of the building to be expressed as follows:

$$\frac{v}{v_0} = \frac{H_b}{H_b + H_f} \tag{3.9}$$

For v/v_0 to approach unity, that is, for the construction of the building to have negligible effect on the response of the footing, $H_b >> H_f$. This is equivalent to saying that the dynamic stiffness of the isolated building – which is the inverse of the displacement FRF – must be much less than that of the foundation.

For the SDOF model the FRF H_b may be derived, using a similar analysis to that in Appendix A, as:

$$H_b = \frac{1-(\omega_n/\omega)^2}{k} \tag{3.10}$$

where $\omega_n = \sqrt{k/M}$ is equivalent to the isolation frequency of the building in rad/s and ω is the frequency of excitation.

The FRF of the footing on the half-space is given by Johnson [62] and may be expressed as:

$$H_f = \frac{1}{\mu r_0 (\alpha + i \frac{\omega r_0}{c_S} \beta)} \tag{3.11}$$

where μ and c_S are the shear modulus and S-wave speed of the half-space respectively, r_0 the radius of the footing and $i = \sqrt{-1}$. Johnson gives α and β, as functions of frequency, for the case of a half-space Poisson's ratio of 0.25. This is a little low for typical soils but is acceptable for the purposes of this model.

Using Equations 3.10 and 3.11, Equation 3.9 is plotted against frequency in Figure 3.4 for the cases of a 5 and 15 Hz isolation frequency, and an 'infinitely stiff' bearing corresponding to an unisolated building. The functions α and β do not vary much (less than 8 %) over the frequency range considered and are assumed constant, for simplicity, at $\alpha = 5.3$ and $\beta = 4.4$. The remaining parameter values are chosen as representative of a base-isolated building: $M = 10^5$ kg; $\mu = 200$ MPa and $c_s = 316$ m/s, as determined by Cryer [33] for the Gloucester Park building; $r_0 = 0.5$ m and nominal damping loss factors of 0.05 are assigned to the spring and the half-space, although the results are insensitive to these values.

At low frequencies, two resonances dominate the behaviour of the model. The resonance of the SDOF system on its foundation occurs first, leading to amplified 'post-construction' vibration levels, followed by the resonance of the mass on the spring, at which the high dynamic stiffness of the SDOF system constrains the foundation resulting in the anti-resonances in the curves. At high frequencies, the dynamic stiffness of the SDOF system tends towards the static stiffness of the spring (see Equation 3.10) and, since this is much lower than the dynamic stiffness of the foundation, the effect of the SDOF system becomes small. Both the '5 Hz' and '15 Hz' curves clearly indicate higher post-construction foundation vibration levels than those for the unisolated building.

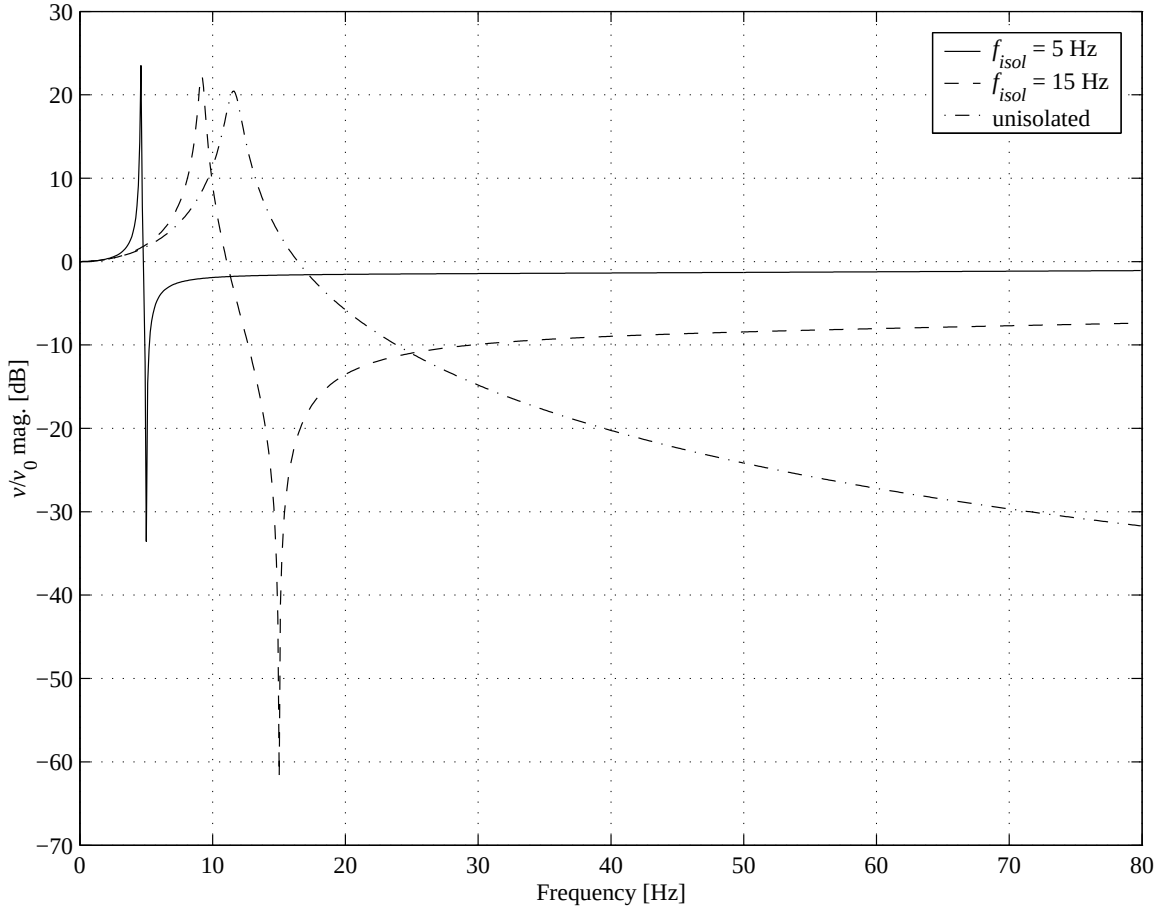

Figure 3.4: Soil-structure interaction of a base-isolated building as predicted by a SDOF building model founded on a footing bonded to the surface of an elastic half-space. The ratio of the final footing amplitude v to that prior to the construction of the building v_0 is shown for different isolation frequencies.

It is instructive to replace the rigid-mass representation of the building with an elastic column of height L, cross-sectional area A, Young's modulus E and density ρ; see Figure 3.5. In this case, Equation 3.10 becomes:

$$H_b = \frac{1}{k} + \frac{1}{EA\lambda}\left(\frac{e^{\lambda L} + e^{-\lambda L}}{e^{\lambda L} - e^{-\lambda L}}\right) \tag{3.12}$$

where the FRF of the column is as derived by Newland [101] with $\lambda = i\omega\sqrt{\rho/E}$.

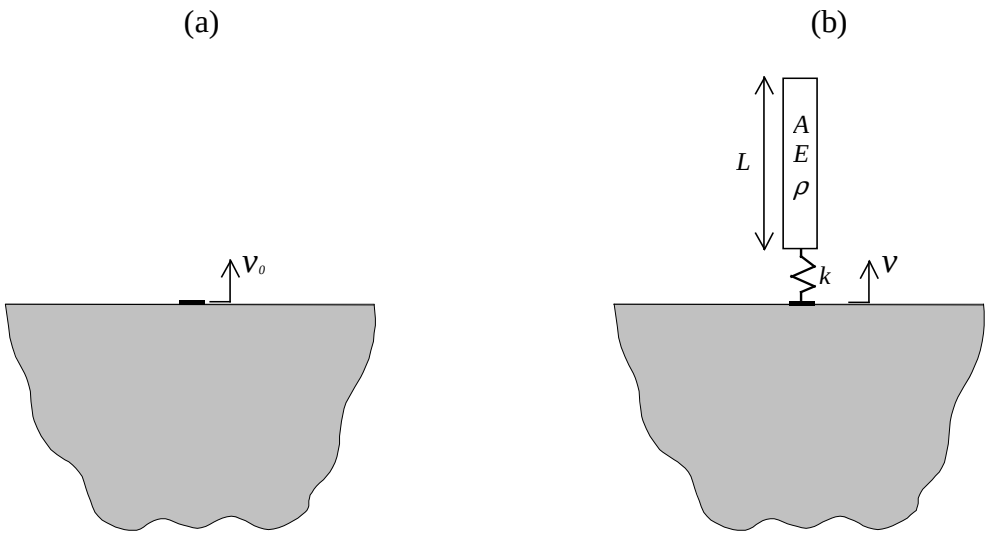

Figure 3.5: An elastic column model of a base-isolated building. An elastic column is founded on a rigid, massless, footing bonded to the surface of an elastic half-space. Prior to construction of the building (a) the footing moves with amplitude v_0; following construction (b) this becomes *v*.

With this new form of FRF describing the building, Equation 3.9 leads to Figure 3.6. The parameter values for the spring, footing and half-space remain the same as before while those of the column are as follows: $L = 30$ m; $E = 10$ GPa, with a nominal damping loss factor of 0.01, and $\rho = 2400$ kg/m^3, representative of concrete; and $A = 1.39$ m^2 such that the overall mass of the column is 10^5 kg, as for the SDOF model. The primary effect of the building's flexibility, as modelled by the elastic column, is to superpose a series of resonance and anti-resonance peaks on the response of the foundation; the mean response remains the same as if the building were rigid. The constraining effect of the building is therefore primarily an 'added-mass effect' due to its inertia, rather than its stiffness. The effect is less noticeable when a lower isolation frequency is used due to the improved decoupling of the column from the footing.

The above models do indeed replicate the behaviour noted by Newland and Hunt [102] during the construction of Gloucester Park, and it is reasonable to conclude that constructing a building on its foundation does reduce the foundation vibration levels. The models also replicate the behaviour observed experimentally by Sharif [119], in that the improved decoupling of the building from its foundation achieved with a lower isolation frequency results in higher post-construction vibration levels of the foundation. The added-mass effect is investigated further in Section 5.3.2.

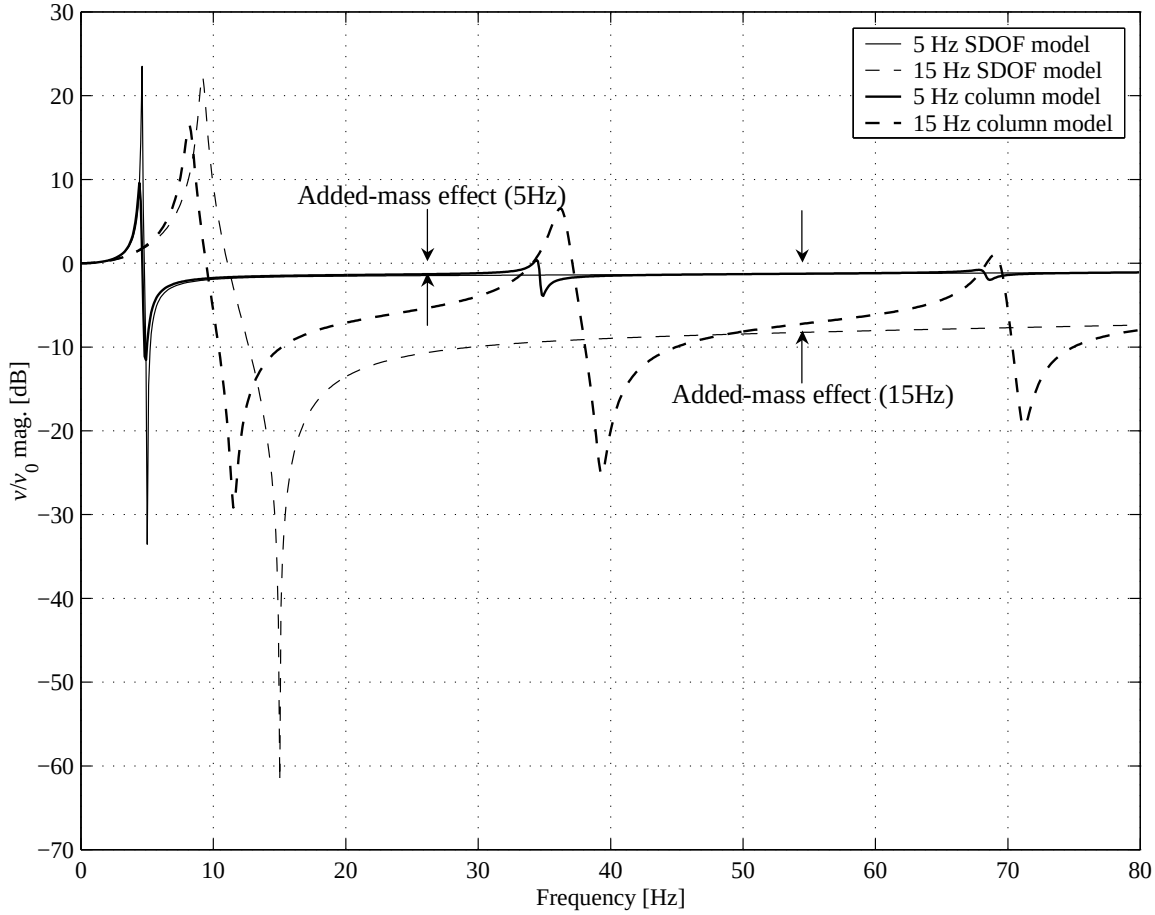

Figure 3.6: Soil-structure interaction of a base-isolated building as predicted by a building model consisting of an elastic column on a spring, founded on a footing bonded to the surface of an elastic half-space. The ratio of the final footing amplitude v to that prior to the construction of the building v_0 is shown for different isolation frequencies, along with the results of Figure 3.4 for comparison.

A Two-Footing Model of Soil-Structure Interaction

The model illustrated in Figure 3.7 extends the SDOF model of the previous section to a 2-DOF model, with mass M and moment of inertia I_G, founded on two footings. This is the simplest possible model that enables wave interaction effects to be studied.

An analysis similar to that for the SDOF is now undertaken. Assume that, prior to the construction of the building, the footings move vertically with amplitudes v_0^1 and v_0^2. Following the construction of the building, these become v^1 and v^2, which may be expressed in a similar form to Equation 3.7:

$$\begin{bmatrix} v^1 \\ v^2 \end{bmatrix} = \begin{bmatrix} H_f^{11} & H_f^{12} \\ H_f^{21} & H_f^{22} \end{bmatrix} \begin{bmatrix} f^1 \\ f^2 \end{bmatrix} + \begin{bmatrix} v_0^1 \\ v_0^2 \end{bmatrix} \tag{3.13}$$

where f^1 and f^2 are the forces applied to the footings by the building and the 2 x 2 matrix $\mathbf{H_f}$ describing the foundation contains the displacement FRFs of the footings on the half-space. Because the system is symmetric $H_f^{11} = H_f^{22} = H_f$, with H_f given by Equation 3.11, and reciprocity implies that $H_f^{12} = H_f^{21}$.

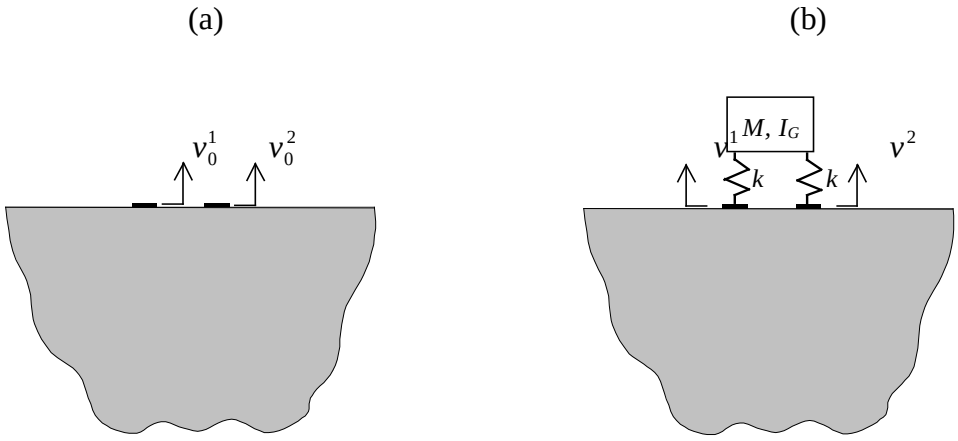

Figure 3.7: A 2-DOF building model of a base-isolated building. A 2-DOF system is founded on rigid, massless, footings bonded to the surface of an elastic half-space. Prior to construction of the building (a) the footings move with amplitudes v_0^1 and v_0^2; following construction (b) these become v^1 and v^2.

The latter two FRFs represent the coupling between the two footings due to wave propagation in the soil. They are specified approximately here using the vertical component of the Rayleigh wave solution for the 'far-field' surface response of the half-space due to a surface point force. This is given by Johnson [62] and enables the FRFs to be specified as:

$$H_f^{12} = H_f^{21} = \frac{0.183}{\mu}\sqrt{\frac{\omega}{2\pi S c_R}}e^{-i\left(\omega S/c_R + \pi/4\right)} \tag{3.14}$$

where c_R is the Rayleigh wave speed of the half-space and S is the spacing of the footings.

Strictly, Equation 3.14 is only valid for 'mid-range' frequencies: at low frequencies the wavelengths are of the order of the footing spacing and the far-field assumption is no longer valid; at high frequencies they are of the order of the footing radius and the load applied by the footing no longer behaves as a point force.

Considering the building and applying equilibrium and compatibility at the footings, the equivalent to Equation 3.8 is:

$$\begin{bmatrix} v^1 \\ v^2 \end{bmatrix} = -\begin{bmatrix} H_b^{11} & H_b^{12} \\ H_b^{21} & H_b^{22} \end{bmatrix} \begin{bmatrix} f^1 \\ f^2 \end{bmatrix} \tag{3.15}$$

where the 2 x 2 matrix $\mathbf{H_b}$ contains the displacement FRFs of the building model, as derived in Appendix D.

Eliminating the forces from Equations 3.13 and 3.15 gives the displacements of the footings following the construction of the building:

$$\begin{bmatrix} v^1 \\ v^2 \end{bmatrix} = \left[\mathbf{I} + \begin{bmatrix} H_f^{11} & H_f^{12} \\ H_f^{21} & H_f^{22} \end{bmatrix} \begin{bmatrix} H_b^{11} & H_b^{12} \\ H_b^{21} & H_b^{22} \end{bmatrix}^{-1} \right]^{-1} \begin{bmatrix} v_0^1 \\ v_0^2 \end{bmatrix} \tag{3.16}$$

where **I** is a 2 x 2 identity matrix. Note that coupling between the footings, both through the building and through the soil, results in the displacements of each footing in the presence of the building (v^1 and v^2) being functions of both displacements in its absence (v_0^1 and v_0^2).

To evaluate Equation 3.16, all that remains is to specify the pre-construction vibration field. The form of Equation 3.16 indicates that the phase difference between the two footings is important and, in practice, they will rarely be in phase. A physically based representation of v_0^1 and v_0^2 is the steady-state excitation due to passing Rayleigh waves (see Section 2.7.1). Assuming that the building is far enough away from the source of the Rayleigh waves, such that the wavefronts are parallel lines, the phase difference between the two footings may be expressed as:

$$v_0^2 = v_0^1 e^{-i\omega S / c_R} \tag{3.17}$$

where the Rayleigh waves pass from left to right in Figure 3.7 such that the 'downstream' footing 2 lags footing 1 by an amount dependent on their spacing *S*.

Figure 3.8 plots the ratio v^1/v_0^1 for the 'upstream' footing, for the cases of a 5 and 15 Hz isolation frequency (the results for v^2/v_0^2 are similar). The parameter values for the footing and

the half-space remain the same as in the two previous models; the building is now modelled as a uniform mass of 10^5 kg, as for the SDOF model, with a width equal to the footing spacing, $S = 8$ m, and a height $L = 30$ m.

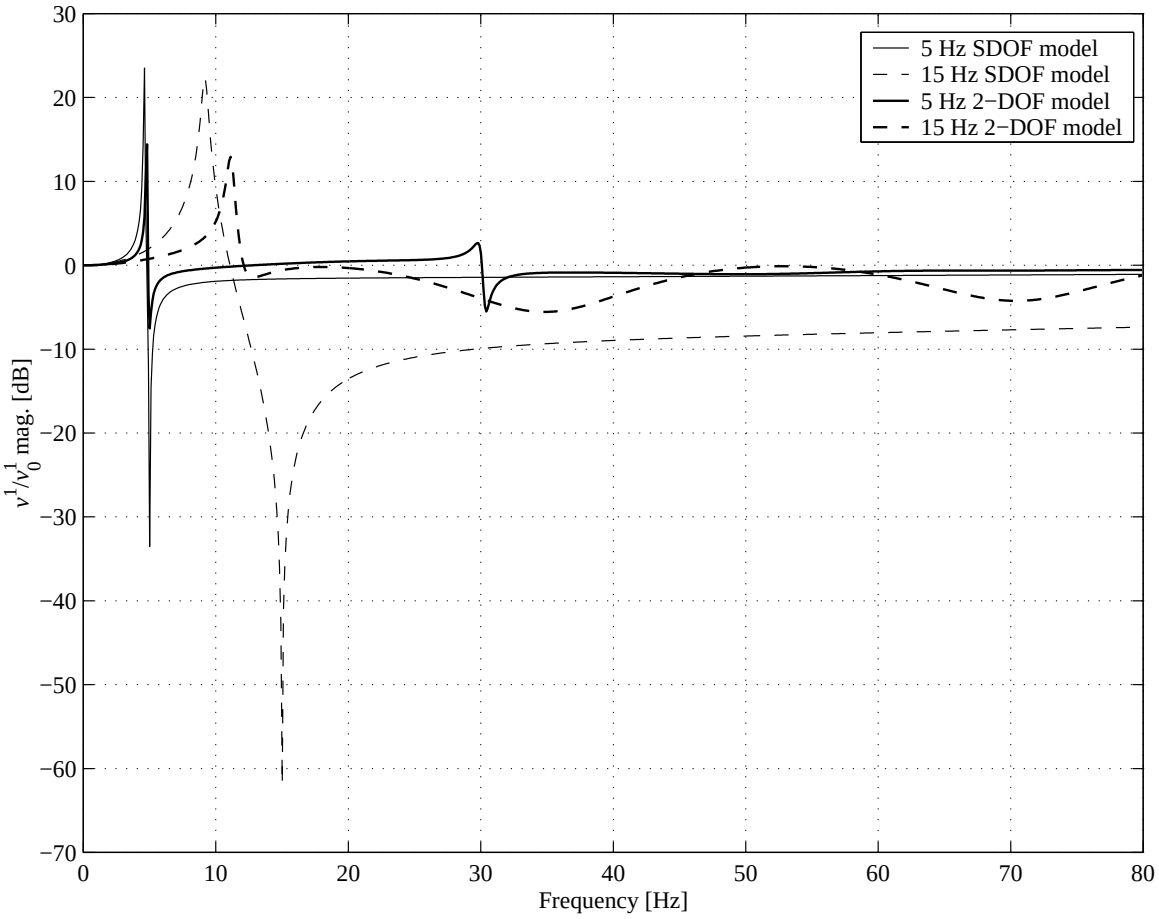

Figure 3.8: Soil-structure interaction of a base-isolated building as predicted by a 2-DOF building model, founded on footings bonded to the surface of an elastic half-space, and excited by passing Rayleigh waves. The ratio of the final amplitude v^1 of the upstream footing to that prior to the construction of the building v_0^1 is shown for different isolation frequencies. The results of Figure 3.4 are shown for comparison.

As with the SDOF model the vertical 'foundation' and 'building' resonances are evident but now there are also equivalent rocking modes evident at higher frequencies, although that of the 15 Hz case lies beyond the frequency range considered. Above the initial resonances, wave interactions occur between the two footings. When the footings move in phase (at 35 and 70 Hz) the building model behaves as a SDOF model and acts to constrain the ground; when they move in antiphase (at 55 Hz) the effect of the building on the ground becomes negligible. Again, a lower isolation frequency affects the foundation to a lesser extent. Although these interaction effects appear

small in this model (less than 6 dB variation) they are expected to be greater in multi-footing foundations or those constructed from piles, which may interact over a significant proportion of their length.

Conclusions

The results of the simple models considered in this section, together with the existing experimental evidence, strongly indicate that constructing a building significantly modifies the original ground vibration field. In particular, the added-mass effect tends to locally reduce ground vibration levels. The base isolation of a building reduces this effect by decoupling the building from its foundation. A low isolation frequency therefore results in higher post-construction vibration levels beneath a building. This again highlights the inadequacy of describing isolation performance in terms of vibration levels above and below the bearings; the performance of a soft isolation is exaggerated by greater vibration amplitudes beneath it.

Wave interaction effects have also been studied for simple footings and it is believed that they may be particularly significant with a piled foundation.

Clearly soil-structure interaction is significant in the behaviour of base-isolated buildings and must be accounted for in any generic model if meaningful predictions of isolation performance are to be made.

3.2.3. Modelling the Foundation

Although surface footings were considered in Section 3.2.2, a piled foundation is a more common design for large buildings, particularly those sited over railways where the structure must be supported on a few highly loaded columns [85]. A model of this type of foundation is therefore chosen for the generic base-isolated building model. Although footings are not considered further in this dissertation, the techniques involved in foundation modelling are generally applicable to piles, footings or raft foundations.

As discussed in Section 2.7.2, a number of piled foundation models currently exist, although none satisfies the current requirement for a comprehensive model that is computationally efficient.

For the generic base-isolated building model, the essential dynamic behaviour that must be accounted for is regarded as follows:

- longitudinal and transverse motion of the pile such that horizontal and rotational, as well vertical, motion of the pile head, is accounted for;
- interaction between neighbouring piles through wave propagation in the surrounding soil, known as pile-soil-pile interaction (PSPI).

The formulation of a suitable piled-foundation model is the subject of Chapter 4. In the remainder of this chapter, an approximate two-pile model is used as part of an initial model of a base-isolated building.

3.3. An Initial Model

In this section, the elements of the previous sections are drawn together in an initial model of a base-isolated building, the primary aim being to address the problem of defining a suitable measure of isolation performance. It was demonstrated in Section 3.2.2 that simple comparisons of vibration levels above and below the isolation bearings are not indicative of performance. This is sometimes done by practitioners [131], [5], although it is more common to consider insertion gain (IG), as discussed in Section 2.4.3. IG has the advantage of directly comparing the isolated and unisolated conditions of a building but the disadvantage that it fails to account for multidirectional vibration and the spatial variation in vibration levels throughout a building. This will be illustrated before an alternative, power flow insertion gain, is introduced as a more useful measure of insertion performance.

3.3.1. Overview of the Model

The model presented here aims to represent the essential characteristics of a base-isolated building while requiring the minimal computational effort; see Figure 3.9. The building is represented by a simple two-dimensional portal frame. This is modelled using the DSM, as described in Section 3.1.1, thereby accounting for the essential behaviour of the columns floors and walls, and the

coupling between them. Each isolation bearing is represented by three linear springs, as described in Section 3.1.2, located on each pile head to represent the vertical, horizontal and rotational stiffness of each bearing.

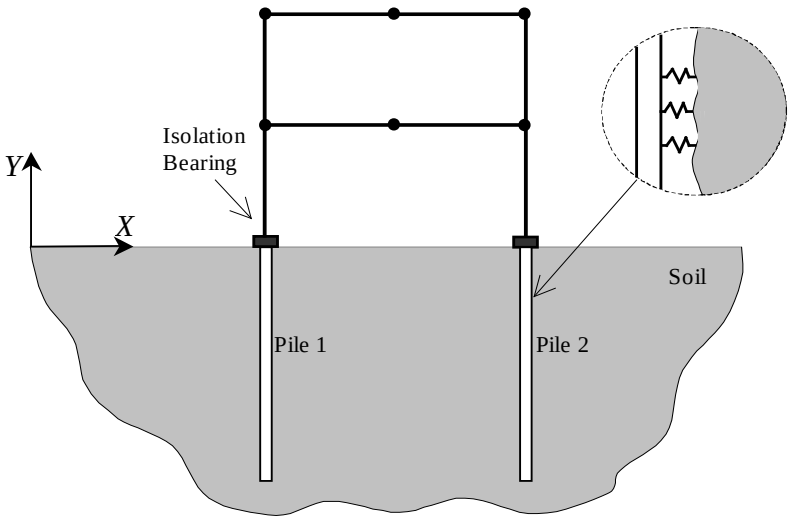

Figure 3.9: An initial model of a base-isolated building. The building is represented by a two-dimensional portal frame while the piled foundation is based on a three-dimensional representation due to Makris *et al*. The soil-pile interface is represented by distributed springs and dashpots; for clarity, only the horizontal springs are shown.

The two-pile foundation model uses the approximate analytical approach of Gazetas and Makris [40, 84]. It is inappropriate to reproduce the full details here; instead, a summary is given and reference should be made to the original papers for further details. The approach uses the solutions for an elastic bar and Euler beam to model the longitudinal and transverse behaviour of each pile, in a similar way to an element of the portal frame of the building. Wave propagation in the free field is accounted for by modelling the soil as a homogeneous isotropic linear-elastic half-space. In the near field, in both the horizontal and vertical directions, the soil-pile interface is modelled as a Winkler foundation with continuously distributed linear springs and dashpots, the latter to represent radiation and hysteretic material damping within the soil. Frequency dependent values are assigned to the spring and dashpot coefficients using algebraic expressions developed by curve-fitting to results from FEM models.

There are three main steps to the modelling as described below.

Calculation of the Building Response

The calculation of the building response is achieved by considering the model as an assembly of two subsystems: the building, complete with isolation bearings, and the half-space containing the two piles. The initial analysis is similar to that in Section 3.2.2. Assume that, prior to the construction of the building, the harmonic, generalised displacement amplitudes of the pile heads are known to be $\mathbf{u}^1_{\mathbf{ph0}} = \begin{bmatrix} u^1_0 & v^1_0 & \theta^1_0 \end{bmatrix}^{\mathrm{T}}$ and $\mathbf{u}^2_{\mathbf{ph0}} = \begin{bmatrix} u^2_0 & v^2_0 & \theta^2_0 \end{bmatrix}^{\mathrm{T}}$, as expressed in the global coordinates (*X*, *Y*). Following the construction of the building, these become $\mathbf{u}^1_{\mathbf{ph}} = \begin{bmatrix} u^1 & v^1 & \theta^1 \end{bmatrix}^{\mathrm{T}}$ and $\mathbf{u}^2_{\mathbf{ph}} = \begin{bmatrix} u^2 & v^2 & \theta^2 \end{bmatrix}^{\mathrm{T}}$ which, by superposition, may be expressed as:

$$\begin{bmatrix} \mathbf{u}^1_{\mathbf{ph}} \\ \mathbf{u}^2_{\mathbf{ph}} \end{bmatrix} = \begin{bmatrix} \mathbf{H}^{11}_{\mathbf{f}} & \mathbf{H}^{12}_{\mathbf{f}} \\ \mathbf{H}^{21}_{\mathbf{f}} & \mathbf{H}^{22}_{\mathbf{f}} \end{bmatrix} \begin{bmatrix} \mathbf{f}^1_{\mathbf{ph}} \\ \mathbf{f}^2_{\mathbf{ph}} \end{bmatrix} + \begin{bmatrix} \mathbf{u}^1_{\mathbf{ph0}} \\ \mathbf{u}^2_{\mathbf{ph0}} \end{bmatrix} \tag{3.18}$$

where $\mathbf{f}^1_{\mathbf{ph}} = \begin{bmatrix} f^1 & s^1 & q^1 \end{bmatrix}^{\mathrm{T}}$ and $\mathbf{f}^2_{\mathbf{ph}} = \begin{bmatrix} f^2 & s^2 & q^2 \end{bmatrix}^{\mathrm{T}}$ are the force amplitudes applied to the pile heads by the building. The 6 x 6 matrix $\mathbf{H}_{\mathbf{f}}$ describing the foundation is assembled from the 3 x 3 FRF matrices describing the piles in the half-space. $\mathbf{H}^{11}_{\mathbf{f}}$ and $\mathbf{H}^{22}_{\mathbf{f}}$ represent the pile-head driving-point FRFs of the of the individual piles; $\mathbf{H}^{12}_{\mathbf{f}}$ and $\mathbf{H}^{21}_{\mathbf{f}}$ represent the coupling FRFs due to PSPI. For example, considering two piles in the absence of a building, the pile-head displacement amplitudes $\mathbf{u}^1_{\mathbf{ph}}$ and $\mathbf{u}^2_{\mathbf{ph}}$ due to harmonic force amplitudes $\mathbf{f}^1_{\mathbf{ph}}$ applied only at the pile head of pile 1 are given by:

$$\mathbf{u}^1_{\mathbf{ph}} = \mathbf{H}^{11}_{\mathbf{f}} \mathbf{f}^1_{\mathbf{ph}} = \begin{bmatrix} H^{11}_{f11} & 0 & H^{11}_{f13} \\ 0 & H^{11}_{f22} & 0 \\ H^{11}_{f31} & 0 & H^{11}_{f33} \end{bmatrix} \begin{bmatrix} f^1 \\ s^1 \\ q^1 \end{bmatrix} \tag{3.19a}$$

and

$$\mathbf{u}^2_{\mathbf{ph}} = \mathbf{H}^{21}_{\mathbf{f}} \mathbf{f}^1_{\mathbf{ph}} = \begin{bmatrix} H^{21}_{f11} & 0 & H^{21}_{f13} \\ 0 & H^{21}_{f22} & 0 \\ H^{21}_{f31} & 0 & H^{21}_{f33} \end{bmatrix} \begin{bmatrix} f^1 \\ s^1 \\ q^1 \end{bmatrix} \tag{3.19b}$$

The frequency-dependent elements of $\mathbf{H}^{11}_{\mathbf{f}}$ and $\mathbf{H}^{21}_{\mathbf{f}}$ are given by analytical expressions based on the solutions for an elastic bar and Euler beam. The piles are identical and therefore $\mathbf{H}^{11}_{\mathbf{f}} = \mathbf{H}^{22}_{\mathbf{f}}$. The coupling matrices $\mathbf{H}^{12}_{\mathbf{f}}$ and $\mathbf{H}^{21}_{\mathbf{f}}$ should be fully populated but the modelling of

PSPI (described later) only approximately accounts for wave propagation in the soil such that the FRFs describing axial-flexural coupling (H_{f12}^{21}, H_{f21}^{21}, H_{f23}^{21} and H_{f32}^{21}) are zero. In this case $\mathbf{H}_{\mathbf{f}}^{12} = \mathbf{H}_{\mathbf{f}}^{21}$, although this is not generally true, as discussed later in Section 4.2.3.

Returning to the building model, an equal but opposite set of forces to those acting on the pile heads act on the building's isolation bearings. The response of the building is determined by its own frequency response and therefore, applying compatibility of displacements at the pile heads and isolation bearings:

$$\begin{bmatrix} \mathbf{u}_{\mathbf{ph}}^{1} \\ \mathbf{u}_{\mathbf{ph}}^{2} \end{bmatrix} = -\begin{bmatrix} \mathbf{H}_{\mathbf{b}}^{11} & \mathbf{H}_{\mathbf{b}}^{12} \\ \mathbf{H}_{\mathbf{b}}^{21} & \mathbf{H}_{\mathbf{b}}^{22} \end{bmatrix}\begin{bmatrix} \mathbf{f}_{\mathbf{ph}}^{1} \\ \mathbf{f}_{\mathbf{ph}}^{2} \end{bmatrix} \tag{3.20}$$

where the 6 x 6 matrix $\mathbf{H}_{\mathbf{b}}$ is assembled from the 3 x 3 FRF matrices describing the building. $\mathbf{H}_{\mathbf{b}}^{11}$ and $\mathbf{H}_{\mathbf{b}}^{22}$ represent the driving-point FRFs of the bases of the two columns; $\mathbf{H}_{\mathbf{b}}^{12}$ and $\mathbf{H}_{\mathbf{b}}^{21}$ represent the coupling FRFs between these two points. These four matrices are sub-matrices of the overall FRF matrix of the building, which is equal to the inverse of its dynamic-stiffness matrix as described in Section 3.1.1.

Eliminating the forces from Equations 3.18 and 3.20 gives the generalised displacements of the pile heads:

$$\begin{bmatrix} \mathbf{u}_{\mathbf{ph}}^{1} \\ \mathbf{u}_{\mathbf{ph}}^{2} \end{bmatrix} = \left[\mathbf{I} + \begin{bmatrix} \mathbf{H}_{\mathbf{f}}^{11} & \mathbf{H}_{\mathbf{f}}^{12} \\ \mathbf{H}_{\mathbf{f}}^{21} & \mathbf{H}_{\mathbf{f}}^{22} \end{bmatrix}\begin{bmatrix} \mathbf{H}_{\mathbf{b}}^{11} & \mathbf{H}_{\mathbf{b}}^{12} \\ \mathbf{H}_{\mathbf{b}}^{21} & \mathbf{H}_{\mathbf{b}}^{22} \end{bmatrix}^{-1} \right]^{-1} \begin{bmatrix} \mathbf{u}_{\mathbf{ph0}}^{1} \\ \mathbf{u}_{\mathbf{ph0}}^{2} \end{bmatrix} \tag{3.21}$$

where $\mathbf{I}$ is a 6 x 6 identity matrix. As with the two-footing model of Section 3.2.2, coupling between the piles, both through the building and through the soil, results in the displacements of each pile head in the presence of the building ($\mathbf{u}_{\mathbf{ph}}^{1}$ and $\mathbf{u}_{\mathbf{ph}}^{2}$) being functions of both pile head displacements in its absence ($\mathbf{u}_{\mathbf{ph0}}^{1}$ and $\mathbf{u}_{\mathbf{ph0}}^{2}$).

The displacements of the pile heads are obtained directly by solving Equation 3.21, for each frequency of interest, followed by inversion of Equation 3.20 to give the corresponding forces $\mathbf{f}_{\mathbf{ph}}^{1}$ and $\mathbf{f}_{\mathbf{ph}}^{2}$. These are then applied, in the opposite sense, to the building model and, knowing the dynamic-stiffness matrix of the building, the full response of the building can be calculated. This

procedure is repeated for a building with and without isolation bearings in order to assess their relative performance.

Specification of the Ground Vibration-Field

A physically based representation of $\mathbf{u}_{\mathbf{ph0}}^{1}$ and $\mathbf{u}_{\mathbf{ph0}}^{2}$ is required and, as in Section 3.2.2, steady-state Rayleigh waves are chosen. Due to the nature of the resulting soil-particle motion, the piles are subject to both vertical and horizontal motion, something not usually considered in modelling isolated buildings. This motion is calculated analytically using the approximate method of Makris and Badoni [82, 83], in which they develop the above pile model for studying the response of pile groups to seismic excitation. As well as providing convenient analytical expressions for $\mathbf{u}_{\mathbf{ph0}}^{1}$ and $\mathbf{u}_{\mathbf{ph0}}^{2}$, the model includes a representation of PSPI.

Pile-Soil-Pile Interaction

The method chosen to model PSPI is described in detail by Makris *et al*. [40, 83, 84]. It involves three consecutive steps: (1) calculate the longitudinal and transverse displacement of a solitary pile, whether subject to either free-field motion (Rayleigh wave) or pile-head forces; (2) calculate the difference between the displacement of the solitary pile and the free-field soil displacement, and 'propagate' this difference to the location of the neighbouring pile with a suitable decay in amplitude; (3) calculate the response of the neighbouring pile to the displacement field calculated in (2). In this way, analytical expressions are derived for both the coupling between piles, and hence the FRF matrix $\mathbf{H}_{\mathbf{f}}^{12}$, and the effect of PSPI on the response of the pile heads in the absence of the building.

This method assumes that the diffracted waves calculated in (2) propagate radially in the horizontal direction only, and that the waves emanate simultaneously from all points along the length of the pile. The result is a cylindrical wave front, concentric with the 'source pile', and with a variation in wave amplitude down the wave front that remains unchanged as it propagates. While this is an approximation it does provide a convenient method for the initial model presented here.

3.3.2. Predictions of Insertion Gain

As discussed in Section 2.4.3, a common measure of isolation performance is insertion gain (IG), the ratio of the building response with the isolation bearings in position to that with no bearings at all. It is usual to take the response of the building at its base, directly above the isolation bearings themselves:

$$\mathrm{IG} = 20\log_{10}\left(\frac{x_{isol}}{x_{unisol}}\right) \tag{3.22}$$

where x_{isol} and x_{unisol} are the amplitudes of the building response in the isolated and unisolated condition respectively. Either the displacement, velocity or acceleration response may be used since it is assumed that the building behaves linearly. Although IG is commonly used, the results presented in this section illustrate that it fails to provide a single measure of insertion performance because it only accounts for vibration occurring in one direction and varies with position in the building. The results correspond to the case of a concrete-framed building with the representative parameter values of Table 3.1. Specification of the isolation bearings is based on a 10 Hz isolation frequency, as described in Section 3.1.2, with an internal damping loss factor of 0.1, unless otherwise stated.

Property	Building	Piles	Soil (free-field)
Height [m]	= width = 8	14	–
Bending stiffness [GPam^4]	0.4	0.4	–
Axial stiffness [GPam^2]	5.0	5.0	–
Density [kg/m^3]	2400	2400	2000
Damping loss factor	0.1	0.1	0.05
Young's modulus [GPa]	10	10	0.1
Poisson's ratio	–	–	0.4

Table 3.1: Parameter values used in the initial base-isolated building model.

Multidirectional Vibration

The horizontal component of ground-borne vibration is rarely considered in assessing the isolation of buildings; it is generally assumed that the building's inherent flexibility in this direction provides

sufficient isolation. This is unlikely to be a valid assumption because vibration entering a building in any direction can lead to various forms of vibration within the building structure. The Rayleigh wave excitation considered here results in vertical, horizontal and rotational motion of the pile heads. As a result, values of IG may be calculated for all three degrees of freedom (u, v and θ).

Figure 3.10 shows the variation with frequency in the vertical and horizontal IG based on the displacements of the base of the 'upstream' building column, that is, the column first met by the Rayleigh wave.

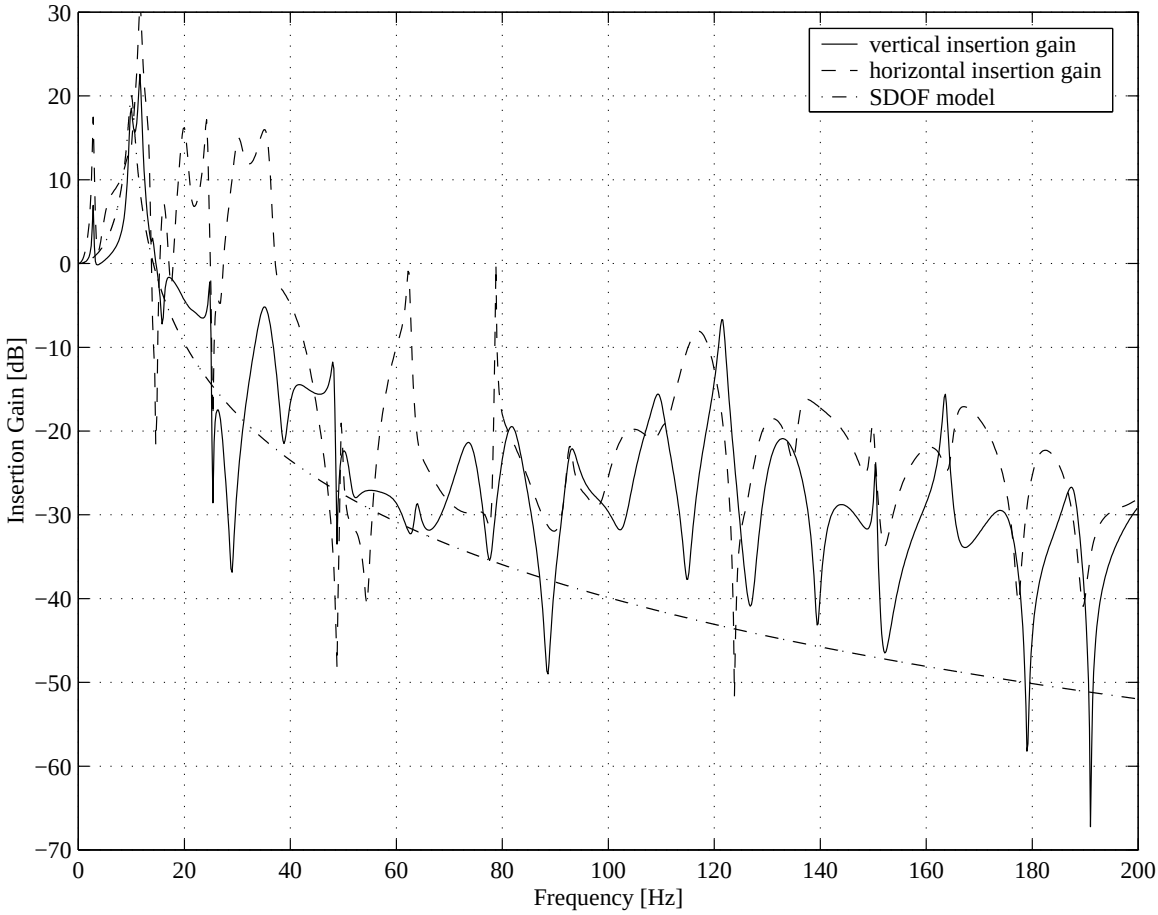

Figure 3.10: Variation with frequency in the vertical and horizontal insertion gain of a '10 Hz' base-isolated building when excited by Rayleigh waves; based on the displacements of the 'upstream' building column of the initial base-isolated building model. The response of an equivalent SDOF model is shown for comparison.

The major peak in the vertical IG at 11.6 Hz corresponds to amplification of the ground vibration by the global 'bounce' mode of the building; see also Figure 3.11. Note that a purely vertical mode at 10 Hz is not evident, as may be expected from the 10 Hz isolation frequency of

the bearings, since the Rayleigh wave excitation results in the motions of the pile heads being out of phase at this frequency. Above these initial peaks the bearings are effective, although their performance is considerably poorer than the SDOF model would suggest due to the flexibility of the building and piles. Note that several of the smaller peaks are due to the phase difference in the motions of the piles.

The horizontal, and in fact the rotational, IG shows a similar variation with frequency to that in the vertical direction. There is no single mode that corresponds to purely horizontal motion since coupling exists between the global horizontal and rotational modes due to the offset of the building's centre of gravity above the bearings. A peak at 2.8 Hz corresponds primarily to horizontal swaying of the building; see Figure 3.11.

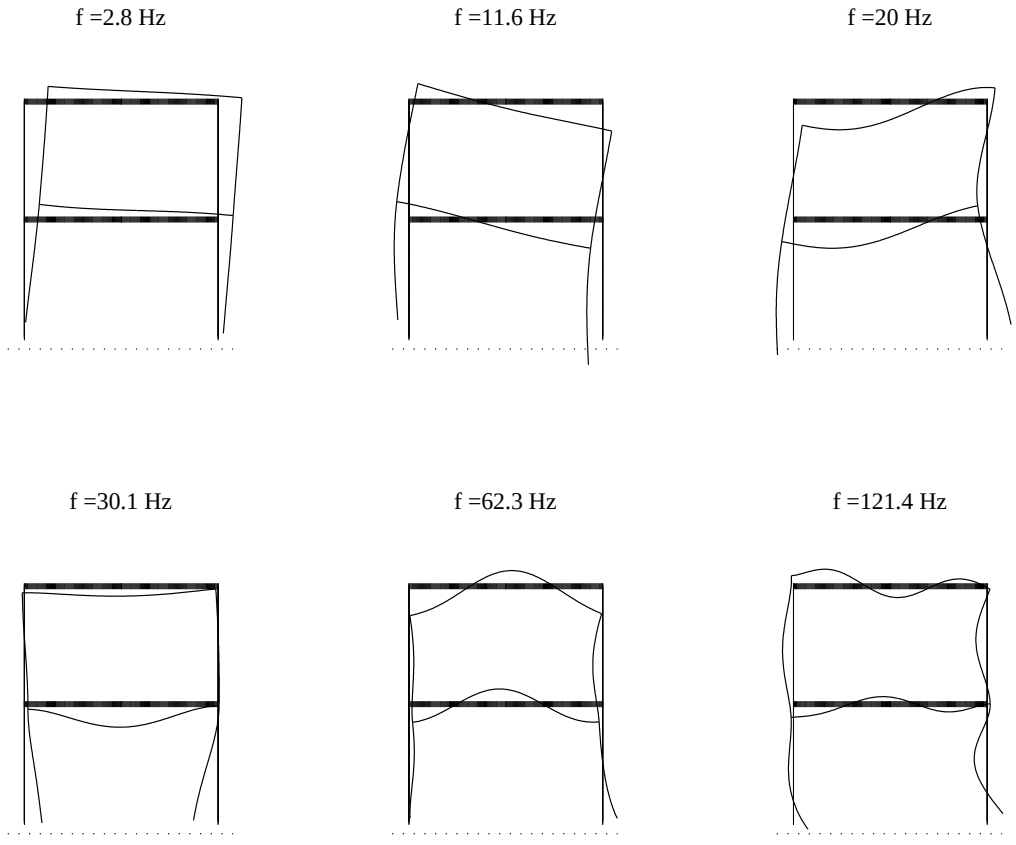

Figure 3.11: Example mode shapes of a '10 Hz' base-isolated building excited by Rayleigh waves passing from left to right, as predicted by the initial base-isolated building model. The modes correspond to peaks in the insertion gain curves of Figure 3.10 (the foundation model is not shown).

Although such predictions of IG are possible when dealing with multidirectional vibration, it is not clear how these should be combined into one overall measure of insertion performance.

Spatial Variation in Insertion Gain

It was noted that the results shown in Figure 3.10 are based on the displacements of the base of the upstream building column. Figure 3.12 illustrates that consideration of the downstream column leads to different values of IG due to the fact that, although the structure itself is symmetrical, the piles are responding to the passage of a wave.

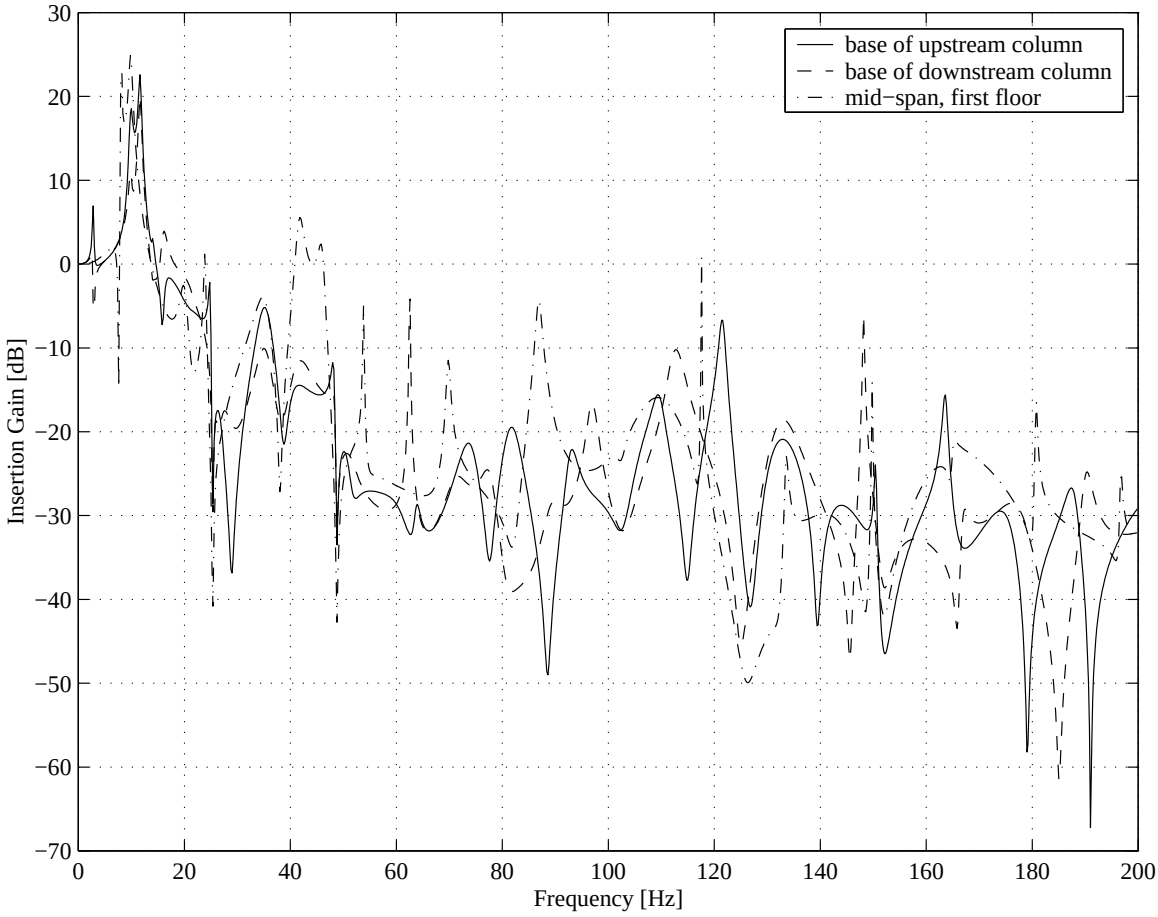

Figure 3.12: Variation with frequency in the vertical insertion gain of a '10 Hz' base-isolated building when excited by Rayleigh waves; based on the displacements of the 'upstream' column, the 'downstream' column and the point mid-span on the first floor, as predicted by the initial base-isolated building model.

This effect is part of a wider problem relating to the spatial variation in IG around the whole building. Figure 3.12 also shows the IG based on the displacements of the point mid-span on the

first floor; this curve is different again. Because, in general, we are dealing with the response of a complex multi-modal structure, there is no guarantee that the response at any point in the building will be representative of the whole; indeed some points may lie close to a significant vibration node of the structure and exhibit deceptively low vibration levels. Clearly, while the concept of IG may be useful for systems consisting of just one input and one output, an improved performance measure is required for the assessment of base-isolated buildings.

3.3.3. Power Flow Insertion Gain

The analysis of vibrational power flow is another way of assessing structures, as reviewed in Section 2.4.4. As an alternative and more appropriate means of assessing base isolation performance, it is proposed to consider the total mean vibrational power flow entering a building. The underlying principle is that the mean vibrational energy entering a building drives all internal structural vibration and re-radiated noise, assuming there are no internal sources of either. This enables a *single* measure of insertion performance to be defined, described henceforth as the *power flow insertion gain* (PFIG):

$$\mathrm{PFIG} = 10\log_{10}\left(\frac{\overline{P}_{isol}}{\overline{P}_{unisol}}\right) \tag{3.23}$$

where $\overline{P}_{isol}$ and $\overline{P}_{unisol}$ are the total mean power flows entering a building in the isolated and unisolated cases respectively.

Defining PFIG in terms of the mean power flow only considers the power dissipated by the internal damping of the building; the *reactive* power is ignored. Reactive power is the component of the input power required to balance the fluctuating total energy (potential plus kinetic) of the building; see Appendix E. Ignoring this raises the important question of whether PFIG is representative of vibration amplitudes: in a lightly damped structure the dissipative power will be small despite the fact that the structure vibrates, and building occupants are concerned with vibration amplitudes rather than power levels. The dissipative power is the component that drives the vibration of the building, delivering in each cycle the energy required to maintain vibration amplitudes at their steady-state levels. Power flow and vibration amplitudes are indeed therefore

related. It is shown in Appendix E that, for the special case of a single-input single-output system, conventional IG is independent of position and directly equivalent to PFIG. Despite ignoring reactive power, PFIG therefore provides a direct measure, in this case, of the reduction in vibration amplitude at any location in the isolated body.

In the case of multiple-input systems IG varies with position, as illustrated in Section 3.3.2, and is unable to provide a single measure of insertion performance. PFIG easily deals with multiple-input systems and is therefore regarded as a more useful measure of insertion performance.

The Advantages of Power Flow Insertion Gain

PFIG has clear advantages over IG given that:

- it accounts for multidirectional vibration – power flows associated with vibration occurring in different directions and with different forms of vibration, such as that associated with axial strain or bending of structural elements, can be easily accounted for;

- it is insensitive to the spatial distribution of vibration levels within a building – vibrational power enters a building at various places but the total power flow can be computed as a straightforward sum.

Because the variation with frequency in the PFIG may be represented by a single curve, it is more useful than conventional IG in the design process. For example, when optimising the isolation bearings for a given building, the minimisation of PFIG is guaranteed to reduce the average levels of structural vibration and re-radiated noise. Such an approach is appropriate for many buildings where an improvement in the average environment is required rather than the environment in a particular room. When a particular room requires consideration, a similar approach may be taken but this time power flow into the room should be considered rather than the building as a whole. It must be acknowledged that the definition of PFIG is based on the *total* mean power flow entering a building despite the fact that this drives axial as well as flexural vibration. Since the latter is more perceptible to occupants, and more efficient at radiating noise, it is possible that a

more appropriate performance measure is based solely on this. However, this would be more costly to predict, since power flows must be calculated around the entire structure and, any case, away from the excitation axial vibration levels are often low due to conversion to flexural vibration at structural joints.

It is worth noting that the measurement of PFIG is just as difficult as IG because, again, the response of a given building is required both with and without the isolation bearings in position. However, the total mean power flow entering a building may be measured more easily and this may be a perfectly useful parameter in its own right. Perhaps a value of input power per unit volume of building can be identified, above which vibration levels become unacceptable. The practical measurement of power flow is discussed further in Chapter 6.

Predictions of Power Flow Insertion Gain

Before considering some predictions of PFIG, the method of calculating power flows around the model will be summarised. An advantage of the dynamic stiffness method is that, once the nodal displacement amplitudes of the portal frame have been calculated, the displaced shape and corresponding force distributions along each element can be easily recovered. This makes the calculation of vibrational power flow straightforward, as demonstrated by Langley [73]. Consider a cross-section located at x along a typical dynamic-stiffness element, as illustrated in Figure 3.13.

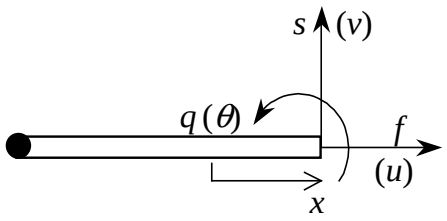

Figure 3.13: Cross-section through a typical dynamic-stiffness element from a two-dimensional portal frame. The mean power flow through the section is calculated as the mean rate at which the element does work against the generalised forces f, s and q when moving through the corresponding generalised displacements (u, v and θ).

The mean power flow through the section is calculated as the mean rate at which the element does work against the generalised forces f, s and q when moving through the corresponding generalised displacements u, v and θ. This may be derived in a similar way to the power flow into

the elastic body considered in Appendix E but now three degrees of freedom must be accounted for. Thus, for time-harmonic motion at angular frequency ω:

$$\overline{P}(x) = -\frac{1}{2}\mathrm{Re}\left\{i\omega\left(uf^{*} + vs^{*} + \theta q^{*}\right)\right\} \tag{3.24}$$

where '$*$' denotes the complex conjugate. The mean power flow may therefore be obtained directly from the generalised displacement and force amplitudes calculated in the dynamic-stiffness model.

To determine the PFIG, as defined by Equation 3.23, the total mean power flow entering the building in the isolated and unisolated cases is calculated by summing the results of applying Equation 3.24 at the bases of the building columns. As mentioned earlier, the minimisation of PFIG enables the design of isolation bearings to be optimised for a given building. To illustrate this, Figure 3.14 shows the variation with frequency in the PFIG predicted by the initial model. The 'baseline' case again concerns bearings with an isolation frequency of 10 Hz; the other two curves are obtained by varying the bearing stiffnesses to achieve isolation frequencies of 5 and 15 Hz.

The general form of the curves is broadly as expected given that the PFIG conveniently combines the responses of the building due vertical, horizontal and rotational motion of the pile heads. At low frequencies, peaks are again evident that correspond to the global modes of the building. Above these the isolation is effective, with subsequent peaks and troughs in the PFIG corresponding to vibration modes of the building. Whether a peak or tough results from a particular mode depends on the relative significance of that mode in the unisolated and isolated cases. These results agree with those from simpler models in that they predict better insertion performance from softer isolation bearings. However, the current model is believed to be too simplistic for these results to be conclusive; this will be considered further in Chapter 5.

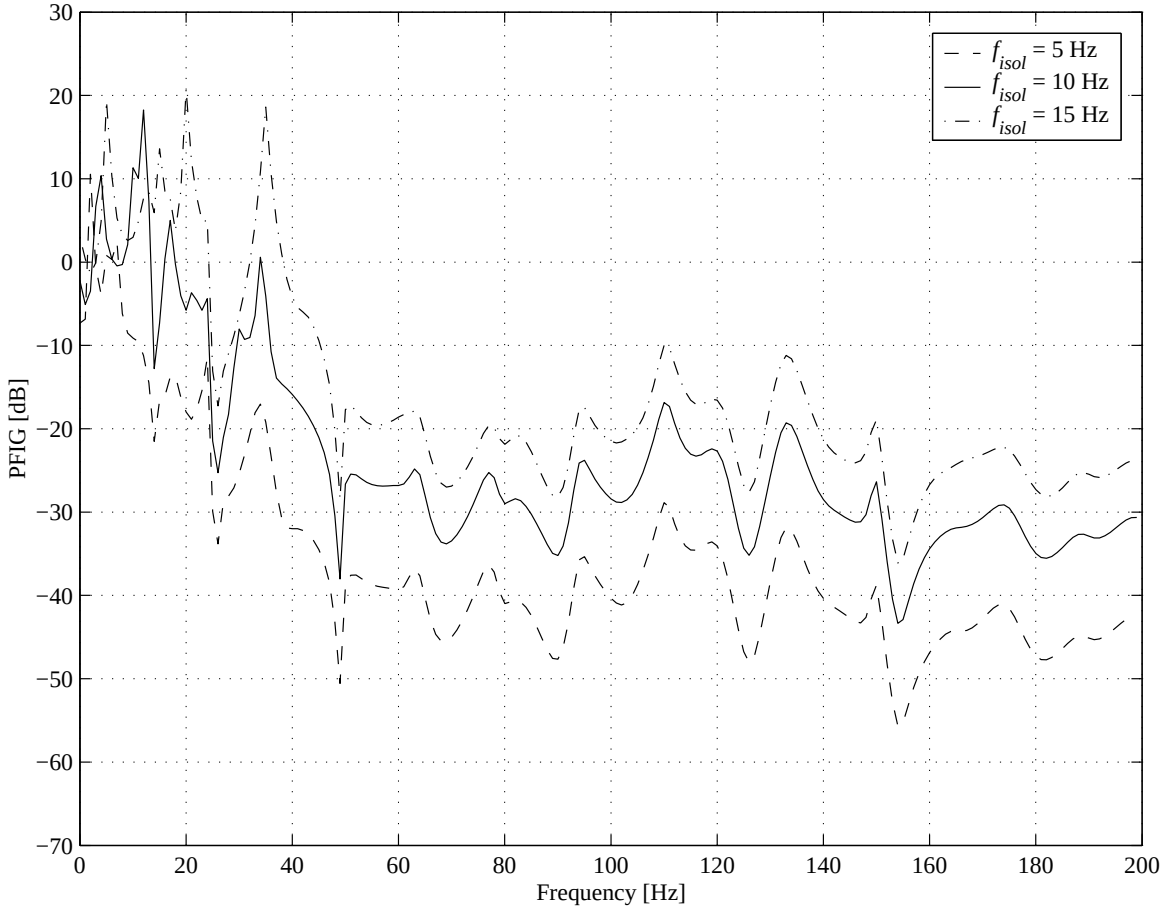

Figure 3.14: Variation with frequency in the power flow insertion gain, as predicted by the initial base-isolated building model with isolation frequencies of 5, 10 and 15 Hz when excited by Rayleigh waves.

The analysis of vibrational power flow in general can provide useful insights into the behaviour of a base-isolated building. The next section considers this in more detail.

3.3.4. Power Flow Analysis

It was noted earlier in Section 3.3.3 that the horizontal component of ground-borne vibration is rarely considered in assessing the isolation of buildings and that this was believed to be an oversimplification in existing models. Power flow analysis enables the validity of this assumption to be investigated.

Figure 3.15 plots the variation with frequency in the vertical, horizontal and rotational components of the mean power flow entering the building as percentages of the total flow. These results are calculated by evaluating Equation 3.24 for the three separate power components at the bases of the two building columns directly above the isolation bearings.

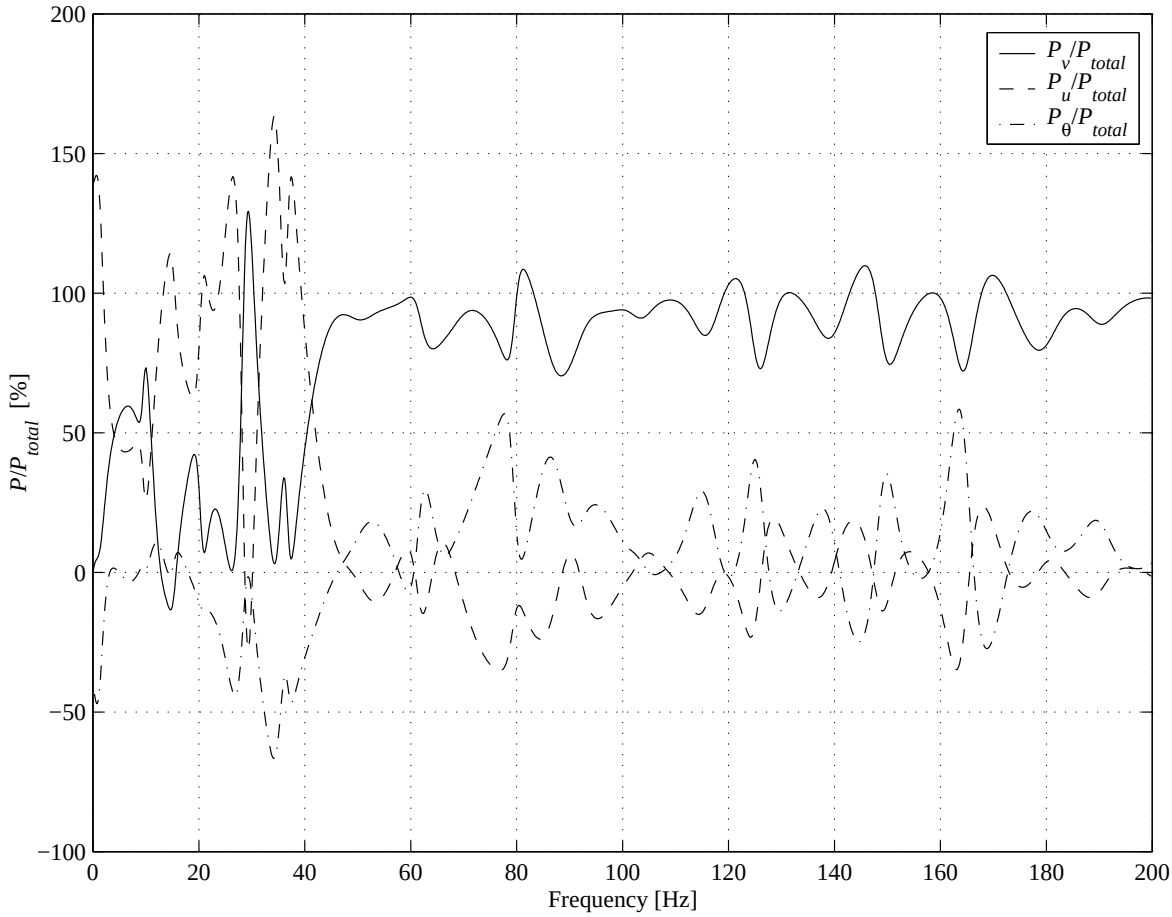

Figure 3.15: Variation with frequency in the vertical $\overline{P}_v$, horizontal $\overline{P}_u$ and rotational $\overline{P}_\theta$ components of the mean power flow entering a '10 Hz' base-isolated building excited by Rayleigh waves. The results are calculated by the initial base-isolated building model and are presented as percentages of the total mean power flow $\overline{P}_{total}$.

It is clear that, although the power flow due to vertical motion dominates, the horizontal and, to a lesser extent, the rotational components are still significant. This is particularly so in the frequency range up to approximately 50 Hz where, in some vibration modes, the total power input is almost entirely due to horizontal motion of the building columns. While these results are specific to the particular model parameters chosen – in particular the specification of the bearing stiffnesses (see Section 3.1.2) – they do suggest that neglecting the horizontal component of ground motion may be an oversimplification and that the extra computational effort required to include this, along with rotation, in the prediction of PFIG is worthwhile. Note that although the total mean power flow into the building is positive, as it must be if no internal sources exist, at some frequencies one or two of the power components is negative. This corresponds to power flowing *from* the building to be dissipated in either the isolation bearings or the foundation.

Further insight may be gained into the behaviour of base-isolated buildings by considering the distribution in power flow around the building itself. Equation 3.24 enables this by allowing the magnitude and direction of the vibrational power flow to be calculated at any point in the portal frame; if $\overline{P} > 0$ then, on average, power flows along the element in the positive *x*-direction, and vice versa. Figure 3.16 illustrates this for the initial building model when excited in the mode at 121.4 Hz.

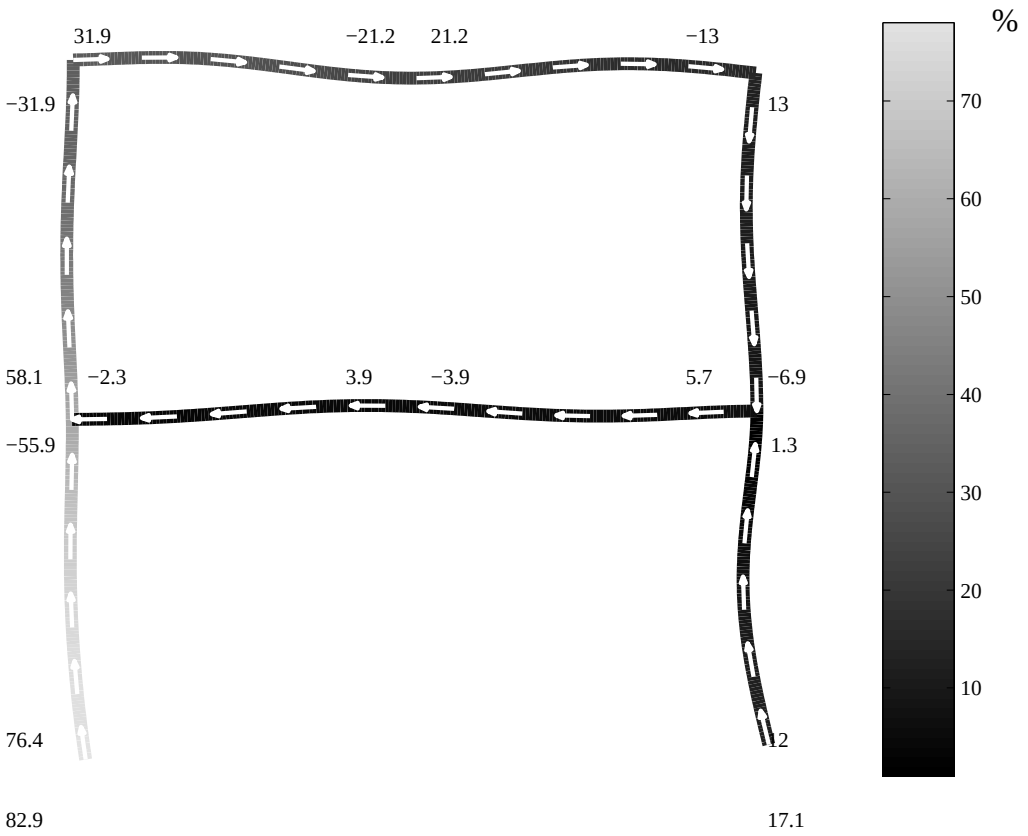

Figure 3.16: Mean power flow around a '10 Hz' base-isolated building excited by 121.4 Hz Rayleigh waves passing from left to right, as predicted by the initial base-isolated building model; the bearing loss factor is 0.01. The flow is calculated as a percentage of the total mean power flow through the pile heads; the shading indicates the magnitude, the arrows its direction, and the numerical values represent the flow *into* a node of the model (the foundation model is not shown).

The plot shows the mean power flow in the building as a percentage of the total mean power flow through the pile heads, which is equivalent to the total power dissipated in the building and isolation bearings together, since there are no internal sources of vibration. In this case, power enters the building via both of the isolation bearings; 82.9 % enters the upstream bearing and 17.1

% the downstream bearing. Of this, 88.4 % (76.4 + 12.0) is dissipated within the building and 11.6 % in the bearings.

Figure 3.17 shows a similar plot for the mode at 11.6 Hz. At this frequency only 70.6 % (184.6-114.0) of the mean power flowing from the piles is dissipated within the building, 29.4 % being lost in the bearings. Of more interest is the fact that, at the downstream bearing, power flows from the building into the foundation. This again illustrates that power may leave as well as enter a building and raises the question of whether or not this is desirable.

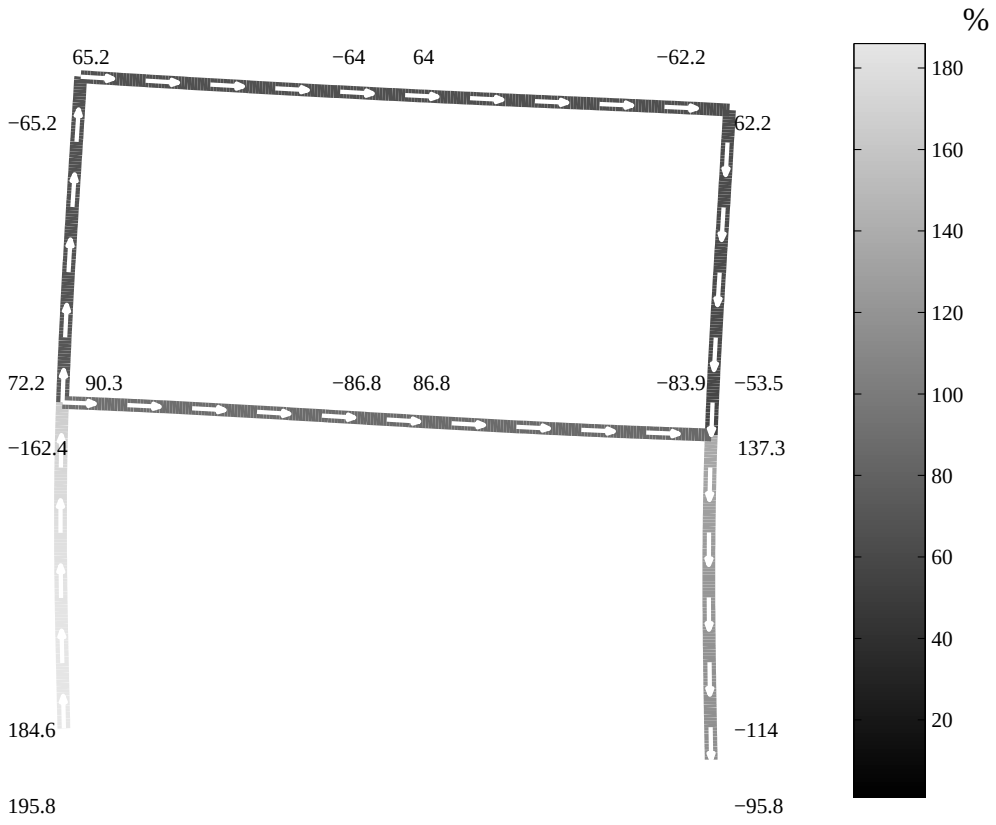

Figure 3.17: Mean power flow around a '10 Hz' base-isolated building excited by 11.6 Hz Rayleigh waves passing from left to right, as predicted by the initial base-isolated building model; the bearing loss factor is 0.01. The flow is calculated as a percentage of the total mean power flow through the pile heads; the shading indicates the magnitude, the arrows its direction, and the numerical values represent the flow *into* a node of the model (the foundation model is not shown).

Consider the more complex building in Figure 3.18. This building contains a 'sensitive room', for example it might house an item of vibration-sensitive equipment, but due to cost constraints it is only possible to partially isolate the structure; a real example of such a structure is the Apex Plaza building in Reading, UK [119].

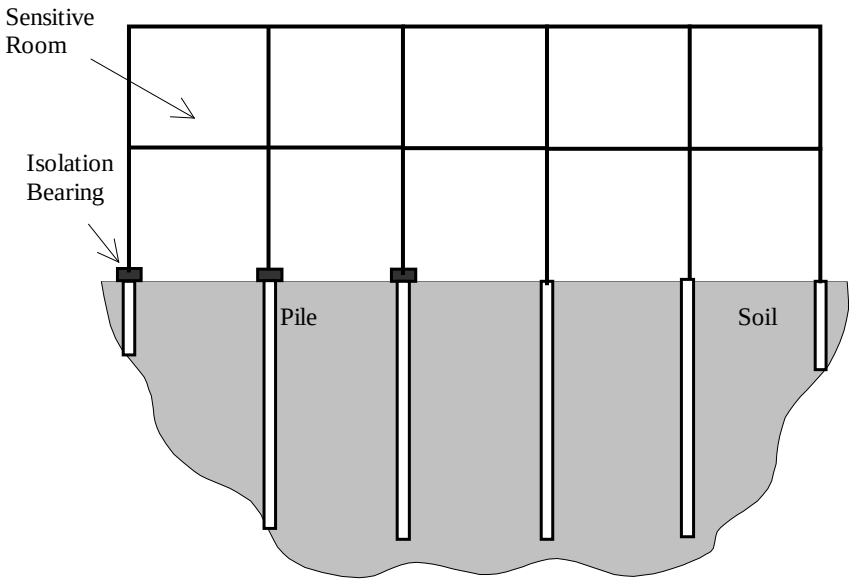

Figure 3.18: Schematic diagram of a partially isolated building founded on a piled foundation.

In this case, it is not obvious whether or not base-isolation would be beneficial. It is possible that the floors from the unisolated side of the building form the dominant vibration transmission path and that isolating the left-hand side of the building offers little benefit. Indeed, the isolation bearings may help to contain vibrational power that would otherwise leave the building and dissipate into the foundation. A 'design assessment' is clearly required and this would greatly benefit from an analysis of the power flows involved. Although this is noted as worthy of further investigation it is beyond the scope of this chapter.

3.3.5. Limitations of the Initial Model

The initial model represents a 'first attempt' at a generic model of a base-isolated building. Although useful for illustrating the ideas presented in this chapter, it is regarded has having two fundamental deficiencies. Firstly, real buildings comprise many columns and floors and therefore the portal-frame model must be extended to include more elements. This must be achieved in a computationally efficient way and is addressed in Chapter 5. Secondly, the approximate representation of the piled foundation is considered inadequate due to the limitations summarised below.

1. When calculating the interaction between two piles, any intermediate piles are ignored. This may be acceptable when dealing with low-frequency seismic waves but, at the upper frequency range of interest here, the wavelengths are comparable with the diameter of a pile. In practice, therefore, the interaction between two distant piles will be reduced due to the reflection of waves by the intermediate piles.

2. Waves from an excited pile are assumed to emanate simultaneously from all points along its length and propagate radially in the horizontal direction only, resulting in the axial-flexural coupling between two piles being ignored. For purely vertical motion at low frequencies, when the flexibility of the pile is less important, this assumption is reasonable. However, this is an oversimplification in the frequency range of interest here, particularly when horizontal loading leads to flexure of a pile.

3. The model relies on original, detailed FEM models to assign values to the coefficients describing the soil-pile interface. The benefit of an analytical formulation for the rest of the model is therefore lost.

Given these limitations a new model of a piled foundation is required, specifically designed for a generic model of a base-isolated building. This is the subject of the next chapter.

3.4. Conclusions

This chapter has considered the essential elements that form the basis of a generic, computationally efficient model of a base-isolated building. In particular, it has been argued that a two-dimensional portal frame, modelled using the dynamic-stiffness method, may adequately represent the behaviour of a typical building, while a three-dimensional model, in the form of an elastic half-space, is considered essential to correctly model wave propagation in the ground.

Simple models have demonstrated the need to model soil-structure interaction such that the added-mass effect of a building on the foundation vibration field, together with wave interaction effects in the foundation, are correctly accounted for.

An initial model of a base-isolated building has been presented which has highlighted the limitations of simpler models, particularly regarding the flexibility of the building and its foundation, and the horizontal component of ground-borne vibration. It has also illustrated fundamental problems with the use of insertion gain, one of the common measures of isolation performance. The concept of power flow insertion gain, based on the total mean vibrational power flow entering a building, has been introduced as a more useful measure of isolation performance. PFIG has been shown to offer clear benefits by providing a *single* measure of insertion performance that accounts for multidirectional vibration at multiple inputs and which is insensitive to the spatial distribution of vibration levels within a building. It has been argued that this is more useful for design purposes because the minimisation of PFIG is guaranteed to reduce the average levels of internal noise and vibration within a building. The more general analysis of power flow has also been shown to offer greater insight into the behaviour of a base-isolated building.

Chapter 4
DEVELOPMENT OF A PILED-FOUNDATION MODEL

The models discussed in Chapter 3 illustrated the importance of modelling a building's foundation when investigating the performance of base-isolation. It was concluded that a generic base-isolated building model requires a comprehensive model of a piled foundation that accounts for the following essential dynamic behaviour:

- vertical, horizontal and rotational motion of the pile head due to longitudinal and transverse motion of the pile;
- interaction between neighbouring piles – pile-soil-pile-interaction (PSPI) – through wave propagation in the surrounding soil.

This chapter describes the development of a computationally efficient piled-foundation model that satisfies the above requirement through the combination of the boundary-element method (BEM) and periodic-structure theory. The chapter begins with the development of a model that provides a good representation of the dynamic behaviour of a single floating pile, given the key assumptions of linear-elasticity and a homogenous isotropic soil. The components of the model are described in detail and the necessary mathematics is summarised. Following the validation of the single-pile model against existing published results, it is then used as the basis for a model of a row of piles. This is achieved in a computationally efficient way by assuming the row comprises an infinite number of identical piles and using periodic-structure theory. The pile-row model is validated against published results from an existing two-pile model. The result is a

computationally efficient model that, as described in Chapter 5, is suitable for incorporation into a generic model of a base-isolated building.

4.1. Modelling a Single Pile

The modelling of a single pile is an obvious prerequisite to considering a row of piles. It enables the essential technique of coupling a pile to the ground to be developed and the approach may be validated by comparing the results with existing published work. The approach taken here is not necessarily the most efficient way to model a single pile. It does not, for example, make use of the fact that the geometry of the system is axisymmetric. However, the particular approach used here will be necessary later when considering a row of piles.

In Section 3.2 it was argued that the soil of a generic base-isolated building model is best represented by a homogeneous, isotropic linear-elastic half-space. This accounts for the essential dynamic behaviour of the soil, including the three fundamental wave types and both radiation and material damping. The half-space is modelled using a constant-element BEM formulation, as summarised in Appendix B. This method is well suited to the modelling of foundations, as discussed in Section 2.7, and is particularly suited to the current requirement for the following reasons:

- a BEM model of the soil may be coupled to a suitable pile model to produce a fully three-dimensional foundation model;
- the solution enables the full displacement and stress field of the soil to be determined, enabling the visualisation of vibration propagation and the use of periodic structure theory (discussed in Section 4.2) to develop a comprehensive model of a row of piles;
- the flexibility of the BEM is essential for future development of the model beyond the scope of this dissertation, such as the investigation of layered soil properties and the inclusion of buried objects and vibration sources.

Steady-state time-harmonic loading is considered throughout and therefore complex notation is used for all field variables in the model. For example, a vector displacement at point **x** is written as:

$$\mathbf{u} = \mathrm{Re}\left\{\mathbf{u}(\mathbf{x},\omega)e^{i\omega t}\right\} \tag{4.1}$$

where t = time, ω = circular frequency and $i = \sqrt{-1}$. In general, the exponential notation will be omitted on the understanding that by '**u**' a vector of complex amplitudes is implied.

An important detail of a piled-foundation model is the soil-pile interface, since this governs how the pile radiates energy into the surrounding soil. This is investigated in the following section before considering further details of the single-pile model.

4.1.1. Pile-Soil Interaction: Modelling the Interface

Consider a pile subject to a time-harmonic load applied to the pile head. In general, both axial and flexural vibrations propagate along the pile and these in turn radiate waves into the surrounding soil. This radiation of energy into the soil has a significant effect on the pile-head dynamic stiffness and it is the radiated wave field that excites any neighbouring piles. This radiation behaviour must therefore be accounted for and the soil-pile interface is an important detail of any comprehensive pile model.

When defining the soil-pile interface in the BEM model, an appropriate number of elements must be chosen along the length of the pile and around its circumference. The latter is particularly important because it determines the geometry of the elements on the free surface of the soil; see Figure 4.1. Discretization of the free surface is required because, as described in Appendix B, the particular BEM formulation used here is based on the full-space Green's functions.

The use of more than four elements around the pile circumference requires non-rectangular elements on the free surface of the half-space. This significantly increases the time required to process the model: more elements require longer computation times and the numerical solution of a model involving non-rectangular elements is more involved; see Appendix B. More time is also required to prepare the more complex mesh geometry. It is therefore important to investigate the

significance of the number of circumferential boundary elements on the pile-soil interaction and select the appropriate number before proceeding with the rest of the modelling.

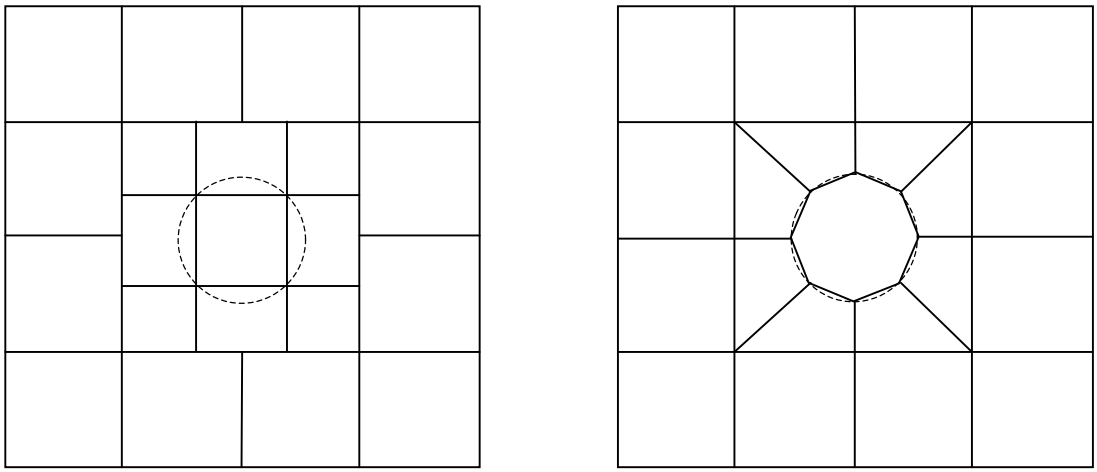

Figure 4.1: Possible boundary-element meshes for use on the free surface of a half-space representing the soil component of a piled-foundation model. The use of more than four elements around the circumference of the pile requires non-rectangular elements on the free surface.

Consider an infinitely long, rigid cylindrical cavity in an infinite elastic solid. Because the cavity is invariant along its longitudinal axis, it may be represented by a two-dimensional BEM model under plane-strain conditions; see Figure 4.2.

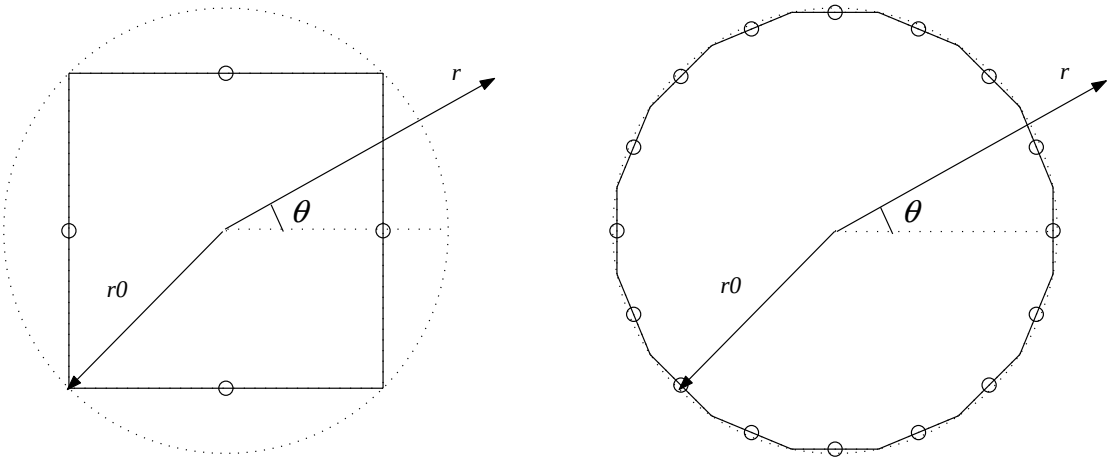

Figure 4.2: A two-dimensional BEM model of an infinitely long, rigid cylindrical cavity in an infinite elastic solid, showing (a) a mesh of four elements and (b) a more representative mesh of 16 elements. Nodes of the constant elements used are represented by ‘o’.

Constant boundary elements are used and therefore the tractions and displacements are assumed to be uniform over each element and equal to the values at their central nodes. Such a model is representative of a transverse section through a rigid massless pile that is perfectly bonded to the surrounding soil, provided the section is far enough away from either end of the pile. By solving the model for both the plane and anti-plane cases (see Appendix B, Section B2.5), that is, for transverse and longitudinal motion of the cavity, the significance of the number of circumferential elements used in a three-dimensional BEM model of a pile may be investigated. The model is particularly useful because an analytical solution exists for motion of the cavity with which the BEM solution may be compared.

Consideration of a rigid cavity is consistent with the assumption that the effects of any local deformation of a given pile section are negligible. It is true that Poisson's ratio effects within a pile lead to local deformation due to coupling between the axial and transverse behaviour; for example, axial compression leads to circumferential expansion of the pile and vice versa. However, such local deformation is a second-order effect and any resulting wave propagation in the soil is assumed negligible. The assumption that the pile is perfectly bonded to the soil is justified given the small amplitude of the ground-borne vibrations of interest.

Plane Solution

Consider first the plane problem corresponding to transverse motion of the cavity. The transverse dynamic stiffness K_t is a function of the cavity radius r_0, the excitation frequency ω and the properties of the elastic solid: the shear modulus μ, density ρ, Poisson's ratio ν and loss factor η.

$$K_t = f\left(r_0, \omega, \mu, \rho, \nu, \eta\right) \tag{4.2}$$

Dimensional analysis enables the non-dimensional transverse stiffness to be written in terms of three non-dimensional parameters:

$$\frac{K_t}{\mu} = g\left(a_0, \nu, \eta\right) \tag{4.3}$$

where $a_0 = \omega r_0 / c_s$ is a non-dimensional frequency based on the S-wave speed in the solid $c_s = \sqrt{\mu/\rho}$.

The value of a_0 is important since it determines the size of the waves in the solid relative to the radius of the cavity; it may be written in terms of the S-wavelength as $a_0 = 2\pi r_0 / \lambda_s$. As a_0 approaches π, the S-wavelength approaches the diameter of the cavity and the BEM model requires a greater number of elements for a given accuracy. Taking the upper frequency limit as 200 Hz and the lowest S-wave speed as 200 m/s, consistent with the majority of practical ground-borne vibration problems, the upper limit of a_0 is 3.1. This is based on an upper limit on r_0 of 0.5 m to accommodate typical designs of pile.

Figure 4.3 plots the real and imaginary components of the non-dimensional transverse stiffness, over this range of a_0, for different numbers of boundary elements. The exact analytical solution is also shown for comparison. The latter is given by Wolf and Song [139] as follows:

$$K_t = \pi \mu a_0^2 \frac{\alpha + \beta - 4}{\alpha\beta - \alpha - \beta} \tag{4.4}$$

where $\alpha = a_0 \dfrac{H_0^{(2)}(a_0)}{H_1^{(2)}(a_0)}$ and $\beta = \dfrac{c_s a_0}{c_p} \dfrac{H_0^{(2)}\left(\dfrac{c_s a_0}{c_p}\right)}{H_1^{(2)}\left(\dfrac{c_s a_0}{c_p}\right)}$, c_p being the P-wave speed.

$H_0^{(2)}$ and $H_1^{(2)}$ being second kind Hankel functions of order zero and one.

It is clear from Figure 4.3 that as the number of elements in the BEM model is increased the solution gradually converges on the analytical solution; with 32 elements the numerical and analytical results are indistinguishable over the frequency range of interest. However, the use of 32 circumferential elements in a three-dimensional pile model would be impractical: a compromise is required between accuracy and processing time to produce an efficient model. The accuracy of a four-element model is therefore investigated further in the remainder of this section.

Equation 4.3 requires the specification of three non-dimensional parameters and the ranges investigated here cover the properties given by Lavergne [74] for a variety of commonly encountered ground types; see Tables 4.1 and 4.2.

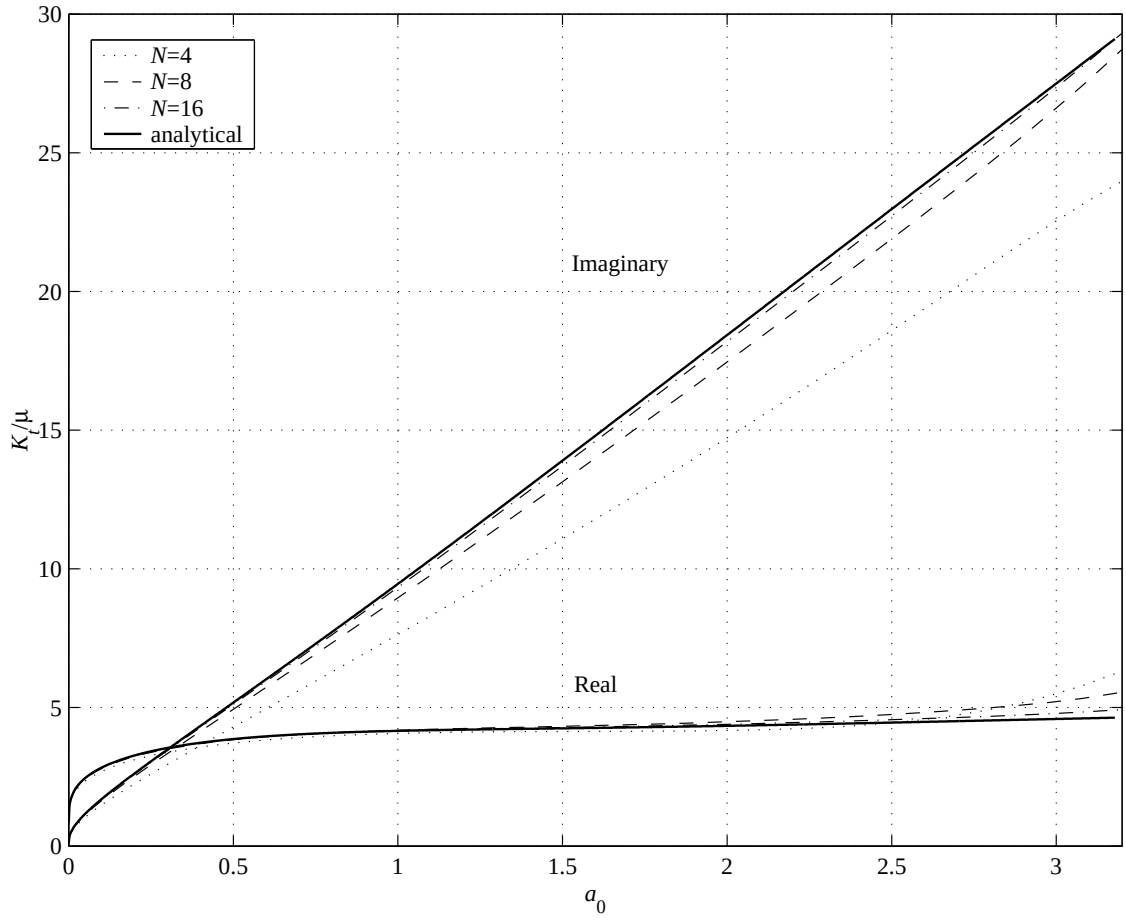

Figure 4.3: The effect of the number of boundary elements N on the transverse dynamic stiffness of an infinitely long, rigid cylindrical cavity in an infinite elastic solid, as calculated by a two-dimensional BEM model. The stiffness K_t is divided by the shear modulus μ of the solid and plotted against non-dimensional frequency $a_0 = \omega r_0 / c_s$. The analytical solution is shown bold for comparison. Typical values for soil of $\nu = 0.30$ and $\eta = 0.02$ are assigned to the solid.

Type of ground	**S-wave velocity [m/s]**	**Density [kg/m^3]**	**Poisson's ratio**
Sands	400-1200	1900-2100	0.46-0.45
Clays	200-800	2000-2400	0.48-0.44
Marls	750 - 1500	2100 - 2600	0.42 - 0.33
Limestones	2000 - 3300	2400 - 2700	0.26 - 0.28
Chalk	1100 - 1300	1800 - 2300	0.35 - 0.33
Granite	2500 - 3300	2500 - 2700	0.28 - 0.29
Basalt	2800 - 3400	2700 - 3100	0.26 - 0.27

Table 4.1: Ranges of S-wave speed, density and Poisson's ratio for a variety of commonly encountered ground types (derived from Lavergne [74]).

Type of ground	**Loss factor**
Clays and marls	0.0143 - 0.0333
Sands and sandstones	0.0067 - 0.0143
Limestones and dolomites	0.0017 - 0.0100
Granites and basalts	0.0017 - 0.0050

Table 4.2: Ranges of damping loss factor for a variety of ground types based on measurements of P-waves over the frequency range from 10 to 250 Hz (derived from Lavergne [74]).

The transverse stiffness of a four-element model has been calculated for the cases when the Poisson's ratio and loss factor of the elastic solid take the limiting values found in the ground, as given in Table 4.1. These results are presented in Figures 4.4 and 4.5.

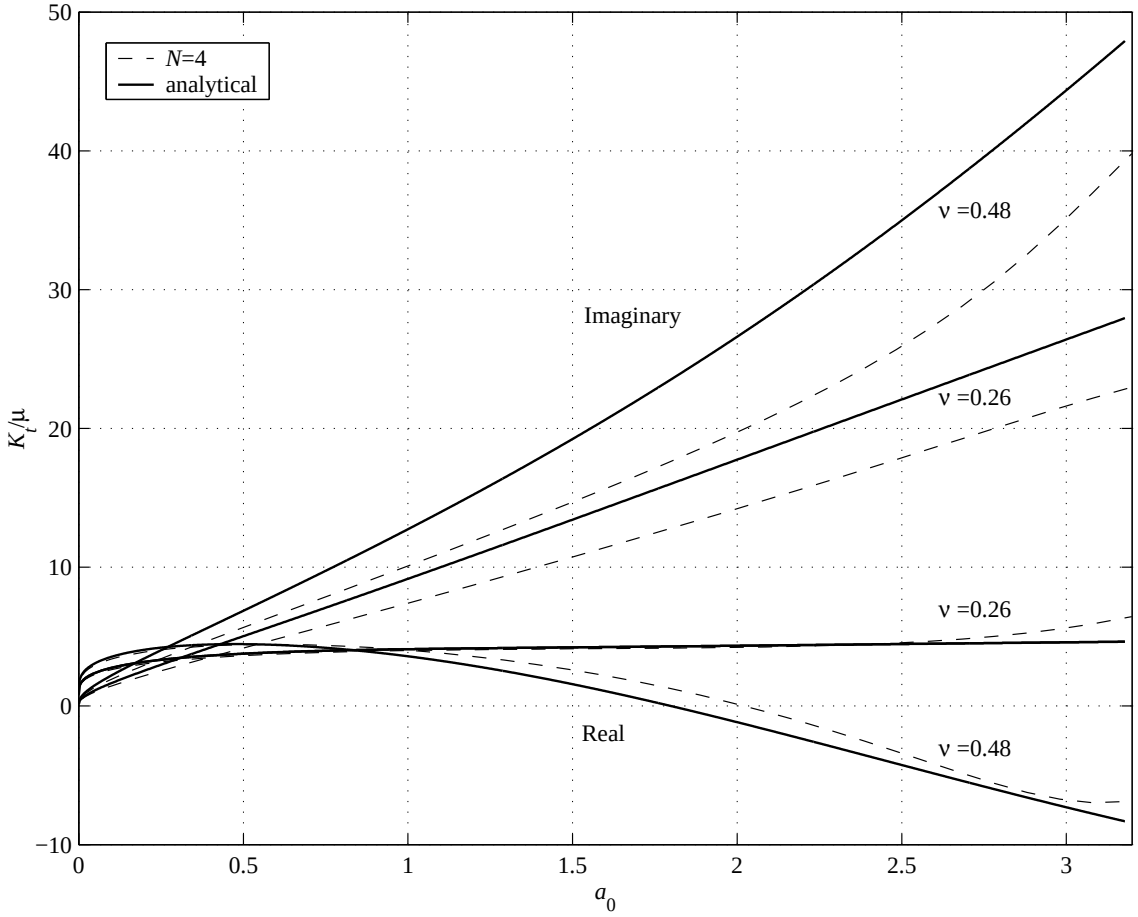

Figure 4.4: Variation with Poisson's ratio ν in the transverse dynamic stiffness of an infinitely long, rigid cylindrical cavity in an infinite elastic solid, as calculated by a two-dimensional four-element BEM model. The stiffness K_t is divided by the shear modulus μ of the solid and plotted against non-dimensional frequency $a_0 = \omega r_0 / c_s$. The analytical solution is shown bold for comparison. A typical value for soil of $\eta = 0.02$ is assigned to the solid.

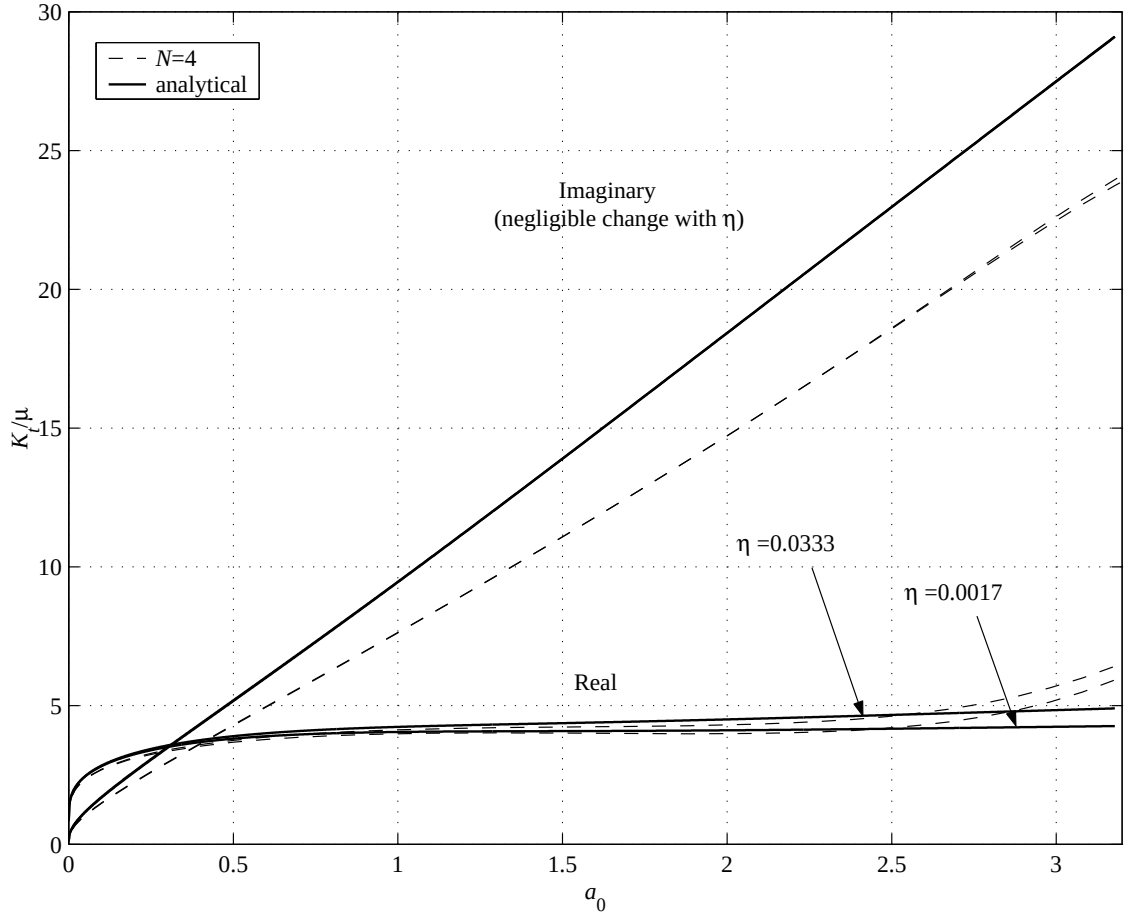

Figure 4.5: Variation with loss factor η in the transverse dynamic stiffness of an infinitely long, rigid cylindrical cavity in an infinite elastic solid, as calculated by a two-dimensional four-element BEM model. The stiffness K_t is divided by the shear modulus μ of the solid and plotted against non-dimensional frequency $a_0 = \omega r_0 / c_s$. The analytical solution is shown bold for comparison. A typical value for soil of $\nu = 0.30$ is assigned to the solid.

In all cases the stiffness is dominated by its imaginary component due to the significant radiation damping provided by the surrounding solid. This is approximately viscous in nature, increasing almost linearly with frequency, and, as is characteristic of radiation damping, the solution is insensitive to the value of the material loss factor η. The four-element BEM model consistently under-predicts the imaginary stiffness component and therefore represents a less heavily damped system than the exact solution. In general, the error in the BEM results increases with frequency as the wavelengths in the solid approach the diameter of the cavity.

The mid-range performance of the model is important since this is where ground-borne vibration levels peak. Analysis of the typical results shown in Figure 4.5 ($\nu = 0.30$) gives the

average error over the frequency range from $a_0 = 0.5$ to 1.5 as –3 % and –19 % in the real and imaginary components respectively. The maximum error of –26 % occurs in the imaginary component at $a_0 = 2.3$ for the limiting case of $\nu = 0.48$. The latter corresponds to an almost incompressible solid and larger errors are to be expected since both the analytical solution and the fundamental solution of the BEM become singular at $\nu = 0.5$.

For any comprehensive pile model, in addition to the dynamic stiffness, the response in the surrounding soil is important since this determines the interaction between neighbouring piles. For the analytical model, the displacement field due to transverse unit-amplitude motion of the cavity is given by Wolf and Song [139] as follows:

$$u_r = \left(\frac{c}{r} \left(\frac{\omega r}{c_p} H_0^{(2)} \left(\frac{\omega r}{c_p} \right) - H_1^{(2)} \left(\frac{\omega r}{c_p} \right) \right) + \frac{d}{r} H_1^{(2)} \left(\frac{\omega r}{c_s} \right) \right) \cos\theta \tag{4.5a}$$

$$u_\theta = -\left(\frac{c}{r} H_1^{(2)} \left(\frac{\omega r}{c_p} \right) + \frac{d}{r} \left(\frac{\omega r}{c_s} H_0^{(2)} \left(\frac{\omega r}{c_s} \right) - H_1^{(2)} \left(\frac{\omega r}{c_s} \right) \right) \right) \sin\theta \tag{4.5b}$$

where $c = \dfrac{(\alpha - 2) r_0}{(\alpha\beta - \alpha - \beta) H_1^{(2)} \left(\dfrac{c_s a_0}{c_p} \right)}$, $d = \dfrac{(\beta - 2) r_0}{(\alpha\beta - \alpha - \beta) H_1^{(2)} (a_0)}$.

θ is the angle from the direction of the cavity motion.

These expressions enable the displacement field predicted by the four-element BEM model to be compared with the exact solution. Figures 4.6 to 4.8 provide a qualitative overview by plotting the radiated displacement field, up to $r = 13.5 r_0$, for frequencies of $a_0 = 0.05$, 0.5 and 1.5 when typical values of Poisson's ratio and loss factor for soil are assigned to the elastic solid.

The nature of the displacement field is correctly predicted by the BEM model. At very low frequencies the field is essentially unidirectional, whereas at higher frequencies the near field is more complex and P- and S-waves are clearly discernable propagating away from the cavity. Pure P-waves are generated along the line of motion of the cavity and pure S-waves along a line perpendicular to this; a mixture of the two wave types occurs in between. Again, the errors in the

BEM results are small at low frequencies but increase as the wavelengths in the solid approach the diameter of the cavity.

(a) (b)

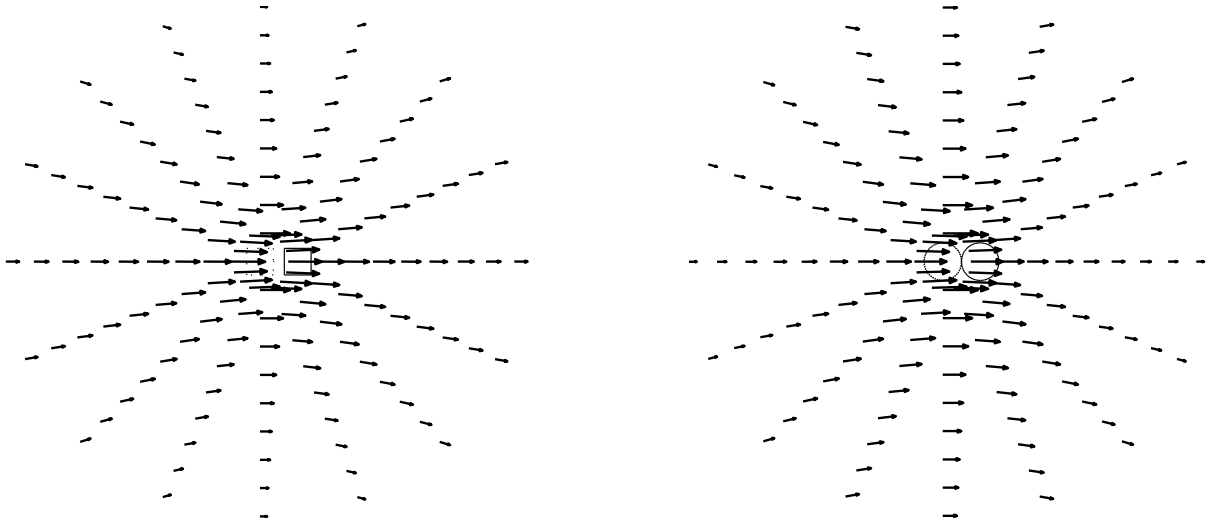

Figure 4.6: The displacement field due to transverse unit-amplitude motion of an infinitely long, rigid cylindrical cavity in an infinite elastic solid, as calculated by (a) a two-dimensional four-element BEM model and (b) the analytical solution. Particle displacement vectors show the direction of the displacement and have lengths equal to the magnitude. Non-dimensional frequency $a_0 = 0.05$ and typical values for soil of $\nu = 0.30$ and $\eta = 0.02$ are assigned to the solid.

(a) (b)

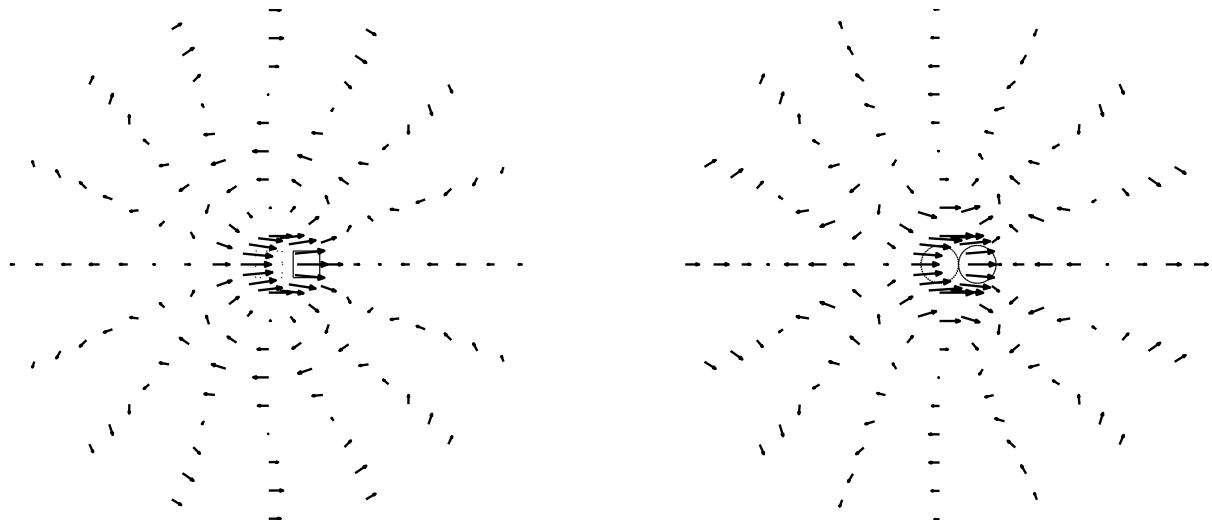

Figure 4.7: The displacement field due to transverse unit-amplitude motion of an infinitely long, rigid cylindrical cavity in an infinite elastic solid, as calculated by (a) a two-dimensional four-element BEM model and (b) the analytical solution. Particle displacement vectors show the direction of the displacement

and have lengths equal to the magnitude. Non-dimensional frequency $a_0 = 0.5$ and typical values for soil of $\nu = 0.30$ and $\eta = 0.02$ are assigned to the solid.

(a) (b)

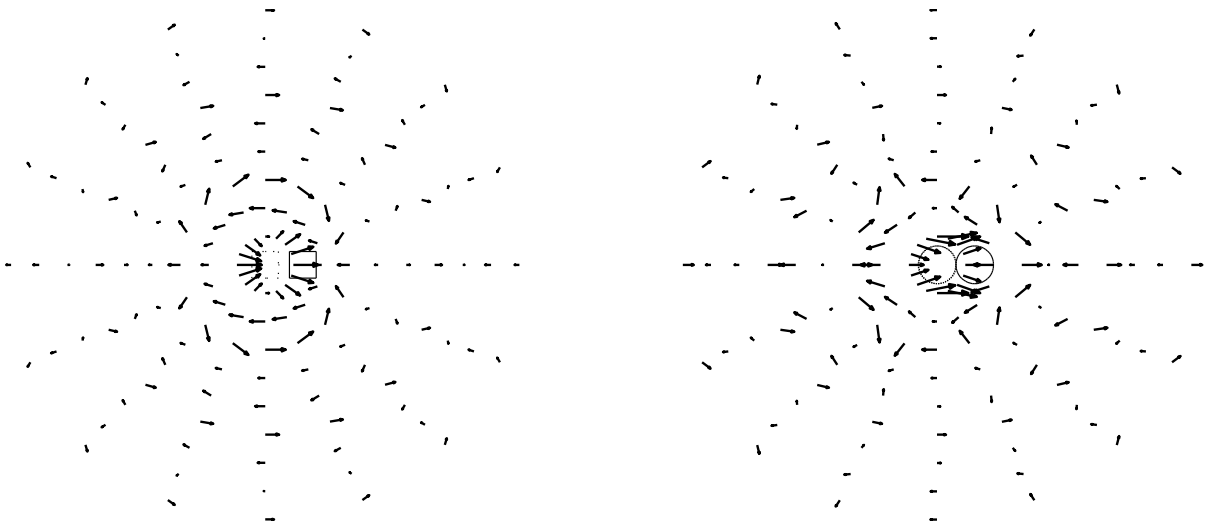

Figure 4.8: The displacement field due to transverse unit-amplitude motion of an infinitely long, rigid cylindrical cavity in an infinite elastic solid, as calculated by (a) a two-dimensional four-element BEM model and (b) the analytical solution. Particle displacement vectors show the direction of the displacement and have lengths equal to the magnitude. Non-dimensional frequency $a_0 = 1.5$ and typical values for soil of $\nu = 0.30$ and $\eta = 0.02$ are assigned to the solid.

A quantitative assessment of the displacement field may be made by considering Figures 4.9 and 4.10, which plot the magnitude and phase of the displacement at points located along the line $\theta = 0$ collinear with the motion of the cavity. These points are chosen as representing neighbouring pile locations in a row of piles. The cases when Poisson's ratio takes the limiting values typically found in the ground are plotted, and a loss factor of 0.02 is used although the solution is insensitive to the precise value. In both cases the agreement between the BEM and analytical results is good and, as expected from Saint Venant's principle, the agreement improves with distance from the cavity. At a typical pile spacing of $r = 4r_0$, the error for the case of $\nu = 0.3$, averaged over the middle frequency range from $a_0 = 0.5$ to 1.5, is –14 % in the displacement magnitude and 9 % in the phase.

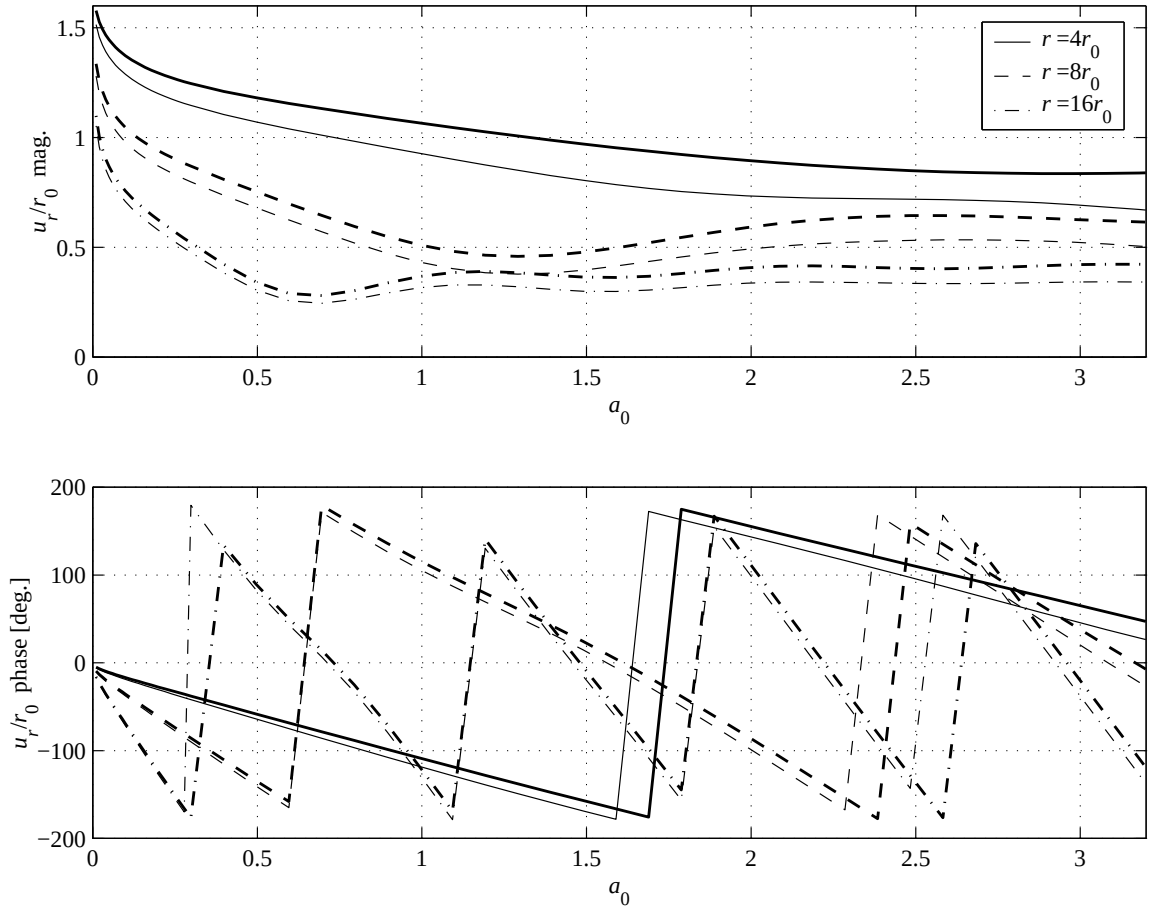

Figure 4.9: Magnitude and phase of the displacement u_r in an infinite elastic solid, of Poisson's ratio $\nu = 0.26$ and loss factor $\eta = 0.02$, due to transverse unit-amplitude motion of an infinitely long, rigid cylindrical cavity. The displacement is calculated by a two-dimensional four-element BEM model for points located at various distances *r* from the centre of the cavity along a line collinear with its motion. The displacement is divided by the cavity radius r_0 and plotted against non-dimensional frequency $a_0 = \omega r_0 / c_s$; the analytical solution is shown bold for comparison.

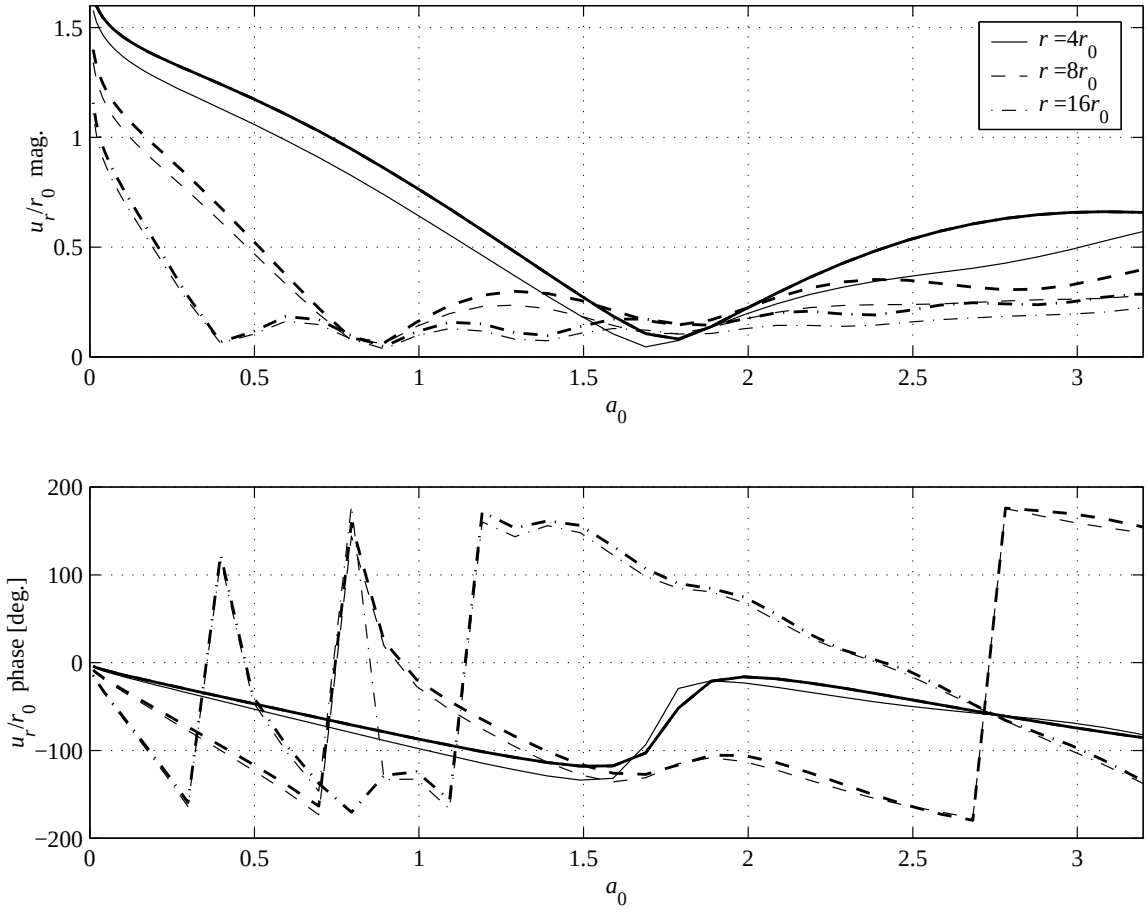

Figure 4.10: Magnitude and phase of the displacement u_r in an infinite elastic solid, of Poisson's ratio $\nu = 0.48$ and loss factor $\eta = 0.02$, due to transverse unit-amplitude motion of an infinitely long, rigid cylindrical cavity. The displacement is calculated by a two-dimensional four-element BEM model for points located at various distances r from the centre of the cavity along a line collinear with its motion. The displacement is divided by the cavity radius r_0 and plotted against non-dimensional frequency $a_0 = \omega r_0 / c_s$; the analytical solution is shown bold for comparison.

Anti-Plane Solution

Before concluding this investigation, the anti-plane case corresponding to longitudinal motion of the cavity must also be considered. Figure 4.11 plots the real and imaginary components of the non-dimensional longitudinal dynamic stiffness of the cavity for different numbers of boundary elements. The results are compared with the exact analytical solution, as derived in Appendix F. Because anti-plane motion involves only shearing of the solid, the stiffness is independent of

Poisson's ratio and, as with plane motion, the behaviour is dominated by radiation damping such that the precise value of the loss factor is unimportant.

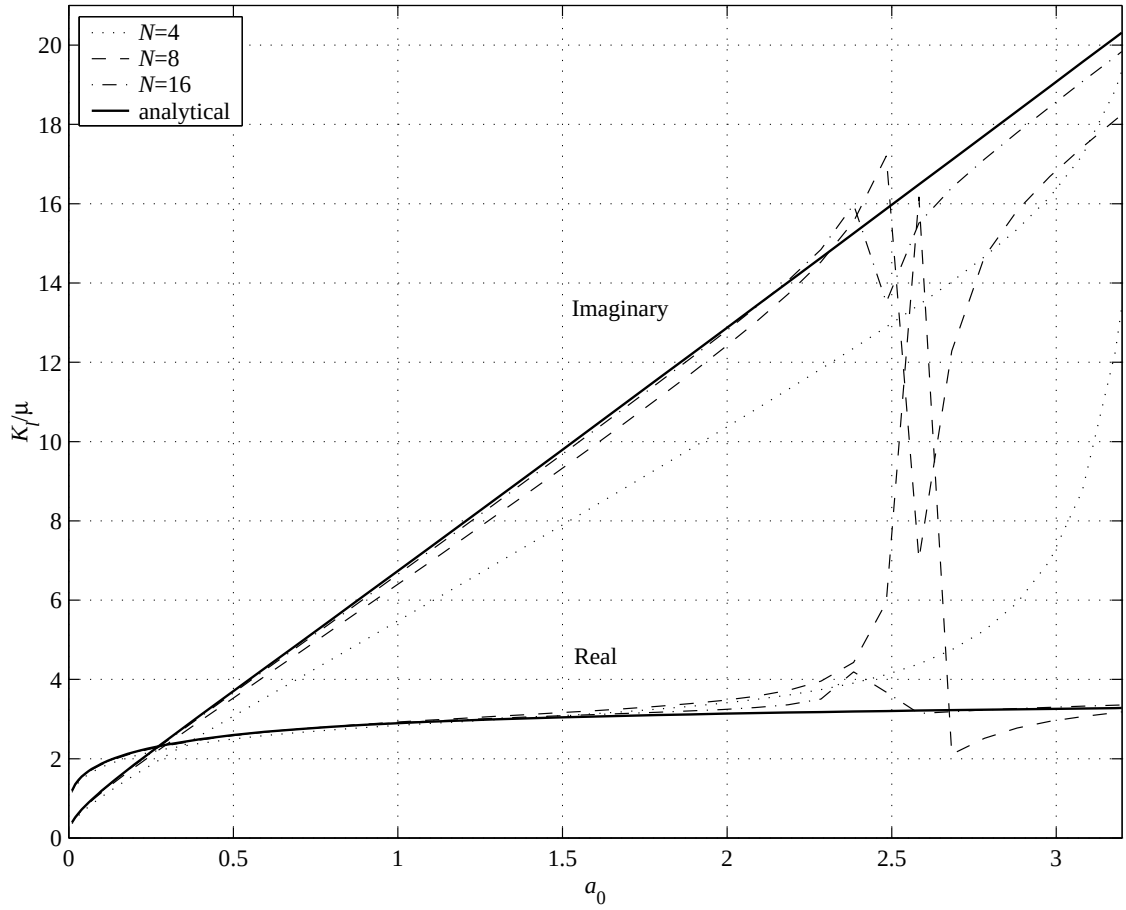

Figure 4.11: The effect of the number of boundary elements *N* on the longitudinal dynamic stiffness of an infinitely long, rigid cylindrical cavity in an infinite elastic solid, as calculated by a two-dimensional BEM model. The stiffness K_l is divided by the shear modulus μ of the solid and plotted against non-dimensional frequency $a_0 = \omega r_0 / c_s$. The analytical solution is shown bold for comparison. A typical value for soil of $\eta = 0.02$ is assigned to the solid.

As with the calculation of transverse stiffness, the BEM solution gradually converges on the analytical solution as the number of elements is increased. Again, the four-element BEM model consistently under-predicts the imaginary stiffness component. A significant feature of Figure 4.11 is the 'resonance' evident in the results from the 8- and 16-element models. This is an example of a fictitious natural frequency, as described in Appendix B. It has no physical meaning for the cavity but occurs due to the excitation frequency coinciding with the first natural frequency of the equivalent internal problem, that is, an infinitely long cylindrical bar subject to

imposed displacements. The four-element model is stiffer and consequently the natural frequencies of the internal problem lie just outside the frequency range of interest. For this model the average error between $a_0 = 0.5$ and 1.5 is –2 % and –18 % in the real and imaginary components respectively. Note that fictitious frequencies do not arise in a three-dimensional pile model due to the presence of the free surface [13].

Figure 4.12 provides a quantitative assessment of the radiated displacement field in a manner similar to Figures 4.9 and 4.10 for the plane solution. Again, the agreement between the BEM and analytical results is good: the average error between $a_0 = 0.5$ and 1.5 at the point $r = 4r_0$ is –11 % in the displacement magnitude and 10 % in the phase.

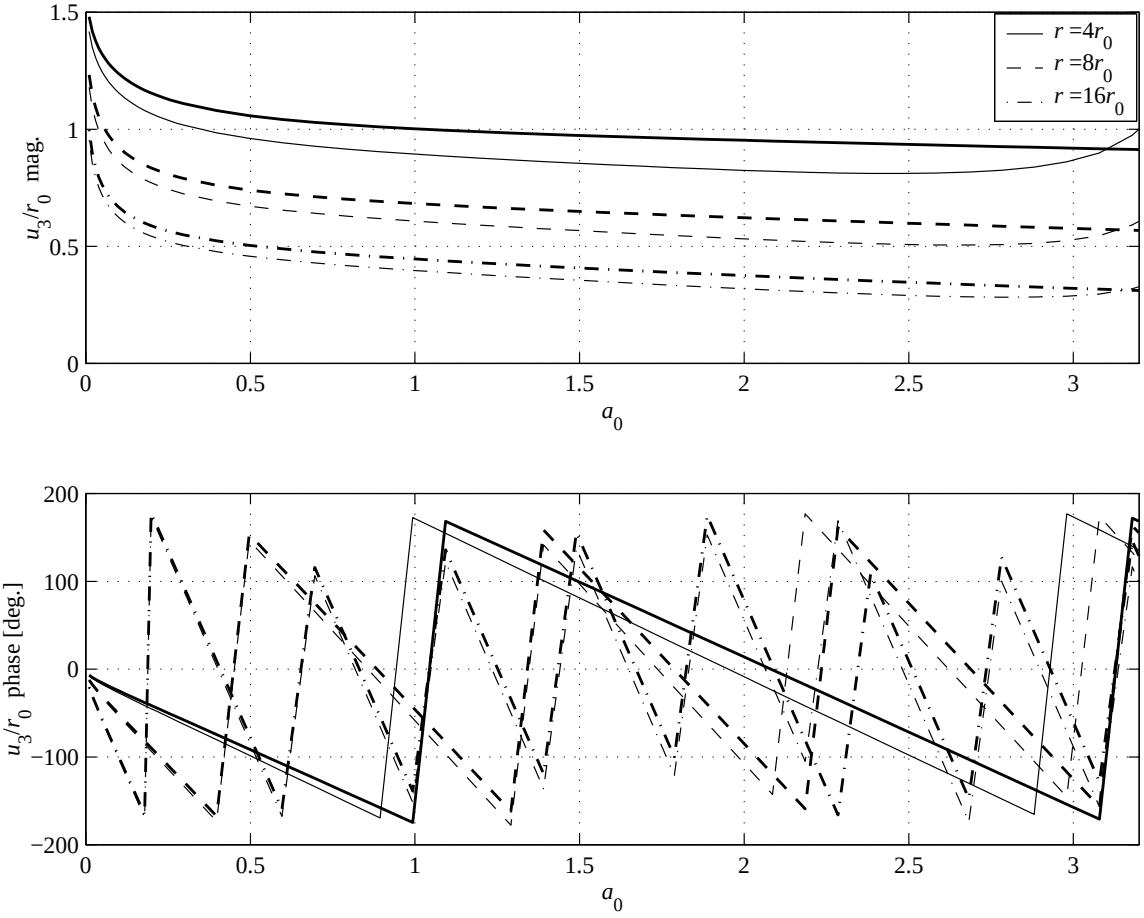

Figure 4.12: Magnitude and phase of the displacement u_3 in an infinite elastic solid, of loss factor $\eta = 0.02$, due to longitudinal unit-amplitude motion of an infinitely long, rigid cylindrical cavity. The displacement is calculated by a two-dimensional four-element BEM model for points located at various distances *r* from the centre of the cavity. The displacement is divided by the cavity radius r_0 and plotted against non-dimensional frequency $a_0 = \omega r_0 / c_s$; the analytical solution is shown bold for comparison.

Conclusions

This investigation has considered the use of a two-dimensional four-element BEM model for modelling the behaviour of an infinitely long, rigid cylindrical cavity in an infinite elastic solid. The conclusions are summarised as follows:

- the qualitative behaviour of the cavity – the form of its dynamic stiffness and the radiated displacement field – is correctly predicted for both transverse and longitudinal motion;
- the behaviour is dominated by radiation damping such that the precise value of the material loss factor is unimportant;
- for typical values of material properties, an average numerical error of up to 20 % may be encountered over the frequency range in which ground-borne vibration levels typically peak;
- the error in the dynamic stiffness manifests primarily as an under-prediction of the imaginary stiffness component, which corresponds to an under-prediction of the level of radiation damping.

Limiting the number of boundary elements to four clearly limits the numerical accuracy of the model, and a similar accuracy may be expected from a three-dimensional pile model based on four elements around the pile circumference. This must be balanced against the shorter processing time required and the advantages of using only rectangular elements. The aim of the final model is to capture the essential dynamic behaviour of a piled-foundation such that, when coupled to a generic building model, predictions of insertion performance may be made; it is not the aim of the model to make predictions of absolute vibration levels. The errors encountered here are therefore considered to be acceptable and the remainder of this chapter proceeds on this basis. Note that, if greater accuracy is required and the necessary computing power becomes available, additional circumferential elements may be added in the future.

4.1.2. The Soil Model

The three-dimensional model of a single pile may now be developed having selected four boundary elements for use around the pile circumference. The BEM model representing the soil

consists of a total of *N* rectangular, constant elements, as illustrated in Figure 4.13. Being constant elements, the tractions and displacements are assumed to be uniform over each element and equal to the values at their central nodes. The free surface may, in general, be represented by a rectangular mesh of N_1 by N_2 elements, minus one for the pile, giving a total of N_{fs}. For the single-pile model a square mesh is used and therefore $N_1 = N_2$ and $N_{fs} = N_1^2 - 1$. N_{sp} elements represent the soil-pile interface. The necessary number and size of elements required will be discussed further in Section 4.1.5.

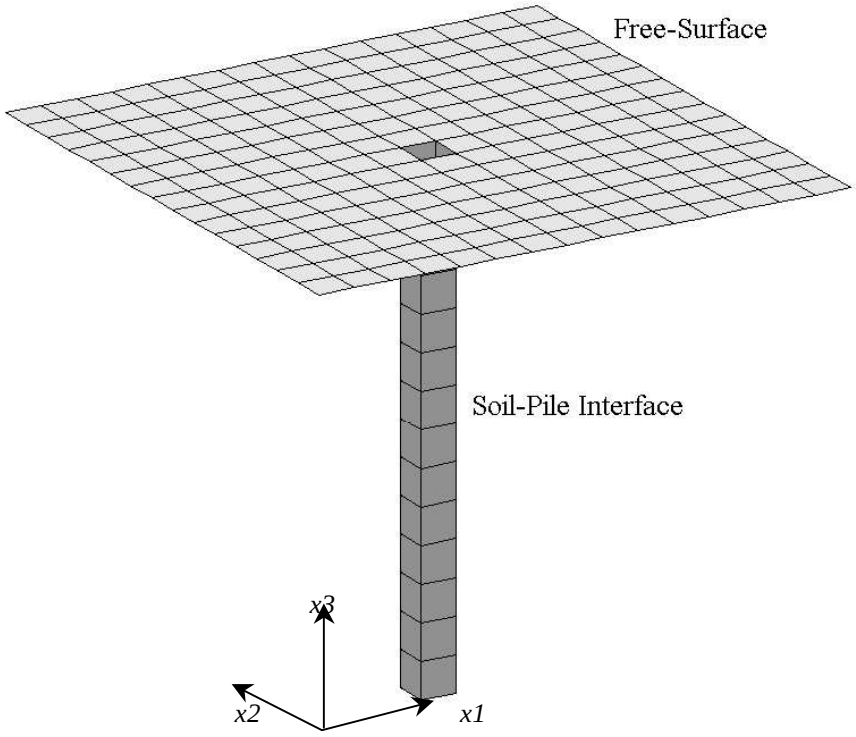

Figure 4.13: The boundary-element mesh representing the free surface and soil-pile interface of the single-pile model. The free surface should be of infinite extent in the x_1x_2-plane but in practice the mesh may be curtailed at a finite distance from the pile; here $N_1 = N_2 = 15$.

For each of the *N* nodes of the boundary-element mesh there are three values of displacement and traction, one for each direction. Equation B9 of Appendix B relates these variables as follows:

$$\mathbf{Hu} = \mathbf{Gp} \tag{4.6}$$

where **H** and **G** are two 3*N* x 3*N* matrices describing the behaviour of the soil in terms of its density, shear modulus, Poisson's ratio, damping loss factor and the frequency of interest. **u** and **p** are two 3*N* x 1 vectors assembled, respectively, from the 3 x 1 vectors containing the complex displacement and traction amplitudes of each node. For example:

$$\mathbf{u} = \begin{bmatrix} u_1^1 & u_2^1 & u_3^1 & u_1^2 & u_2^2 & u_3^2 & \cdots & u_1^N & u_2^N & u_3^N \end{bmatrix}^{\mathrm{T}} \tag{4.7}$$

where $\mathbf{u}^j$ is the displacement vector of node '*j*' and 'T' denotes the vector transpose. The corresponding traction vector **p** takes a similar form.

Equation 4.7 may be rearranged and the resulting matrix partitioned, along with **u** and **p**, to give:

$$\begin{aligned} \mathbf{u} &= [\mathbf{H}]^{-1}\mathbf{G}\mathbf{p} \\ &= \mathbf{H}_s\mathbf{p} \end{aligned} \tag{4.8}$$

$$\begin{bmatrix} \mathbf{u}_{fs} \\ \mathbf{u}_{sp} \end{bmatrix} = \begin{bmatrix} \mathbf{H}_s^{11} & \mathbf{H}_s^{12} \\ \mathbf{H}_s^{21} & \mathbf{H}_s^{22} \end{bmatrix} \begin{bmatrix} \mathbf{p}_{fs} \\ \mathbf{p}_{sp} \end{bmatrix} \tag{4.9}$$

where the vector subscripts 'fs' and 'sp' denote variables on the free surface and soil-pile interface respectively. $\mathbf{H}_s$ will be known as the soil frequency-response function (FRF) matrix, taking care to note that it relates displacements and tractions, rather than forces, at the particular frequency of interest.

Equation 4.9 fully describes the three-dimensional behaviour of the soil. In the next section, the model chosen for the pile is described.

4.1.3. The Pile Model

The aim of the pile model is to represent the global, longitudinal and transverse behaviour of the pile when time-harmonic forces and moments are applied to the pile head. This is achieved by combining the behaviour of an elastic bar and Euler beam with the following properties: length *L*,

cross-sectional area *A*, second moment of area *I*, density ρ_p and Young's modulus E_p. As discussed in Section 4.1.1, local deformation of the pile cross-section is neglected. A complex value of Young's modulus may be specified to account for material damping in the pile, as described in Section 3.1.1. However, this is unnecessary given that the pile behaviour is dominated by the damping in the soil.

The pile is represented by its centroidal axis along which are defined N_p equally spaced nodes; see Figure 4.14. A further two nodes are added at the head and tip of the pile. The nodes are simply defined as points at which forces may be applied to the pile and at which the resulting displacements may be calculated.

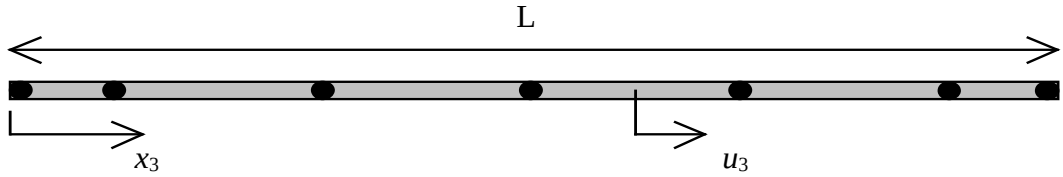

Figure 4.14: Schematic diagram of the pile model for the case of $N_p = 5$. A further two nodes are added at the head and tip of the pile (for convenience the x_3-axis is drawn horizontally).

Consider the response of the pile to a time-harmonic force of unit amplitude applied in the x_3-direction at node '*j*'. To find the displacement u_3 at any location along the pile, the pile must be considered in two lengths, one either side of node '*j*'. The theory governing longitudinal vibration of an elastic bar, as given by Newland [101], gives the following general equation for u_3:

$$u_3(x_3,t) = \mathrm{Re}\left\{u_3(x_3,\omega)e^{i\omega t}\right\} \tag{4.10}$$

where

$$u_3(x_3,\omega) = u_3^I = A^I \cos\alpha x_3 + B^I \sin\alpha x_3 \qquad \text{for } 0 \le x_3 \le x_3^j$$
$$u_3(x_3,\omega) = u_3^{II} = A^{II} \cos\alpha x_3 + B^{II} \sin\alpha x_3 \qquad \text{for } x_3^j \le x_3 \le L$$

The superscripts '*I*' and '*II*' denote the two sections of the pile and $\alpha = \omega\sqrt{\rho_p / E_p}$.

Compatibility of displacements requires the solution for u_3 to be continuous at node '*j*':

$$u_3^I(x_3^j) = u_3^{II}(x_3^j) \tag{4.11}$$

In addition, the following boundary conditions arise from considering equilibrium of forces. Since the pile is otherwise unloaded, the ends of the pile must be stress-free:

$$\left(\frac{du_3^I}{dx_3}\right)_{x_3=0} = \left(\frac{du_3^{II}}{dx_3}\right)_{x_3=L} = 0 \tag{4.12}$$

And equilibrium applied at node '*j*' gives:

$$EA\left(\frac{du_3^I}{dx_3}\right)_{x_3=x_3^j} - EA\left(\frac{du_3^{II}}{dx_3}\right)_{x_3=x_3^j} = 1 \tag{4.13}$$

By incorporating these boundary conditions into the general solution, the following expressions for the constants of Equation 4.10 may be derived:

$$A^I = \frac{-\cos\alpha x_3^j - \sin\alpha x_3^j \tan\alpha L}{EA\alpha\tan\alpha L}; \quad A^{II} = \frac{-\cos\alpha x_3^j}{EA\alpha\tan\alpha L}; \quad B^I = 0; \quad B^{II} = \frac{-\cos\alpha x_3^j}{EA\alpha} \tag{4.14}$$

Thus, for the given unit force at x_3^j, the pile response at the frequency of interest may be calculated at any of the nodes by substituting for the appropriate value of x_3.

Now consider applying the unit force in the x_1-direction. For transverse loading the pile is assumed to behave as an Euler beam [101], one in which shear deformation and the effects of rotary inertia are assumed to be negligible. As discussed in Section 3.1.1 in the context of building structures, this is an appropriate model for the frequency range of interest. The Euler theory allows the general equation for u_1 to be written as follows:

$$u_1(x_3,t) = \mathrm{Re}\left\{u_1(x_3,\omega)e^{i\omega t}\right\} \tag{4.15}$$

where

$$u_1(x_3,\omega) = u_1^I = A^I e^{\beta x_3} + B^I e^{i\beta x_3} + C^I e^{-\beta x_3} + D^I e^{-i\beta x_3} \qquad \text{for } 0 \le x_3 \le x_3^j$$

$$u_1(x_3,\omega) = u_1^{II} = A^{II} e^{\beta x_3} + B^{II} e^{i\beta x_3} + C^{II} e^{-\beta x_3} + D^{II} e^{-i\beta x_3} \qquad \text{for } x_3^j \le x_3 \le L$$

and

$$\beta = \left(\frac{\rho_p A \omega^2}{E_p I} \right)^{1/4}$$

Compatibility requires the solutions for both displacement and rotation to be continuous at node '*j*':

$$u_1^I(x_3^j) = u_1^{II}(x_3^j) \quad \text{and} \quad \left(\frac{du_1^I}{dx_3} \right)_{x_3=x_3^j} = \left(\frac{du_1^{II}}{dx_3} \right)_{x_3=x_3^j} \tag{4.16}$$

In addition, the following boundary conditions arise from considering equilibrium of forces and moments. Since the pile is otherwise unloaded, there are no moments or shear forces at the ends of the pile:

$$\left(\frac{d^2 u_1^I}{dx_3^{\,2}} \right)_{x_3=0} = \left(\frac{d^3 u_1^I}{dx_3^{\,3}} \right)_{x_3=0} = 0 \quad \text{and} \quad \left(\frac{d^2 u_1^{II}}{dx_3^{\,2}} \right)_{x_3=L} = \left(\frac{d^3 u_1^{II}}{dx_3^{\,3}} \right)_{x_3=L} = 0 \tag{4.17}$$

And equilibrium applied at node '*j*' gives:

$$\left(\frac{d^2 u_1^I}{dx_3^{\,2}} \right)_{x_3=x_3^j} = \left(\frac{d^2 u_1^{II}}{dx_3^{\,2}} \right)_{x_3=x_3^j} \quad \text{and} \quad EI \left(\frac{d^3 u_1^I}{dx_3^{\,3}} \right)_{x_3=x_3^i} - EI \left(\frac{d^3 u_1^{II}}{dx_3^{\,3}} \right)_{x_3=x_3^i} = 1 \tag{4.18}$$

By incorporating these boundary conditions into the general solution, eight equations are obtained which may be assembled into the matrix form of Equation 4.19.

$$\begin{bmatrix} e^{\beta x_3^j} & e^{i\beta x_3^j} & e^{-\beta x_3^j} & e^{-i\beta x_3^j} & -e^{\beta x_3^j} & -e^{i\beta x_3^j} & -e^{-\beta x_3^j} & -e^{-i\beta x_3^j} \\ e^{\beta x_3^j} & ie^{i\beta x_3^j} & -e^{-\beta x_3^j} & -ie^{-i\beta x_3^j} & -e^{\beta x_3^j} & -ie^{i\beta x_3^j} & e^{-\beta x_3^j} & ie^{-i\beta x_3^j} \\ 1 & -1 & 1 & -1 & 0 & 0 & 0 & 0 \\ 1 & -i & -1 & i & 0 & 0 & 0 & 0 \\ 0 & 0 & 0 & 0 & e^{\beta L} & -e^{i\beta L} & e^{-\beta L} & -e^{-i\beta L} \\ 0 & 0 & 0 & 0 & e^{\beta L} & -ie^{i\beta L} & -e^{-\beta L} & ie^{-i\beta L} \\ e^{\beta x_3^j} & -e^{i\beta x_3^j} & e^{-\beta x_3^j} & -e^{-i\beta x_3^j} & -e^{\beta x_3^j} & e^{i\beta x_3^j} & -e^{-\beta x_3^j} & e^{-i\beta x_3^j} \\ e^{\beta x_3^j} & -ie^{i\beta x_3^j} & -e^{-\beta x_3^j} & ie^{-i\beta x_3^j} & -e^{\beta x_3^j} & ie^{i\beta x_3^j} & e^{-\beta x_3^j} & -ie^{-i\beta x_3^j} \end{bmatrix} \begin{bmatrix} A^I \\ B^I \\ C^I \\ D^I \\ A^{II} \\ B^{II} \\ C^{II} \\ D^{II} \end{bmatrix} = \begin{bmatrix} 0 \\ 0 \\ 0 \\ 0 \\ 0 \\ 0 \\ 0 \\ 1/EI\beta^3 \end{bmatrix} \tag{4.19}$$

Inversion of Equation 4.19 enables the constants of Equation 4.15 to be determined for the particular frequency of interest.

Using Equations 4.10 and 4.15, the response of the pile to forces applied in any direction at any of the $N_p + 2$ nodes may be calculated. To complete the pile model it must be possible to

also calculate the response to a moment applied at the pile-head. Equation 4.15 is again used but, since the moment is applied at the pile head, the response is fully described by u_1^I and only four constants are required. These constants are found in a similar way to before but now the boundary conditions are derived by considering equilibrium at the ends of the pile. Moment equilibrium gives:

$$EI\left(\frac{d^2u_1^I}{dx_3^{\,2}}\right)_{x_3=0}=0 \quad \text{and} \quad \left(\frac{d^2u_1^I}{dx_3^{\,2}}\right)_{x_3=L}=1 \tag{4.20}$$

And equilibrium of shear forces gives:

$$\left(\frac{d^3u_1^I}{dx_3^{\,3}}\right)_{x_3=0}=\left(\frac{d^3u_1^I}{dx_3^{\,3}}\right)_{x_3=L}=0 \tag{4.21}$$

These are assembled into the following matrix equation, which is then inverted to give the four constants of u_1^I.

$$\begin{bmatrix} 1 & -1 & 1 & -1 \\ e^{\beta L} & -e^{i\beta L} & e^{-\beta L} & -e^{-i\beta L} \\ 1 & -i & -1 & i \\ e^{\beta L} & -ie^{i\beta L} & -e^{-i\beta L} & ie^{-i\beta L} \end{bmatrix}\begin{bmatrix} A^I \\ B^I \\ C^I \\ D^I \end{bmatrix}=\begin{bmatrix} 1/EI\beta^2 \\ 0 \\ 0 \\ 0 \end{bmatrix} \tag{4.22}$$

Using the above approach, with the exception of torsion about the longitudinal axis, a fully three-dimensional model of the pile may be constructed. The form of the FRF matrix describing this model will be described later; first the nature of the coupling conditions between the pile and soil are described.

4.1.4. Coupling the Pile and Soil

The first thing to note is that the only external loads are applied to the pile head; the free surface of the soil is stress free and therefore $\mathbf{p_{fs}}=\mathbf{0}$. Equation 4.9 can therefore be written as the following two matrix equations:

$$\mathbf{u}_{\mathbf{fs}} = \mathbf{H}_{\mathbf{s}}^{12}\mathbf{p}_{\mathbf{sp}} \tag{4.23}$$

and

$$\mathbf{u}_{\mathbf{sp}} = \mathbf{H}_{\mathbf{s}}^{22}\mathbf{p}_{\mathbf{sp}} \tag{4.24}$$

Now consider the coupling conditions at the soil-pile interface; see Figure 4.15. The soil model represents the soil-pile interface by N_{sp} boundary elements, each having a central node. The pile is represented by its centroidal axis along which lie $N_p + 2$ nodes (N_p equally spaced nodes plus one at the pile head and one at the tip). All nodes on the pile are coupled to those of the soil-pile interface except the pile-head node; this is reserved for the application of external loads.

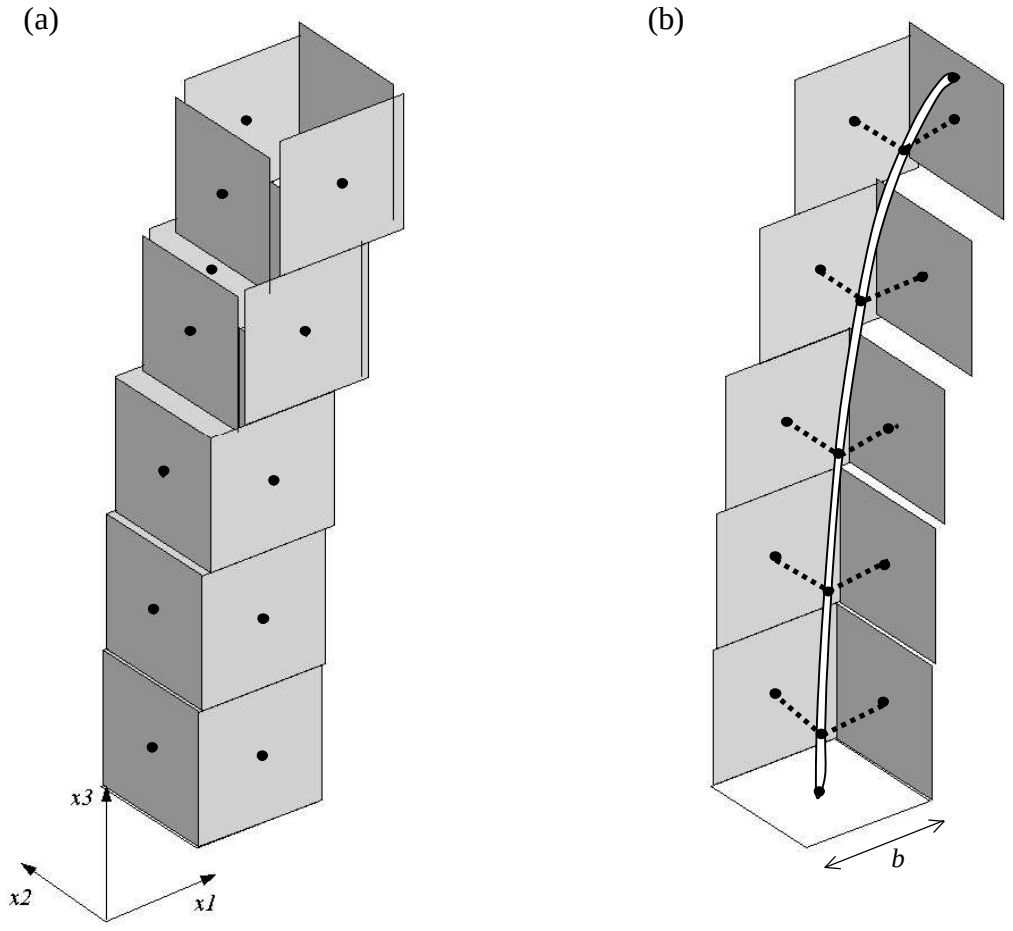

Figure 4.15: Schematic diagram illustrating the coupling between the soil and pile models for the case of $N_p = 5$ ($N_{sp} = 21$), showing, in a general displaced configuration, (a) the boundary elements of the soil-pile interface and (b) the location of the pile centroid with the front boundary elements removed (the free-surface is not shown). Coupled nodes are joined with dashed lines.

As discussed in Section 4.1.1, the local deformation of the pile is neglected and it is assumed that the pile is perfectly bonded to the soil. These assumptions cause the boundary elements representing the soil-pile interface to move together with the pile centroid:

$$\mathbf{u}_{\mathbf{sp}}^{4j-3} = \mathbf{u}_{\mathbf{sp}}^{4j-2} = \mathbf{u}_{\mathbf{sp}}^{4j-1} = \mathbf{u}_{\mathbf{sp}}^{4j} = \mathbf{u}_{\mathbf{p}}^{j} \qquad \text{for } j = 1,...N_p \tag{4.25a}$$

and

$$\mathbf{u}_{\mathbf{sp}}^{4N_p+1} = \mathbf{u}_{\mathbf{p}}^{N_p+1} \tag{4.25b}$$

where $\mathbf{u_p}$ is a vector containing the nodal displacements of the pile, except those at the pile-head node, and the node numbering is assumed to extend from the first node below the pile head to the last node at the pile tip. The last node of the soil mesh is coupled directly to the last node of the pile since this represents the interface with the pile tip.

Equation 4.25 leads to an expression of displacement compatibility between the soil and the pile:

$$\mathbf{u_{sp}} = \mathbf{Q_1 u_p} \tag{4.26}$$

where $\mathbf{Q_1}$ is a $(12N_p + 3)$ x $(3N_p + 3)$ transformation matrix given in Appendix G.

A similar expression of force equilibrium exists. By summing up the effects of the tractions acting on the soil-pile interface, the resultant forces acting on the pile centroid are found:

$$\mathbf{f}_{\mathbf{p}}^{j} = -b^2\left(\mathbf{p}_{\mathbf{sp}}^{4j-3} + \mathbf{p}_{\mathbf{sp}}^{4j-2} + \mathbf{p}_{\mathbf{sp}}^{4j-1} + \mathbf{p}_{\mathbf{sp}}^{4j}\right) \qquad \text{for } j = 1,...N_p \tag{4.27a}$$

and

$$\mathbf{f}_{\mathbf{p}}^{N_p+1} = -b^2\mathbf{p}_{\mathbf{sp}}^{4N_p+1} \tag{4.27b}$$

where $\mathbf{f_p}$ is a vector containing the nodal forces of the pile, except those at the pile-head node and *b* is the side length of the square boundary-elements representing the soil-pile interface. As a matrix equation:

$$\mathbf{f_p} = -b^2 [\mathbf{Q_1}]^{\mathrm{T}} \mathbf{p_{sp}} \tag{4.28}$$

Further consideration must now be given to the form of the FRF matrix describing the behaviour of the pile. With the soil and pile models so far described, a fully three-dimensional model, with the exception of pile torsion, may be assembled. It is now worth considering the nature of the particular pile-head loading that is of interest. As discussed in Section 3.1, the overall objective is to assemble a generic model of a base-isolated building based on a planar building coupled to a row of piles. The planar building model results in a simplified state of loading at the pile head; see Figure 4.16. Forces are only applied to the pile head in the x_1- and x_3-directions, and moments only about the x_2-direction: the resulting motion of the pile lies in the $x_1 x_3$-plane due to the symmetry of the model.

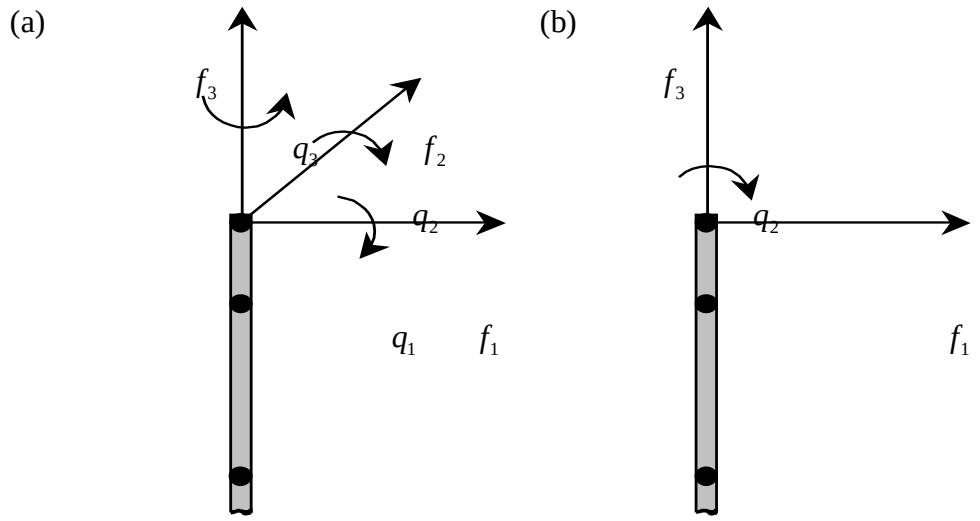

Figure 4.16: Pile-head loading in (a) a fully three-dimensional base-isolated building model and (b) a model in which the building is planar.

Given this load state at the pile head, the required FRF matrix of the pile $\mathbf{H_p}$ may now be assembled from the equations of Section 4.1.3. By considering the application of unit forces in the x_1- and x_3-directions at each node along the pile, and for the pile-head node the additional

application of a moment about the x_2-direction, the FRFs describing the pile behaviour may be calculated. These functions are assembled into the following matrix:

$$\begin{bmatrix} \mathbf{u}_{\mathbf{ph}} \\ \mathbf{u}_{\mathbf{p}} \end{bmatrix} = \begin{bmatrix} \mathbf{H}_{\mathbf{p}}^{11} & \mathbf{H}_{\mathbf{p}}^{12} \\ \mathbf{H}_{\mathbf{p}}^{21} & \mathbf{H}_{\mathbf{p}}^{22} \end{bmatrix} \begin{bmatrix} \mathbf{f}_{\mathbf{ph}} \\ \mathbf{f}_{\mathbf{p}} \end{bmatrix} \tag{4.29}$$

where the vector subscripts 'ph' and 'p' denote variables at the pile head and at the remaining pile nodes respectively. Note that, unlike the soil FRF matrix of Equation 4.9, $\mathbf{H}_{\mathbf{p}}$ relates displacements and forces, rather than tractions. The displacements and applied forces at the pile head are given by:

$$\mathbf{u}_{\mathbf{ph}} = \begin{bmatrix} u_1 & u_3 & \theta_2 \end{bmatrix}^{\mathrm{T}} \quad \text{and} \quad \mathbf{f}_{\mathbf{ph}} = \begin{bmatrix} f_1 & f_3 & q_2 \end{bmatrix}^{\mathrm{T}} \tag{4.30}$$

where θ_2 is the rotation at the pile head and q_2 the applied moment. The remaining nodal displacements and forces of the pile are given by:

$$\mathbf{u}_{\mathbf{p}} = \begin{bmatrix} u_1^1 & u_3^1 & u_1^2 & u_3^2 & \cdots & u_1^{N_p+1} & u_3^{N_p+1} \end{bmatrix}^{\mathrm{T}} \tag{4.31}$$

The corresponding force vector $\mathbf{f}_{\mathbf{p}}$ takes a similar form. Only the components in the x_1x_3-plane have been retained since the displacements and resultant forces in the x_2-direction are zero along the entire pile centroid. Due to the coupling conditions assumed at the soil-pile interface, there are also no external moments applied to the pile other than that at the pile head.

Equations 4.25 to 4.28 are now inconsistent with Equations 4.29 to 4.31 since the latter set refers to vectors $\mathbf{u}_{\mathbf{p}}$ and $\mathbf{f}_{\mathbf{p}}$ in which the x_2-components have been discarded. However, to be compatible with the three-dimensional soil model, the full three-dimensional form of the vectors $\mathbf{u}_{\mathbf{sp}}$ and $\mathbf{f}_{\mathbf{sp}}$ must be retained. Equations 4.26 and 4.28 must therefore be amended with an additional matrix to complete the transformation from the two-dimensional vectors of the pile to the three-dimensional vectors of the soil-pile interface:

$$\mathbf{u}_{\mathbf{sp}} = \mathbf{Q}_1\mathbf{Q}_2\mathbf{u}_{\mathbf{p}} \tag{4.32}$$

$$\begin{aligned}\mathbf{f}_{\mathbf{p}} &= -b^2\left[\mathbf{Q}_2\right]^{\mathrm{T}}\left[\mathbf{Q}_1\right]^{\mathrm{T}}\mathbf{p}_{\mathbf{sp}} \\ &= -b^2\left[\mathbf{Q}_1\mathbf{Q}_2\right]^{\mathrm{T}}\mathbf{p}_{\mathbf{sp}}\end{aligned} \tag{4.33}$$

The details of both transformation matrices are given in Appendix G.

The system of equations derived above is now ready to be solved for a prescribed pile-head load $\mathbf{f}_{\mathbf{ph}}$. Firstly, Equation 4.29 is written as the following two matrix equations:

$$\mathbf{u}_{\mathbf{ph}} = \mathbf{H}_{\mathbf{p}}^{11}\mathbf{f}_{\mathbf{ph}} + \mathbf{H}_{\mathbf{p}}^{12}\mathbf{f}_{\mathbf{p}} \tag{4.34}$$

and

$$\mathbf{u}_{\mathbf{p}} = \mathbf{H}_{\mathbf{p}}^{21}\mathbf{f}_{\mathbf{ph}} + \mathbf{H}_{\mathbf{p}}^{22}\mathbf{f}_{\mathbf{p}} \tag{4.35}$$

Combining Equations 4.35, 4.33, 4.24 and 4.32 enables the nodal displacements of the pile to be found given the applied load:

$$\mathbf{u}_{\mathbf{p}} = \left[\mathbf{I} + b^2\mathbf{H}_{\mathbf{p}}^{22}\left[\mathbf{Q}_1\mathbf{Q}_2\right]^{\mathrm{T}}\left[\mathbf{H}_{\mathbf{s}}^{22}\right]^{-1}\mathbf{Q}_1\mathbf{Q}_2\right]^{-1}\mathbf{H}_{\mathbf{p}}^{21}\mathbf{f}_{\mathbf{ph}} \tag{4.36}$$

The remaining unknowns are then found in succession: $\mathbf{u}_{\mathbf{sp}}$ follows directly from Equation 4.32; inversion of Equation 4.24 gives $\mathbf{p}_{\mathbf{sp}}$; $\mathbf{f}_{\mathbf{p}}$ and $\mathbf{u}_{\mathbf{ph}}$ follow directly from Equations 4.33 and 4.34; and, finally, $\mathbf{u}_{\mathbf{fs}}$ from Equation 4.23.

This completes the mathematical description of the single-pile model. In the next section the model is validated against published results from two existing models.

4.1.5. Validation of the Single-Pile Model

Before any validation is undertaken, the necessary number and size of the boundary elements used in the model must be determined. This is achieved by varying the number and size of the elements until convergence of the results is observed, over the frequency range of interest, for each possible load-case. The results of interest here are the predictions of the driving-point FRFs of the pile head, as defined originally by Equation 3.19a. They are presented in the form of *flexibility coefficients* $F_{ij} = I_{ij} + iJ_{ij}$, which is the form commonly found in the literature obtained by

normalising the FRFs with respect to their predicted static values. For example, $F_{11} = I_{11} + iJ_{11} = H^{11}_{f11}(\omega) \big/ H^{11}_{f11}(0)$.

Figure 4.17 illustrates the effect on the flexibility coefficients of increasing the number of elements in the free-surface mesh for a pile with slenderness ratio $L/r_0 = 21.2$, where L is the length of the pile and r_0 its radius. The remaining parameter values represent a typical flexible pile and are given in the figure caption.

As with the planar models of Section 4.1.1, the solutions are insensitive to the particular values of material loss factor and a nominal value of $\eta = 0.02$ is assigned to both the pile and the soil. Only the non-dimensional frequency range from $a_0 = 0$ to 0.5 is considered as this is the range considered in the literature; existing published results are generally concerned with seismic excitation and therefore do not consider higher frequencies. The size of the elements is chosen to ensure nine elements per S-wavelength at the highest frequency of interest. This satisfies the general condition recommended by Dominguez [35] that at least six constant elements per wavelength are used in elastodynamic analysis. In the current model, increasing the free-surface element density above nine per wavelength has no effect on the presented results. The element mesh on the soil-pile interface is fixed at four elements around the circumference, while increasing the element density along the length of the pile by using rectangular elements is avoided to control the overall size of the model and prevent the numerical ill-conditioning associated with elements with a high aspect ratio.

Figure 4.17 illustrates how, for the particular parameter values chosen, the different solutions converge on that corresponding to a free-surface mesh of $N_{fs} = 440$, equivalent to $N_1 = N_2 = 21$. The solutions for the horizontal and rotational coefficients converge more quickly than the vertical coefficient. This is possibly due to the existence of a more localised wave field in the soil when the pile is subject to horizontal or moment loads. The bottom two plots confirm that the model satisfies reciprocity, given that $F_{13} = F_{31}$.

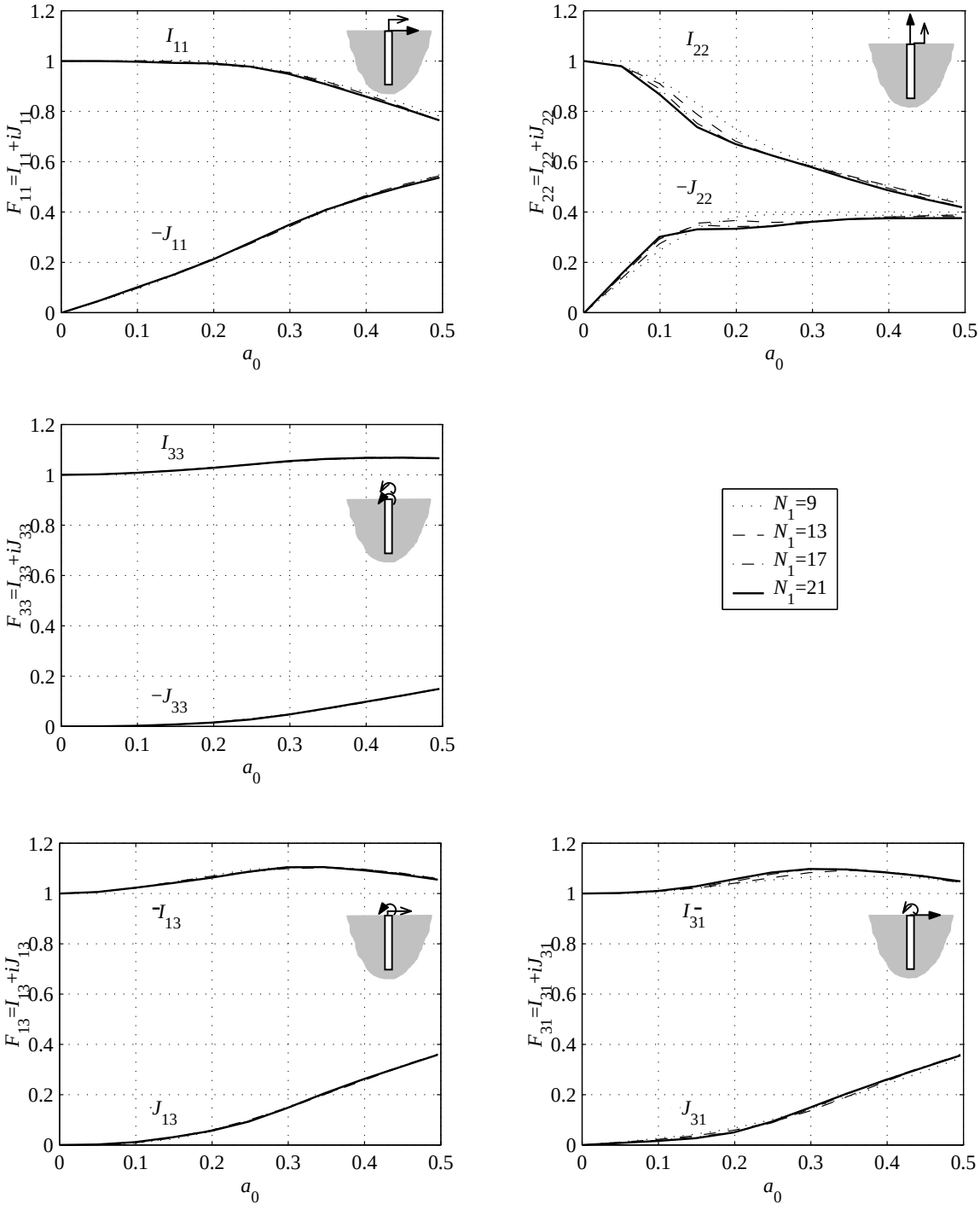

Figure 4.17: The effect of the number of free-surface boundary elements N_{fs} on the pile-head flexibility coefficients of the single-pile model ($N_{fs}=N_1^2-1$). The coefficients are plotted against non-dimensional frequency $a_0=\omega r_0/c_s$ and correspond to a pile with the following parameter values: $L/r_0=21.2$, $E_p/E_s=100$, $\rho_p/\rho_s=0.75$ and $\nu=0.4$.

The converged solution may now be compared with the chosen published results. Firstly, an initial check must be made on the static solution, since this is the basis of the normalisation used to obtain the flexibility coefficients. Appendix H calculates an alternative solution using the results of Poulos and Davis [112] for the static pile-head compliance of a single floating pile in a uniform half-space. Table 4.3 compares this solution with the 0.1 Hz solution from the current model, this being essentially the static solution. It is clear from Table 4.3 that the static solution of the current model is in good agreement with the alternative results. There is some disagreement in the values of C_{22}, although the reason for this is uncertain.

	$\boldsymbol{C}_{11}$ [10^{-9} m/N]	$\boldsymbol{C}_{31}$ [10^{-9} rad/N]	$\boldsymbol{C}_{22}$ [10^{-10} m/N]	$\boldsymbol{C}_{33}$ [10^{-9} rad/Nm]
Current model	3.30	2.23	9.47	3.50
Poulos & Davis	3.3	2.2	8.3	3.5

Table 4.3: Comparison of the static (0.1 Hz) solution of the single-pile model with that due to Poulos and Davis for the static pile-head compliance of a single floating pile in a uniform half-space; see also Appendix H.

In Section 2.7.2, the models of Kuhlemeyer [69, 70] and Sen *et al*. [118] were noted as two rigorous dynamic models of a single pile embedded in homogeneous soil. These are now considered as two suitable models against which to verify the dynamic results of the current model. They are chosen because they use two independent methods, the FEM and BEM respectively. Figures 4.18 and 4.19 compare the horizontal and vertical pile-head flexibility coefficients with those predicted by Kuhlemeyer and Sen *et al*. Note that the horizontal results are for a stiffer and more slender pile ($E_p / E_s = 567$, $L / r_0 = 30.0$) than those shown in Figures 4.17 and 4.19.

The results from all three models, for both the real and imaginary components of the horizontal coefficient, agree well. Similarly, all three models agree on the real component of the vertical coefficient. In predicting the imaginary component of the vertical coefficient, the current model agrees much better with Kuhlemeyer's model than with Sen's. It is difficult to explain this. One possible reason may be an under-prediction of the level of radiation damping both in the current model, which is likely given the findings of the two-dimensional model considered in

Section 4.1.1, and Kuhlemeyer's FEM model, which relies on approximate non-reflecting boundaries to model wave propagation into the soil surrounding the pile. The reason for this being less noticeable in the horizontal results is possibly due to the existence of a more localised wave field when the pile is subject to a horizontal load. However, most importantly, Figures 4.18 and 4.19 provide adequate quantitative validation of the current single-pile model over the frequency range for which published results are available.

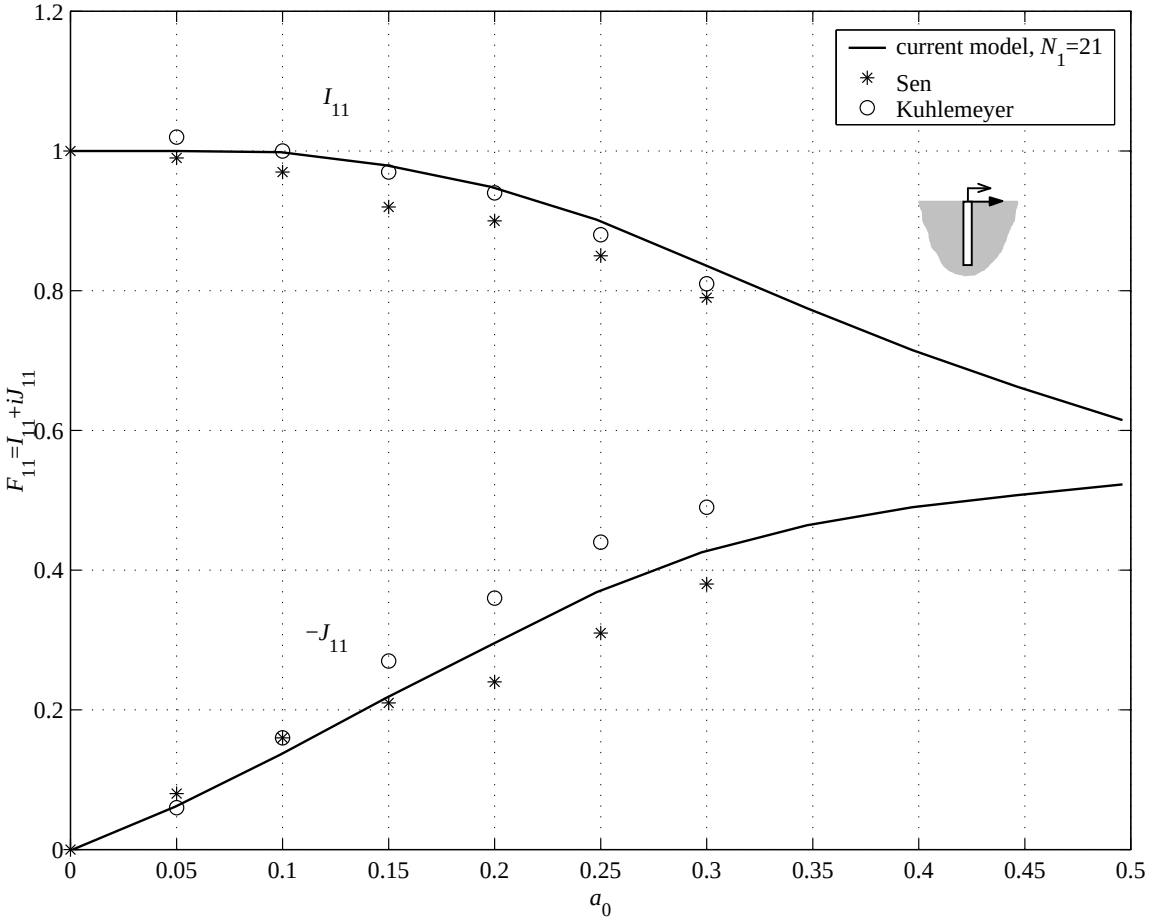

Figure 4.18: Comparison of the horizontal pile-head flexibility coefficient predicted by the current single-pile model with those predicted by the models of Kuhlemeyer and Sen *et al*. The coefficients are plotted against non-dimensional frequency $a_0 = \omega r_0 / c_s$ and correspond to a pile with the following parameter values: $L / r_0 = 30.0$, $E_p / E_s = 567$, $\rho_p / \rho_s = 0.75$ and $\nu = 0.4$. The imaginary component is negated for convenience of plotting.

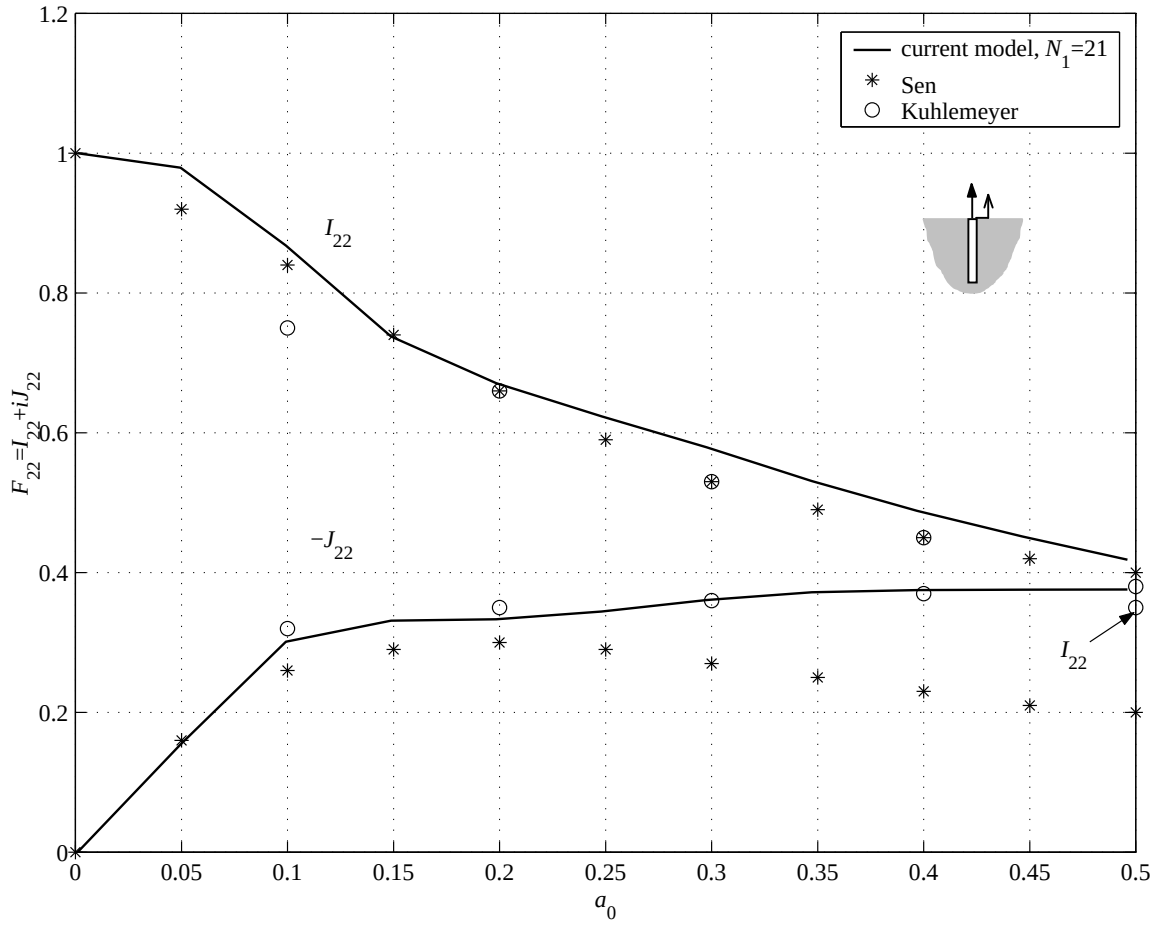

Figure 4.19: Comparison of the vertical pile-head flexibility coefficient predicted by the current single-pile model with those predicted by the models of Kuhlemeyer and Sen *et al*. The coefficients are plotted against non-dimensional frequency $a_0 = \omega r_0 / c_s$ and correspond to a pile with the following parameter values: $L/r_0 = 21.2$, $E_p / E_s = 100$, $\rho_p / \rho_s = 0.75$ and $\nu = 0.4$. The imaginary component is negated for convenience of plotting.

To conclude this section, Figure 4.20 shows the boundary-element mesh of the soil model when a vertical unit load is applied to the pile head at a non-dimensional frequency of $a_0 = 0.5$. The displaced geometry of the mesh is plotted with all displacements magnified by 3×10^9. It is clear from Figure 4.20(a) that the model correctly predicts concentric circular wavefronts on the free-surface of the soil. Figure 4.20(b) indicates the wavelength to be approximately 4.1 m. This agrees well with the Rayleigh wavelength, which, for the particular parameters of the model, is 4.22 m at $a_0 = 0.5$. The agreement is not perfect due to a combination of the coarseness of the boundary-element mesh and the fact that the comparison should be made in the far field, rather than the immediate wave-field surrounding the pile.

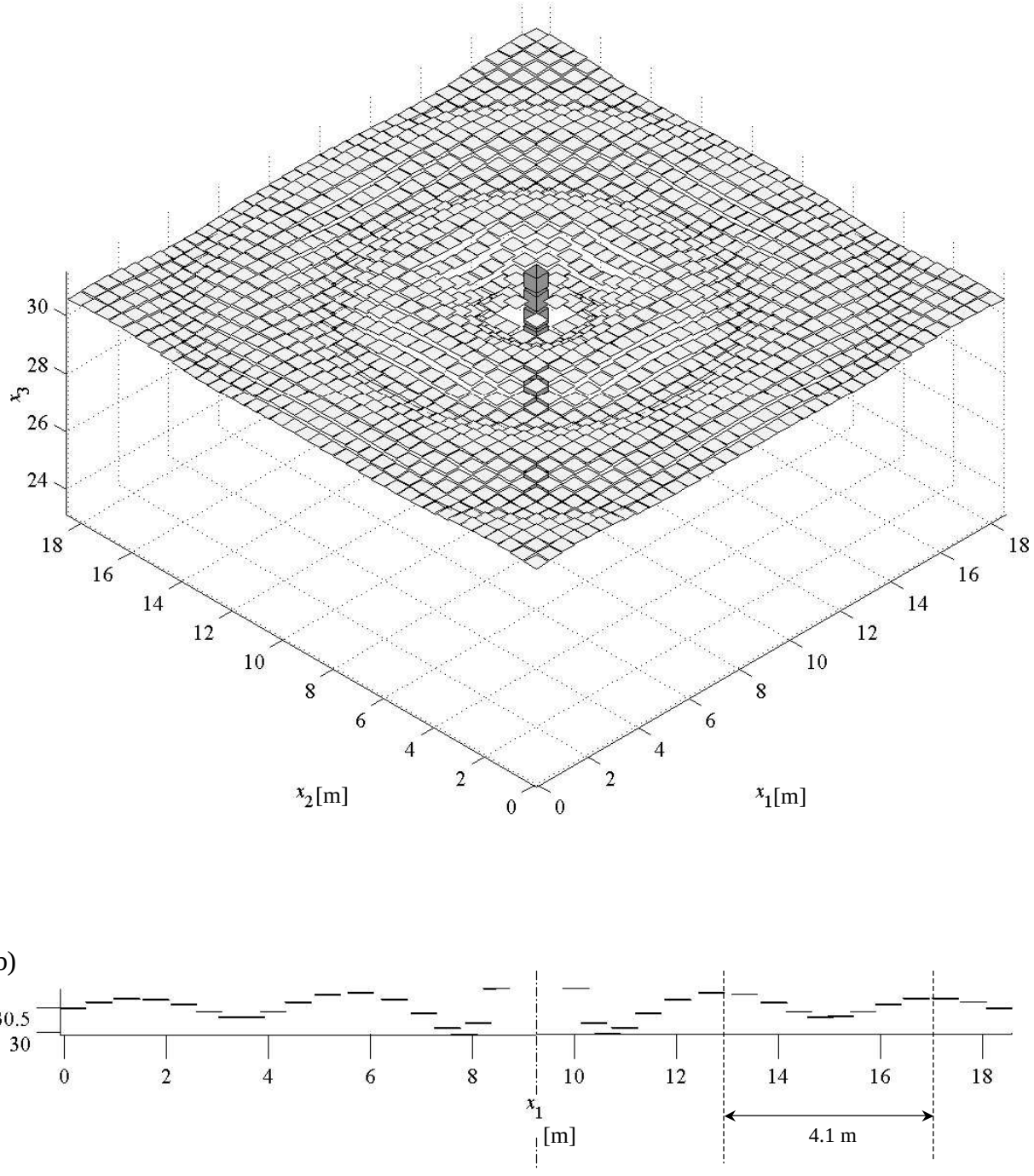

Figure 4.20: The displacement field predicted by the single-pile model when a vertical unit load is applied to the pile head at a non-dimensional frequency of $a_0 = 0.5$. In addition to the soil-pile interface, the isometric view (a) clearly shows the concentric circular wavefronts on the free-surface. The vertical section through the free-surface at the location of the pile centroid (b) shows that the model correctly predicts the Rayleigh wavelength, which, for the particular parameters used, is 4.22 m. All displacements are magnified by 3×10^9.

This concludes the development of the single-pile model. In the next section this model is used as the basis for developing a model of a row of piles.

4.2. Modelling a Row of Piles

Before considering the details of the pile-row model, it is important to note the computation time required for the single-pile model of Section 4.1. Figure 4.21 illustrates the increase in computation time required when using increasing numbers of boundary-elements in the free-surface mesh.

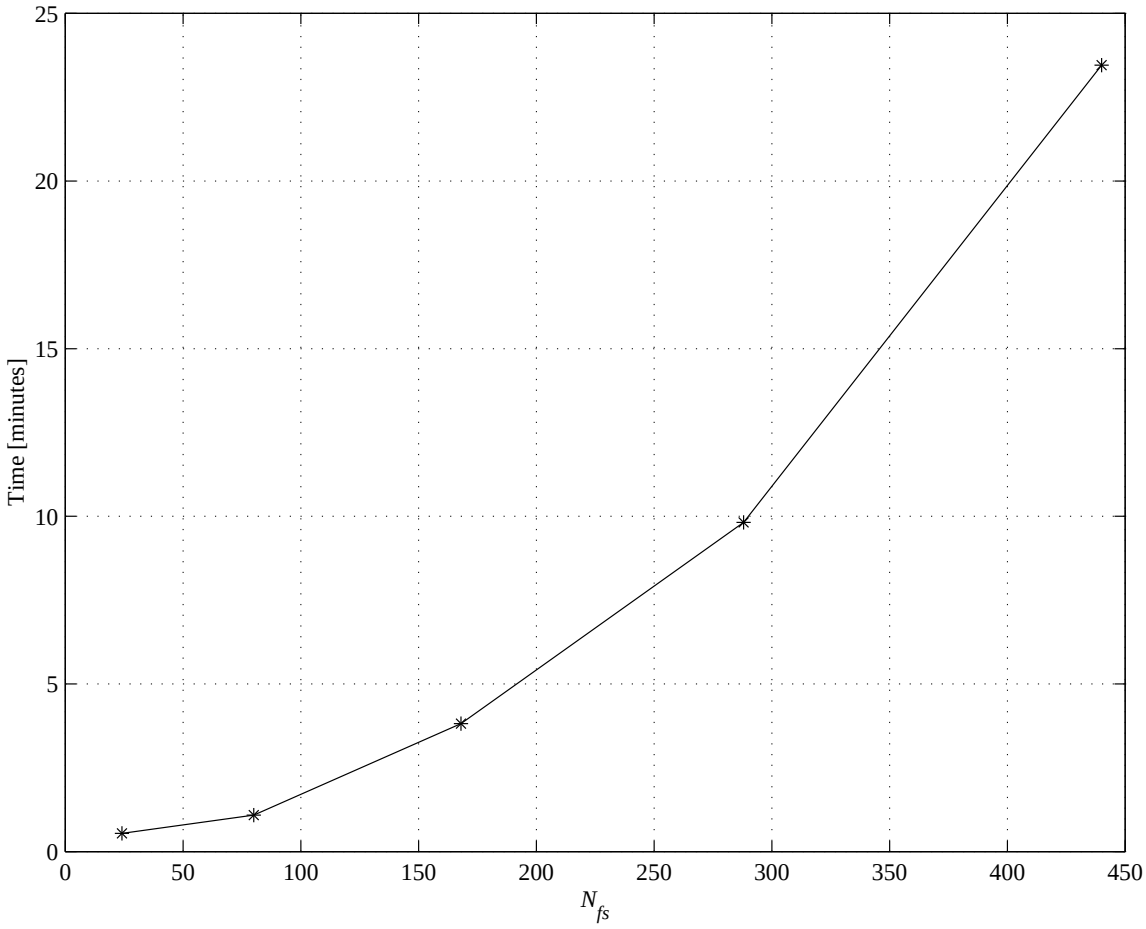

Figure 4.21: The variation in computation time required, per frequency step, for the single-pile model when using increasing numbers of elements in the free-surface mesh N_{fs}. All calculations are performed on a 1 GHz Pentium 3 processor with 512 MB of RAM.

The time required depends primarily on the size of the soil FRF matrix $\mathbf{H_s}$, which increases in size with the square of the number of elements used. For this reason the number of elements must be kept to a minimum. Clearly, with the current computing resources available, adding extra piles to the soil mesh of the single-pile model to represent a row of piles would soon involve impractical computation times.

An alternative approach is required to model a row of piles. The approach adopted here is to use the BEM formulation of the single-pile model in conjunction with periodic structure theory. This requires the fundamental assumption that the row comprises an infinite number of identical piles but offers significant computational advantages. A brief summary of periodic structure theory is now given before the pile-row model is described in detail.

4.2.1. Periodic Structure Theory

A periodic structure consists of a number of identical structural elements, or 'repeating units', which are coupled together end-to-end and/or side-by-side to form the whole structure. Periodic structures may be one-, two- or three-dimensional; examples include pipelines, aerospace structures and buildings.

The theory governing periodic structures was initially developed by Newton for the study of one-dimensional systems of discrete masses and springs, and much of the early work concerned crystal lattices [18]. The application of the theory to engineering structures came later; see the review by Mead [88]. The theory used in this dissertation applies to one-dimensional and quasi-one-dimensional structures, that is, those in which wave propagation occurs in one dimension only. Two recent examples of the application of this theory for studying ground-borne vibration are Cryer's periodic building model [33] and Forrest's periodic model of an underground railway tunnel [38].

The advantage of using periodic structure theory is a significant reduction in the computation time required. Rather than modelling the entire structure, only one repeating unit is considered and, by assuming the structure is infinitely long, the mathematics is reduced to an eigenvalue problem. The necessary mathematics will be included in the next section when the pile-row model is described in detail.

4.2.2. Modelling an Infinite Row of Piles

The aim of this section is to apply periodic structure theory to produce a model of an infinite row of piles. A vertical section through such a row is shown schematically in Figure 4.22. This shows the row split into three parts: there is a central unit, containing a single pile with an externally

applied pile-head load, and two semi-infinite rows of piles either side. The repeating units are defined by the dashed vertical lines; each consists of a vertical *slice* of the half-space complete with a central pile.

Each of the three parts shown in Figure 4.22 is modelled separately and then coupled together to form the final model. The equations describing the behaviour of the repeating unit are first derived and then periodic structure theory is used to derive the matrices that describe the behaviour of the semi-infinite rows. Finally, these are combined with the equations governing the central loaded unit.

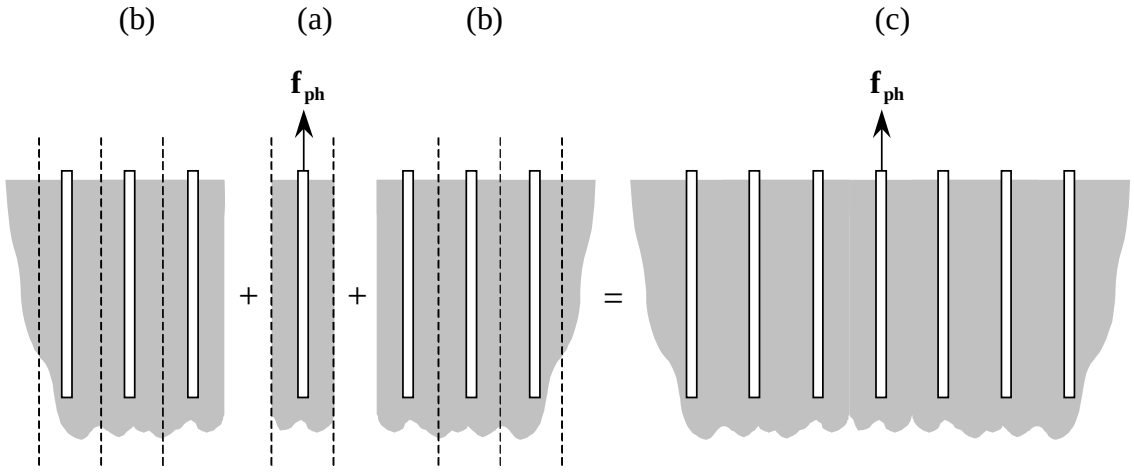

Figure 4.22: Vertical section through an infinite row of piles showing (a) the central loaded unit, (b) the semi-infinite rows of piles either side and (c) the complete row. The repeating units constituting the system are defined by vertical dashed lines.

Calculation of the Central-Unit Response

The repeating unit of the system is modelled using a development of the single-pile model described in Section 4.1. The model consists of a central pile, as described in Section 4.1.3, coupled to a BEM model representing the surrounding soil. The BEM model consists of a total of *N* rectangular, constant elements, as illustrated in Figure 4.23, and is comprised as follows: the free surface is represented by a rectangular mesh of N_1 by N_2 elements, minus one for the pile, giving a total of N_{fs}; each side of the unit is represented by a rectangular mesh of N_2 by N_3 elements; and N_{sp} elements represent the soil-pile interface. The model is effectively a vertical slice of the half-space and, as such, the mesh should extend to minus infinity in the x_3-direction

and plus and minus infinity in the x_2-direction. In practice the mesh may be curtailed at a finite distance from the pile; the necessary number of elements is discussed in Section 4.2.3.

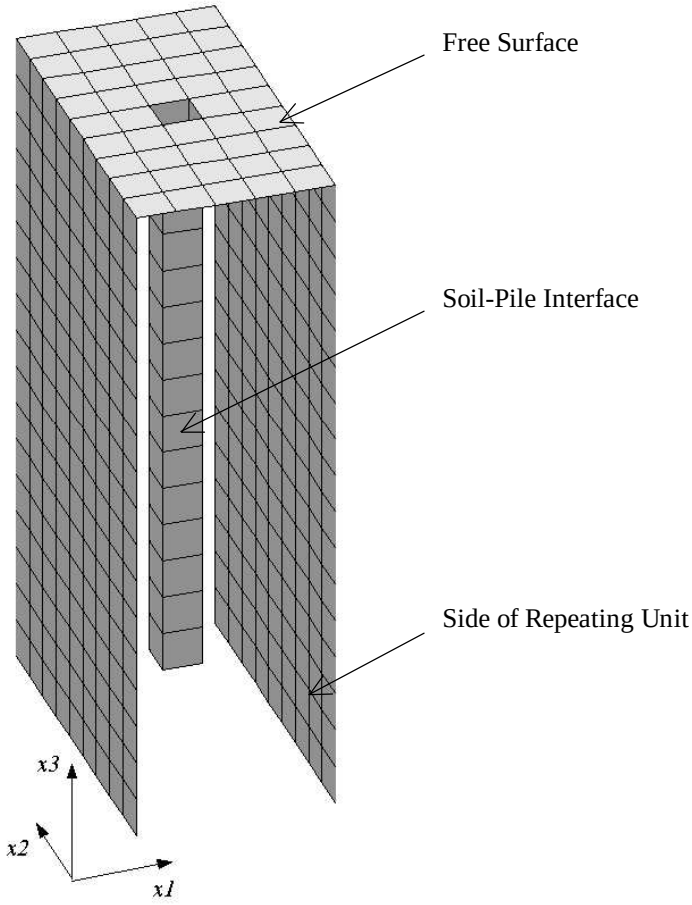

Figure 4.23: The boundary-element mesh representing the soil component of the repeating unit in an infinite row of piles. As a vertical slice of the half-space, the model should extend to minus infinity in the x_3-direction and plus and minus infinity in the x_2-direction but in practice the mesh may be curtailed at a finite distance from the pile; here $N_1 = 5$, $N_2 = 9$ and $N_3 = 17$.

The FRF matrix describing the soil of the repeating unit, analogous to that of Equation 4.9, takes the following form:

$$\begin{bmatrix} \mathbf{u}_\mathbf{r} \\ \mathbf{u}_\mathbf{fs} \\ \mathbf{u}_\mathbf{sp} \\ \mathbf{u}_\mathbf{l} \end{bmatrix} = \begin{bmatrix} \mathbf{H}_\mathbf{s}^{11} & \mathbf{H}_\mathbf{s}^{12} & \mathbf{H}_\mathbf{s}^{13} & \mathbf{H}_\mathbf{s}^{14} \\ \mathbf{H}_\mathbf{s}^{21} & \mathbf{H}_\mathbf{s}^{22} & \mathbf{H}_\mathbf{s}^{23} & \mathbf{H}_\mathbf{s}^{24} \\ \mathbf{H}_\mathbf{s}^{31} & \mathbf{H}_\mathbf{s}^{32} & \mathbf{H}_\mathbf{s}^{33} & \mathbf{H}_\mathbf{s}^{34} \\ \mathbf{H}_\mathbf{s}^{41} & \mathbf{H}_\mathbf{s}^{42} & \mathbf{H}_\mathbf{s}^{43} & \mathbf{H}_\mathbf{s}^{44} \end{bmatrix} \begin{bmatrix} \mathbf{p}_\mathbf{r} \\ \mathbf{0} \\ \mathbf{p}_\mathbf{sp} \\ \mathbf{p}_\mathbf{l} \end{bmatrix} \tag{4.37}$$

Where $\mathbf{u}_\mathbf{fs}$, $\mathbf{u}_\mathbf{sp}$ and $\mathbf{p}_\mathbf{sp}$ take the same form as in the single-pile model, and $\mathbf{u}_\mathbf{l}$, $\mathbf{u}_\mathbf{r}$, $\mathbf{p}_\mathbf{l}$ and $\mathbf{p}_\mathbf{r}$ contain the nodal displacements and tractions of the left- and right-hand sides of the unit. Note

that the free-surface traction vector $\mathbf{p}_{\mathbf{fs}}$ has already been set to zero because the only external load is applied at the pile head of the central unit. Equation 4.37 provides the following matrix equations:

$$\mathbf{u}_{\mathbf{r}} = \mathbf{H}_{\mathbf{s}}^{11}\mathbf{p}_{\mathbf{r}} + \mathbf{H}_{\mathbf{s}}^{13}\mathbf{p}_{\mathbf{sp}} + \mathbf{H}_{\mathbf{s}}^{14}\mathbf{p}_{\mathbf{l}} \tag{4.38}$$

$$\mathbf{u}_{\mathbf{sp}} = \mathbf{H}_{\mathbf{s}}^{31}\mathbf{p}_{\mathbf{r}} + \mathbf{H}_{\mathbf{s}}^{33}\mathbf{p}_{\mathbf{sp}} + \mathbf{H}_{\mathbf{s}}^{34}\mathbf{p}_{\mathbf{l}} \tag{4.39}$$

$$\mathbf{u}_{\mathbf{l}} = \mathbf{H}_{\mathbf{s}}^{41}\mathbf{p}_{\mathbf{r}} + \mathbf{H}_{\mathbf{s}}^{43}\mathbf{p}_{\mathbf{sp}} + \mathbf{H}_{\mathbf{s}}^{44}\mathbf{p}_{\mathbf{l}} \tag{4.40}$$

Combining Equation 4.39 with Equations 4.32, 4.33 and 4.35 describing the pile couples the pile to the soil and enables the tractions on the soil-pile interface to be expressed in terms of the pile-head load and the tractions on either side of the unit:

$$\mathbf{p}_{\mathbf{sp}} = \mathbf{A}\left(\mathbf{Q}_1\mathbf{Q}_2\mathbf{H}_{\mathbf{p}}^{21}\mathbf{f}_{\mathbf{ph}} - \mathbf{H}_{\mathbf{s}}^{31}\mathbf{p}_{\mathbf{r}} - \mathbf{H}_{\mathbf{s}}^{34}\mathbf{p}_{\mathbf{l}}\right) \tag{4.41}$$

where $\mathbf{A} = \left[\mathbf{H}_{\mathbf{s}}^{33} + b^2\mathbf{Q}_1\mathbf{Q}_2\mathbf{H}_{\mathbf{p}}^{22}\left[\mathbf{Q}_1\mathbf{Q}_2\right]^{\mathrm{T}}\right]^{-1}$.

Now consider units 'j' and '$j+1$' of the semi-infinite row of piles extending to the right of the central unit, see Figure 4.24. These units have no externally applied loads but the pile-head load of the central unit causes waves to propagate along the pile row from left to right. Setting $\mathbf{f}_{\mathbf{ph}}$ to zero and substituting Equation 4.41 into Equations 4.38 and 4.40 gives expressions involving only the nodal variables on the sides of unit 'j'. These may be expressed as the following matrix equation:

$$\begin{bmatrix}\mathbf{u}_{\mathbf{r}}\\ \mathbf{p}_{\mathbf{r}}\end{bmatrix} = \begin{bmatrix}\mathbf{R}^{11} & \mathbf{R}^{12}\\ \mathbf{R}^{21} & \mathbf{R}^{22}\end{bmatrix}\begin{bmatrix}\mathbf{u}_{\mathbf{l}}\\ \mathbf{p}_{\mathbf{l}}\end{bmatrix} \tag{4.42}$$

where

$$\mathbf{R}^{11} = \left(\mathbf{H}_{\mathbf{s}}^{11} - \mathbf{H}_{\mathbf{s}}^{13}\mathbf{A}\mathbf{H}_{\mathbf{s}}^{31}\right)\left[\mathbf{H}_{\mathbf{s}}^{41} - \mathbf{H}_{\mathbf{s}}^{43}\mathbf{A}\mathbf{H}_{\mathbf{s}}^{31}\right]^{-1}, \quad \mathbf{R}^{12} = \mathbf{R}^{11}\left(\mathbf{H}_{\mathbf{s}}^{43}\mathbf{A}\mathbf{H}_{\mathbf{s}}^{34} - \mathbf{H}_{\mathbf{s}}^{44}\right) - \mathbf{H}_{\mathbf{s}}^{13}\mathbf{A}\mathbf{H}_{\mathbf{s}}^{34} + \mathbf{H}_{\mathbf{s}}^{14},$$
$$\mathbf{R}^{21} = \left[\mathbf{H}_{\mathbf{s}}^{41} - \mathbf{H}_{\mathbf{s}}^{43}\mathbf{A}\mathbf{H}_{\mathbf{s}}^{31}\right]^{-1}, \quad \mathbf{R}^{22} = \mathbf{R}^{21}\left[\mathbf{H}_{\mathbf{s}}^{44} - \mathbf{H}_{\mathbf{s}}^{43}\mathbf{A}\mathbf{H}_{\mathbf{s}}^{34}\right].$$

In this form the nodal displacements and tractions on the right-hand side of the unit are expressed in terms of those on the left.

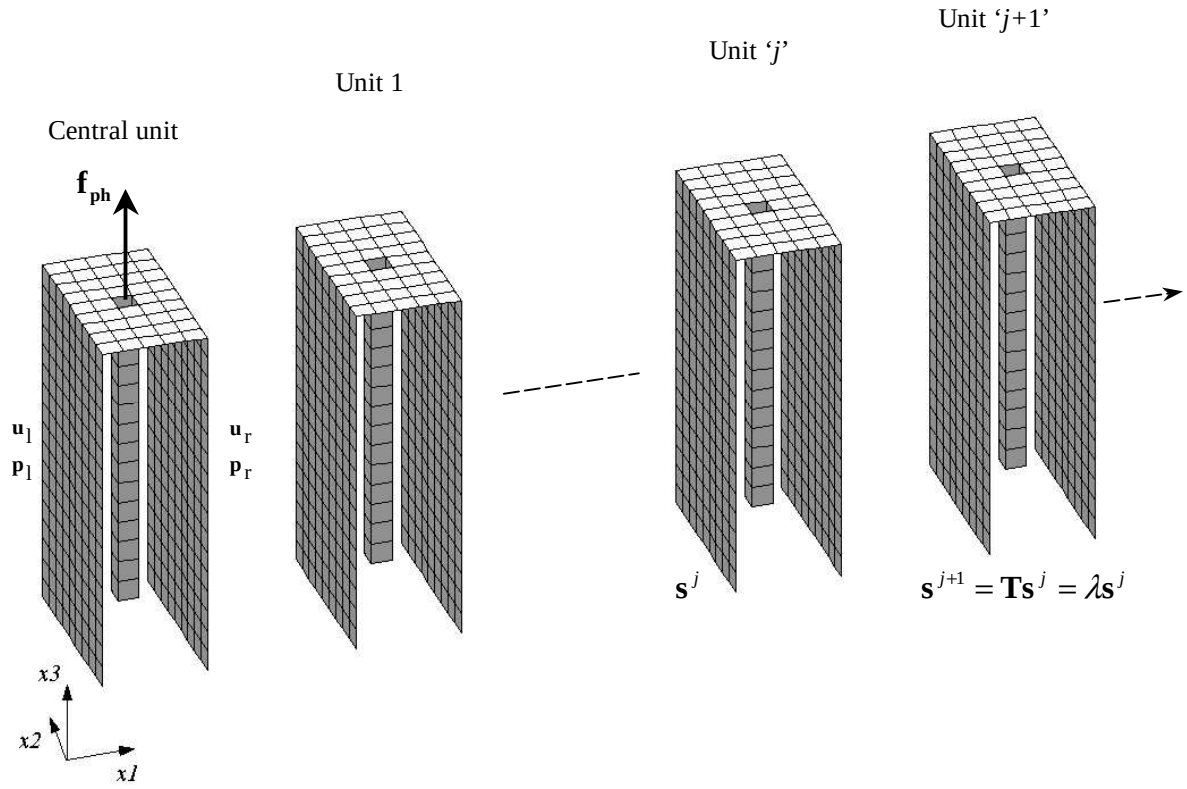

Figure 4.24: Repeating units representing the soil component of the semi-infinite row of piles extending to the right of the loaded central unit.

The displacements and tractions on the left-hand side of the unit are defined as the *state* of the unit, $\mathbf{s}^j = \left[\left[\mathbf{u_l}\right]^T \quad \left[\mathbf{p_l}\right]^T\right]^T$. Compatibility of displacements requires the displacements on the right-hand side of unit 'j' to be equal to those on the left-hand side of unit '$j+1$' and, since both unit 'j' and unit '$j+1$' have no externally applied loads, equilibrium of forces requires the tractions to be equal and opposite. The *transfer matrix* **T** of the system therefore follows directly from Equation 4.42 by changing the sign of the lower sub-matrices of **R**:

$$\mathbf{T} = \begin{bmatrix} \mathbf{R}^{11} & \mathbf{R}^{12} \\ -\mathbf{R}^{21} & -\mathbf{R}^{22} \end{bmatrix} \tag{4.43}$$

such that

$$\mathbf{s}^{j+1} = \mathbf{T}\mathbf{s}^j \tag{4.44}$$

This is a key equation of periodic-structure theory, which, at a given frequency, governs the propagation of states from one repeating unit to the next. Given that the repeating units are identical, the states are identical in form and propagate along the row with only a change in amplitude and phase:

$$\mathbf{s}^{j+1} = \lambda \mathbf{s}^{j} \tag{4.45}$$

where λ is a complex amplitude-modifying factor. Equation 4.45 represents a statement of Bloch's or Floquet's theorem [18].

Equations 4.44 and 4.45 constitute an eigenvalue problem in $\mathbf{T}$, with eigenvectors $\mathbf{s}^{j}$ and eigenvalues λ. $\mathbf{T}$ is a $6N_s$ x $6N_s$ matrix with $6N_s$ eigenvectors and eigenvalues. The eigenvalues occur in inverse pairs, half of which have magnitudes less than one and correspond to decaying solutions as the distance from the central unit increases. The remaining half have magnitudes greater than one and correspond to growing solutions. The latter are non-physical since the response of the system must decay as the distance from the excitation is increased.

The eigenvectors $\bar{\mathbf{s}}^{j}$, corresponding to the eigenvalues with magnitudes less than one, represent the states that are able to propagate along the system at a given frequency. They are mutually orthogonal and any general state may therefore be represented by a linear combination of these eigenvectors. This includes the state of the first unit in the right-hand semi-infinite row:

$$\mathbf{s}^{1} = \sum_{j=1}^{3N_s} a_j \bar{\mathbf{s}}^{j} \tag{4.46}$$

The coefficients a_j are now eliminated as follows. Equation 4.46 is written in terms of a matrix containing the eigenvectors and a vector of the coefficients:

$$\mathbf{s}^{1} = \bar{\mathbf{S}}\mathbf{a} \tag{4.47}$$

The eigenvector matrix $\bar{\mathbf{S}}$ is then partitioned, to separate the rows associated with the displacement and traction components of $\mathbf{s}^{1}$, and the sub-matrices separated:

$$\mathbf{s}^1 = \begin{bmatrix} \mathbf{u}^1 \\ \mathbf{p}^1 \end{bmatrix} = \begin{bmatrix} \overline{\mathbf{U}} \\ \overline{\mathbf{P}} \end{bmatrix} \mathbf{a}$$

$$\mathbf{u}^1 = \overline{\mathbf{U}}\mathbf{a} \quad \text{and} \quad \mathbf{p}^1 = \overline{\mathbf{P}}\mathbf{a} \tag{4.48}$$

Finally, the matrices of Equation 4.48 are recombined to give:

$$\begin{aligned} \mathbf{u}^1 &= \overline{\mathbf{U}}\left[\overline{\mathbf{P}}\right]^{-1}\mathbf{p}^1 \\ &= \mathbf{H}_\mathbf{r}\mathbf{p}^1 \end{aligned} \tag{4.49}$$

where $\mathbf{H}_\mathbf{r}$ is the FRF matrix of the right-hand semi-infinite row of piles. The equivalent matrix for the left-hand row $\mathbf{H}_\mathbf{l}$ is obtained by considering the symmetry of the system and negating the appropriate elements of $\mathbf{H}_\mathbf{r}$.

It is now evident why this approach leads to a computationally efficient model. The full dynamic behaviour of the semi-infinite rows of piles, including the effects of PSPI, is described by these two $3N_s$ x $3N_s$ matrices.

To complete the model the semi-infinite rows must be coupled to the central unit; see Figure 4.25. To calculate the response of the piles and the free surface, the nodal displacements and tractions $\mathbf{u}_\mathbf{l}$, $\mathbf{u}_\mathbf{r}$, $\mathbf{p}_\mathbf{l}$ and $\mathbf{p}_\mathbf{r}$ on the sides of the central unit are required. From considerations of compatibility and equilibrium:

$$\mathbf{u}_\mathbf{r} = -\mathbf{H}_\mathbf{r}\mathbf{p}_\mathbf{r} \quad \text{and} \quad \mathbf{u}_\mathbf{l} = -\mathbf{H}_\mathbf{l}\mathbf{p}_\mathbf{l} \tag{4.50}$$

These may now be combined with Equation 4.41, this time with a non-zero $\mathbf{f}_\mathbf{ph}$, and Equations 4.38 and 4.40 to eliminate the displacements:

$$\begin{bmatrix} \mathbf{H}_\mathbf{s}^{13}\mathbf{A}\mathbf{H}_\mathbf{s}^{31} - \mathbf{H}_\mathbf{s}^{11} - \left[\mathbf{H}_\mathbf{r}\right]^{-1} & \mathbf{H}_\mathbf{s}^{13}\mathbf{A}\mathbf{H}_\mathbf{s}^{34} - \mathbf{H}_\mathbf{s}^{14} \\ \mathbf{H}_\mathbf{s}^{43}\mathbf{A}\mathbf{H}_\mathbf{s}^{31} - \mathbf{H}_\mathbf{s}^{41} & \mathbf{H}_\mathbf{s}^{43}\mathbf{A}\mathbf{H}_\mathbf{s}^{34} - \mathbf{H}_\mathbf{s}^{44} - \left[\mathbf{H}_\mathbf{l}\right]^{-1} \end{bmatrix} \begin{bmatrix} \mathbf{p}_\mathbf{r} \\ \mathbf{p}_\mathbf{l} \end{bmatrix} = \begin{bmatrix} \mathbf{H}_\mathbf{s}^{13} \\ \mathbf{H}_\mathbf{s}^{43} \end{bmatrix} \left[\mathbf{A}\mathbf{Q}_1\mathbf{Q}_2\mathbf{H}_\mathbf{p}^{21}\mathbf{f}_\mathbf{ph}\right] \tag{4.51}$$

By inverting the above left-hand matrix the tractions resulting from the applied $\mathbf{f}_{ph}$ can be calculated. Equation 4.41 then gives the soil-pile interface tractions $\mathbf{p}_{sp}$ and Equation 4.37 the displacements of the entire central unit.

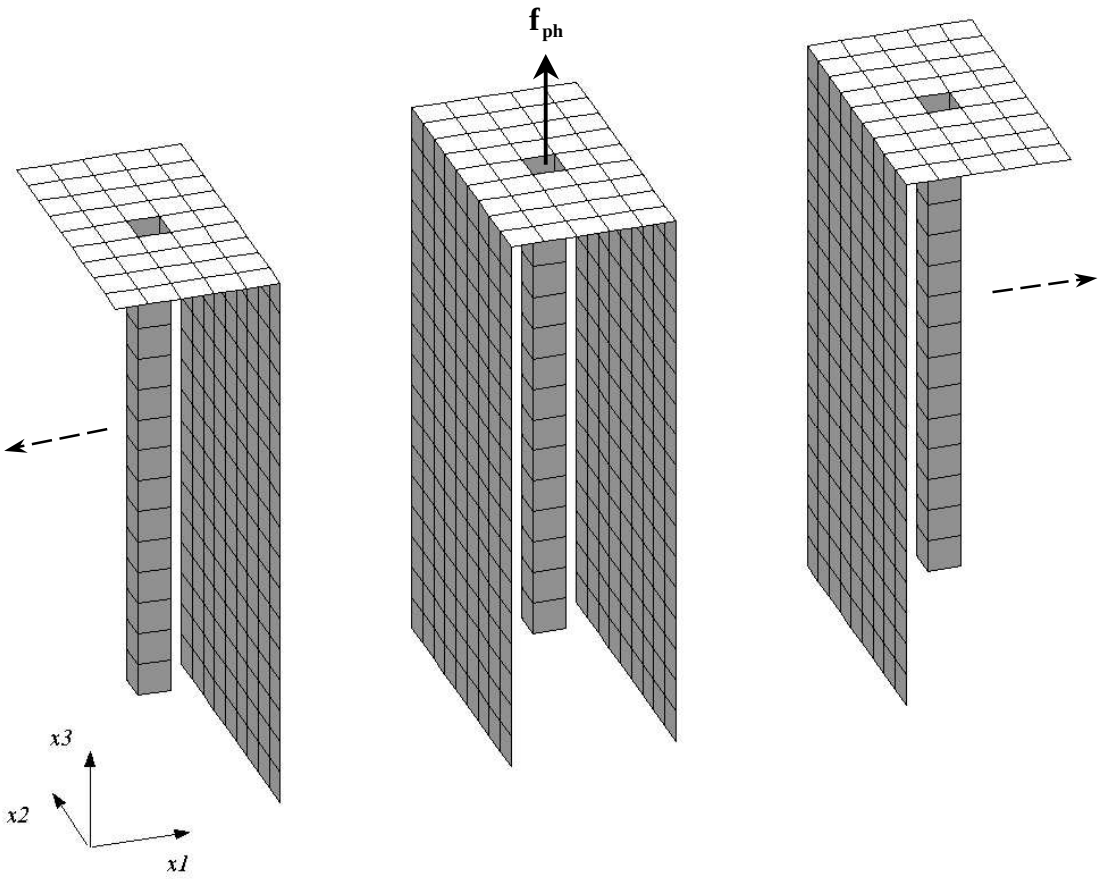

Figure 4.25: Formation of the soil component of the pile-row model by coupling together left- and right-hand semi-infinite rows to a central unit.

The above calculations enable the response of the loaded pile to be found for a given pile-head load, together with the associated displacements of the central unit. Of greater interest is the nature of the interaction between the piles in the row and the response of the *downstream* piles.

Calculation of the Downstream States

Equation 4.46 gives an expression for the state of the first unit in the right-hand semi-infinite row of piles. Successive downstream states of units further along the positive x_1-axis are obtained by

repeated multiplication of the constituent eigenvectors by their corresponding eigenvalues, as stated in Equation 4.45. Thus, for state '*j*':

$$\mathbf{s}^j = \sum_{k=1}^{3N_s} (\lambda_k)^{(j-1)} a_k \bar{\mathbf{s}}^k \tag{4.52}$$

The traction component of state '*j*' may therefore be written as:

$$\mathbf{p}^j = \bar{\mathbf{P}} \text{diag}\left\{(\lambda_k)^{(j-1)}\right\} \mathbf{a} \tag{4.53}$$

where $\text{diag}\left\{(\lambda_k)^{(j-1)}\right\}$ is a diagonal matrix containing the propagating eigenvalues raised to the appropriate power '$j-1$'. Combining Equations 4.48 and 4.53, and noting that $\mathbf{p}^1 = -\mathbf{p}_\mathbf{r}$, enables the tractions of any downstream state to be found from those on the right-hand side of the central unit:

$$\mathbf{p}^j = -\bar{\mathbf{P}} \text{diag}\left\{(\lambda_k)^{(j-1)}\right\} \left[\bar{\mathbf{P}}\right]^{-1} \mathbf{p}_\mathbf{r} \tag{4.54}$$

Using Equation 4.54 to find $\mathbf{p}^j$ and $\mathbf{p}^{j+1}$, and noting that the tractions on the left-hand side of unit '$j+1$' are always equal and opposite to those on the right-hand side of unit '*j*', the tractions on the soil-pile interface of unit '*j*' are found from Equation 4.41. This gives the complete set of tractions for unit '*j*' of the right-hand semi-infinite row and, by using Equation 4.37, the corresponding displacements. The states of units in the left-hand semi-infinite row are obtained by symmetry from those of the right-hand row.

This completes the mathematical description of the pile-row model. To conclude this section, the complete model is summarised in Figures 4.26 and 4.27. These show isometric and orthographic views of the boundary-element mesh representing the soil. Because the particular BEM formulation used is based on the full-space Green's functions, the entire model is defined within an infinite elastic space, as represented by the dotted lines in Figure 4.26. This space is actually formed by the intersection of the individual full-spaces in which each repeating unit is defined. These spaces are only coupled together over the rectangular planes formed by the side

meshes of adjacent repeating units; they otherwise act independently. This is illustrated in Figure 4.27 where the rectangular area in Section A-A and the solid vertical lines between each pile in Section C-C represent the coupling planes between adjacent full-spaces.

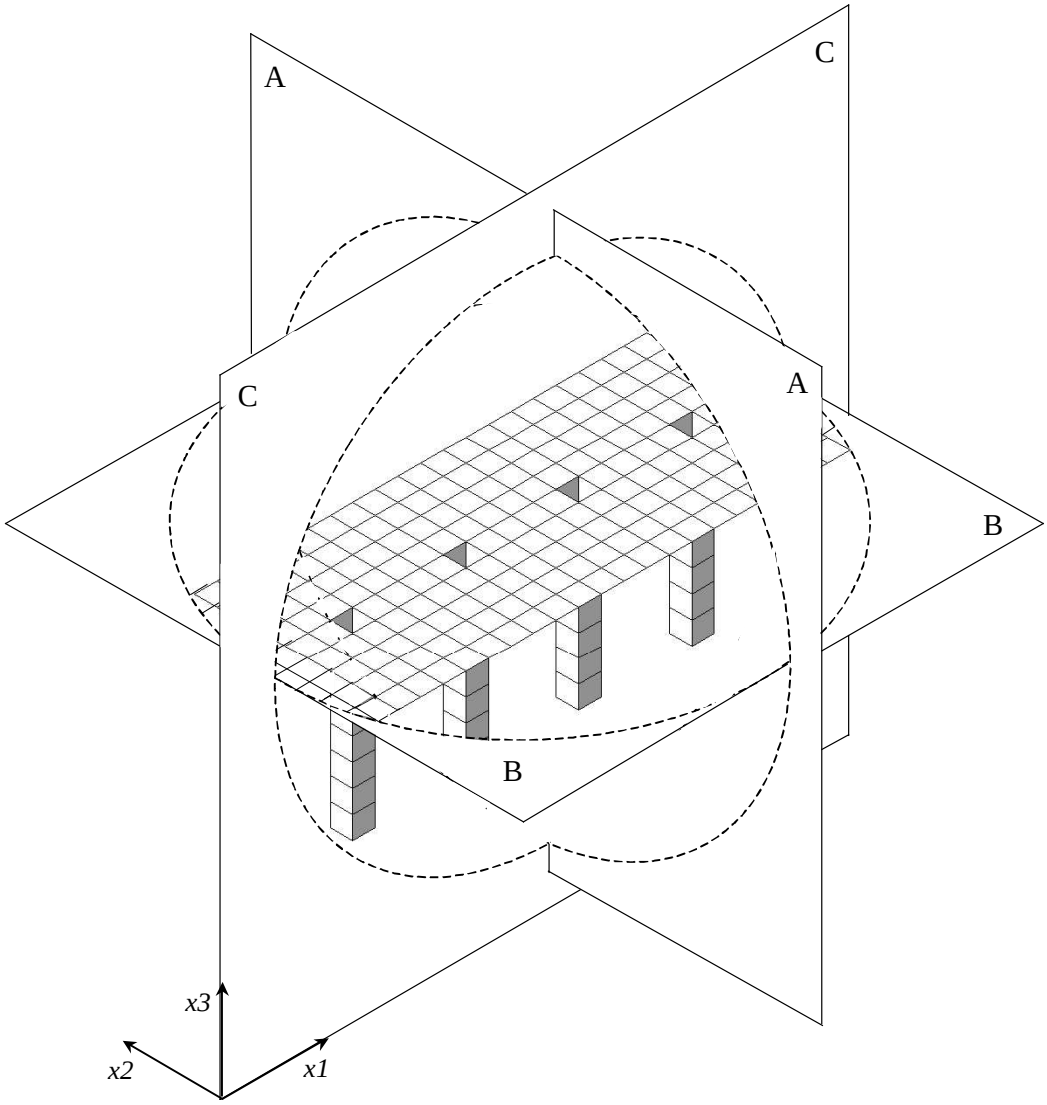

Figure 4.26: Schematic isometric projection showing the boundary-element mesh representing the soil component of the pile-row model. The dotted lines define a spherical volume in an infinite elastic space within which the free surface and soil-pile interfaces are defined. The planes A-A, B-B and C-C correspond to the sections shown in Figure 4.27.

The dashed double lines in Sections B-B and C-C indicate where these spaces overlap but are not coupled together. The solid double lines in Sections A-A and C-C indicate the continuous traction-free strip formed by the coupled free-surfaces of the repeating units. The result is effectively an open waveguide along which waves propagate from one pile to the next. Waves are

contained by the free-surface but may otherwise leave the waveguide from any of the repeating units and radiate to infinity within the respective full-space. In practice, the mesh of the repeating units is large enough such that the amplitudes of any waves crossing its boundary are insignificant and the waveguide behaves as a half-space containing an infinite row of piles.

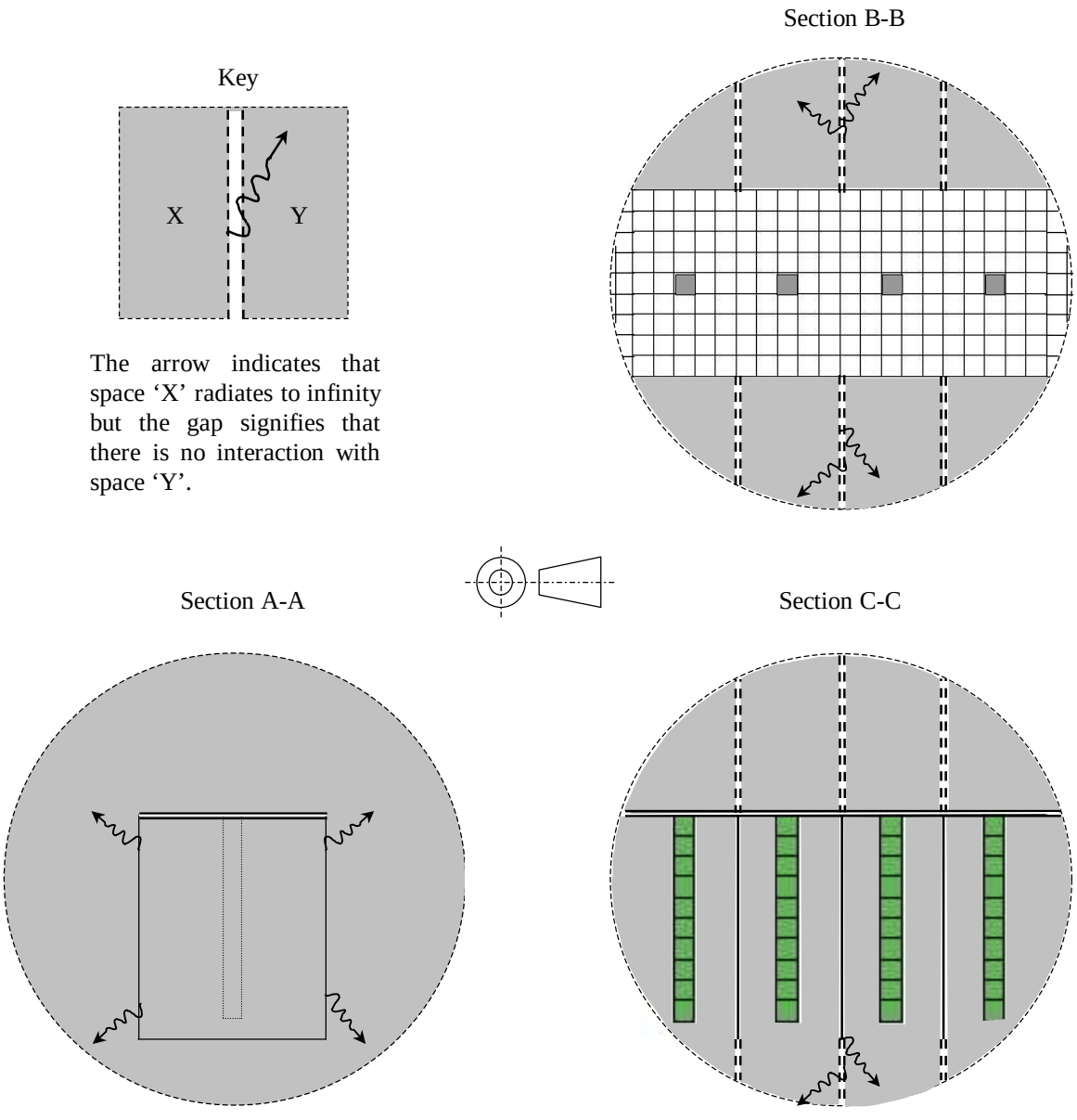

Figure 4.27: Schematic orthographic projection showing the boundary-element mesh representing the soil component of the pile-row model. The three sections correspond to the planes A-A, B-B and C-C shown in Figure 4.26, and the shading indicates where these cut through the elastic space of the model.

4.2.3. Validation of the Pile-Row Model

In this section the pile-row model is validated in two ways. Firstly, a model of a single pile is produced using periodic structure theory to model the surrounding soil and comparisons are made with the single-pile model of Section 4.1. In this way a check is made on the repeating-unit approach to modelling the behaviour of a half-space. Secondly, some of the results from the pile-row model are compared with published results describing the interaction between two neighbouring piles.

Validation of Single-Pile Behaviour

Section 4.22 describes how the soil component of the pile-row model is formed by coupling left- and right-hand semi-infinite rows to a central unit. In a similar way, a model of a single pile may be produced by taking the same central unit, complete with its pile, and coupling it to two semi-infinite models representing the neighbouring soil; see Figure 4.28. The latter are formed by coupling together repeating units identical to that shown in Figure 4.23 except that the pile is removed and the free-surface made continuous.

In Section 4.1.5 it was found that, for the parameter values chosen, a converged solution was obtained from the single-pile model with a free-surface mesh of $N_{fs} = 440$, equivalent to $N_1 = N_2 = 21$. For computational efficiency, the solution corresponding to $N_1 = N_2 = 17$ is chosen here since the differences between this and the converged solution are negligible but the latter takes 2.4 times longer to compute. Figure 4.29 compares the pile-head driving-point FRFs predicted by this model with those from the equivalent model based on periodic structure theory; the notation used for the FRFs is the same as that in Equation 3.19a. The repeating unit of the periodic model uses the same number of elements in the x_2-direction as the single-pile model ($N_2 = 17$), while $N_1 = 3$ in order to minimise the total number of free-surface elements. To achieve convergence, the side meshes of the unit must extend to the depth of the pile but beyond this is unnecessary, as are meshes with a higher element density. Both the single-pile model and the central unit of the periodic model use the same number of elements for the soil-pile interface ($N_{sp} = 61$).

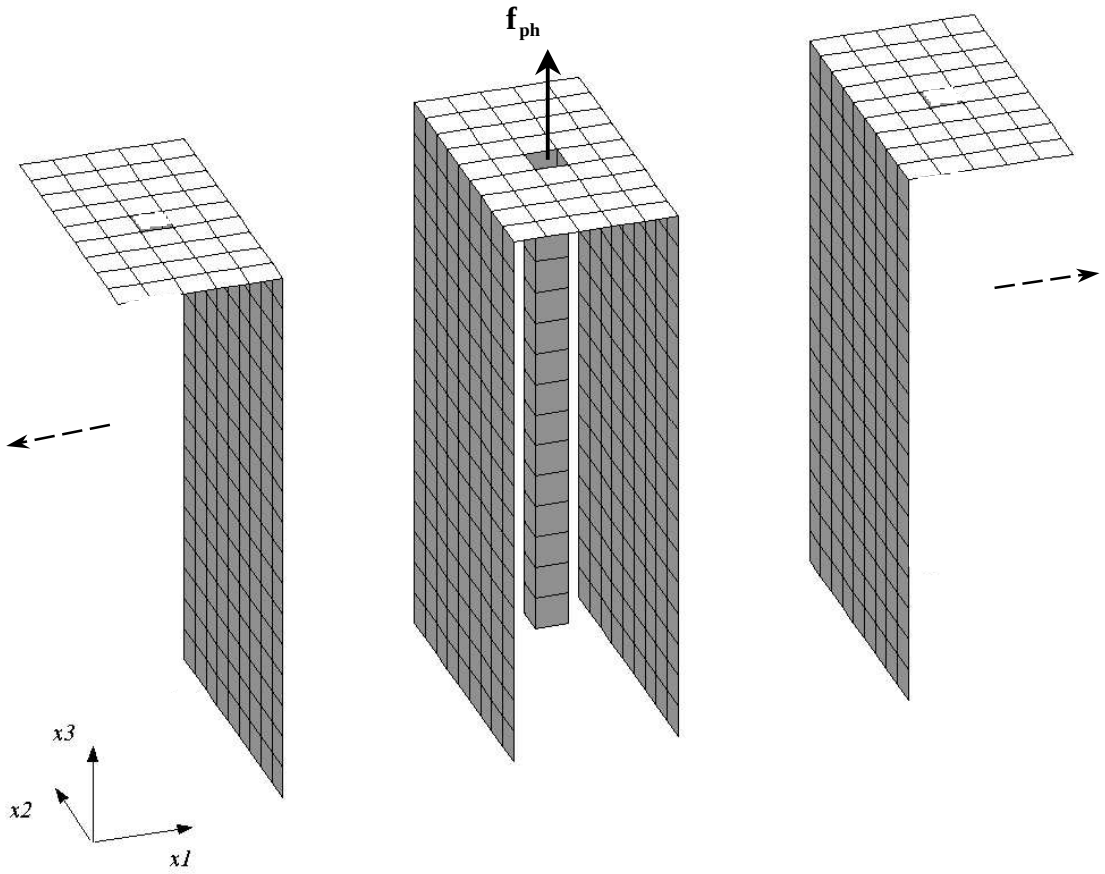

Figure 4.28: Formation of the soil component of a model of a single pile, based on periodic structure theory, by coupling a central unit, complete with pile, to two semi-infinite models representing the neighbouring soil.

The two sets of results agree very well. The largest differences appear in the low-frequency predictions of the vertical driving-point response H_{f22}^{11}. This is the reason why the results have not been presented as normalised flexibility coefficients; the static solution distorts the results. It is not clear why these differences exist and this is a subject for future investigation.

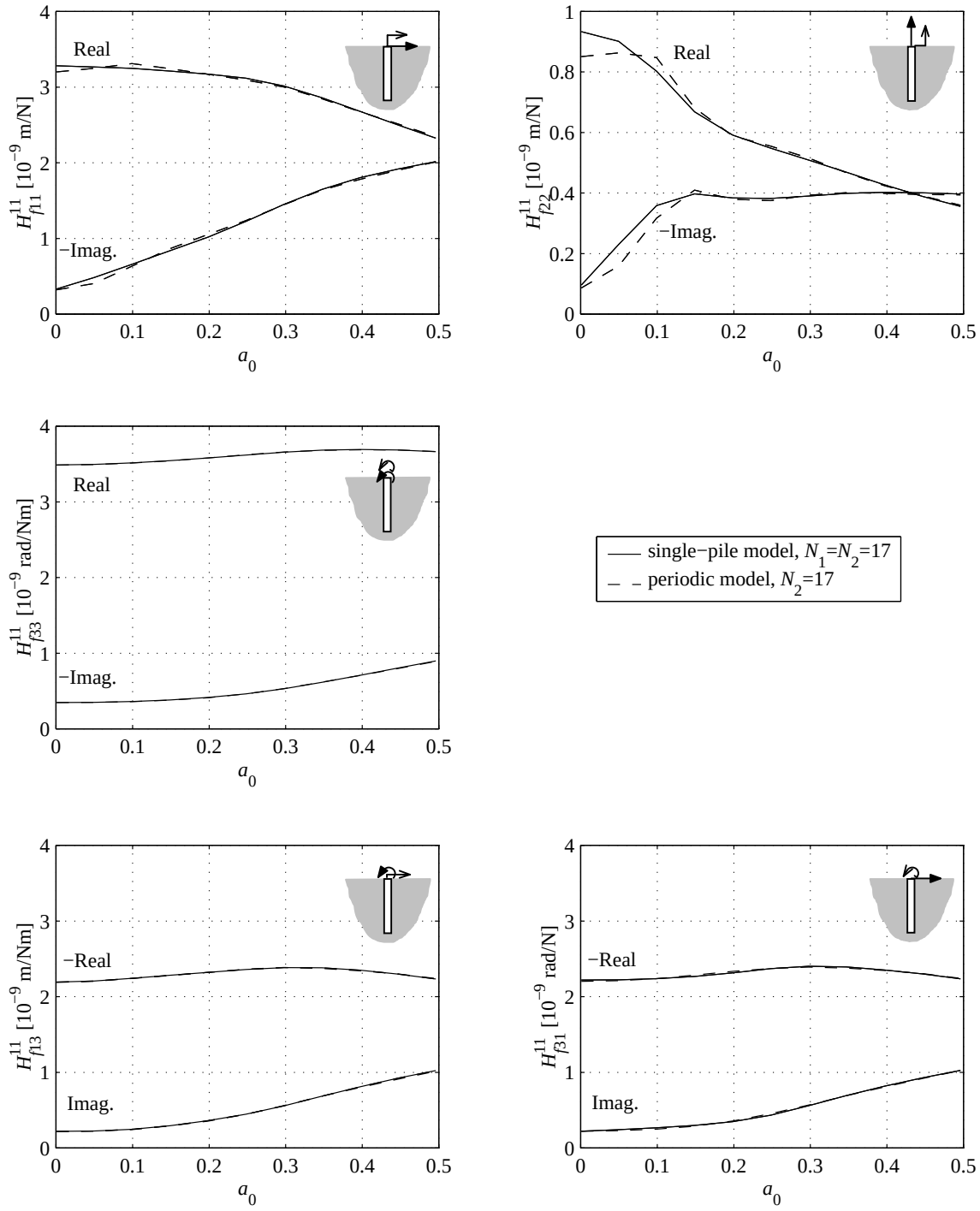

Figure 4.29: Pile-head driving-point FRFs as predicted by the single-pile model of Section 4.1 and an equivalent model based on periodic structure theory. The FRFs are plotted against non-dimensional frequency $a_0 = \omega r_0 / c_s$ and correspond to a pile with the following parameter values: $L/r_0 = 21.2$, $E_p / E_s = 100$, $\rho_p / \rho_s = 0.75$ and $\nu = 0.4$.

Further validation of the periodic model is gained by considering Figure 4.30. This illustrates how the model correctly predicts the concentric circular wavefronts on the free-surface, as predicted by the single-pile model; see Figure 4.20. This surface comprises the free-surfaces of a

central unit, containing the pile, plus six repeating units either side, as illustrated in Figure 4.31. The power of the method is impressive: it is remarkable that a parallel-sided periodic structure should correctly reproduce the circular wavefronts of a point source in an infinite medium.

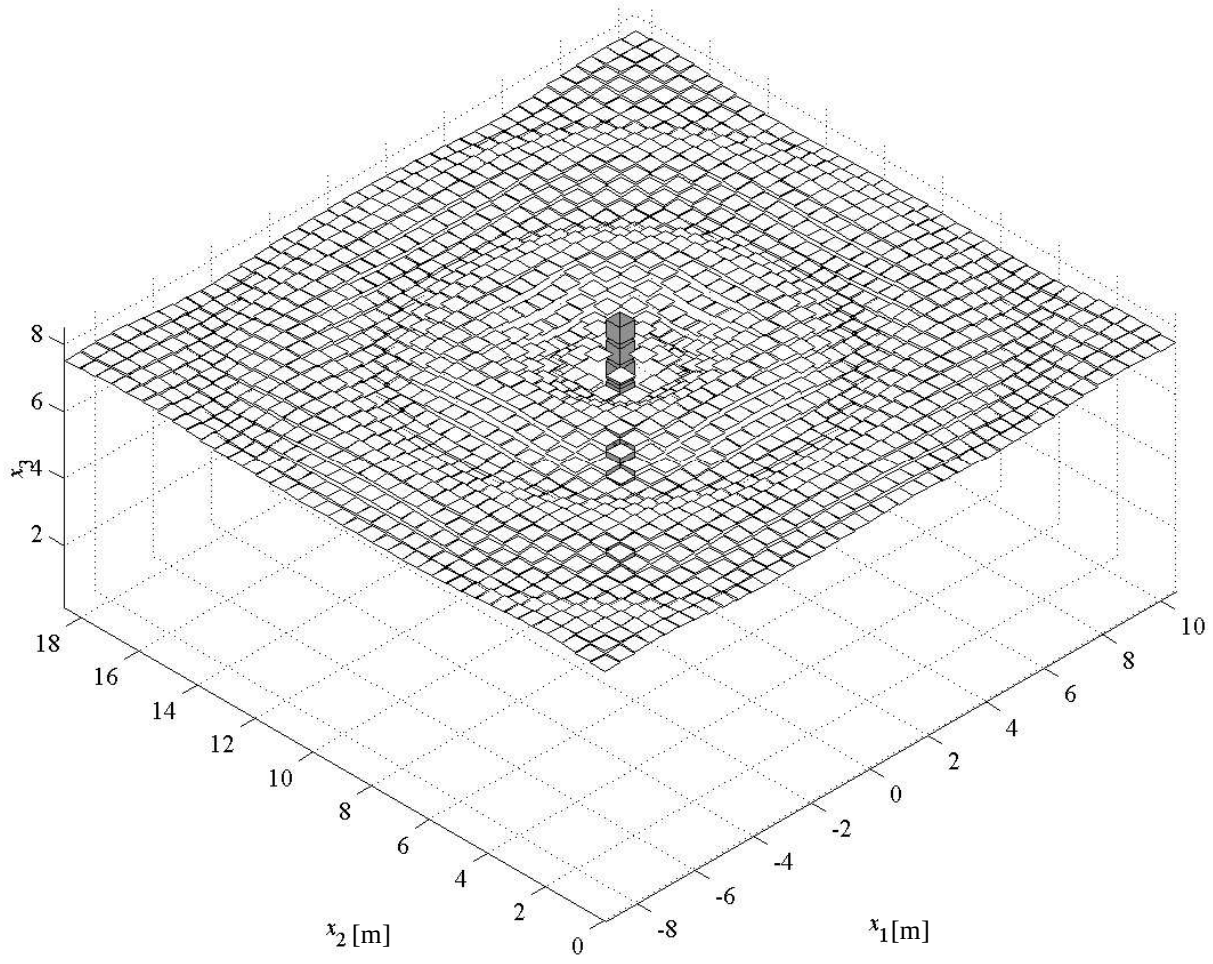

Figure 4.30: The displacement field predicted by the periodic model of a single pile when a vertical unit load is applied to the pile head at a non-dimensional frequency of $a_0 = 0.5$. The free-surface and soil-pile interface is shown and all displacements are magnified by 3×10^9. The pile has the following parameter values: $L / r_0 = 21.2$, $E_p / E_s = 100$, $\rho_p / \rho_s = 0.75$ and $\nu = 0.4$.

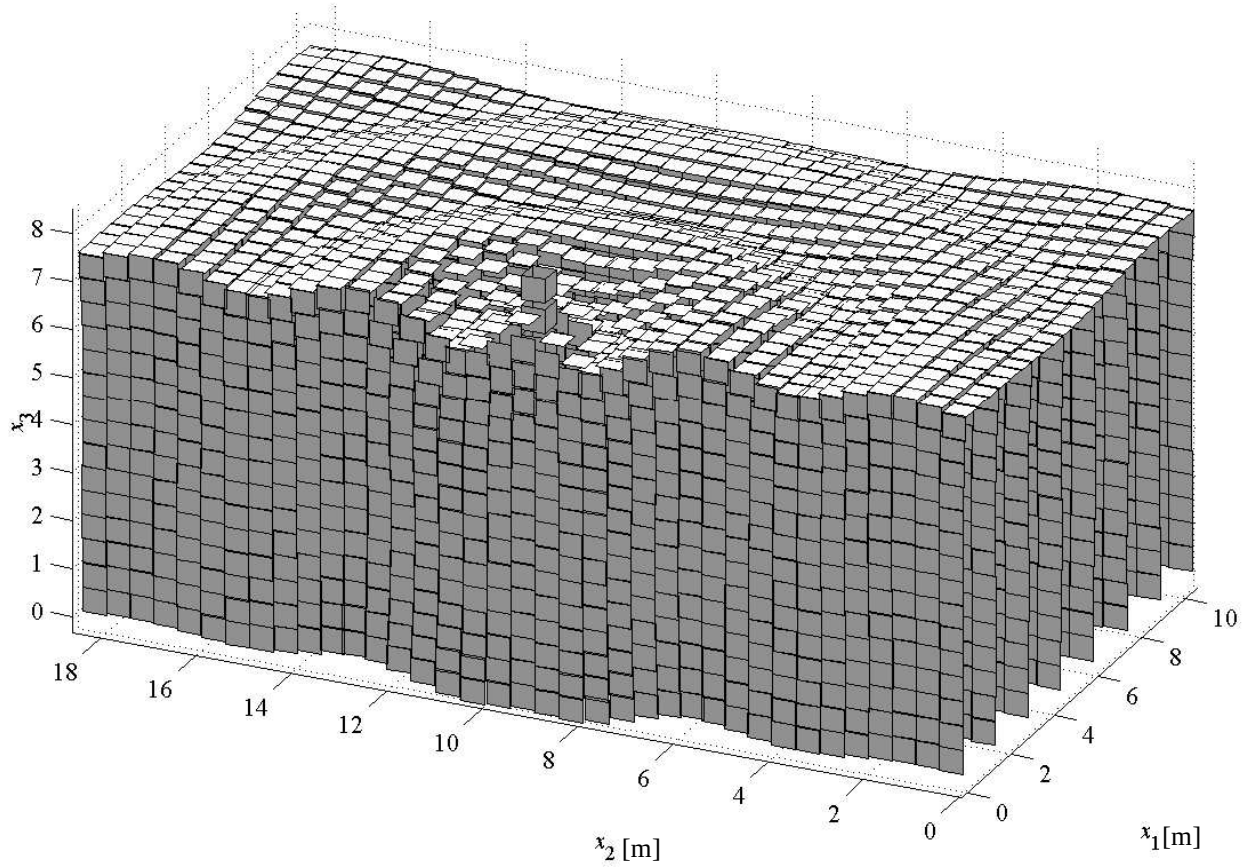

Figure 4.31: An alternative view of one half of Figure 4.30. The full boundary-element meshes of the central unit, containing the pile, plus six downstream repeating units are shown. All displacements are magnified by 3×10^9.

The use of periodic structure theory to model the surrounding soil is not a computationally efficient method for modelling a single pile. However, the results presented in Figures 4.29 and 4.30 confirm that the repeating-unit approach is able to model the behaviour of a half-space. All that remains to be confirmed is the ability of the pile-row model to account for PSPI.

Validation of Pile-Soil-Pile Interaction

The ability of the pile-row model to account for PSPI may be confirmed by comparing selected results with published results from an existing two-pile model. Firstly, it should be confirmed that the pile-row model produces a converged solution.

It was found with the periodic single-pile model, investigated in the previous section, that the boundary-element mesh parameter of primary importance for the repeating unit is the number of

elements in the x_2-direction. With the pile-row model the number of elements in the x_1-direction defines the spacing of the piles, and in the x_3-direction it is assumed that it is acceptable to terminate the side meshes at the depth of the pile, as found earlier. The same mesh density is used as before.

Figure 4.32 illustrates the effect on the pile-head coupling FRFs, as defined originally by Equation 3.19b, between two adjacent piles of the pile-row model. Typical flexible piles are considered with a slenderness ratio $L/r_0 = 21.2$ and a centre-to-centre spacing $S = 4r_0$; the remaining parameter values are given in the figure caption. It is worth emphasising that the coupling matrix $\mathbf{H}_\mathbf{f}^{21}$ is now fully populated: waves generated by the loaded pile, whatever the load, propagate through the soil, as illustrated in Figure 4.33, and lead to both linear and rotational motion of the neighbouring pile head. Note that the FRFs describing axial-flexural coupling (H_{f12}^{21}, H_{f21}^{21}, H_{f23}^{21} and H_{f32}^{21}) are an order of magnitude less than the other FRFs. As with the periodic single-pile model, $N_2 = 17$ is found to be adequate at representing the free surface. It is also clear from Figure 4.32 that the pile-row model satisfies reciprocity, given that $H_{f13}^{21} = H_{f31}^{21}$, $H_{f12}^{21} = -H_{f21}^{21}$ and $H_{f23}^{21} = -H_{f32}^{21}$, although the latter two relations suffer from some numerical errors due to the weakness of the coupling.

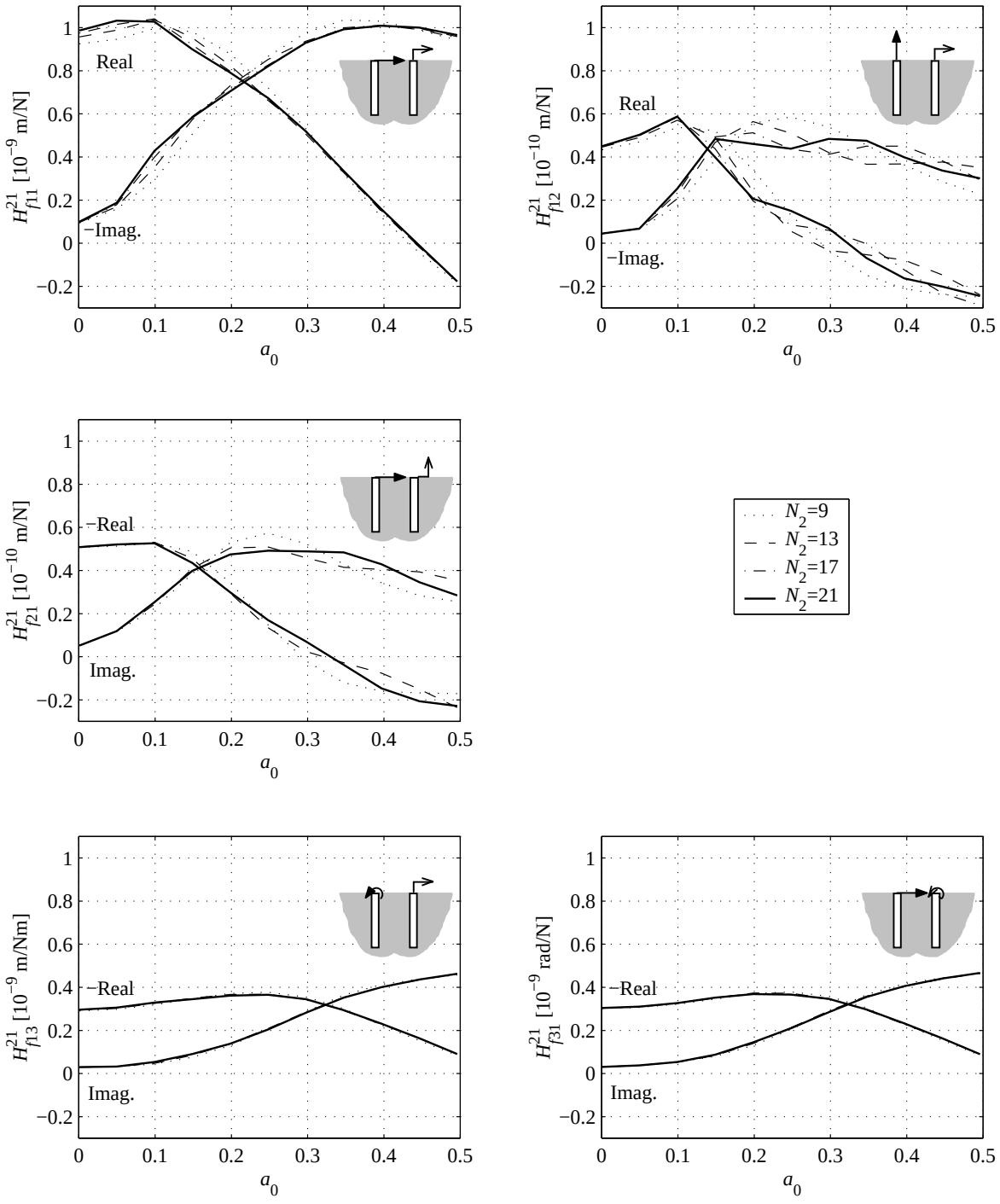

Figure 4.32 continues over page.

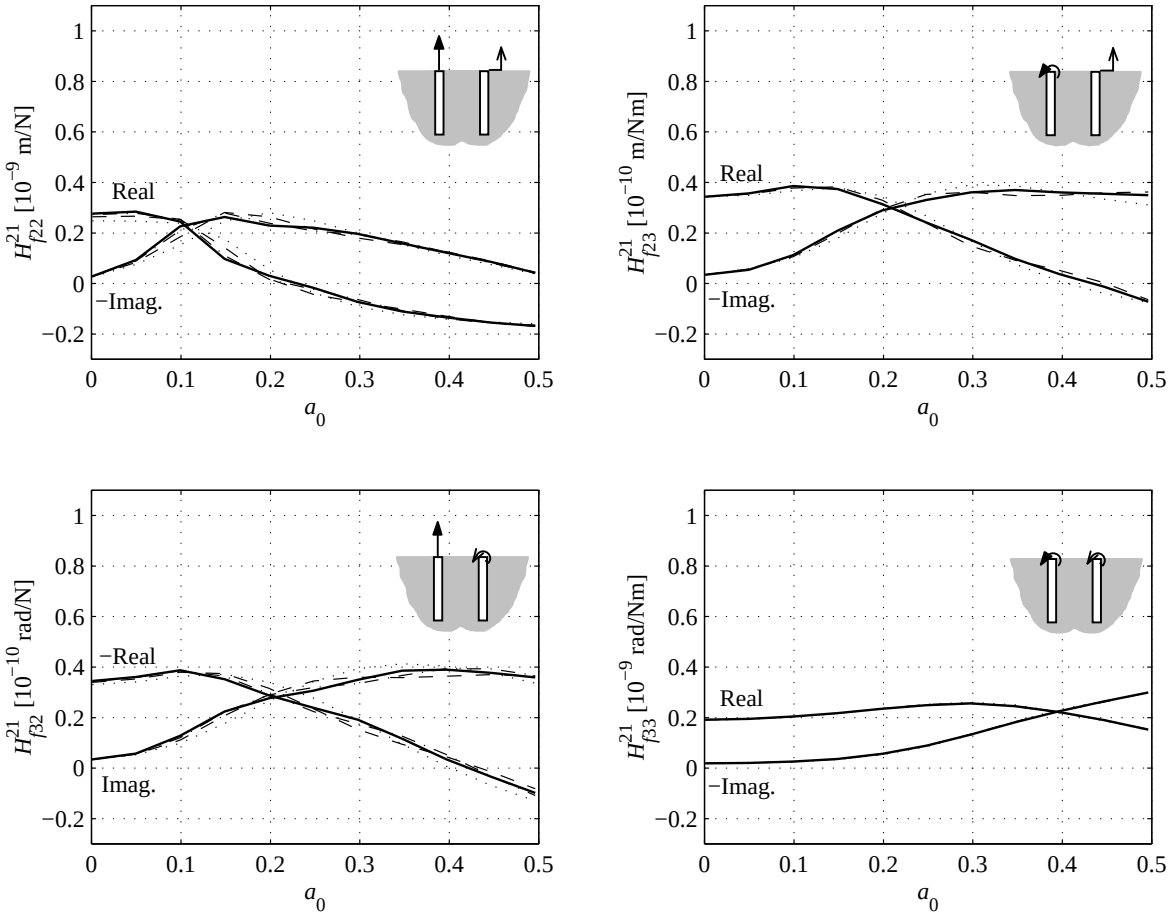

Figure 4.32: The effect of the number of free-surface boundary elements in the x_2-direction N_2 on the pile-head coupling FRFs between two adjacent piles of the pile-row model. The FRFs are plotted against non-dimensional frequency $a_0 = \omega r_0 / c_s$ and correspond to piles with the following parameter values: $L/r_0 = 21.2$, $S/r_0 = 4$, $E_p / E_s = 100$, $\rho_p / \rho_s = 0.75$ and $\nu = 0.4$.

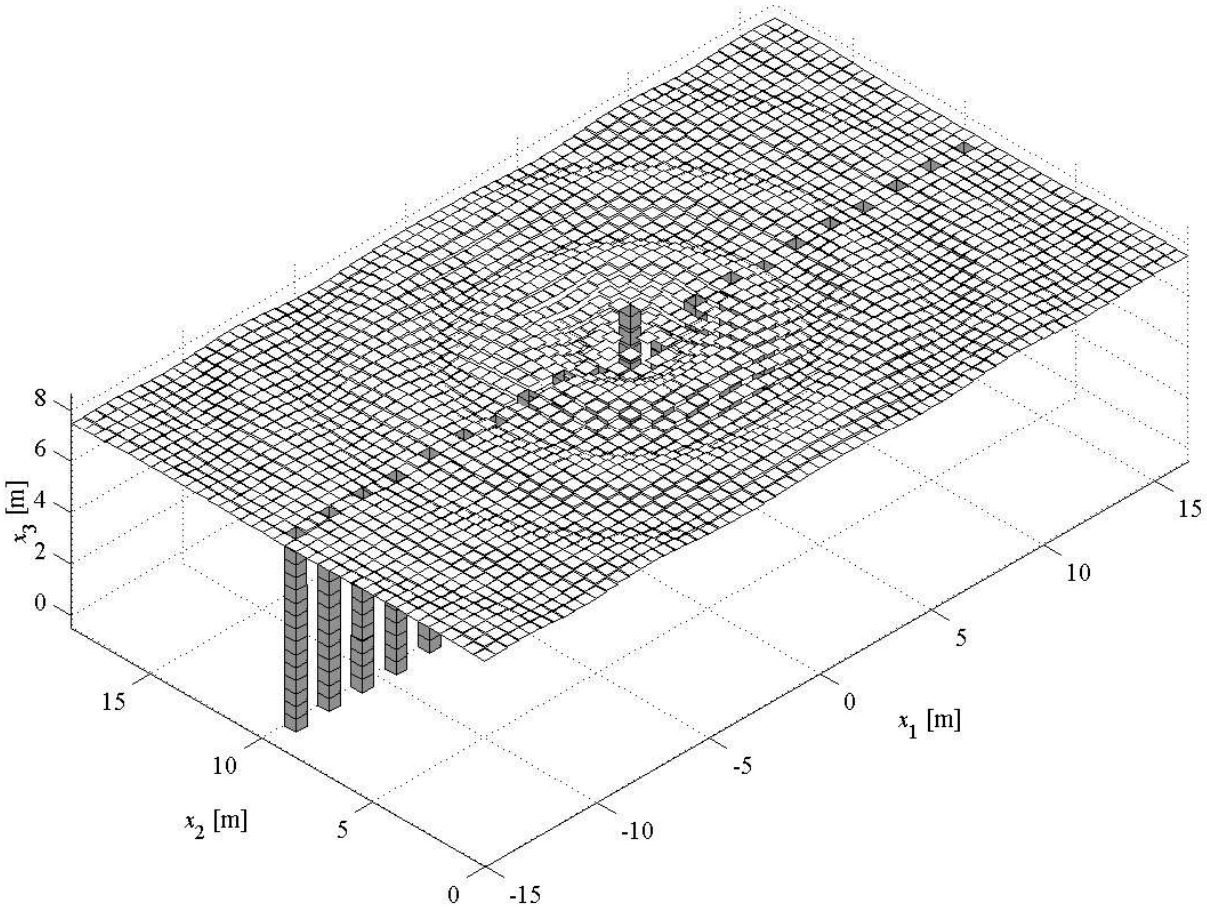

Figure 4.33: The displacement field predicted by the pile-row model when a vertical unit load is applied to the central pile-head at a non-dimensional frequency of $a_0 = 0.5$. The free-surface and soil-pile interface of 21 piles is shown and all displacements are magnified by 3×10^9. The piles have the following parameter values: $L/r_0 = 21.2$, $S/r_0 = 4$, $E_p/E_s = 100$, $\rho_p/\rho_s = 0.75$ and $\nu = 0.4$.

The nature of the PSPI is illustrated in Figure 4.34. This shows vertical sections through the pile-row model for the three different load-cases at a frequency $a_0 = 0.1$ around which, for the particular parameter values chosen, PSPI is greatest. Similar plots are given in Figure 4.35 for the frequency $a_0 = 0.5$. It is clear that axial motion of the loaded pile leads to flexure of the neighbouring piles, and vice versa. The significance of this PSPI when modelling a base-isolated building will be considered in Chapter 5.

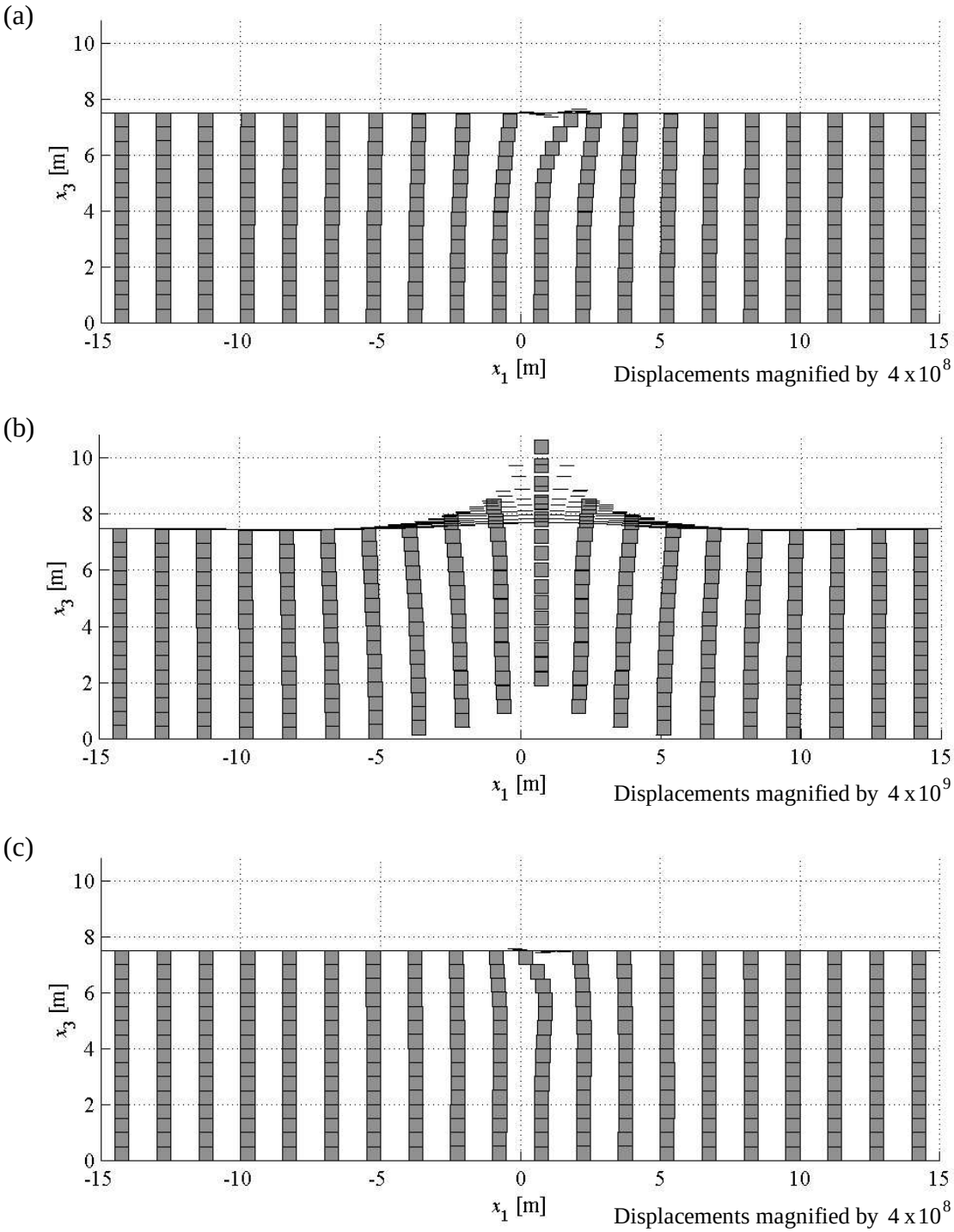

Figure 4.34: Vertical sections through the pile-row model illustrating the nature of the PSPI when (a) a unit horizontal load, (b) a unit vertical load and (c) a unit moment is applied to the central pile-head at a non-dimensional frequency of $a_0 = 0.1$. The piles have the following parameter values: $L/r_0 = 21.2$, $S/r_0 = 4$, $E_p/E_s = 100$, $\rho_p/\rho_s = 0.75$ and $\nu = 0.4$.

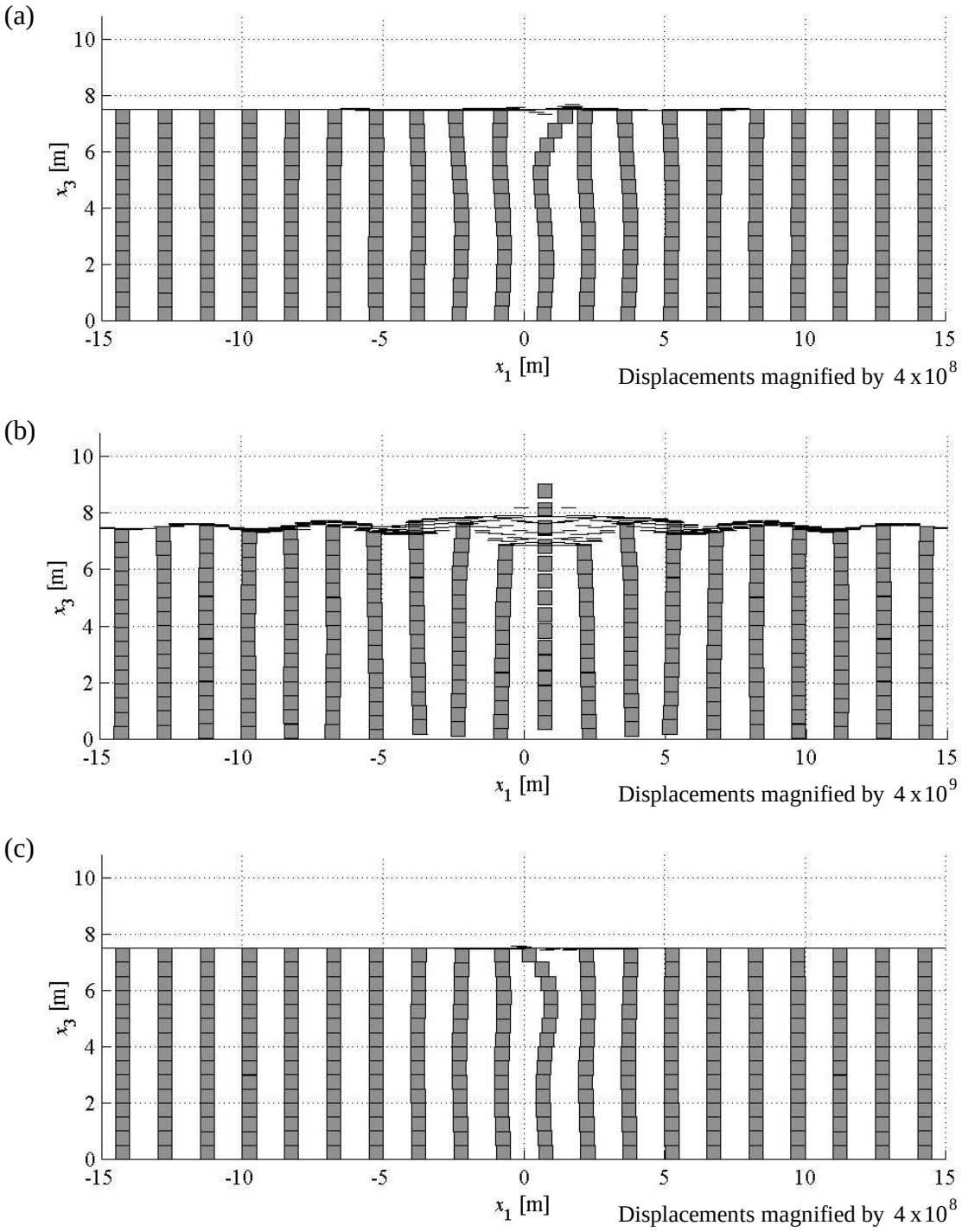

Figure 4.35: Vertical sections through the pile-row model illustrating the nature of the PSPI when (a) a unit horizontal load, (b) a unit vertical load and (c) a unit moment is applied to the central pile-head at a non-dimensional frequency of $a_0 = 0.5$. The piles have the following parameter values: $L/r_0 = 21.2$, $S/r_0 = 4$, $E_p / E_s = 100$, $\rho_p / \rho_s = 0.75$ and $\nu = 0.4$.

Predictions of PSPI between two adjacent piles of the pile-row model may now be compared with published results from an existing two-pile model. In common with the literature, these results are presented in the form of *dynamic interaction factors*, which are defined as follows: a dynamic interaction factor between pile 1 and pile 2 is equal to the pile-head displacement of the unloaded pile 2 due to the generalised force applied to pile-head 1, normalised by the static displacement of pile-head 1. For example:

$$\alpha_{\theta f} = \frac{\text{rotation of pile 2 due to horizontal load applied to pile 1}}{\text{static rotation of pile 1 due horizontal load applied to pile 1}} \tag{4.55}$$

Strictly the comparison is not valid since two-pile models do not account for interaction effects from other piles in the row. However, provided that two adjacent piles of the pile-row model are considered with no intermediate piles, the comparison is fair.

Figure 4.36 compares the four interaction factors published by Kaynia [65] with the corresponding factors predicted by the pile-row model. As noted in Section 2.7.2, Kaynia's model is similar to that of Sen *et al*. [118] but uses different Green's functions for the half-space. The results from the pile-row model are normalised with respect to the static results from the single-pile model of Section 4.1. The two sets of results agree well and it may be concluded that the pile-row model behaves as intended.

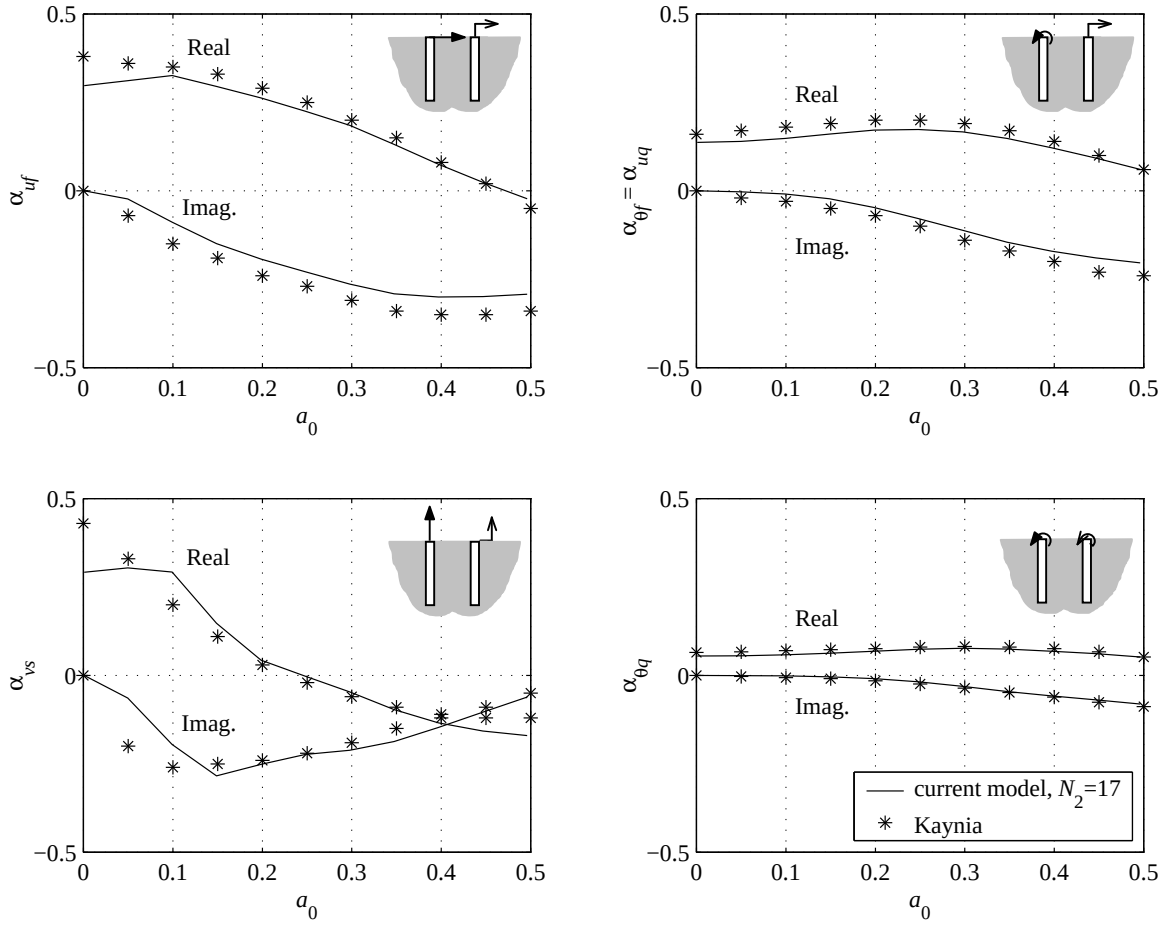

Figure 4.36: Comparison of dynamic interaction factors predicted by the current pile-row model for two adjacent piles with those predicted by the two-pile model of Kaynia. The factors are plotted against non-dimensional frequency $a_0 = \omega r_0 / c_s$ and correspond to a pile with the following parameter values: $L/r_0 = 21.2$, $S/r_0 = 4$, $E_p / E_s = 100$, $\rho_p / \rho_s = 0.75$ and $\nu = 0.4$.

4.3. Conclusions

This chapter has described the systematic development of a comprehensive three-dimensional model of a piled foundation. This has been achieved in a computationally efficient way by assuming the foundation consists of an infinitely long row of identical piles and using a combination of the boundary-element method and periodic structure theory. By comparison with existing published models, it has been demonstrated that this model accounts for the essential dynamic behaviour of a piled foundation, namely the vertical, horizontal and rotational motion of the pile heads due to both direct pile-head loading and interaction through wave propagation in the surrounding soil.

The agreement with published results is good over the frequency range considered, which corresponds to the lower range of interest when dealing with ground-borne vibration – typically from 0 to 50 Hz. Over the upper frequency range of interest – typically from 50 to 150 Hz – the accuracy is expected to decrease with frequency and an error of up to 20 % may be expected based on the behaviour of two-dimensional plane and anti-plane models. This reduction in accuracy with frequency is due to the limitations of using four boundary elements around the pile circumference. The number of elements may be increased in the future if greater accuracy is required and the necessary computing power becomes available.

In the next chapter the pile-row model is incorporated into a generic model of a base-isolated building. The importance of pile-soil-pile interaction is investigated, together with other aspects of base-isolated building behaviour.

Chapter 5
A GENERIC MODEL OF A BASE-ISOLATED BUILDING

This chapter draws together the work of Chapters 3 and 4 and describes the assembly of a generic model of a base-isolated building. The first section describes an existing two-dimensional model of a building, which is based on the dynamic-stiffness method (DSM) and the same periodic structure theory used to model the piled foundation of Chapter 4. The coupling of the building and foundation models is then described before a virtual case study is presented to illustrate the practical application of the final model. Along with some initial observations, the case of a point-load excitation of the foundation is used to investigate three aspects of base-isolated building behaviour: the added-mass effect associated with a building and the vibration of its foundation; the insertion performance of typical isolation bearings; and the importance of accounting for pile-soil-pile interaction in the foundation model.

5.1. The Infinite Building Model

In Chapter 3 the DSM was introduced as an appropriate means of modelling a typical building and this was illustrated with a simple portal-frame model. Real buildings contain many more columns and floors and the generic base-isolated building model must reflect this. The chosen building model is that developed by Cryer [33]; see Figure 5.1. This is an infinitely long two-dimensional portal-frame model produced by combining the DSM with the same periodic structure theory used to model the pile row of Chapter 4. The primary reason for choosing this approach is the computational efficiency with which a multi-story building may be modelled. It has also been

validated by Cryer's experiments in Gloucester Park, London, which show that predictions of vibration transmissibility agree well with measurements made in a real building.

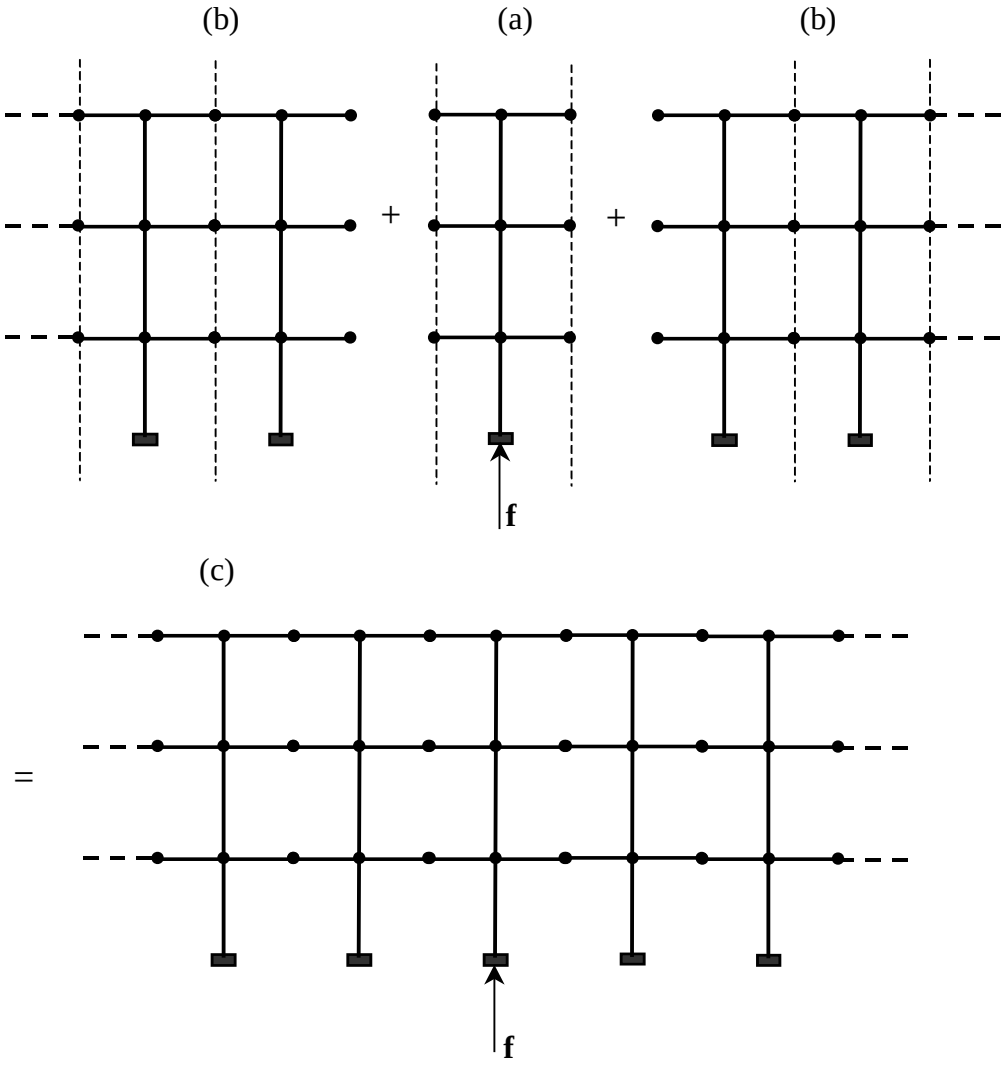

Figure 5.1: Cryer's infinitely long two-dimensional portal-frame model of a building, based on a combination of the dynamic-stiffness method and periodic structure theory. The central loaded unit (a) is coupled to two semi-infinite structures (b) to form the complete model (c). The repeating units are defined by dashed vertical lines.

The mathematics describing the building model is very similar to that describing the pile-row model given in Section 4.2.2. The key equation again involves a transfer matrix but this now relates the generalised forces and displacements at the ends of each floor of the portal frame's repeating unit. The transfer matrix is derived from the repeating unit's frequency-response function (FRF) matrix, as calculated by the DSM. Further details may be found in Cryer [33].

When the model is used to represent an isolated building the repeating unit has an isolation bearing added to the base of the column. This is modelled using the approach described in Section 3.1.2.

5.2. Coupling the Infinite Building and Pile-Row Models

In principle, an infinitely long model of a building and its foundation may be produced by using the periodic structure theory described in Section 4.2.2 with a new form of repeating unit. The unit would be formed by coupling together the repeating units of the building and pile-row models. This approach has the advantage of producing a fully coupled model, with the base of every building column coupled to a pile, but the disadvantage of requiring a new solution to the entire model, including the foundation, whenever a parameter change is made.

The approach chosen here is to solve the infinite building and pile-row models separately and then couple the two together at a *finite* number of pile heads, in a similar way to that used for the initial model of Section 3.3.1. The necessary number of coupling points is determined by observing the convergence of the solution as more piles are included. The advantage of this approach is that parameter changes may be made to the building model without the need to re-solve the pile-row model, which is by far the more computationally expensive component. A schematic diagram of the complete model is shown in Figure 5.2.

The details of the coupling procedure are as follows. A general form of Equation 3.18 is used to relate the generalised forces and displacements of the N_{ph} pile heads that are to be coupled to the building:

$$\begin{bmatrix} \mathbf{u}_{\mathbf{ph}}^{1} \\ \mathbf{u}_{\mathbf{ph}}^{2} \\ \vdots \\ \mathbf{u}_{\mathbf{ph}}^{N_{ph}} \end{bmatrix} = \begin{bmatrix} \mathbf{H}_{\mathbf{f}}^{11} & \mathbf{H}_{\mathbf{f}}^{12} & \cdots & \mathbf{H}_{\mathbf{f}}^{1N_{ph}} \\ \mathbf{H}_{\mathbf{f}}^{21} & \mathbf{H}_{\mathbf{f}}^{22} & & \\ \vdots & & \ddots & \\ \mathbf{H}_{\mathbf{f}}^{N_{ph}1} & & & \mathbf{H}_{\mathbf{f}}^{N_{ph}N_{ph}} \end{bmatrix} \begin{bmatrix} \mathbf{f}_{\mathbf{ph}}^{1} \\ \mathbf{f}_{\mathbf{ph}}^{2} \\ \vdots \\ \mathbf{f}_{\mathbf{ph}}^{N_{ph}} \end{bmatrix} + \begin{bmatrix} \mathbf{u}_{\mathbf{ph0}}^{1} \\ \mathbf{u}_{\mathbf{ph0}}^{2} \\ \vdots \\ \mathbf{u}_{\mathbf{ph0}}^{N_{ph}} \end{bmatrix} \tag{5.1a}$$

or

$$\mathbf{u}_{\mathbf{ph}} = \mathbf{H}_{\mathbf{f}}\mathbf{f}_{\mathbf{ph}} + \mathbf{u}_{\mathbf{ph0}} \tag{5.1b}$$

The $3N_{ph}$ x $3N_{ph}$ FRF matrix $\mathbf{H}_{\mathbf{f}}$ describes the behaviour of the foundation and is assembled from the 3 x 3 matrices describing the individual piles. The three $3N_{ph}$ x 1 vectors $\mathbf{f}_{\mathbf{ph}}$, $\mathbf{u}_{\mathbf{pho}}$ and

$\mathbf{u}_{\mathbf{ph}}$ are assembled, respectively, from the 3 x 1 vectors containing the complex amplitudes of the generalised forces, and the generalised displacements before and after construction of the building, of each pile-head.

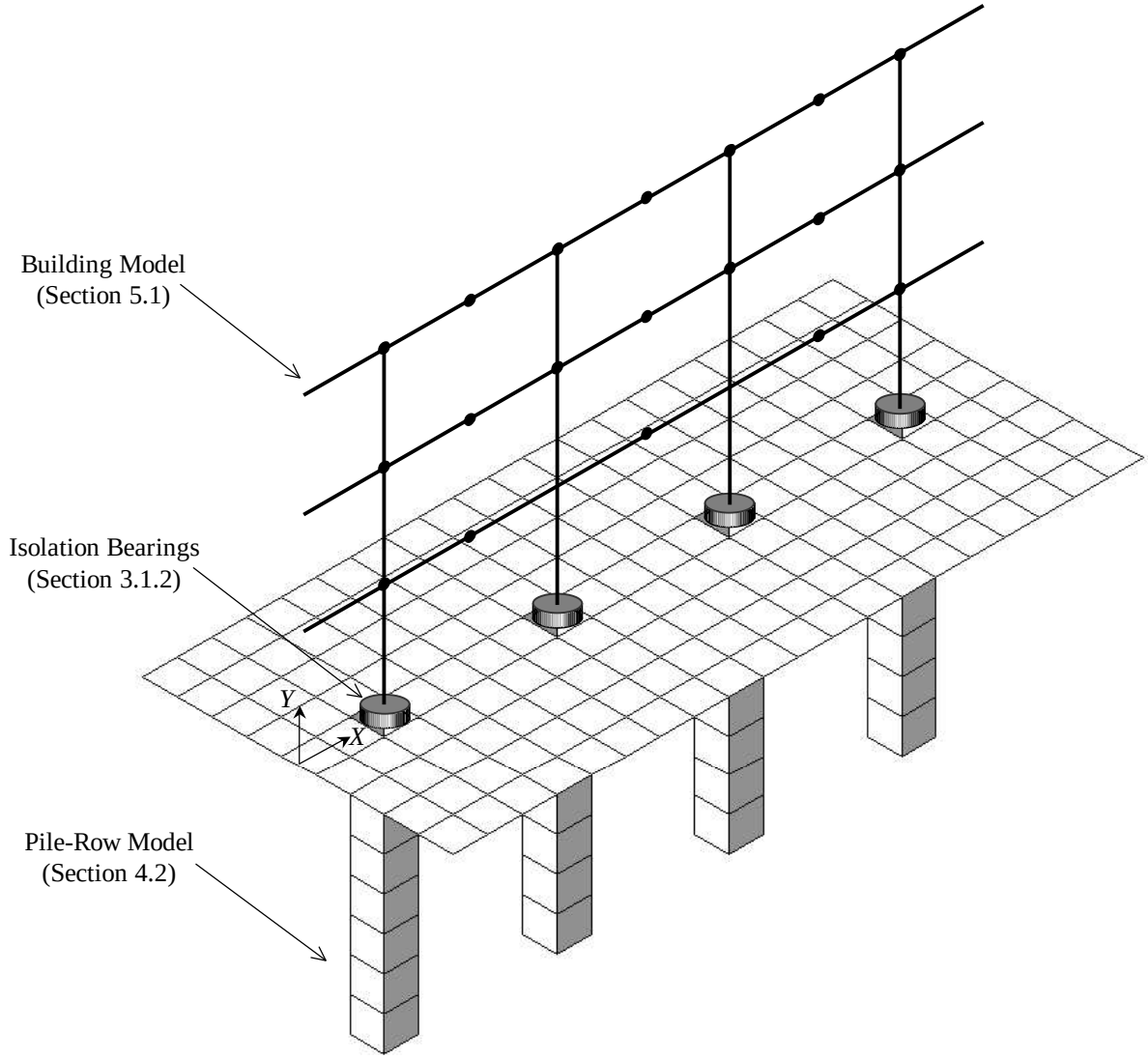

Figure 5.2: Schematic isometric projection of the generic model of a base-isolated building. The infinitely long two-dimensional portal-frame model of a building is coupled to the infinitely long three-dimensional model of a piled foundation.

Because the foundation comprises identical piles, the matrices $\mathbf{H}_{\mathbf{f}}^{ii}$ along the diagonal of $\mathbf{H}_{\mathbf{f}}$, which contain the pile-head driving-point FRFs of each pile, are all equal. The off-diagonal matrices describe the PSPI, and reciprocity and symmetry imply that:

$$\mathbf{H}_{\mathbf{f}}^{ij} = \mathbf{H}_{\mathbf{f}}^{ji} \bullet \begin{bmatrix} 1 & -1 & 1 \\ -1 & 1 & -1 \\ 1 & -1 & 1 \end{bmatrix} \tag{5.2}$$

where '•' implies element-by-element matrix multiplication.

The force and displacement amplitudes of the pile heads, after construction of the building, are also related through a general form of Equation 3.20:

$$\begin{bmatrix} \mathbf{u}_{\mathbf{ph}}^{1} \\ \mathbf{u}_{\mathbf{ph}}^{2} \\ \vdots \\ \mathbf{u}_{\mathbf{ph}}^{N_{ph}} \end{bmatrix} = -\begin{bmatrix} \mathbf{H}_{\mathbf{b}}^{11} & \mathbf{H}_{\mathbf{b}}^{12} & \cdots & \mathbf{H}_{\mathbf{b}}^{1N_{ph}} \\ \mathbf{H}_{\mathbf{b}}^{21} & \mathbf{H}_{\mathbf{b}}^{22} & & \\ \vdots & & \ddots & \\ \mathbf{H}_{\mathbf{b}}^{N_{ph}1} & & & \mathbf{H}_{\mathbf{b}}^{N_{ph}N_{ph}} \end{bmatrix} \begin{bmatrix} \mathbf{f}_{\mathbf{ph}}^{1} \\ \mathbf{f}_{\mathbf{ph}}^{2} \\ \vdots \\ \mathbf{f}_{\mathbf{ph}}^{N_{ph}} \end{bmatrix} \tag{5.3a}$$

or

$$\mathbf{u}_{\mathbf{ph}} = -\mathbf{H}_{\mathbf{b}}\mathbf{f}_{\mathbf{ph}} \tag{5.3b}$$

Eliminating the forces from Equations 5.1 and 5.3 gives the final displacements of the pile heads in terms of those prior to the construction of the building, as in Equation 3.21:

$$\mathbf{u}_{\mathbf{ph}} = \left[\mathbf{I} + \mathbf{H}_{\mathbf{f}}\left[\mathbf{H}_{\mathbf{b}}\right]^{-1}\right]^{-1}\mathbf{u}_{\mathbf{ph0}} \tag{5.4}$$

where $\mathbf{I}$ is a $3N_{ph}$ x $3N_{ph}$ identity matrix.

For any chosen pre-construction displacements of the pile-heads, the displacements given by Equation 5.4 may be used to find the corresponding forces by inversion of Equation 5.3. These forces are then applied, in the opposite sense, to the building model to determine the full response.

This concludes the mathematical description of the generic model. The model is flexible, computationally efficient and there are many possible studies that may now be undertaken. These include investigations into the following:

- the importance of the stiffness – vertical, horizontal and rotational – and internal damping of isolation bearings in determining base-isolation performance;
- the significance of different ground vibration fields when designing for maximum base isolation, and the effects of horizontal and rotational motion of a foundation in addition to vertical motion;

- the nature of the soil-structure interaction between a building and its foundation and how this influences isolation performance;
- the nature of pile-soil-pile interaction in piled foundations and how this influences isolation performance.

The next section presents three selected studies as those of most immediate interest.

5.3. A Virtual Case Study

This section discusses some initial observations along with three studies undertaken with the generic base-isolated building model. The results are presented in the form of a virtual case study in order to illustrate the practical application of the model.

Figure 5.3 shows a schematic elevation of a design for a new hospital.

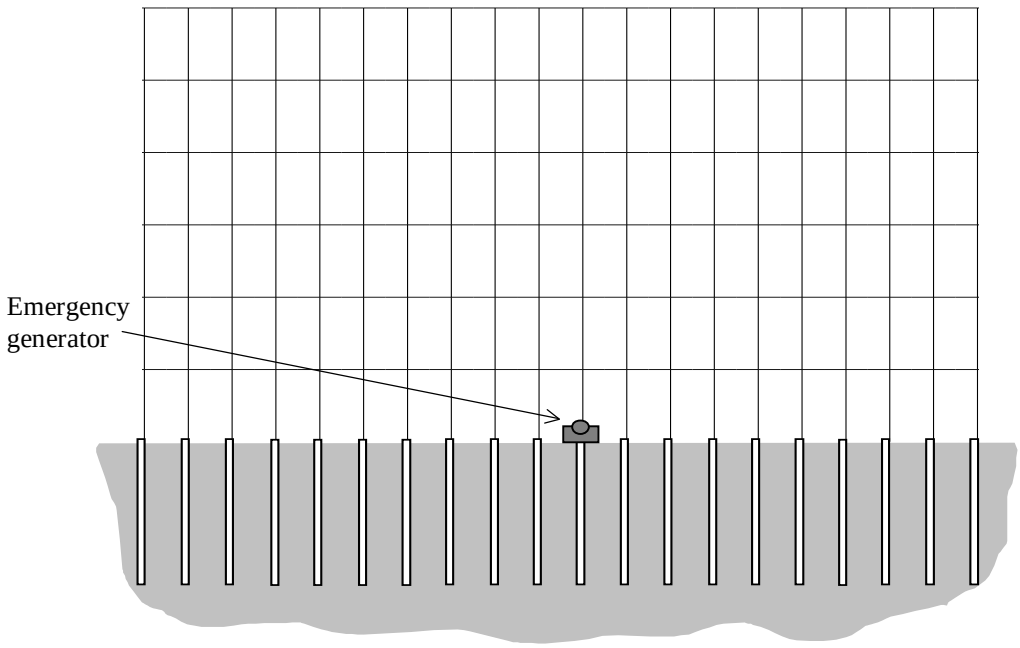

Figure 5.3: Schematic elevation of a design for a new hospital. An emergency generator located at ground-floor level may lead to excessive levels of internal vibration and base isolation of the building is a potential solution.

The design is based on a typical concrete-framed structure founded on piles and includes an emergency generator at ground-floor level located close to one of the central piles. It is recognised that the generator may lead to excessive vibration levels in the hospital. Consequently,

following construction of the foundation, a consultant is asked to simulate operation of the generator by using a harmonic shaker mounted on the pile head nearest to the location of the generator. Based on measurements of the resulting motion of the pile heads, the consultant concludes that vibration would indeed be a problem in the completed hospital and that base isolation of the structure should be investigated.

Three questions are of primary concern: how significant is the added-mass effect, first discussed in Section 3.2.2; what level of insertion performance should be expected from the base isolation; and how important is the modelling of PSPI? These questions are addressed in turn using results from the generic model. The results are all based on a model of a concrete-framed building founded on concrete piles, with the parameter values given in Table 5.1.

Building property	**Value**	**Foundation property**	**Value**
Number of storeys	6	Length of piles [m]	7.5
Height of columns [m]	3	Radius of piles [m]	0.354
Length of floors [m]	1.5	Spacing of piles [m]	1.5
Bending stiffness of elements [GPam^4]	0.4	Bending stiffness of piles [GPam^4]	0.34
Axial stiffness of elements [GPam^2]	5.0	Axial stiffness of piles [GPam^2]	11.0
Young's modulus of elements [GPa]	10	Young's modulus of piles [GPa]	28
Density of elements [kg/m^3]	2400	Density of piles [kg/m^3]	2667
Damping loss factor of elements	0.1	Young's modulus of soil [GPa]	0.28
		Density of soil [kg/m^3]	2000
		Poisson's ratio of soil	0.4
		Damping loss factor of soil	0.02

Table 5.1: The parameter values used in the generic base-isolated building model for the virtual case study.

The excitation from the harmonic shaker is modelled as a vertical unit-amplitude force applied to the central pile-head. This results in the pre-construction pile-head vibration amplitudes $\mathbf{u}_{\mathbf{ph0}}$, which are calculated using the pile-row model alone. The piled foundation model uses the same boundary-element mesh as used in the final validated model of Section 4.2.3 and an upper frequency limit of 80 Hz is chosen, which includes the range of frequencies in which ground-borne vibration levels typically peak. At 80 Hz the mesh provides six elements per S-wavelength, as recommended by Dominguez [35] for use in elastodynamic analysis. When calculating the final

response, observations of the convergence of the various results show that, for the particular parameter values chosen, the number of piles that must be coupled to the building is 23.

5.3.1. Initial Observations

Figures 5.4 and 5.5 illustrate the predicted response of the hospital in the event that it is left unisolated and the columns of the buildings are directly coupled to the piles. In this case it is clear that the building and foundation experience comparable vibration amplitudes and behave as one system. It is also clear that the piles undergo horizontal, as well as vertical, motion.

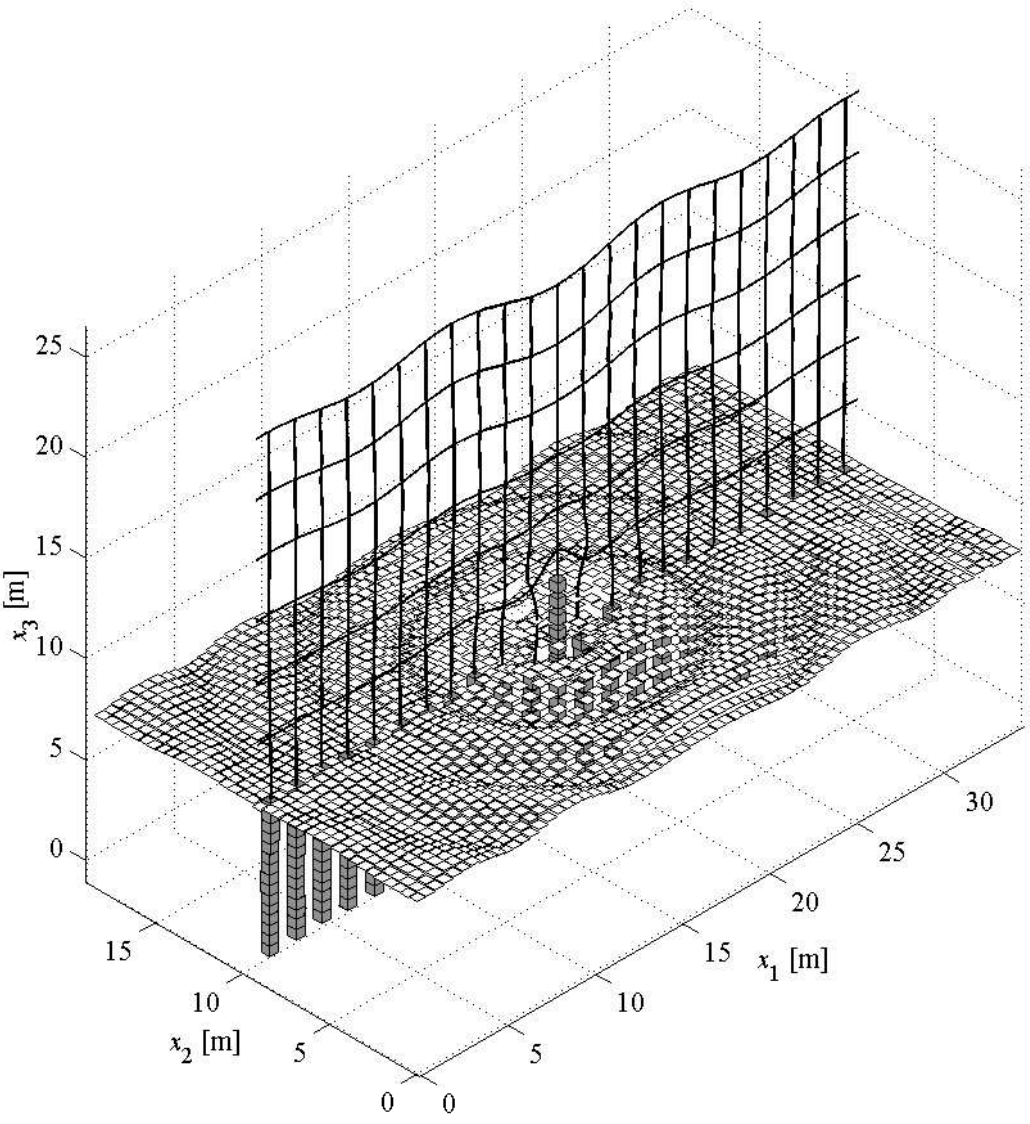

Figure 5.4: Vibration of an unisolated hospital as predicted by the generic base-isolated building model. The 50 Hz excitation corresponds to a vertical unit-amplitude force applied to the central pile-head prior to the construction of the building. All displacements are magnified by 1×10^{10}; a side elevation is shown in Figure 5.5.

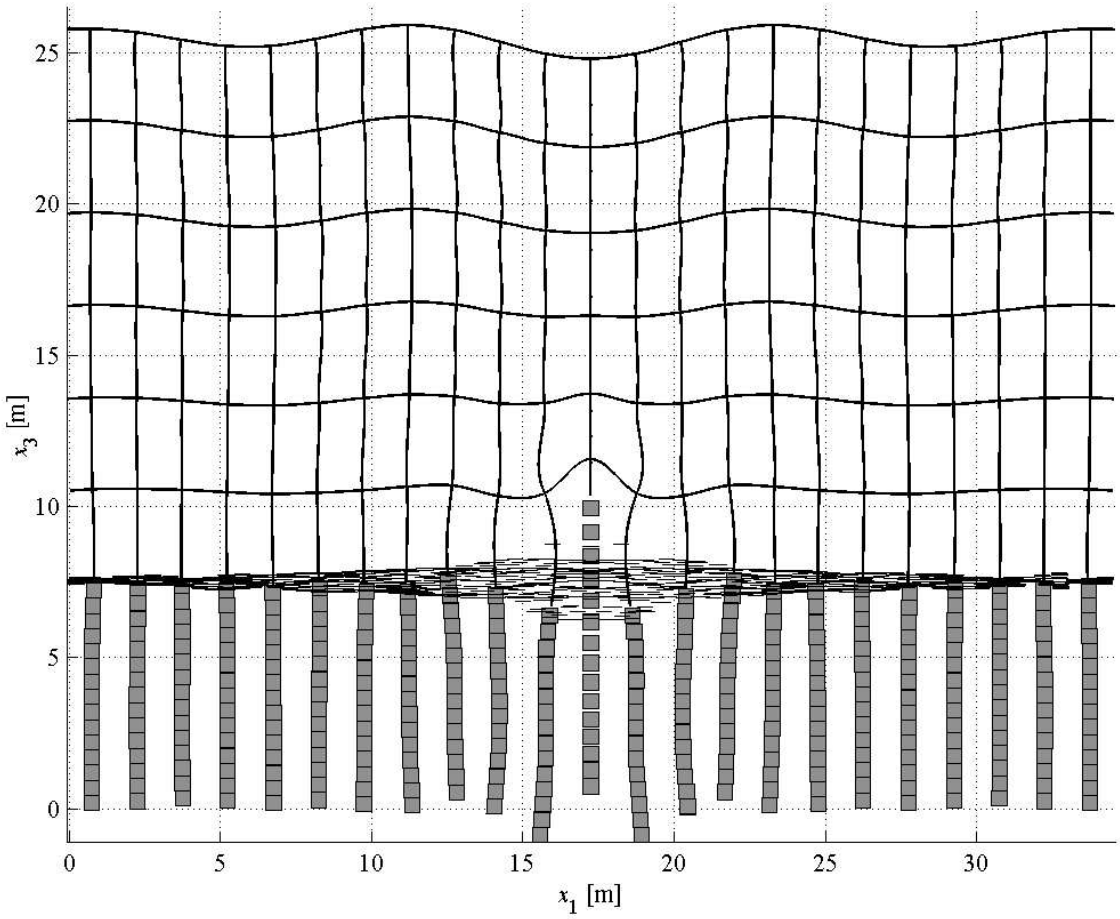

Figure 5.5: Side elevation of Figure 5.4 showing the vibration of an unisolated hospital as predicted by the generic base-isolated building model. The 50 Hz excitation corresponds to a vertical unit-amplitude force applied to the central pile-head prior to the construction of the building. All displacements are magnified by 1×10^{10}.

Figures 5.6 and 5.7 illustrate the equivalent results when the building is base-isolated with an isolation frequency of 5 Hz; the damping loss factor of the bearings is 0.01. The same displacement magnification factor is used in Figures 5.5 and 5.7 (a), and it is clear that the isolation significantly reduces the vibration amplitudes of the building. This is achieved by the isolation bearings allowing relative motion between the pile heads and the bases of the building columns. The latter is clear in Figure 5.7 (b) where the displacement magnification factor is an order of magnitude greater than in the other figures: the bending of the ground-floor columns either side of the applied load is as though they were freely vibrating cantilevers.

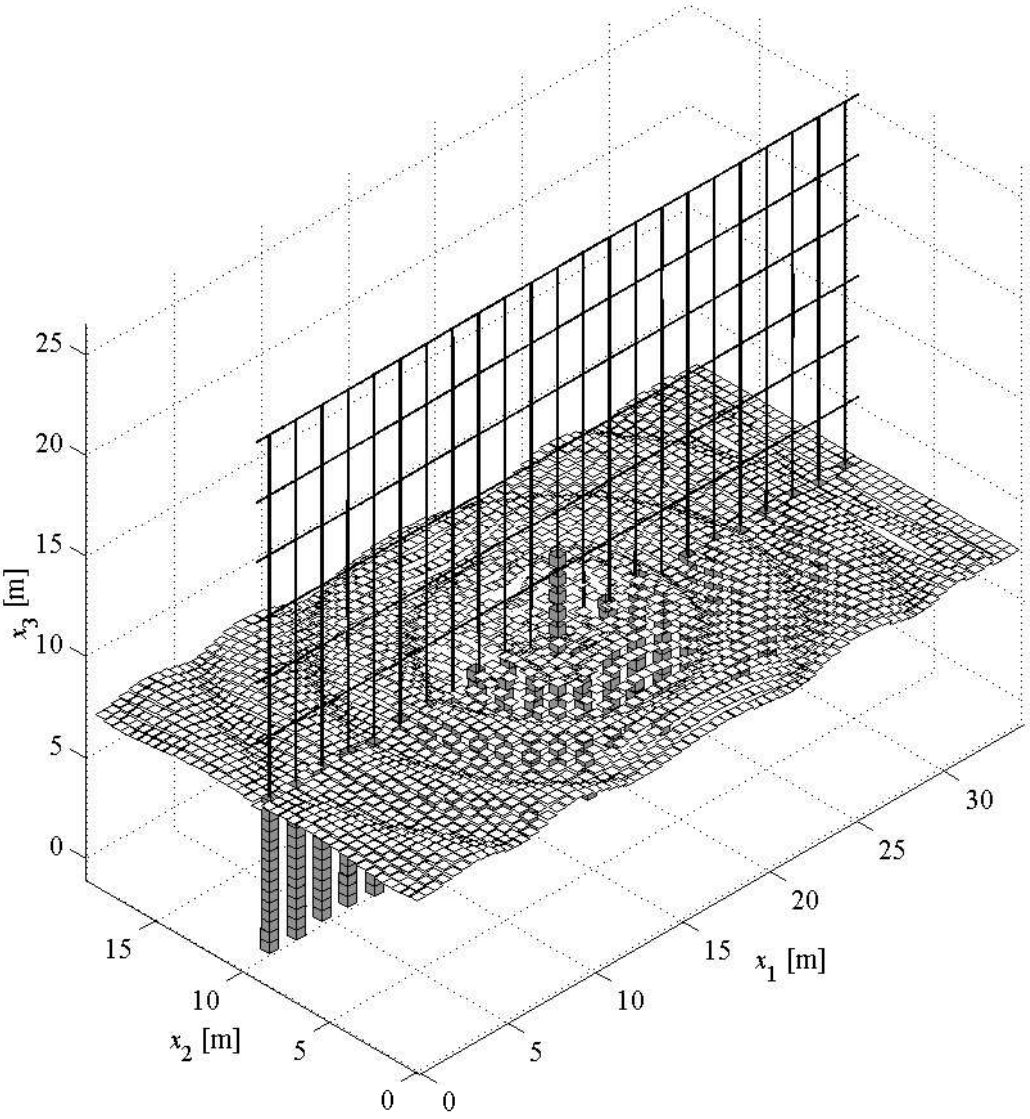

Figure 5.6: Vibration of a '5 Hz' base-isolated hospital as predicted by the generic base-isolated building model. The 50 Hz excitation corresponds to a vertical unit-amplitude force applied to the central pile-head prior to the construction of the building. All displacements are magnified by 1×10^{10}; a side elevation is shown in Figure 5.7.

(a)

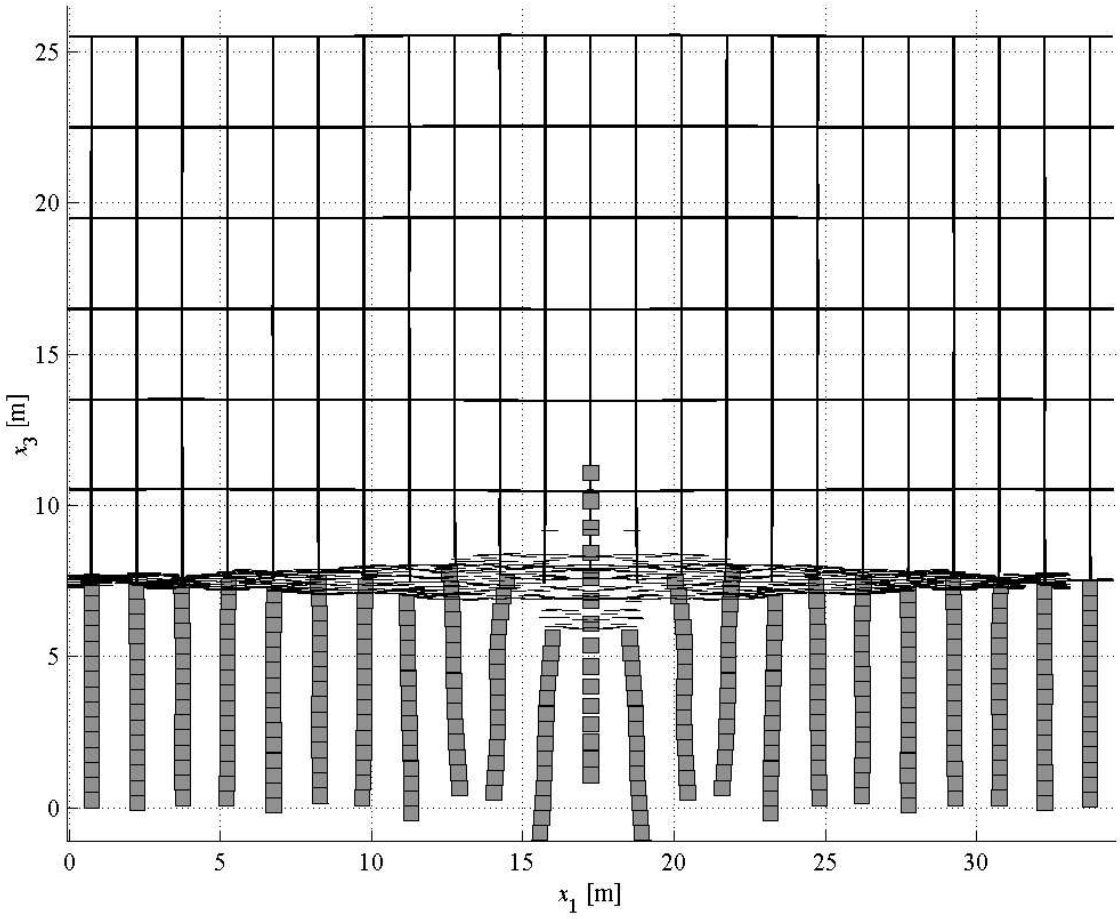

(b)

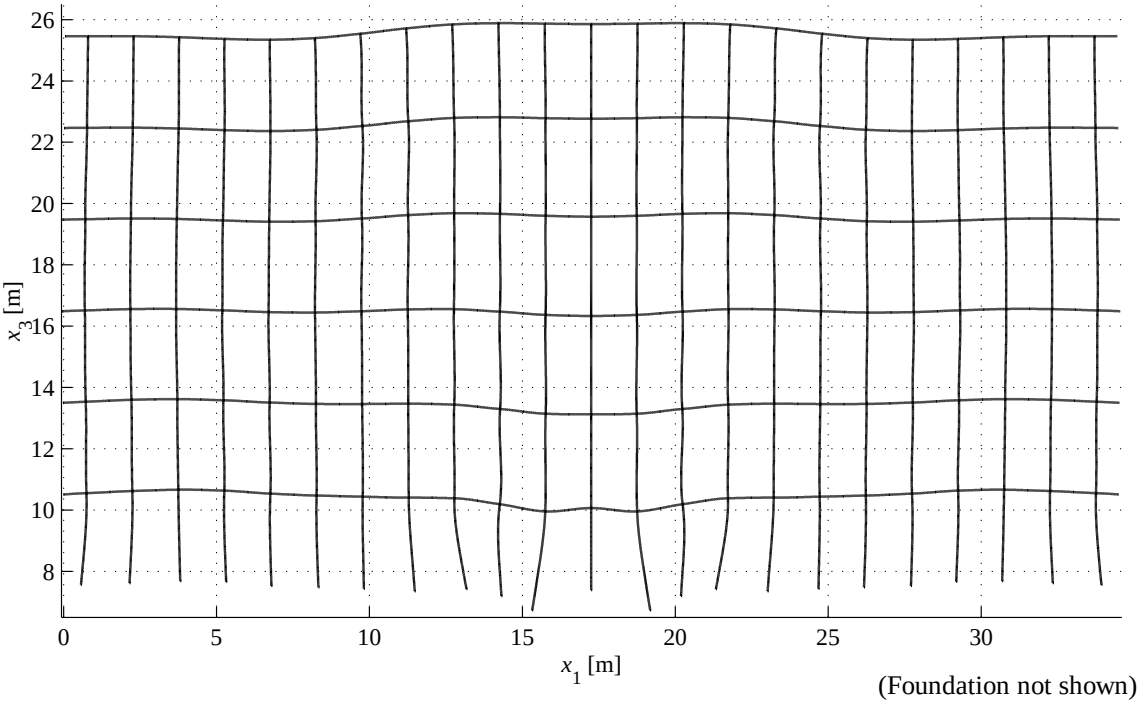

(Foundation not shown)

Figure 5.7: Side elevation of Figure 5.6 showing the vibration of a '5 Hz' base-isolated hospital as predicted by the generic base-isolated building model. The 50 Hz excitation corresponds to a vertical unit-amplitude force applied to the central pile-head prior to the construction of the building. The displacements are magnified by (a) 1×10^{10} and (b) 1×10^{11}.

These initial observations indicate qualitatively that base-isolation would be beneficial for the hospital, at least at 50 Hz. A quantitative measure of this, for different isolation bearings and over a range of frequencies, is considered in Section 5.3.3.

5.3.2. The Added-Mass Effect

In Section 3.2.2 it was demonstrated, using simple models, how the construction of a building acts to constrain its foundation and reduce the original foundation vibration levels. It was also demonstrated how the level of this added-mass effect depended on whether or not the building is base-isolated, the effect being less significant with a base-isolated building due to the decoupling of the building from its foundation. It is important to investigate this effect with the more comprehensive generic model.

To quantify the effect, comparisons are made of the vertical pile-head displacement amplitudes before and after the construction of the hospital building. Figure 5.8 summarises the results in the event that the building is left unisolated. In this case the added-mass effect leads to a reduction in the pile-head amplitude of the loaded pile of approximately 4 dB, which is approximately constant over the frequency range considered. Piles 'downstream' of the loaded pile, in general, experience an amplification of vibration levels, which is greatest at low frequencies, and the level of amplification increases the further downstream the pile. This is due to the building transmitting vibration to the pile heads in addition to that propagating through the soil, the lower frequencies being more efficiently transmitted along the building. The effect is more noticeable with the more distant piles due to their lower pre-construction vibration levels. The troughs in the curves are believed to occur when the vibration transmitted via the building arrives out-of-phase with that transmitted via the ground.

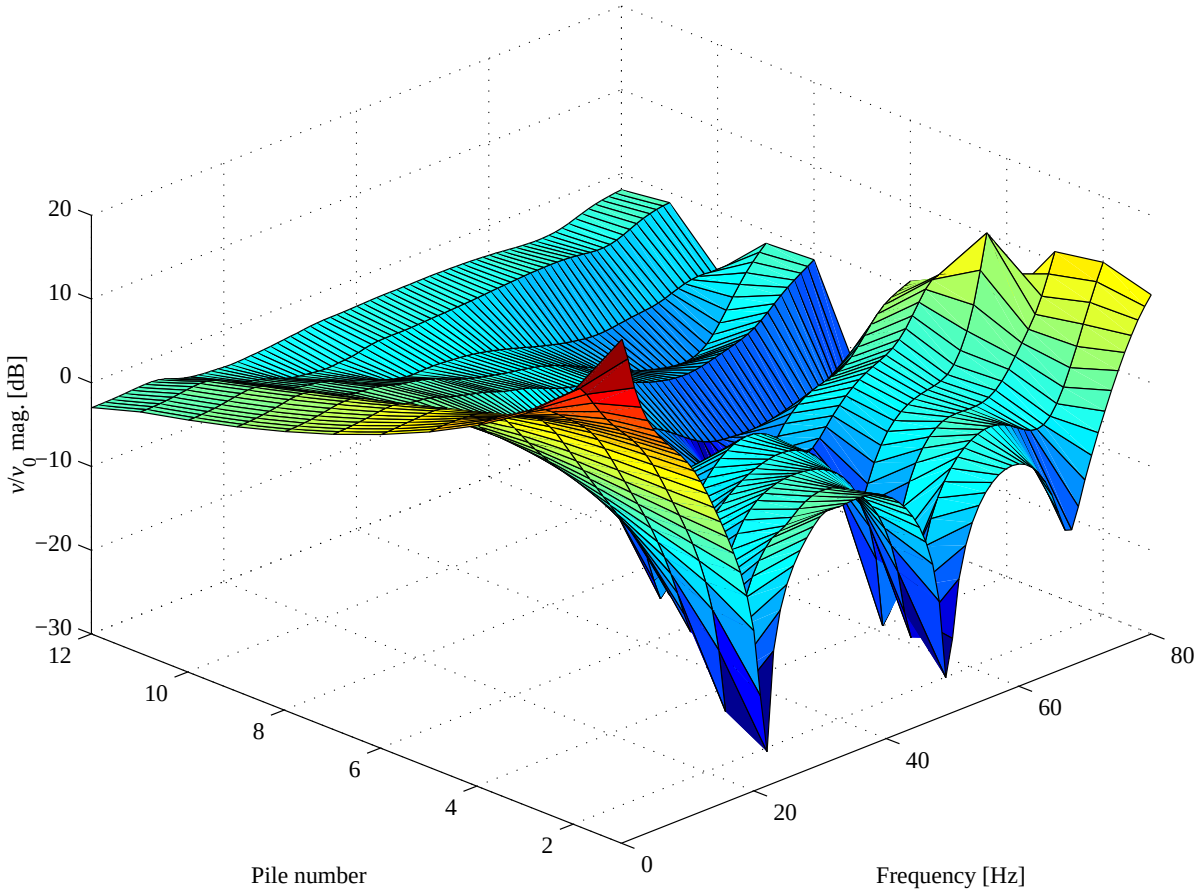

Figure 5.8: Soil-structure interaction of an unisolated hospital, as predicted by the generic base-isolated building model. The ratio of the final vertical pile-head displacement amplitudes v to those prior to the construction of the building v_0 is plotted against frequency for the central loaded pile (no.12) and those at increasing distances from it (nos.11-1). Only one half of the foundation is considered due to the symmetry of the response.

Figure 5.9 summarises the results for the case of a 5 Hz isolation frequency; the damping loss factor of the bearings is 0.01. The change in vibration levels is now negligible except for a small amount of amplification of the downstream pile amplitudes at low frequencies. Note that neither the isolated nor the unisolated results show the peaks and troughs due to 'foundation' and 'ground' resonances, as discussed in Section 3.2.2. This is due to the nature of the infinite model.

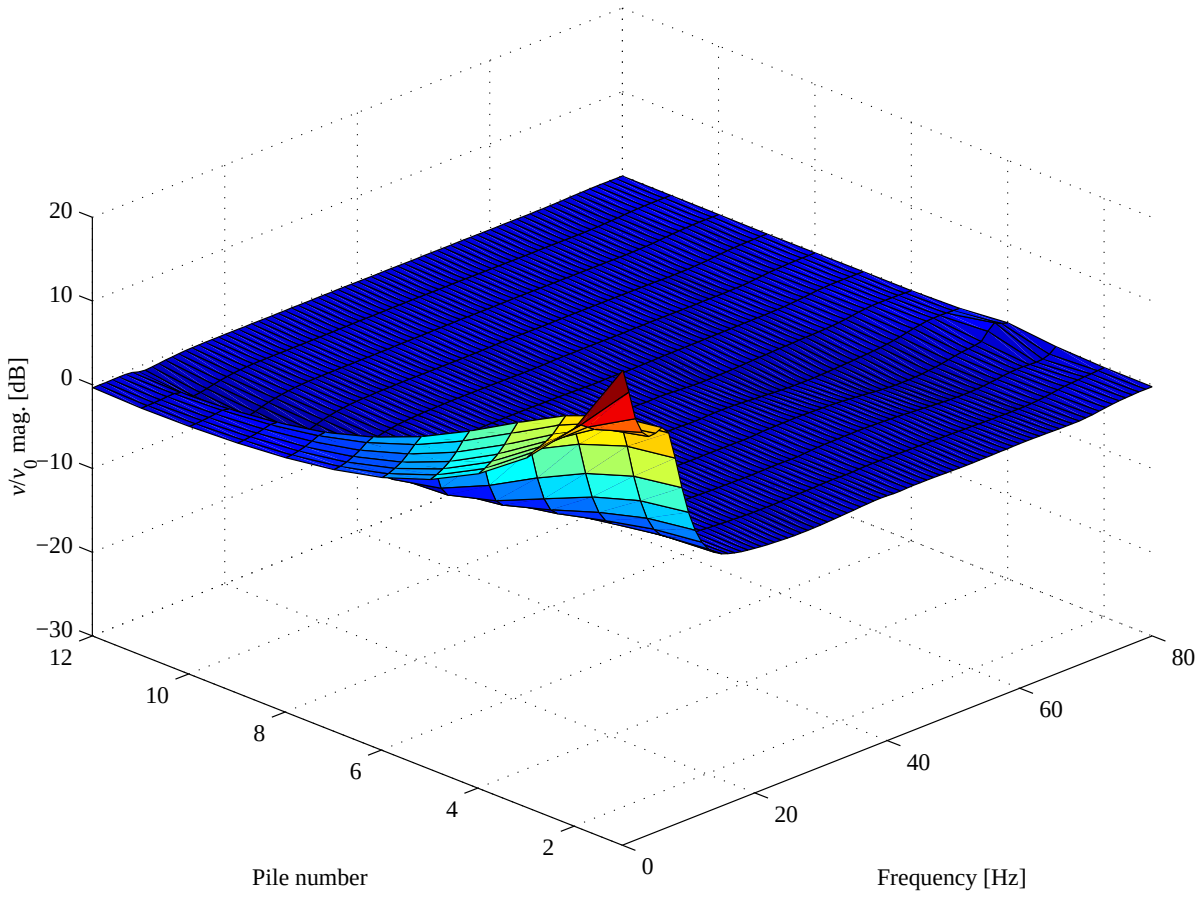

Figure 5.9: Soil-structure interaction of a '5 Hz' base-isolated hospital, as predicted by the generic base-isolated building model. The ratio of the final vertical pile-head displacement amplitudes v to those prior to the construction of the building v_0 is plotted against frequency for the central loaded pile (no.12) and those at increasing distances from it (nos.11-1). Only one half of the foundation is considered due to the symmetry of the response.

These results confirm the general conclusions drawn in Section 3.2.2 that constructing a building modifies the original, foundation vibration field and that the effect is less significant when the building is decoupled from the foundation by the use of base isolation. However, whether or not this leads to a reduction in foundation vibration levels depends on the nature of the excitation. When subject to localised excitation, as investigated here, the additional vibration transmission path through the building leads, in general, to an increase in foundation vibration at points remote from the excitation. In the case of distributed excitation, where pre-construction vibration levels are comparable across the whole foundation, the added-mass effect is expected to lead to a general reduction in foundation vibration levels.

It is clear that the consultant concerned with the hospital needs a comprehensive model to make predictions of base-isolation performance. It is not possible to make these predictions by simply taking measurements of foundation vibration and using them as the inputs to a building model: the building and foundation act as one system and must be modelled as such.

It should be noted that this case study has avoided the need to consider the effect of a *foundation* on a pre-existing ground vibration field. In practice, this is a common problem and is the subject of further work; see Section 7.2.

5.3.3. Predictions of Insertion Performance

The most important question for any base-isolated building project is what level of insertion performance should be expected. The consultant's predictions have significant implications for the hospital project, from the specification of the isolation frequency to a potential redesign of major parts of the building structure. In Section 3.3.3 power flow insertion gain (PFIG) was introduced as a more useful measure of insertion performance than those currently used, which are based on vibration amplitudes. Predictions of PFIG from the generic model are discussed here.

Figure 5.10 shows the variation with frequency in the PFIG when the hospital is base-isolated on bearings giving isolation frequencies of 5, 10 and 15 Hz, with internal damping loss factors of 0.1 and 0.01. This range of parameters is typically found in practice: a 15 Hz isolation with a loss factor of 0.1 is representative of high-hysteresis rubber bearings while a 5 Hz isolation with a loss factor of 0.01 is representative of undamped steel springs.

The first thing to note about Figure 5.10 is the smoothness of the curves; the series of resonant peaks predicted by the initial model of Section 3.3, as in Figure 3.14, are no longer evident. This is due to the infinite nature of the model, which radiates energy away from the excitation and prevents resonances from being established. This behaviour was originally noted by Cryer [33] when developing the infinite building model and was found to be more representative of real buildings, which do not exhibit the strong resonant behaviour of finite models.

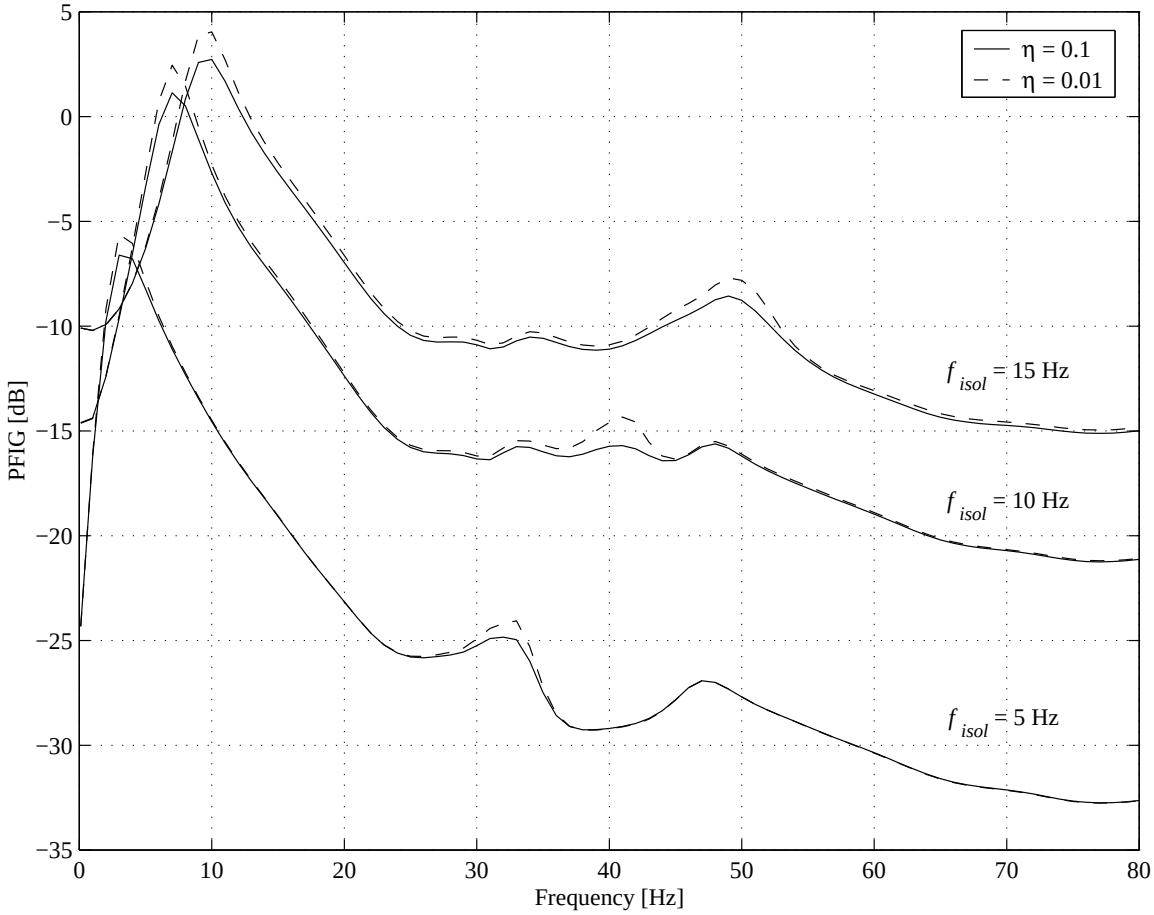

Figure 5.10: Variation with frequency in the power flow insertion gain of a base-isolated hospital, as predicted by the generic base-isolated building model. Isolation frequencies of 5, 10 and 15 Hz are considered, provided by bearings with internal damping loss factors of 0.1 and 0.01. The excitation corresponds to a vertical unit-amplitude force applied to the central pile-head prior to the construction of the building.

The peaks that are evident in Figure 5.10 are due to peaks in the total mean vibrational power flow into the isolated building; see Figure 5.11. The first of these occurs near the isolation frequency and corresponds, in essence, to the global ‘bounce’ mode of the building on the isolation bearings, although the response is localised around the excitation; see for example Figure 5.12. The smaller peaks – in the region of 30, 40 and 50 Hz – appear to occur at frequencies when vibration can propagate freely along the structure in the region of the building-foundation interface; see for example Figures 5.13 and 5.14.

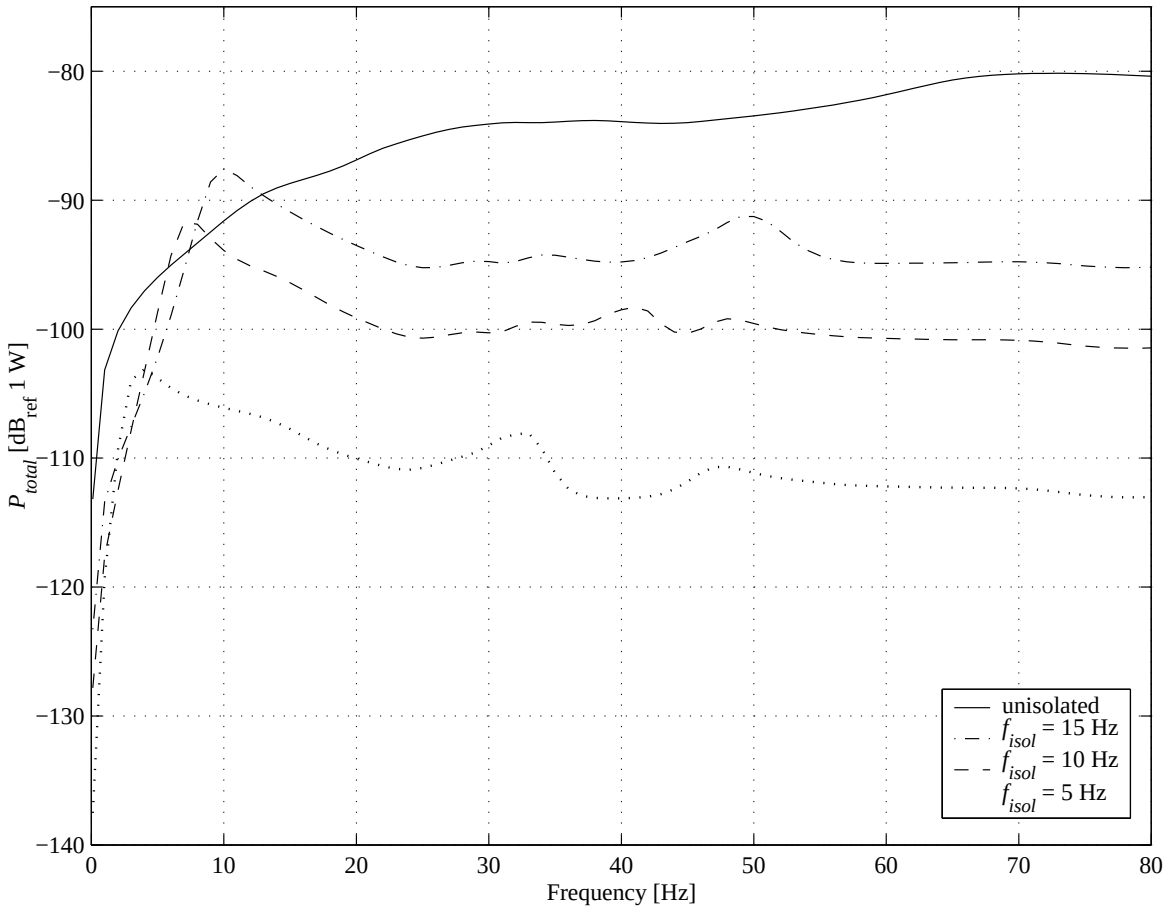

Figure 5.11: Variation with frequency in the total mean power flow $\overline{P}_{total}$ into a base-isolated hospital, as predicted by the generic base-isolated building model. Isolation frequencies of 5, 10 and 15 Hz are considered, provided by bearings with an internal damping loss factor of 0.01. The excitation corresponds to a vertical unit-amplitude force applied to the central pile-head prior to the construction of the building.

Of interest to the consultant is the fact that the choice of isolation frequency makes a large difference to the efficiency of the isolation. The differences are not as great as predicted by the initial model – approximately 15 dB, rather than 20 dB, between a 5 and 15 Hz isolation – but they are nevertheless significant and would certainly influence a design decision. It must be stressed that the predictions are expected to depend on the nature of the excitation and that a different conclusion may be drawn for less localised excitation.

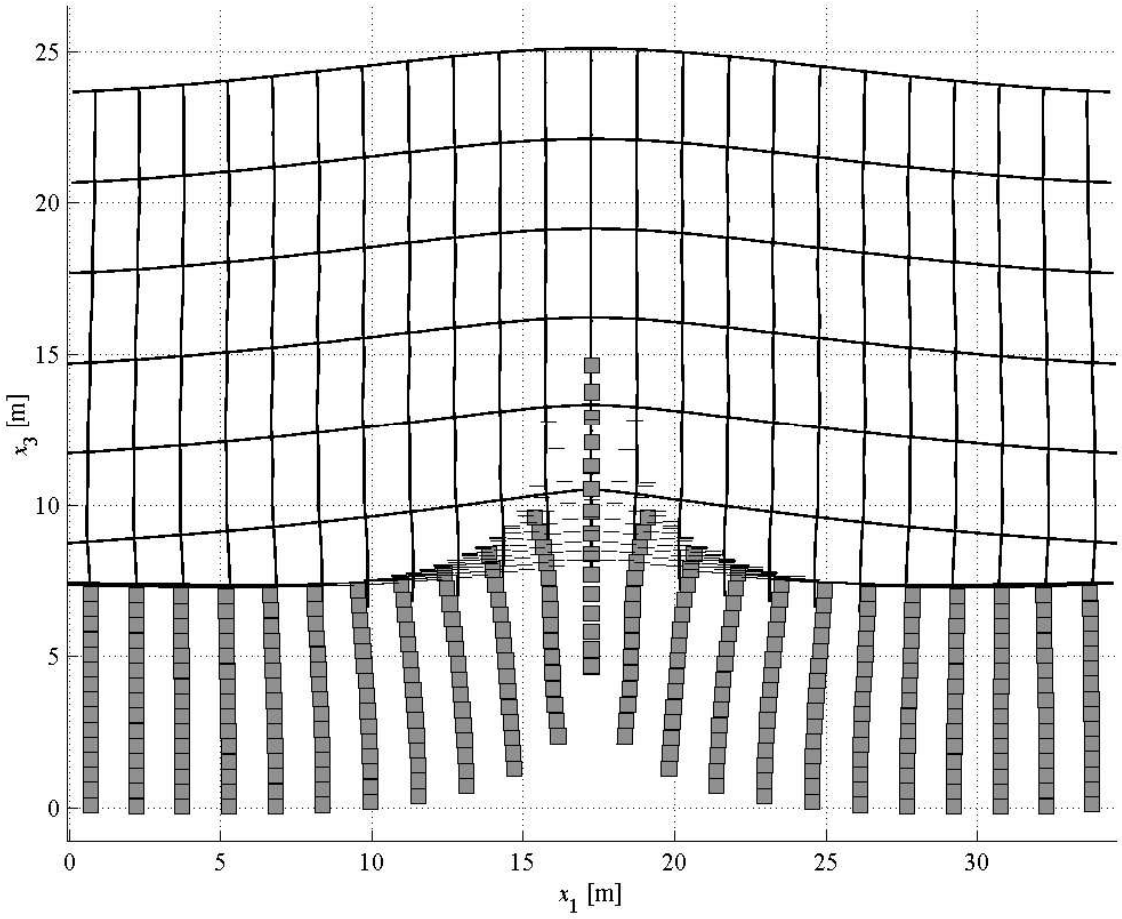

Figure 5.12: Side elevation showing the vibration of a '10 Hz' base-isolated hospital, as predicted by the generic base-isolated building model. A vertical unit-amplitude force is applied to the central pile-head prior to the construction of the building at a frequency of 7 Hz. This corresponds to a peak in the PFIG curve of Figure 5.10. All displacements are magnified by 1×10^{10}.

In general, the level of internal damping in the bearings has a negligible effect on the PFIG. However, it does have an effect at frequencies when relative motion between the pile heads and the bases of the building columns is significant, that is, when the isolation bearings undergo significant deformation. This is evident in Figures 5.12 to 5.14. The relative vertical motion at 7 Hz (Figure 5.12) and that in the horizontal direction at 41 Hz (Figure 5.14) is large: increasing the internal damping therefore increases the power dissipation in the bearings and reduces the total power flow into the building. When the bearing deformation is small, such as at 34 Hz (Figure 5.13) the internal damping has little effect on the efficiency of the isolation.

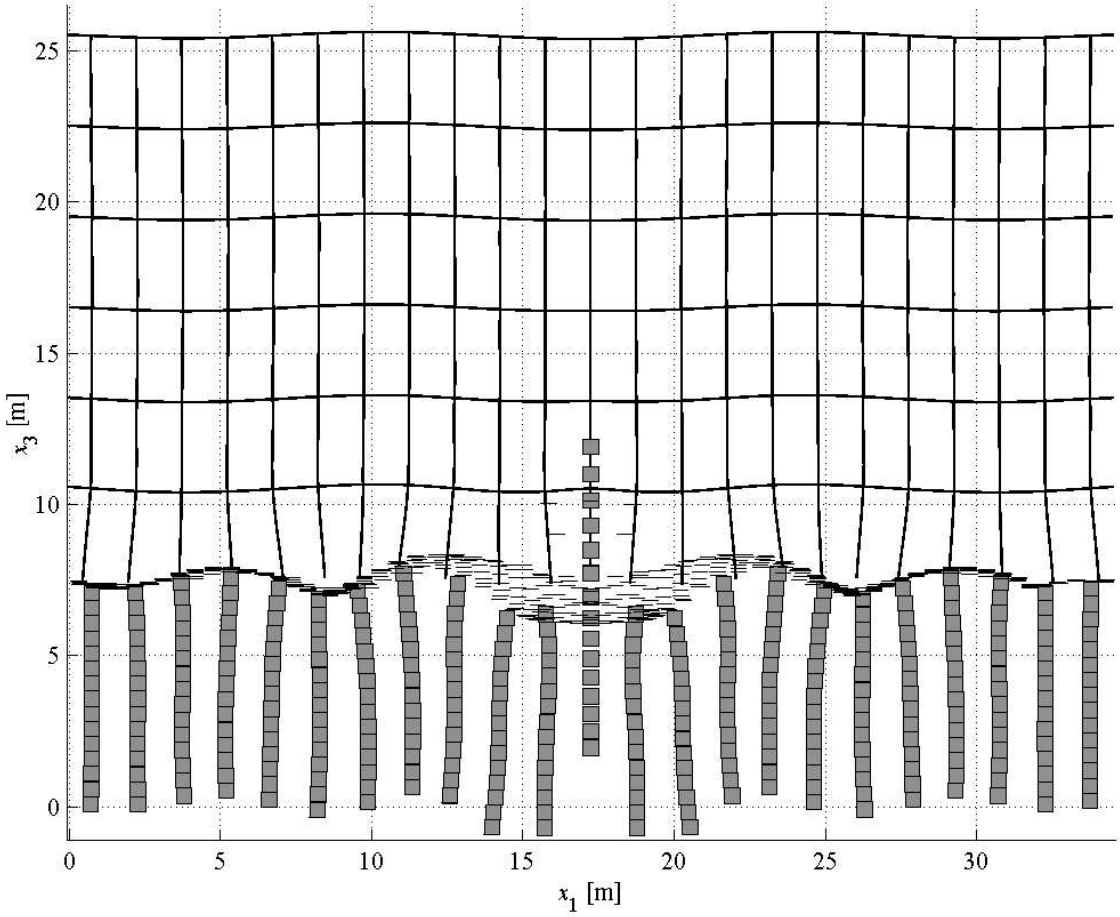

Figure 5.13: Side elevation showing the vibration of a '10 Hz' base-isolated hospital, as predicted by the generic base-isolated building model. A vertical unit-amplitude force is applied to the central pile-head prior to the construction of the building at a frequency of 34 Hz. This corresponds to a peak in the PFIG curve of Figure 5.10. All displacements are magnified by 1×10^{10}.

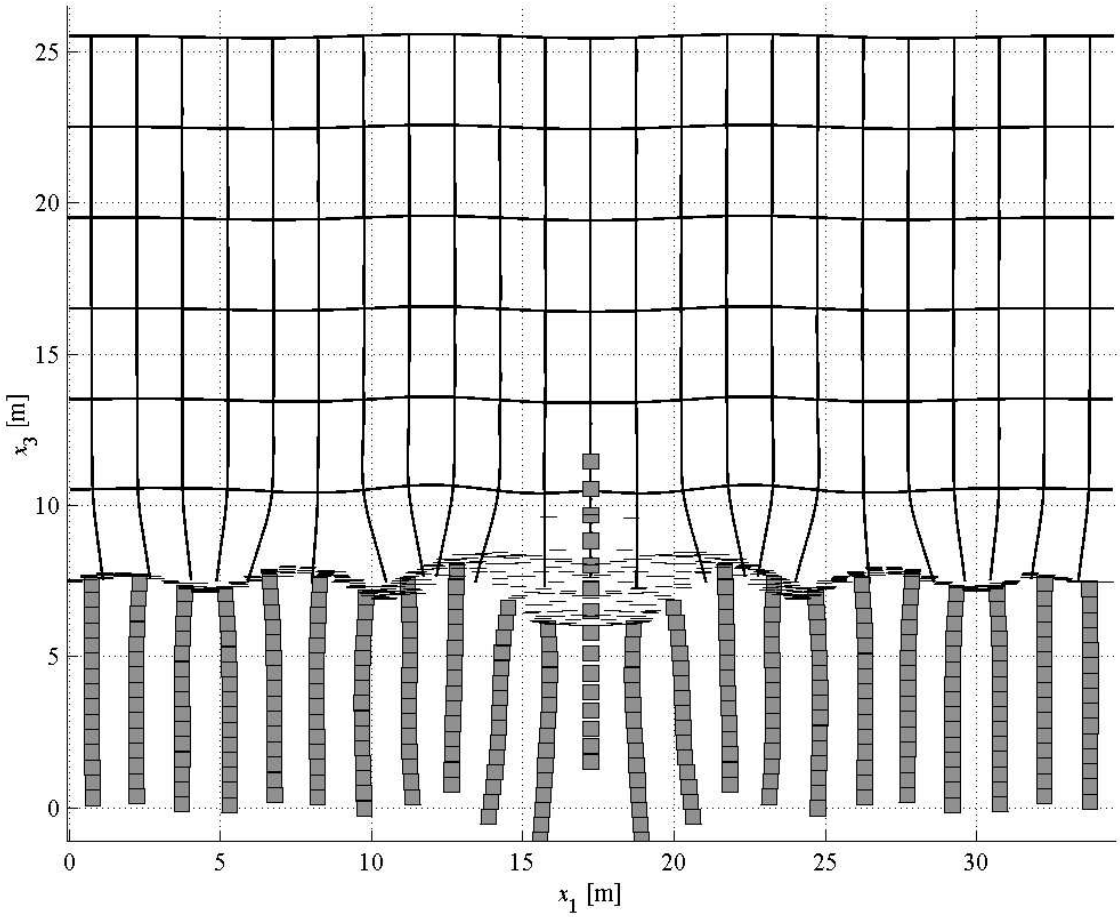

Figure 5.14: Side elevation showing the vibration of a '10 Hz' base-isolated hospital, as predicted by the generic base-isolated building model. A vertical unit-amplitude force is applied to the central pile-head prior to the construction of the building at a frequency of 41 Hz. This corresponds to a peak in the PFIG curve of Figure 5.10. All displacements are magnified by 1×10^{10}.

Before leaving the discussion on power flow it is worth noting again the significance of horizontal motion. Figure 5.15 shows the variation with frequency in the three components of the mean power flow entering the hospital as percentages of the total flow. It is clear that horizontal motion can contribute a significant proportion of the total power flow and this should not be ignored.

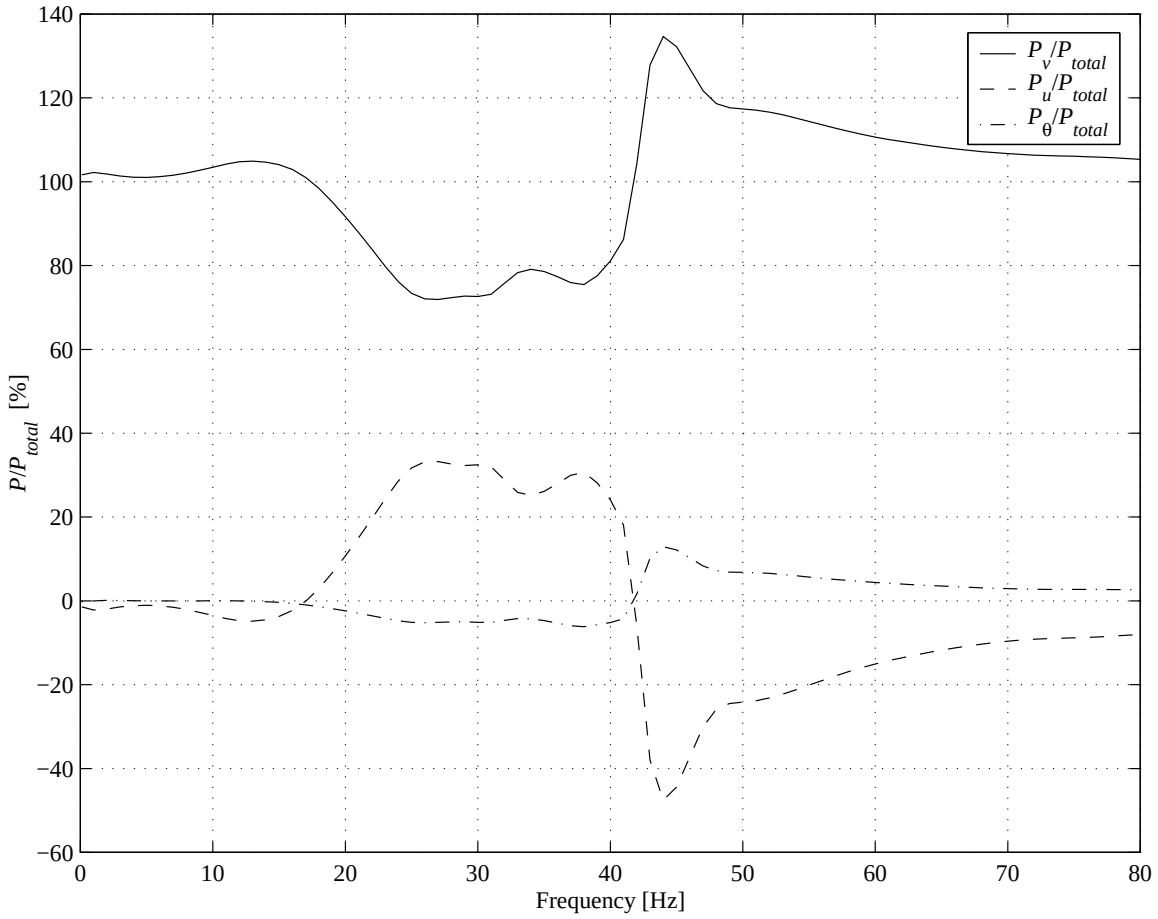

Figure 5.15: Variation with frequency in the vertical $\overline{P}_v$, horizontal $\overline{P}_u$ and rotational $\overline{P}_\theta$ components of the mean power flow entering a '10 Hz' base-isolated hospital, as predicted by the generic base-isolated building model. The excitation corresponds to a vertical unit-amplitude force applied to the central pile-head prior to the construction of the building. The results are presented as percentages of the total mean power flow $\overline{P}_{total}$.

5.3.4. The Importance of Pile-Soil-Pile Interaction

Chapter 4 was concerned entirely with the development of a new piled-foundation model, which, most significantly, fully accounts for the effects of PSPI. It is now important to establish whether or not the extra effort this involves is necessary. This is investigated here by comparing results from the generic base-isolated building model with those from a model that disregards PSPI. The latter is identical to the generic model in all respects except that the foundation is based on the single-pile model of Section 4.1. The foundation FRF matrix $\mathbf{H_f}$ is therefore a banded matrix, since $\mathbf{H}_\mathbf{f}^{ij} = 0$, and includes only the pile-head driving-point FRFs of the single-pile.

Figure 5.16 illustrates qualitatively the effect of PSPI on the response of the hospital in the unisolated state.

(a)

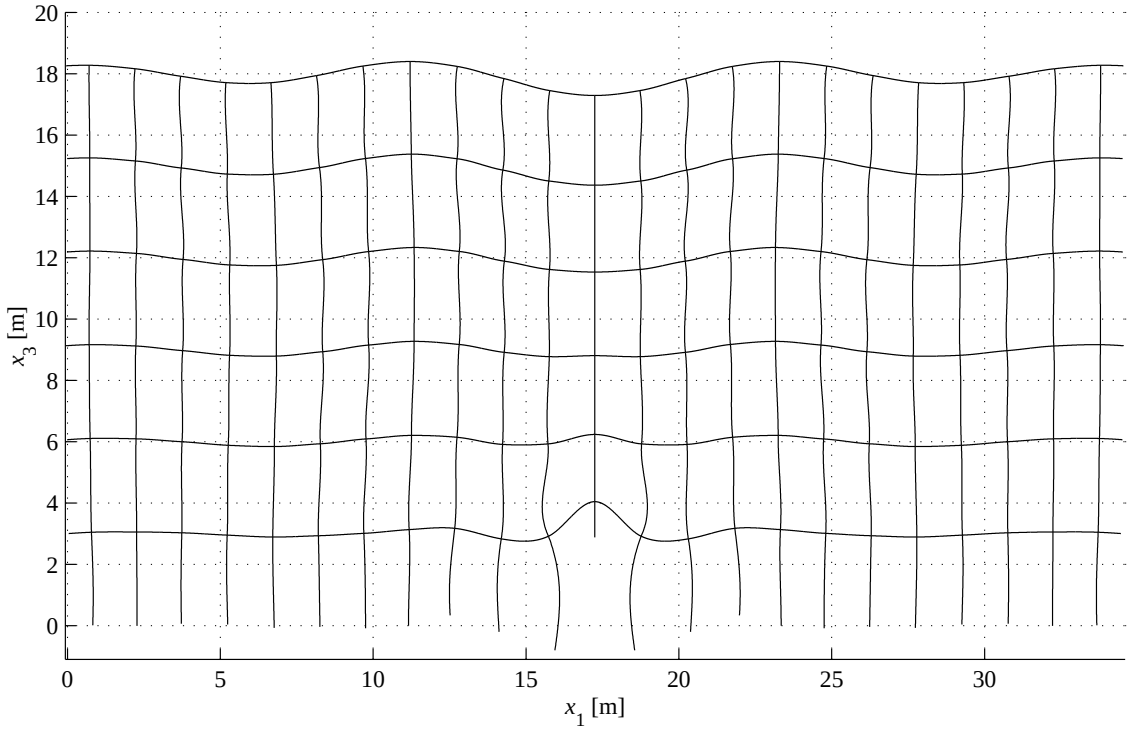

(b)

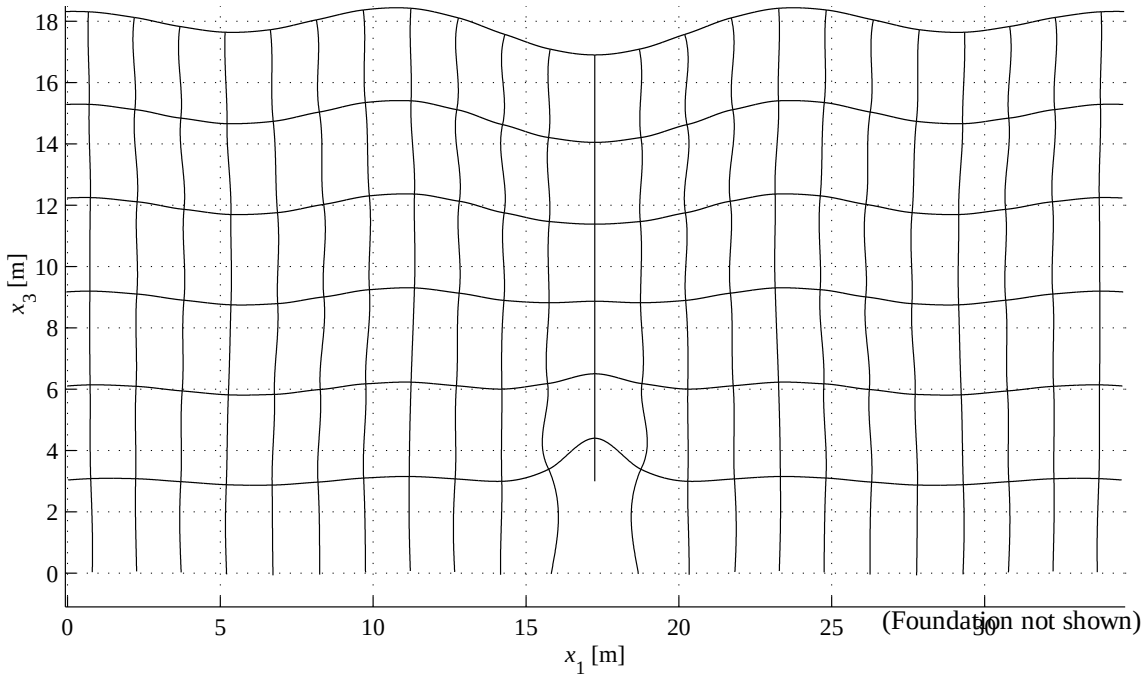

Figure 5.16: Side elevation showing the vibration of an unisolated hospital, as predicted by (a) the generic base-isolated building model and (b) a model that disregards PSPI. The 50 Hz excitation corresponds to a vertical unit-amplitude force applied to the central pile-head prior to the construction of the building. All displacements are magnified by 1×10^{10}.

In this example, neglecting the interaction between piles significantly reduces the response of the columns either side of the loaded pile. Disregarding PSPI ignores half of the vibration transmission path from the loaded pile and vibration of neighbouring piles is due solely to vibration transmission through the building.

The effect of this on the predictions of insertion performance are shown in Figures 5.17 and 5.18.

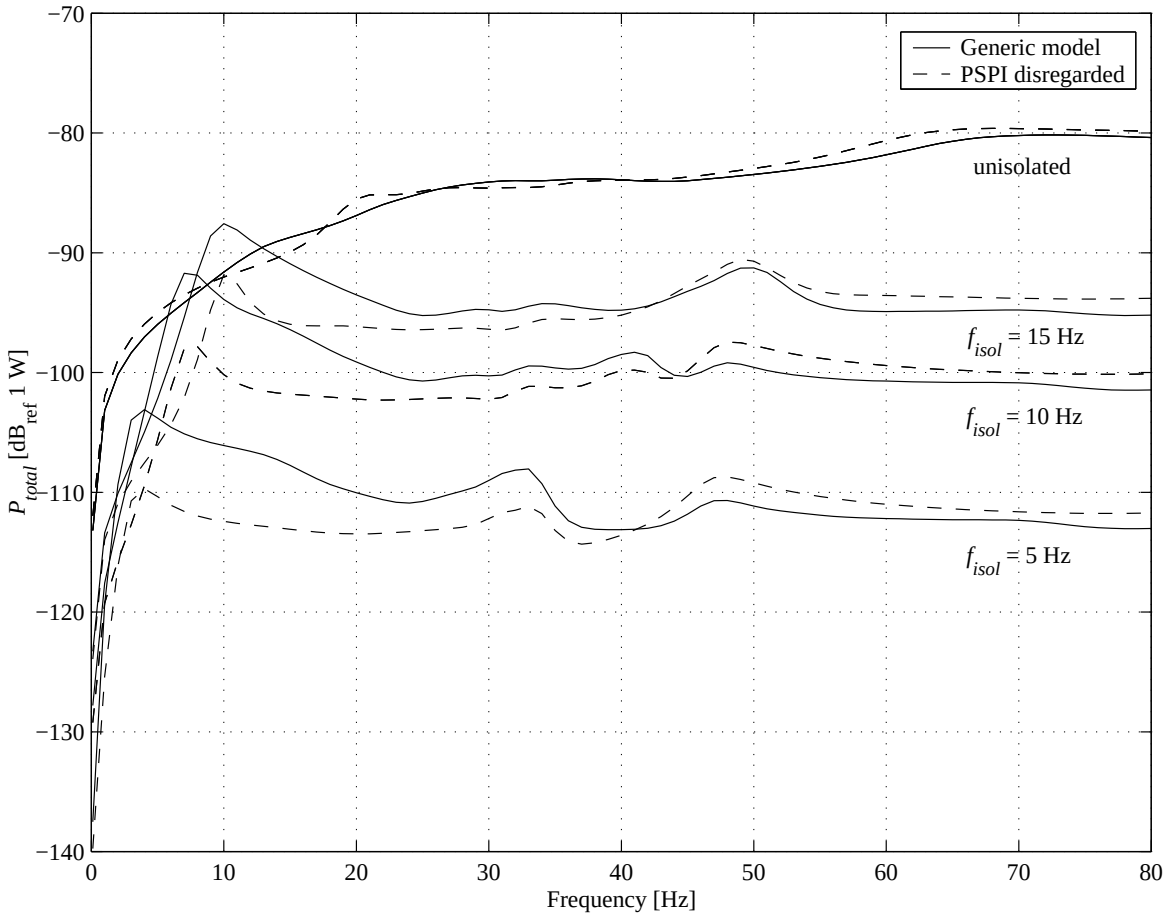

Figure 5.17: Variation with frequency in the total mean power flow $\overline{P}_{total}$ into a base-isolated hospital, as predicted by the generic base-isolated building model and a model that disregards PSPI. Isolation frequencies of 5, 10 and 15 Hz are considered, provided by bearings with an internal damping loss factor of 0.01. The excitation corresponds to a vertical unit-amplitude force applied to the central pile-head prior to the construction of the building.

Figure 5.17 shows how PSPI leads primarily to a change in the total power flow into the isolated building. At frequencies below approximately 40 Hz, PSPI leads to an increase in power flow; at higher frequencies there is a small decrease. This may be due to the more effective propagation of

vibration through the foundation, and subsequently into the building, at lower frequencies; at higher frequencies, as the wavelengths approach the diameter of the piles, there is an increased tendency of wave scattering and propagation along the foundation is more difficult.

Figure 5.18 shows how these changes are reflected in the predictions of PFIG. The increase in power flow into the isolated building results in values of PFIG below 40 Hz that are approximately 4 dB greater, although this can be as much as 7 dB. Neglecting PSPI therefore leads to an over-prediction of the isolation efficiency, and by an amount that is significant for the consultant working to meet a noise or vibration standard. It is again worth noting that these results are for the particular case of point excitation and a different conclusion may be drawn for other ground vibration fields.

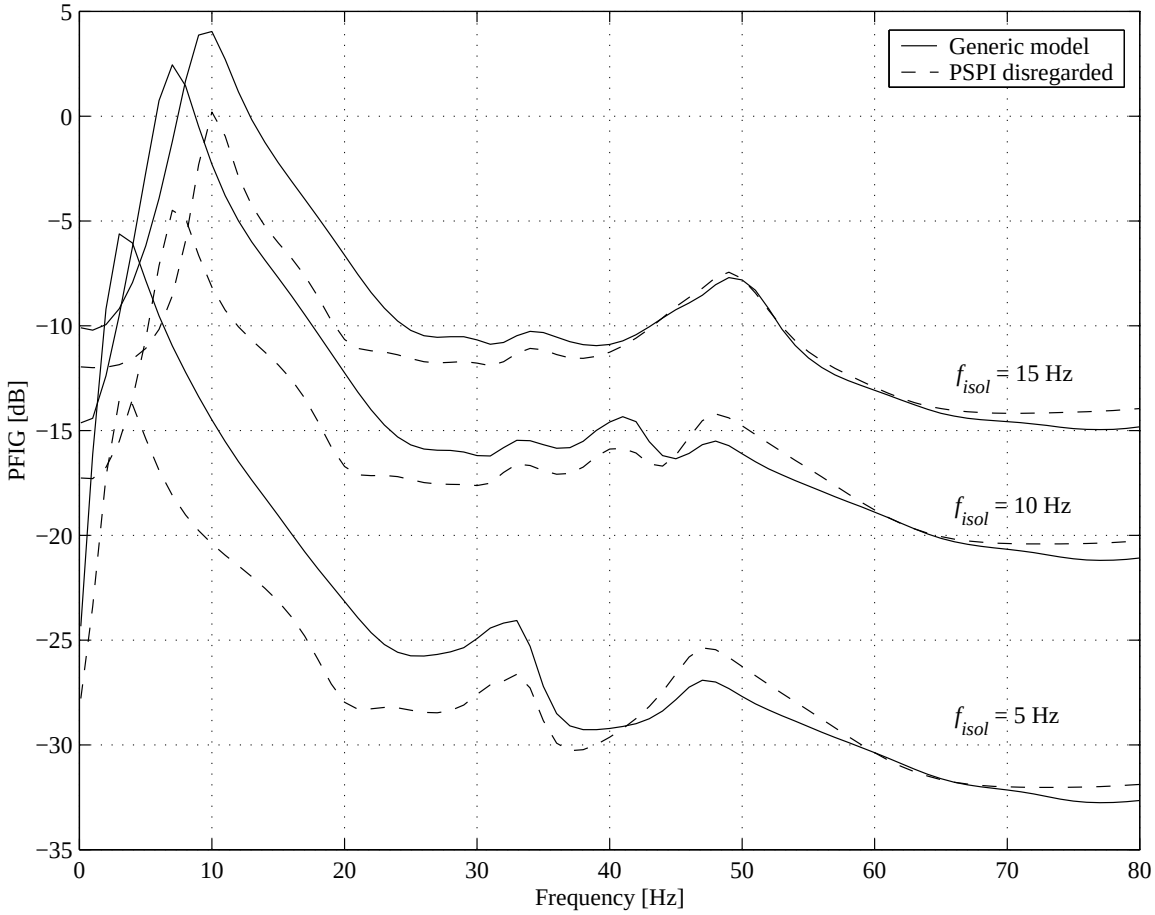

Figure 5.18: Variation with frequency in the power flow insertion gain of a base-isolated hospital, as predicted by the generic base-isolated building model and a model that disregards PSPI. Isolation frequencies of 5, 10 and 15 Hz are considered, provided by bearings with an internal damping loss factor of 0.01. The excitation corresponds to a vertical unit-amplitude force applied to the central pile-head prior to the construction of the building.

5.4. Conclusions

Building on the work of Chapters 3 and 4, this chapter has described the assembly of a generic base-isolated building model, comprising an infinitely long two-dimensional model of a building coupled to an infinitely long three-dimensional model of a piled foundation. By considering the specific case of a ground vibration field due to a point-load excitation of the foundation, three aspects of base-isolated building behaviour have been investigated. The main conclusions of these are summarised below.

1. The building and foundation act as one system: changes to the building affect the foundation and vice versa. This means that it is impossible to make good predictions of building behaviour by modelling the building alone.

2. Constructing a building on a foundation modifies any pre-existing vibration field due to the constraining effect of the added mass together with the vibration transmission within the building. The former leads to a reduction in foundation vibration, while the latter can lead to an increase if the excitation is localised and the building is able to transmit vibration to remote parts of the foundation that originally experienced little vibration. In either case, the effect is less significant when the building is base-isolated.

3. The choice of isolation frequency can make up to a 15 dB difference to the efficiency of the isolation for typical bearing designs. This is significant for the design of a particular building but the difference may depend on the nature of the excitation, in particular, whether or not the ground vibration field is small compared to the size of the building.

4. In general, the level of internal damping in the isolation bearings has a negligible effect on the PFIG. However, it does increase internal power dissipation at frequencies when the isolation bearings undergo significant deformation. It is therefore important for controlling local resonant behaviour of the base of the building structure, which would otherwise lead to an increase in the vibrational power entering the building.

5. The comprehensive modelling of a piled foundation is important. Horizontal, and to a lesser extent, rotational motion of the pile heads can contribute significant proportions of the total vibrational power flow entering a building. Interaction between piles through wave propagation in the surrounding soil should be included as an important vibration transmission path. Neglecting this pile-soil-pile interaction can result in an under-prediction of the power flow entering an isolated building and consequently an over-prediction, of up to 7 dB, of the isolation efficiency. Again this may depend on the nature of the excitation.

These conclusions are based on a specific ground vibration field and it is not yet possible to say whether they are applicable to base-isolation in general. The frequency range considered extends up to 80 Hz, which includes the range in which ground-borne vibration levels typically peak but excludes the upper frequencies of interest. Furthermore, as noted in Section 4.3, the accuracy of the foundation model with the current boundary-element mesh is expected to decrease with frequency above 50 Hz. These represent the primary limitations of the results presented in this chapter and are the subject of further work, as discussed in Chapter 7.

This dissertation has discussed in detail the advantages of a theoretical power-based approach to predicting base-isolation performance. In the next chapter the practical feasibility of these ideas is considered by exploring the possibility of a force-sensitive vibration isolation bearing.

Chapter 6

INITIAL DEVELOPMENT OF A FORCE-SENSITIVE VIBRATION ISOLATION BEARING

The theoretical analysis of vibrational power flow discussed in the previous chapters raises the question of whether or not the measurement of isolation performance in terms of power flow is feasible in practice for a particular base-isolated building. This chapter attempts to address this question in part by exploring the possibility of a force-sensitive vibration isolation bearing. The concept of such a device is described, together with the design and testing of an initial prototype. Test results are presented and recommendations are made for the future development of a practical force-sensitive bearing for base-isolated buildings.

6.1. The Concept of a Force-Sensitive Isolation Bearing

In Section 3.3.3, power flow insertion gain (PFIG) was introduced as a more useful measure of base-isolation performance than the commonly quoted insertion gain based on vibration amplitudes. PFIG deals with the mean vibrational power flow through the isolation bearings and is based on the principle that it is the mean vibrational power entering a building which drives all internal structural vibration and re-radiated noise. It was also noted that analysis of the power flow distribution within a building can provide valuable insight into the various vibration transmission paths.

In practice, to measure vibrational power flow at a particular point in a structure, both the velocity of the point in question, be it linear or angular, and the associated force or moment acting in the structure at that point must be measured. Measurement of velocity can generally be

achieved with the use of standard accelerometers, or similar devices. Measurement of force is more difficult. The problem lies with the fact that introducing a force-sensitive device, such as a standard load-cell, to a structure, in general, alters the dynamic behaviour under investigation. What is required is a *non-invasive* means of measuring dynamic force.

The concept of a force-sensitive vibration isolation bearing is therefore one that enables a measurement of the dynamic force transmitted through it but which, in all other respects, behaves as a standard isolation bearing. While the overall principles involved are similar irrespective of the application, the remainder of this chapter is specifically concerned with a prototype force-sensitive bearing for base-isolated buildings.

6.2. Design of the Prototype

As described in Section 2.3, there are two different designs of base-isolation bearings currently available for buildings, namely steel helical springs or laminated rubber bearings. The type of bearing considered here is one manufactured from vulcanised laminates of polychlorprene-based rubber; see Figure 6.1. The rubber is made more flexible by the addition of cork particles and reinforced with layers of woven nylon cloth.

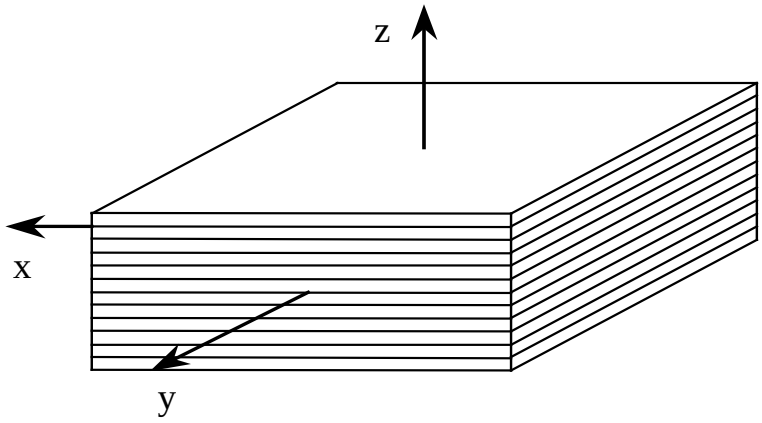

Figure 6.1: Schematic diagram of a laminated rubber bearing for base isolation of buildings. The z-axis represents the vertical axis of the building.

Power may be transmitted through the bearing in a number of ways; as well as vertical motion along the z-axis, shear of the bearing in the x-y plane and rotation about all three axes may take place. It is unrealistic, at least in an initial prototype, to attempt to account for all of these transmission paths and typically only the vertical path is considered during the design of a

building. As a result, while no assumptions are made about the significance of the other paths, the prototype force-sensitive bearing is designed to measure the dynamic force acting along the z-axis only.

Power flowing along the z-axis may be obtained by two simultaneous measurements of dynamic force and velocity along the z-axis. A time-integrated accelerometer signal can provide the latter and, in principle, the accelerometer may be located within the bearing. The location of the accelerometer is not critical since the wavelengths of vibration concerned are much larger than the bearing dimensions. A suitable location may therefore be found on the steel plates that are typically located above and below the bearing when it is installed in a building.

It is worth noting that one possible way of obtaining the dynamic force in the bearing is by using two displacement measurements, made above and below the bearing, together with the value of the bearing's stiffness. However, rubber is a non-linear material whose stiffness varies with frequency and static load, and this method is regarded as being insufficiently accurate.

6.2.1. Outline of Design

The design of the prototype bearing has concentrated on the ability to measure dynamic force alone. To achieve this, while still providing effective vibration isolation, the design must satisfy the following essential criteria:

- the dynamic behaviour of the bearing, characterised in particular by its stiffness and mass distribution, must not differ significantly from that of a conventional isolation bearing;
- the overall dimensions of the bearing must not differ significantly from those of a conventional bearing, in particular the bearing's thickness since this has implications for the design of a building if only a proportion the bearings used are force-sensitive;
- the bearing must provide a measure of the dynamic force applied normal to the bearing faces;
- the sensitivity of the bearing must be linear over the frequency range of interest, that is, approximately 1 to 200 Hz;

- the bearing must be robust and withstand the normal static load experienced by isolation bearings for buildings.

The above criteria are essential for the operation of the force-sensitive bearing and its acceptability to building designers. In addition, it is desirable that the construction of the bearing is as similar as possible to a conventional bearing for ease of manufacture. Consideration of the above criteria leads to the design shown schematically in Figure 6.2.

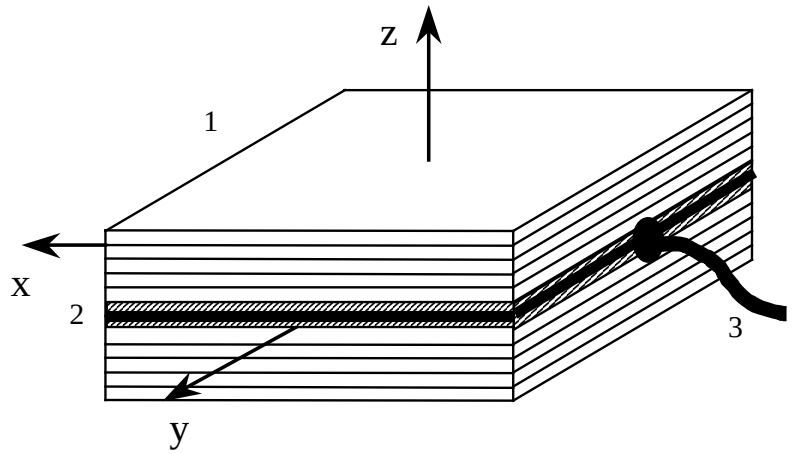

Figure 6.2: Schematic diagram of the prototype force-sensitive bearing showing (1) conventional laminated rubber bearing material, (2) a sheet of piezoelectric material between two aluminium plates and (3) a cable to carry the charge signal.

The design is based on a sheet of piezoelectric material, which produces a charge proportional to the applied dynamic load. This is placed between two thin aluminium plates which, as well as providing electrodes to conduct away the charge, protect the piezoelectric material from in-plane stresses when the bearing is under static loading. A cable to carry the charge signal to an appropriate amplifier is bonded to the aluminium plates using conductive epoxy resin.

6.2.2. Piezoelectric Films

All piezoelectric materials used for sensor applications are based on the same principle. They consist of elemental dipoles that are aligned during manufacture such that the material becomes polarized. In the case of a sheet material, when it is strained, the dipole alignment changes and a potential difference is generated across the thickness of the sheet. Conducting layers are formed

on both sides of the sheet so that a charge may gather which can then be measured either directly or via a charge amplifier. Two types of piezoelectric material have been tested for the force-sensitive bearing: PVDF film and '0-3 composite'. Complimentary samples of each were provided by GEC Marconi Ltd.

PVDF (polyvinylidene fluoride) film is a polarized fluoropolymer closely related to PTFE. Along with its copolymers it is commonly known as *piezo film*. The film is polarized during manufacture by stretching and applying an electric field. Aluminium is then deposited on each surface to form electrodes. PVDF film is a flexible, lightweight, tough plastic film with many desirable properties suitable for a force-sensitive bearing [90]. These include:

- wide frequency range - 0.001 to 10^9 Hz;
- wide dynamic range - 10^{-10} to 10^4 MPa;
- high elastic compliance;
- high sensitivity - typically 30 pC/N in the through-thickness direction;
- low thickness - typically 10 to 100 µm (the sample from GEC is approximately 25 µm);
- easily handled, fabricated and glued.

When a load is applied across the film's thickness, the charge generated is independent of the area over which the load is applied. Consequently, when used in a force-sensitive bearing as outlined above, the film generates a charge proportional to the total vertical dynamic load acting on the bearing; it is insensitive to variations in the stress distribution over the bearing faces.

0-3 composite is an alternative to PVDF film produced solely by GEC Marconi. It consists of a neoprene rubber matrix, approximately 0.5 mm thick, with a 50 % volume fraction of piezoelectric crystals of modified lead titanate. Conductive paint is applied to each surface of the composite to form electrodes. Detailed information regarding the properties of 0-3 composite is not currently publicly available, although it is known to behave in a broadly similar manner to PVDF film.

6.3. Design of the Test Apparatus

A prototype force-sensitive bearing has been constructed according to the design outlined in Section 6.2.1. The prototype is nominally one third the size of a conventional building isolation bearing in order to reduce the amount of materials required and the size of the static load which must be applied to the bearing to simulate the 'in-service' static stress conditions. The result is a bearing with overall dimensions of 100 x 100 x 55 mm and a static load requirement of approximately 50 kN.

Testing of the prototype bearing has been undertaken using the experimental apparatus shown in Figure 6.3.

1. Loading platens
2. Conventional bearing
3. Load distribution plates
4. Shaker unit
5. Shaker voltage input signal
6. Load-cell charge output signal
7. Force-sensitive bearing charge output signal

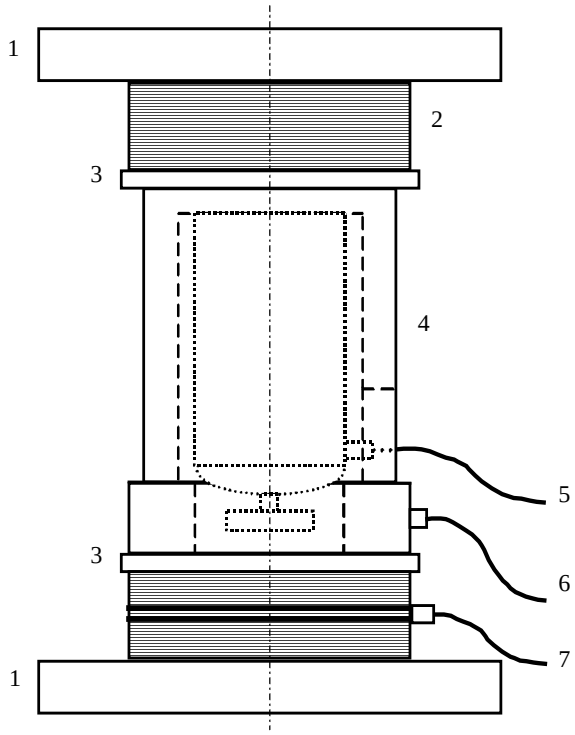

Figure 6.3: Cross-section through the experimental apparatus for the dynamic testing of the prototype force-sensitive bearing.

The apparatus behaves as a moving mass, consisting essentially of the shaker unit and load-cell, supported between the two bearings. A dynamic load, of up to 1.0 N r.m.s. amplitude, can be superimposed on top of the static compression by driving the shaker with a random noise signal-generator via a 200 Hz low-pass filter. The resulting charge signals from the load-cell and force-sensitive bearing are amplified by nominally identical charge amplifiers and then logged by a personal computer (PC) for subsequent analysis.

The sensitivity of the load-cell is known from the manufacturer's calibration certificate. This has been confirmed by comparing the dynamic load measured by the load-cell with that derived from the acceleration of the moving shaker mass, as measured by a shaker-mounted accelerometer. Knowing the load-cell sensitivity, that of the force-sensitive bearing can be determined by comparing the signals from the load-cell and the bearing.

The variation in the force-sensitive bearing's sensitivity with frequency and with both the static and dynamic load level has been investigated. The analysis consisted of removing any non-zero mean from the signals, computing their fast Fourier transforms (FFTs) [101] and then dividing the bearing FFT by that of the load-cell to form a transfer function. In this way the magnitude and phase of the bearing's sensitivity may be determined relative to that of the load-cell.

6.4. Experimental Results

This section presents an essential summary of the experimental results used to evaluate the prototype force-sensitive bearing. The nominally identical charge amplifiers were found to behave slightly differently at frequencies less than 20 Hz. In addition, the data logging card in the PC introduces a phase error due to the sequential sampling of the amplifier outputs, an error that increases with frequency. These effects have been quantified by comparing the amplifier outputs when identical random charge signals, similar to those generated during the tests, are supplied as inputs. This has enabled correction of the data so that the outputs from the load-cell and force-sensitive bearing may be compared directly.

6.4.1. Variation in Sensitivity with Frequency

Figure 6.4 shows a typical plot of the variation in the force-sensitive bearing's sensitivity with frequency when using the PVDF film. The various traces correspond to a nominal r.m.s. dynamic load amplitude of 1.0 N and static loads from 5 to 50 kN; the sensitivity decreases with increasing static load. The corresponding plot when using the 0-3 composite is shown in Figure 6.5.

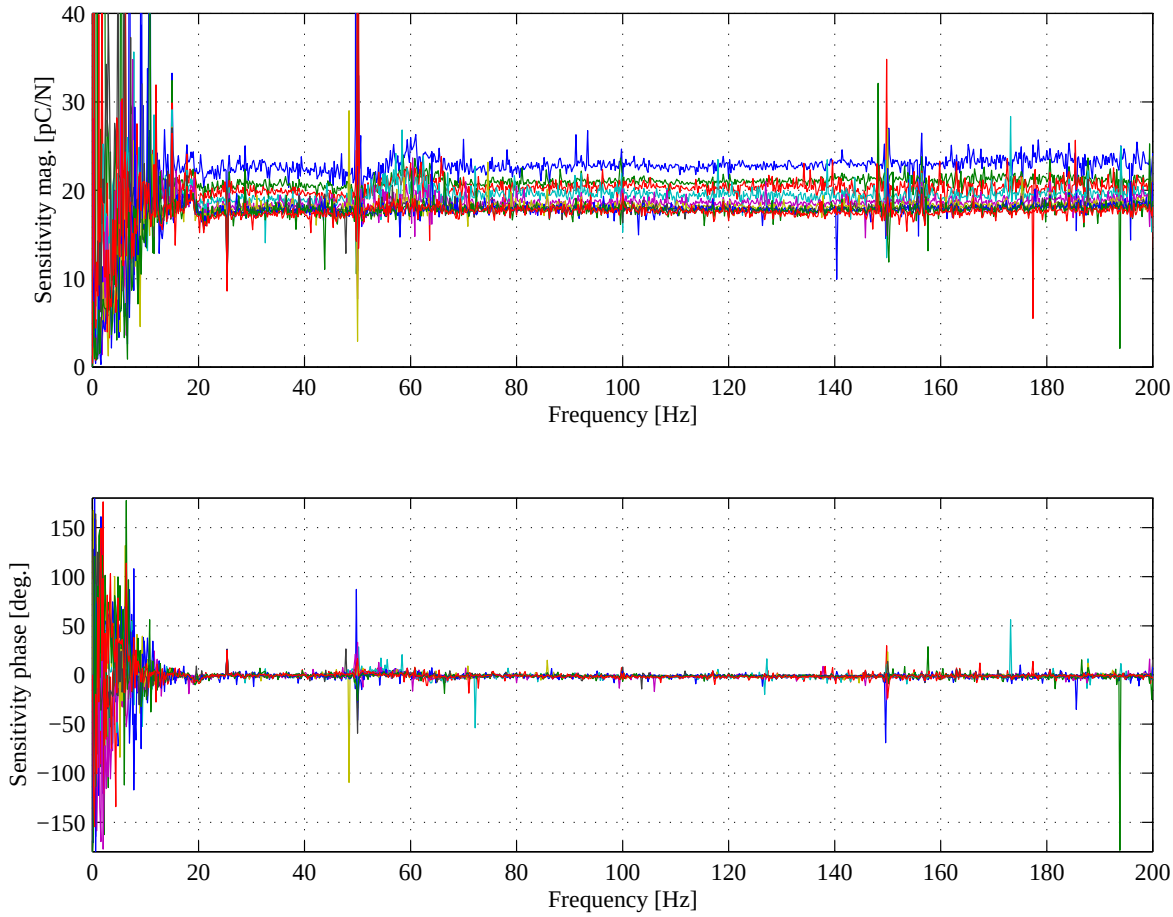

Figure 6.4: Variation with frequency in the sensitivity of the force-sensitive bearing based on PVDF film. The results correspond to a nominal r.m.s. dynamic load amplitude of 1.0 N and the phase is calculated relative to the load-cell output. The sensitivity decreases with the increase in static load from 5 to 50 kN.

There are three features of the data displayed in Figures 6.4 and 6.5 that are not directly attributable to the behaviour of the bearing. One problem is that the aluminium plates either side of the piezoelectric material act as an aerial and the signal suffers from 50 Hz noise due to the laboratory mains supply. An attempt at shielding the bearing with aluminium foil reduced the noise but did not eliminate the 50 Hz peaks and their harmonics evident in the figures. In addition, limitations in the experimental apparatus, in particular the low frequency behaviour of the signal generator, result in the noise evident below 20 Hz. The broad peak centred on 60 Hz is due to a resonance of the shaker unit and load-cell between the bearings in the test machine.

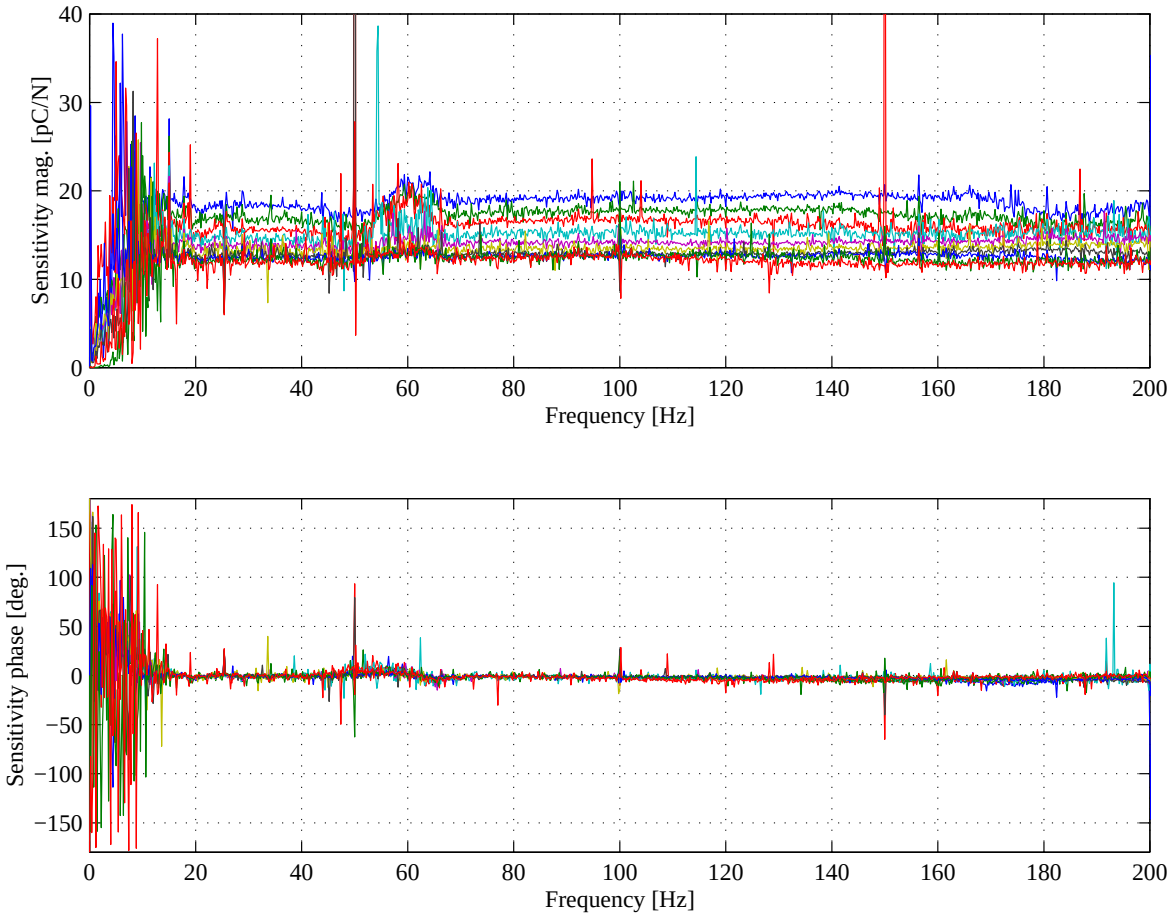

Figure 6.5: Variation with frequency in the sensitivity of the force-sensitive bearing based on 0-3 composite. The results correspond to a nominal r.m.s. dynamic load amplitude of 1.0 N and the phase is calculated relative to the load-cell output. The sensitivity decreases with the increase in static load from 5 to 50 kN.

The main point to note from Figures 6.4 and 6.5 is that the variation in sensitivity, for a given static load, over the frequency range of interest is insignificant. The data may therefore be averaged over frequency to obtain one value representing the sensitivity for a given static load.

6.4.2. Variation in Sensitivity with Static and Dynamic Load

As the static load is increased, the sensitivity of both piezoelectric materials decreases but at a diminishing rate. To investigate this behaviour more fully, and also check the linearity of the bearing with dynamic load, a series of 60 tests has been undertaken with both the PVDF film and 0-3 composite. These tests covered the static load range from 5 to 50 kN, with six tests at each static load covering the dynamic load range from 0.1 to 1.0 N r.m.s.

One of the main problems with the experimental apparatus is associated with the use of an imposed displacement to generate the required static load. Due to stress relaxation within the rubber bearings under the imposed displacement, the static load gradually falls with time. Over the six minutes or so of each test, when the load was required to remain constant, the maximum reduction in load was 5 % with a mean of 3 %.

The results of all 60 tests are summarised in Figure 6.6, which shows the variation in mean bearing sensitivity with static load and dynamic load amplitude.

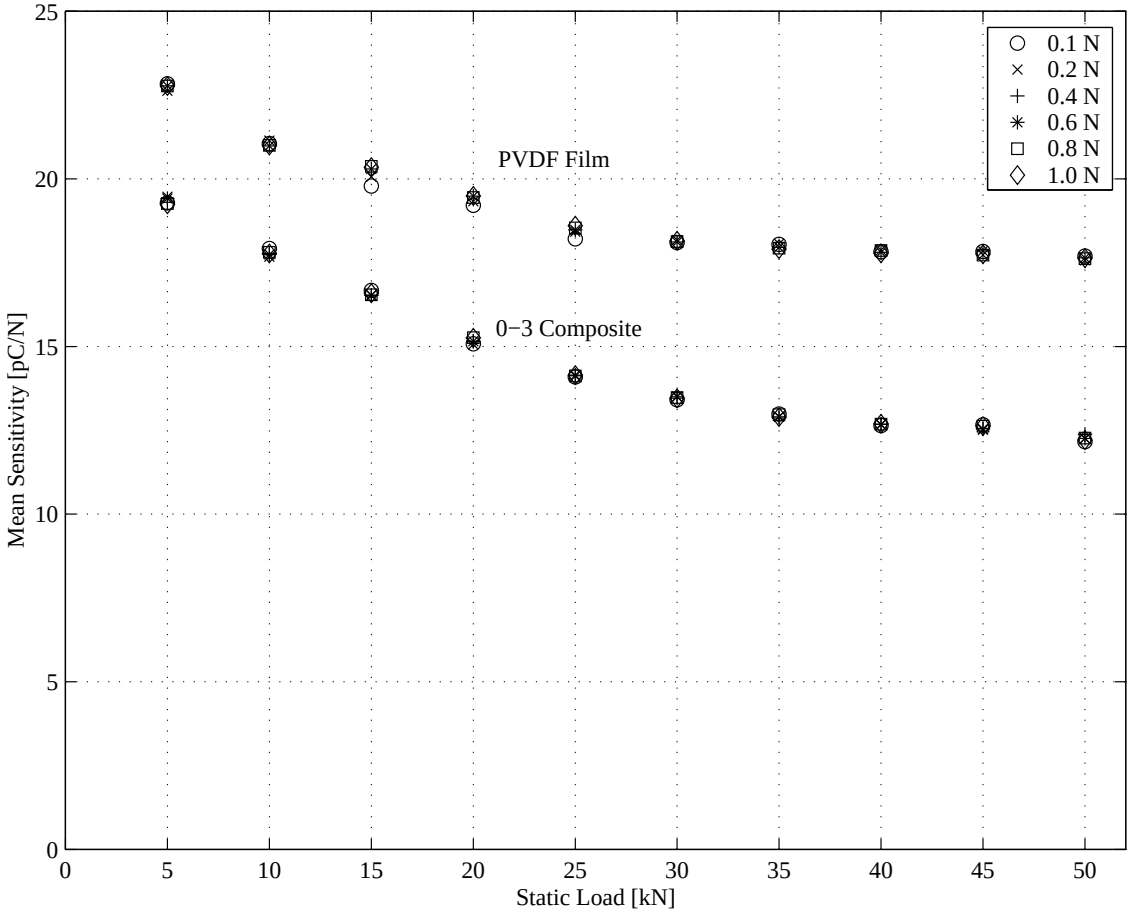

Figure 6.6: Variation in mean force-sensitive bearing sensitivity with static load and with r.m.s. dynamic load amplitudes between 0.1 and 1.0 N.

The mean is calculated over the middle frequency range from 70 to 145 Hz in order to avoid the data corrupted by significant noise. The first point to note is that the PVDF film is between 30 and 40 % more sensitive than the 0-3 composite, depending on the static load considered. Secondly, with both materials, the reduction in sensitivity with increasing static load is significant;

the PVDF shows a reduction of 23 % and the 0-3 composite a reduction of 38 % over the 45 kN range of the tests. However, it is clear that the linearity of the bearing with dynamic load, using either of the piezoelectric materials, is good up to the 1.0 N r.m.s. limit of the shaker. The slight changes in sensitivity over the dynamic load range are likely to be due to the reduction in the static load due to stress relaxation within the bearings.

6.5. Conclusions and Recommendations for Future Development

This chapter has described the design and testing of a prototype force-sensitive vibration isolation bearing for determining the effectiveness of base-isolation bearings for buildings based on power-flow measurements. Tests have been conducted with two samples of piezoelectric material, PVDF film and 0-3 composite, and the major conclusions are as follows:

- the sensitivity of either the PVDF film or the 0-3 composite is more than adequate for the application considered given a dynamic force resolution of at least 0.1 N r.m.s.;
- the sensitivity of either material does not vary significantly over the frequency range of interest for a given static load;
- with both materials, the reduction in sensitivity with increasing static load is significant - the PVDF shows a reduction of 23 % and the 0-3 composite a reduction of 38 % over the 45 kN range of the tests;
- under a typical in-service static load of between 40 and 50 kN, the PVDF film is approximately 40 % more sensitive than the 0-3 composite;
- the linearity of the bearing with dynamic load, using either of the piezoelectric materials, is good up to the 1.0 N r.m.s. limit of the tests.

The concept of a force-sensitive bearing, capable of providing a measure of the dynamic load under which it is operating, has been shown to be worthy of further development. The following recommendations are made.

6.5.1. Variation in Sensitivity with Time

Of primary interest is the long-term behaviour of the bearing under in-service conditions. The susceptibility of the bearing's sensitivity to both long-term static loading and ambient temperature fluctuations should be investigated separately. Long-term loading may lead to creep of the piezoelectric material itself and this may or may not lead to a change in sensitivity. In addition, the sensitivity of piezoelectric material is known to increase with temperature and the significance of this should be investigated, although this effect is reversible and repeatable [90] and, as such, may be corrected for as part of the data processing.

Two tests are therefore recommended. The bearing should be held under a fixed load, rather than an imposed displacement, at a known fixed temperature and the sensitivity tested periodically. This should then be repeated with the ambient temperature varying. Ideally these tests should be conducted with a full-scale bearing as the thermal insulation offered by the bulk rubber is likely to be significant.

6.5.2. Choice of Piezoelectric Material

The tests reported here have shown the PVDF film to be more sensitive than the 0-3 composite. However, given that both materials are adequately sensitive for the application under consideration, there are additional considerations that are more important. Both materials suffer under prolonged exposure to high temperatures. At approximately 80 °C PVDF film begins to depolarise. With the 0-3 composite the piezoelectric crystals are much more stable and the limiting factor is degradation of the neoprene matrix, which begins at approximately 100 °C. The greater resistance of the 0-3 composite to elevated temperatures may be beneficial when considering the manufacture of a full size bearing.

In addition, following discussions with GEC Marconi, it is understood that the 0-3 composite is a more robust material and its sensitivity is less susceptible to ambient temperature fluctuations. It is therefore recommended that future development work concentrates on the use of 0-3 composite for the piezoelectric element.

6.5.3. Removal of Aluminium Plates

As described in Section 6.2.1, the piezoelectric material is placed between two thin aluminium plates to provide electrodes and protect the material from in-plane stresses. These plates are additional components that may be redundant provided that the piezoelectric material is not adversely affected by in-plane stresses. As well as altering the sensitivity of the bearing, the in-plane stresses due to in-service loads may simply tear the material. It is therefore recommended that a test be undertaken to check the performance of the bearing without the aluminium plates in position.

If the plates are indeed required, consideration should be given to the long-term electrical contact between them and the piezoelectric material given the possibility of oxidation of the aluminium.

6.5.4. Structural Integrity

A practical force-sensitive bearing must be robust enough to withstand the loads experienced during installation and it must also provide a moisture-free environment for the piezoelectric element. The latter requirement must be considered during the detailed design of a full-scale bearing.

A requirement of building isolation bearings is that they pass an industry-standard shear test. This involves imposing a 25 mm shear displacement across a 125 mm thick bearing. The inclusion of the piezoelectric element must not, therefore, introduce a plane of weakness into the bearing and this requires confirmation following the design of a full-scale bearing.

6.5.5. Long-Term Developments

In addition to the above recommendations, provided that the development of a full-scale bearing is successful, there are two additional developments worthy of consideration in the long term:

- location of an accelerometer and integral charge amplifiers within the bearing;
- addition of piezoelectric crystals to the bearing compound in order to reproduce an ‘0-3 type’ composite but using the bearing rubber itself.

Chapter 7

CONCLUSIONS AND RECOMMENDATIONS FOR FURTHER WORK

This chapter reviews the original objectives of the research and considers the extent to which they have been met. The main conclusions drawn from the work of previous chapters are summarised and, based on these, recommendations are then made for further work.

7.1. Conclusions

The primary aim of this research has been to develop a generic computational model that accounts for the essential dynamic behaviour of a base-isolated building and allows predictions to be made of the isolation performance against ground-borne vibration. To achieve this aim, a number of specific objectives were set, as given in Section 1.2. These are now reviewed and consideration is given to the extent to which they have been met.

It is now clear that a building and foundation act as one system and that they must be modelled together in order to fully describe the behaviour of a base-isolated building. Constructing a building on its foundation modifies any pre-existing vibration field and may lead to either a reduction or an increase in foundation vibration. In either case, the effect is less significant when the building is base-isolated. While consideration has been given to the effect of a building on its foundation, none has been given to the effect of a foundation on a vibration field existing prior to any construction work.

It has been demonstrated that fundamental problems exist with the use of insertion gain, one of the common measures of isolation performance, due to the dynamic behaviour of a building

and its foundation. The concept of power flow insertion gain (PFIG), based on the total mean vibrational power flow entering a building, has been introduced as a more useful measure of isolation performance. PFIG has been shown to offer clear benefits by providing a single measure of insertion performance that accounts for multidirectional vibration at multiple inputs and which is insensitive to the spatial distribution of vibration levels within a building. PFIG is useful for design purposes because the minimisation of PFIG is guaranteed to reduce the average internal noise and vibration levels within a building.

A comprehensive three-dimensional model of a piled foundation has been developed that accounts for the essential dynamic behaviour of a piled foundation, namely the vertical, horizontal and rotational motion of the pile heads due to both direct pile-head loading and interaction through wave propagation in the surrounding soil. This has been achieved in a computationally efficient way by assuming the foundation consists of an infinitely long row of identical piles and using a combination of the boundary-element method and periodic structure theory. By comparison with results from alternative theoretical models, the accuracy of the piled-foundation model has been shown to be good over the lower frequency range of interest, typically from 0 to 50 Hz, but above this the accuracy is expected to decrease due to limitations of the boundary-element mesh.

A generic model of a base-isolated building has been produced by combining the piled-foundation model with an existing, infinitely long two-dimensional model of a building. Initial investigations have concluded that the choice of isolation frequency can make up to a 15 dB difference to the effectiveness of the base isolation against a specific, locally generated ground vibration field. The level of internal damping in the bearings has been found to have a negligible effect on isolation efficiency, although it is important for controlling local resonant behaviour of the base of the building. It has been demonstrated that the modelling of the piled foundation is important, in particular, the ability to model both horizontal and vertical motion of the pile heads and the interaction between piles through wave propagation in the surrounding soil. Neglecting the latter has been found to result in the over-prediction of base isolation efficiency by up to 7 dB.

Finally, initial progress has been made towards making power flow measurements on a real structure by developing a prototype force-sensitive isolation bearing. This is based on the incorporation of a thin, flexible piezoelectric element into a conventional rubber base-isolation bearing, such that measurements may be made without affecting the isolation performance. An experimental test programme has proved the operation of the prototype under simulated 'in-service' conditions and shown it to be worthy of further development.

7.2. Recommendations for Further Work

In its present form, the generic base-isolated building model provides a flexible and computationally efficient means of investigating base-isolation performance. There are several valuable studies, in addition to those described in Section 5.3, which may be undertaken with little further development work. These include the investigation of: different ground vibration fields; the effects of different piled-foundation designs; and the significance of the isolation bearing stiffnesses. The analysis of power flow has been shown to offer insight into the behaviour of base-isolated buildings. This is also worthy of further investigation, particularly given the flexibility of the piled-foundation model, which enables the displacement and stress fields in the soil to be calculated. In addition to this work, the model has the potential for significant further development.

It is particularly important to understand the effect of a foundation on a vibration field existing prior to any construction work, such as when design assessments involve performance predictions based on 'green field' site measurements. This should be investigated by applying the techniques used in seismic analysis [35].

Further work is required to improve the accuracy of the boundary-element mesh used in the piled-foundation model, particularly at the higher frequencies of interest. There are two possibilities worth exploring. Firstly, higher-order boundary-elements may enable fewer numbers of elements to be used for the same accuracy achieved with constant elements. Secondly, the numerical modelling has been undertaken using BEM programs written by the author and, while every effort has been made to ensure their efficiency, improved performance may be gained by using a commercial boundary-element code.

Longer-term developments of the foundation-model may include the modelling of layered soils and the direct incorporation of a vibration source, such as an underground railway tunnel. The limiting factor here is computing power and it should be remembered that it is desirable for the final model to be solved on a standard personal computer.

There remains a need for experimental validation of both the piled-foundation model and the final base-isolated building model. Future construction projects should be identified and attempts made to gain access for measurements on a real base-isolated building. Several recommendations have been made for the future development of the force-sensitive isolation bearing and progress should be made on these with the aim of determining base-isolation performance from power-flow measurements.

During the course of the research undertaken for this dissertation, the European Union extended its *Growth 2000* programme to address the problem of noise and vibration from underground railways. The project CONVURT [27] is concerned with the control of vibration from underground rail traffic and has the primary objective of developing experimentally validated software to predict noise and vibration in buildings. The author is part of the project team and it is hoped that the work described here will go some way to helping CONVURT achieve its aims.

REFERENCES

[1] S. Adhikari and J. Woodhouse, *Identification of damping: part 1, viscous damping*. Journal of Sound and Vibration, 2001, 243(1), pp. 43-61.

[2] S. Adhikari and J. Woodhouse, *Identification of damping: part 2, non-viscous damping*. Journal of Sound and Vibration, 2001, 243(1), pp. 63-88.

[3] A.J. Alder and K.N.G. Fuller, *Elastomeric isolation mounts for buildings and structures: from design to installation.* Proceedings of the Institute of Acoustics, 1999, 21(3), pp. 17-25.

[4] M.O. Al-Hunaidi *et al*., *Control of traffic-induced vibration in buildings using vehicle suspension systems.* Soil Dynamics and Earthquake Engineering, 1996, 15, pp. 245-254.

[5] D. Anderson, *Isolation of buildings from railway vibration: a case study*. Proceedings of the 5th International Congress on Sound and Vibration, Adelaide, Australia, 1997. International Institute of Acoustics and Vibration.

[6] L. Auersch, *Wave propagation in layered soils: theoretical solution in wavenumber domain and experimental results of hammer and railway traffic excitation*. Journal of Sound and Vibration, 1994, 173(2), pp. 233-264.

[7] T. Balendra *et al*., *Dynamic response of buildings due to trains in underground tunnels*. Earthquake Engineering and Structural Dynamics, 1991, 20, pp. 275-291.

[8] P.K. Banerjee and S.M. Mamoon, *A fundamental solution due to a periodic point force in the interior of an elastic half-space*. Earthquake Engineering and Structural Dynamics, 1990, 19, pp. 91-105.

[9] F.C.P. de Barros and J.E. Luco, *Discrete models for vertical vibrations of surface and embedded foundations*. Earthquake Engineering and Structural Dynamics, 1990, 19, pp. 289-303.

[10] R. Bean and J. Page, *Traffic induced ground vibration in the vicinity of road tunnels*. Transport and Road Research Laboratory Supplementary Report, 1976.

[11] A.A. Becker, *The Boundary Element Method in Enginnering: a Complete Course*. Mcgraw-Hill, 1992.

[12] A. Bedford and D.S. Drumheller, *Introduction to Elastic Wave Propagation.* John Wiley & Sons Ltd, 1994.

[13] D.E. Beskos, *Wave propagation through ground* in Boundary Element Techniques in Geomechanics, G.D. Manolis and T.G. Davies (eds.), 1993. Computational Mechanics Publications & Elsevier Applied Science.

[14] P. Bettess, *Infinite Elements.* Penshaw Press, 1992.

[15] D.R. Bland, *Theory Of Linear Viscoelasticity*. Pergamon Press, 1960.

[16] M.D. Bolton and J.M.R. Wilson, *An experimental and theoretical comparison between static and dynamic torsional soil tests.* Geotechnique, 1989, 39(4), pp. 585-599.

[17] C.A. Brebbia and J. Dominguez, *Bounday Elements: An Introductory Course.* Mcgraw-Hill, 1992.

[18] L. Brillouin, *Wave Propagation in Periodic Structures.* Mcgraw-Hill, 1946.

[19] British Standards Institution, G*uide to selection and use of elastomeric bearings for vibration isolation of buildings.* BS 6177, 1982.

[20] British Standards Institution, G*uide to evaluation of human exposure to vibration in buildings (1 to 80hz).* BS 6472, 1984.

[21] P. Carels, *personal communication.* CDM Vibration Isolation Systems, Overijse, Belgium, 2001.

[22] CDM Vibration Isolation Systems, Overijse, Belgium. Manufacturers product guide, interactive CD-ROM, 2001.

[23] J.A. Cheney *et al.*, *Modelling free-field conditions in centrifuge models.* Journal of Geotechnical Engineering Division, American Society of Civil Engineers, 1990, 116(9), pp. 1347-1367.

[24] K.H. Chua *et al*., *Building response due to subway train traffic*. Journal of Geotechnical Engineering, American Society of Civil Engineers, Nov. 1995, pp. 747-754.

[25] D.J. Cole and D. Cebon, *Truck suspension design to minimize road damage*. Proceedings of the Institution of Mechanical Engineers, Part D: Journal of Automobile Engineering, 1996, 210, pp. 95-107.

[26] D.E. Commins *et al*., *Vibration isolation of trains in a French arts complex.* Proceedings of the Institute of Acoustics, 1990, 12, pp. 31-38.

[27] CONVURT, *The control of vibration from underground rail traffic.* RTD Project Report, Part B, 2001.

[28] G.I. Crabb *et al*., *Measurement and prediction of groundbourne vibration due to construction operations.* Ground Dynamics and Man-Made Processes: Prediction, Design and Measurement, 1997. A conference of the Institution of Civil Engineers, London.

[29] R.J.M. Craik, *Sound Transmission Through Buildings using Statistical Energy Analysis.* Gower, 1996.

[30] S.H. Crandall, *The role of damping in vibration theory.* Journal of Sound and Vibration, 1970, 11, pp. 3-18.

[31] L.M. Cremer *et al*., *Structure-Borne Sound* (2nd ed.). Springer-Verlag, 1988.

[32] J.H.A. Crockett, *Soil vibration insulation for buildings and structures.* Plastics and Rubber Processing and Applications, 1985, 5(3), pp. 267-275.

[33] D.P. Cryer, *Modelling of vibration in buildings with application to base isolation.* Ph.D. dissertation, University of Cambridge, 1994.

[34] G. Degrande *et al*., *Wave propagation in layered dry, saturated and unsaturated poroelastic media.* International Journal of Solids and Structures, 1998, 35(34-35), pp. 4753-4778.

[35] J. Dominguez, *Boundary Elements in Dynamics.* Computational Mechanics Publications & Elsevier Applied Science, 1993.

[36] F.J. Fahy, *Sound Intensity* (2nd ed.). E & FN Spon, 1995.

[37] E. Forchap and B. Verbic, *Field tests on wave propagation and reduction of foundation vibrations.* Wave '94: Wave Propagation and Reduction of Vibrations, Bochum, Germany, 1994.

[38] J.A. Forrest, *Modelling of ground vibration from underground railways*. Ph.D. dissertation, University of Cambridge, 1999.

[39] G. Gazetas, *Soil dynamics: an overview* in Dynamic Behaviour of Foundations and Buried Structures: Vol. 3, P.K. Banerjee and R. Butterfield (eds), 1987. Elsevier Applied Science.

[40] G. Gazetas and N. Makris, *Dynamic pile-soil-pile interaction part 1: analysis of axial vibration*. Earthquake Engineering and Structural Dynamics, 1991, 20, pp. 115-132.

[41] B.M. Gibbs, *Can airborne and structure-borne sources be treated in the same way?* International Journal of Acoustics and Vibration, 2000, 5(1), pp. 114-115.

[42] K.F. Graff, *Wave Motion in Elastic Solids.* Clarendon Press, Oxford, 1975.

[43] M.J. Griffin, *Handbook of Human Vibration.* Academic Press, 1990.

[44] P. Grootenhuis, *Structural elastomeric bearings and resilient seatings* in Polymers and Polymer Composites in Construction, L. Hollaway (ed.), 1990. Thomas Telford.

[45] P. Grootenhuis, *Noise generated by intermittent structure borne vibrations.* Building Research and Information, 1992, 20(3), pp. 157-161.

[46] H. Hao *et al.*, *Building vibration to traffic-induced ground motion.* Building and Environment, 2001, 36, pp. 321-336.

[47] B.O. Hardin and V.P. Drnevich, *Shear modulus and damping in soils: measurement and parameter effects.* Journal of Soil Mechanics and Foundations, American Society of Civil Engineers, 1972, 98(sm6), pp. 603-624.

[48] M. Heckl *et al.*, *Structure-borne sound and vibration from rail traffic.* Journal of Sound and Vibration, 1996, 193(1), pp. 175-184.

[49] P. Henson and J.G. Charles, *Vibration isolation of the IMAX cinema, Waterloo, London.* Proceedings of the Institute of Acoustics, 2000, 22(2), pp. 255-262.

[50] P. Henson, *personal communication.* Bickerdike, Allen & Partners, London, 2001.

[51] C. Hepburn and R.J.W. Reynolds, *Elastomers: Criteria for Engineering Design.* Applied Science Publishers, 1979.

[52] D.M. Hiller and V.S. Hope, *Groundborne vibration generated by mechanized construction activities.* Proceedings of the Institution of Civil Engineers: Geotechnical Engineering, 1998, 131(4), pp. 223-232.

[53] R.A. Hood *et al.*, *The calculation and assessment of ground-borne noise and perceptible vibration from trains in tunnels.* Journal of Sound and Vibration, 1996, 193(1), pp. 215-225.

[54] H.V.C. Howarth and M.J. Griffin, *The annoyance caused by simultaneous noise and vibration from railways.* Journal of the Acoustical Society of America, 1991, 89(5), pp. 2317-2323.

[55] Q. Huang and T.A. Cruse, *Some notes on singular integration techniques in boundary element analysis.* International Journal for Numerical Methods in Engineering, 1993, 36, pp. 2643-2659.

[56] G.K. Huffmann, *Spring support of buildings: a Gerb system for full base isolation and for protection against subsidences.* American Society of Mechanical Engineers, Pressure Vessels and Piping Division (publication), 1988, 147, pp. 101-107.

[57] H.E.M. Hunt, *Measurement and modelling of traffic-induced ground vibration.* Ph.D. dissertation, University of Cambridge, 1988.

[58] H.E.M. Hunt, *Measures for reducing ground vibration generated by trains in tunnels* in Noise and Vibration from High-Speed Trains, V.V. Krylov (ed.), 2001. Thomas Telford.

[59] International Standards Organisation, *Evaluation of human expose to whole-body vibration - part 2: human exposure to continous and shock-induced vibrations in buildings (1 to 80hz).* ISO 2631-2, 1989.

[60] International Standards Organisation, *Guidelines for the design and implementation of base isolation systems to attenuate ground borne vibration.* Proposed standard, 1998, ISO/TC 108/SC 2/WG 3.

[61] International Standards Organisation, *Prediction of groundborne vibration arising from rail systems in tunnels.* Proposed standard, 1998, ISO/TC 108/SC 2/WG 8.

[62] K.L. Johnson, *Contact Mechanics.* Cambridge, 1985.

[63] D.L. Karabalis and D.C. Rizos, *Dynamic analysis of 3-d foundations* in Boundary Element Techniques in Geomechanics, G.D. Manolis and T.G. Davies (eds.), 1993. Computational Mechanics Publications & Elsevier Applied Science.

[64] S.E. Kattis *et al*., *Vibration isolation by a row of piles using a 3-d frequency domain BEM.* International Journal of Numerical Methods in Engineering, 1999, 46, pp. 713-728.

[65] A.M. Kaynia, *Piles* in Boundary Element Techniques in Geomechanics, G.D. Manolis and T.G. Davies (eds.), 1993. Computational Mechanics Publications & Elsevier Applied Science.

[66] S. Kraemer, *Noise and vibration in buildings from underground railway lines.* Ph.D. dissertation, University of London, 1984.

[67] E. Kreyszig, *Advanced Engineering Mathematics* (7th ed.). John Wiley & Sons, 1993.

[68] V.V. Krylov, *Generation of ground vibration boom by high-speed trains* in Noise and Vibration from High-Speed Trains, V.V. Krylov (ed.), 2001. Thomas Telford.

[69] R.L. Kuhlemeyer, *Static and dynamic laterally loaded floating piles.* Journal of Geotechnical Engineering, American Society of Civil Engineers, 1979, 105(2), pp. 289-304.

[70] R.L. Kuhlemeyer, *Vertical vibration of piles.* Journal of Geotechnical Engineering, American Society of Civil Engineers, 1979, 105(2), pp. 273-287.

[71] H. Kuppelwieser, *A tool for predicting vibration and structure-borne noise immissions caused by railways.* Journal of Sound and Vibration, 1996, 193(1), pp. 261-267.

[72] J. Lang, *Ground-borne vibrations caused by trams, and control measures.* Journal of Sound and Vibration, 1988, 120(2), pp. 407-412.

[73] R.S. Langley, *Analysis of power flow in beams and frameworks using the direct-dynamic stiffness method.* Journal of Sound and Vibration, 1990, 136(3), pp. 439-452.

[74] M. Lavergne, *Seismic Methods.* Graham & Trotman Ltd, 1989.

[75] P.B. Lindley, *Engineering Design with Natural Rubber* (5th ed.). The Malaysian Rubber Producer's Research Association, 1984.

[76] K.T. Lo, *Measurement and modelling of vibration transmission through piled foundations.* Ph.D. dissertation, University of Cambridge, 1994.

[77] J.E. Luco. and R.A. Westmann, *Dynamic response of circular footings.* Journal of Engineering Mechanics, American Society of Civil Engineers, 1971, 77, pp. 1381-1395.

[78] J.E. Luco. and R.J. Apsel, *On the green's functions for a layered half-space: parts 1 & 2.* Bulletin of the Seismological Society of America, 1983, 73(4), pp. 909-951.

[79] S.P.G. Madabhushi, *Response of tower structures to earthquake perturbations.* Ph.D. dissertation, University of Cambridge, 1991.

[80] C. Madshus *et al.*, *Prediction model for low frequency vibration from high speed railways on soft ground.* Journal of Sound and Vibration, 1996, 193(1), pp. 195-203.

[81] C. Madshus and A.M. Kaynia, *High-speed railway lines on soft ground: dynamic behaviour at critical train speed.* Journal of Sound and Vibration, 2000, 231(3), pp. 689-701.

[82] N. Makris, *Soil-pile interaction during the passage of Rayleigh waves: an analytical solution.* Earthquake Engineering and Structural Dynamics, 1994, 23, pp. 153-167.

[83] N. Makris and D. Badoni, *Seismic response of pile groups under oblique-shear and Rayleigh waves.* Earthquake Engineering and Structural Dynamics, 1995, 24, pp. 517-532.

[84] N. Makris and G. Gazetas, *Dynamic pile-soil-pile interaction part 2: lateral and seismic response.* Earthquake Engineering and Structural Dynamics, 1992, 21, pp. 145-162.

[85] C.J. Manning, *Air rights buildings.* Proceedings of the Institute of Acoustics, 1990, 12(7), pp. 23-30.

[86] G.D. Manolis and D.E. Beskos, *Boundary Element Methods in Elastodynamics.* Unwin Hyman, 1988.

[87] Mathworks Ltd., Cambridge, U.K., *Matlab version 5.3.1.* 1999.

[88] D.J. Mead, *Wave propagation in continuous periodic structures: research contributions from Southampton, 1964-1995.* Journal of Sound and Vibration, 1996, 190(3), pp. 495-524.

[89] D.J. Mead, *Passive Vibration Control.* John Wiley & Sons, 1999.

[90] Measurement Specialities Inc., New Jersey, U.S.A., *Piezo film sensors technical manual.* Manufacturers product guide, 1998.

[91] J. Melke, *Noise and Vibration from underground railway lines: proposals for a prediction procedure*. Journal of Sound and Vibration, 1988, 120(2), pp. 391-406.

[92] R.D. Mindlin, *Force at a point in the interior of a semi-infinite solid*. Physics, 1936, 7, pp. 195.

[93] A. Mita and J.E. Luco, *Impedance functions and input motions for embedded square foundations.* Journal of Geotechnical Engineering, American Society of Civil Engineers, 1989, 115, pp. 491-503.

[94] F.A. Mohammad and V.V. Krylov, *Finite element calculation of elasto-dynamic fields generated by a point source in the layered ground.* Proceedings of the Institute of Acoustics, 2000, 22(2), pp. 271-278.

[95] A.T. Moorhouse and B.M. Gibbs, *Vibrational power flow from machines into structures*. Proceedings of the Institute of Acoustics, 1987, 9(3), pp. 389-395.

[96] P. Moss, *Resilient mounting of structures on difficult sites.* Noise & Vibration Control Worldwide, 1982, 13(7), pp. 288-291.

[97] P. Moss, *Isolating apartments and offices from ground borne vibrations.* Noise and Vibration Control Worldwide, 1983, pp. 183-185.

[98] A.H. Muhr, *A comparison of rubber and metal springs for vibration isolation.* Plastics, Rubber and Composites Processing and Applications, 1992, 18, pp. 3-7.

[99] F. Naeim and J.M. Kelly, *Design of Seismic Isolated Structures.* John Wiley & Sons, 1999.

[100] J.T. Nelson, *Recent developments in ground-borne noise and vibration control.* Journal of Sound and Vibration, 1996, 193(1), pp. 367-376.

[101] D.E. Newland, *Mechanical Vibration Analysis and Computation.* Longman, 1989.

[102] D.E. Newland and H.E.M. Hunt, *Isolation of buildings from ground vibration: a review of recent progress.* Proceedings of the Institution of Mechanical Engineers, Part C: Mechanical Engineering Science, 1991, 205(1), pp. 39-52.

[103] S.L.D. Ng, *Transmission of ground-borne vibration from surface railway trains.* Ph.D. dissertation, University of Cambridge, 1995.

[104] Y. Nii, *Experimental half-space dynamic stiffness.* Journal of Geotechnical Engineering, American Society of Civil Engineers, 1987, 113(11), pp. 1359-1371.

[105] M. Novak, *Dynamic stiffness and damping of piles.* Canadian Geotechnical Journal, 1974, 11(4), pp. 574-598.

[106] M. Novak and R.F. Grigg, *Dynamic experiments with small pile foundations.* Canadian Geotechnical Journal, 1976, 13(4), pp. 372-385.

[107] O.R.E. D151 Specialists' Committee, *An assessment of vibration counter-measures in current use*. Report No. 2, *Question D151: Vibrations transmitted through the ground,* 1982. Office for Research & Experiments of the International Union of Railways, Utrecht, Netherlands.

[108] O.R.E. D151 Specialists' Committee, *Effect of vibration on buildings and their occupants - analysis of the literature and commentary*. Report No. 4, *Question D151: Vibrations transmitted through the ground,* 1982. Office for Research & Experiments of the International Union of Railways, Utrecht, Netherlands.

[109] O.R.E. D151 Specialists' Committee, *Study of the long term behaviour of various antivibration measures in the track*. Report No. 6, *Question D151: Vibrations transmitted through the ground*, 1984. Office for Research & Experiments of the International Union of Railways, Utrecht, Netherlands.

[110] O.R.E. D151 Specialists' Committee, *An investigation of resilient pads for ballasted track in metro tunnels.* Report No. 8, *Question D151: Vibrations transmitted through the ground*, 1984. Office for Research & Experiments of the International Union of Railways, Utrecht, Netherlands.

[111] A.T. Peplow *et al*., *Vibration transmission in a layered ground with a wave impedance block.* Ground Dynamics and Man-Made Processes: Prediction, Design and Measurement, 1997. A conference of the Institution of Civil Engineers, London.

[112] H.G. Poulos. and E.H. Davis, *Pile Foundation Analysis and Design.* John Wiley & Sons, 1980.

[113] B. Prange, *Parameters affecting damping properties* in Dynamical Methods in Soil and Rock Mechanics 1: Dynamic Response and Wave Propagation in Soils, B. Prange (ed.), 1977. Balkema.

[114] C. Pronello, *Vibrations caused by trams.* Proceedings of the 6th International Congress on Sound and Vibration, Copenhagen, Denmark, 1999. International Institute of Acoustics and Vibration.

[115] J. Qian and L.G. Tham, *Dynamic interaction among footings.* Journal of Sound and Vibration, 2001, 239(1), pp. 157-177.

[116] Lord Rayleigh, *On waves propagated along the plane surface of an elastic solid.* Proceedings of the London Mathematical Society, 1887, 17, pp. 4-11.

[117] Lord Rayleigh, *The Theory of Sound*, vol. 1 of 2 (2nd ed.). New York: Dover Publications, 1894, 1945 reprint.

[118] R. Sen *et al*., *Dynamic analysis of piles and pile groups embedded in homogeneous soils.* Earthquake Engineering and Structural Dynamics, 1985, 13, pp. 53-65.

[119] A.K. Sharif, *Dynamic performance investigation of base-isolated structures.* Ph.D. dissertation, Imperial College of Science, Technology and Medicine, 1999.

[120] A. Stevenson, *Longevity of natural rubber in structural bearings.* Plastics and Rubber Processing and Applications, 1985, 5, pp. 253-258.

[121] J.C. Swallow, *Modelling of isolation of buildings from ground-borne vibration.* Proceedings of the 12th International Conference on Acoustics, Canada, 1986.

[122] H. Takemiya, *Traffic induced vibrations and wave propagation*. Wave '94: Wave Propagation and Reduction of Vibrations, 1994, Bochum, Germany.

[123] H. Takemiya, *Simulation of high-speed train induced ground vibration and its mitigation by WIB.* Proceedings of the 6th International Congress on Sound and Vibration, Garmisch-Partenkirchen, Germany, 2000. International Institute of Acoustics and Vibration.

[124] B.P. Temple, *Recent developments in standards for the evaluation of human exposure to vibration in buildings*. Proceedings of the London Authorities Rail Impact Forum: Vibration from Railways, 1999.

[125] R.M. Thornely-Taylor, *Modelling of vibration and ground-borne noise from underground railway tunnels by a finite difference method.* Proceedings of the 6th International Congress on Sound and Vibration, Copenhagen, Denmark, 1999. International Institute of Acoustics and Vibration.

[126] Tiflex Ltd, Old Woking, U.K., *Tico structural bearings.* Manufacturers product guide, 1998.

[127] S. Timoshenko *et al.*, *Vibration Problems in Engineering* (4th ed.). New York, 1974.

[128] A. Trochides, *Ground-borne vibrations in buildings near subways.* Applied Acoustics, 1991, 32, pp. 289-296.

[129] E.G. Vadillo *et al.*, *Subjective reaction to structurally radiated sound from underground railways: field results.* Journal of Sound and Vibration, 1996, 193(1), pp. 65-74.

[130] G. Volberg, *Propagation of ground vibrations near railway tracks.* Journal of Sound and Vibration, 1983, 87(2), pp. 371-376.

[131] H.G. Wagner, *Application of steel springs in the support of buildings.* Proceedings of the Institute of Acoustics, 2000, 22(2), pp. 221-230.

[132] T. Wah and L.R. Calcote, *Structural Analysis by Finite Difference Calculus.* New York, 1970.

[133] A.M. Wahl, *Mechanical Springs.* Mcgraw-Hill, 1963.

[134] R.A. Waller, *Building on Springs.* Pergamon Press, 1969.

[135] G.R. Watts, *Vehicle generated ground-bourne vibration alongside speed control cushions and road humps.* Ground Dynamics and Man-Made Processes: Prediction, Design and Measurement, 1997. A conference of the Institution of Civil Engineers, London.

[136] R.G. White, *Power transmission measurement and control in structures*. Proceedings of NOVEM 2000, Lyon, France, 2000. Institut National des Sciences Appliquées de Lyon.

[137] G.P. Wilson *et al.*, *Control of ground-borne noise and vibration*. Journal of Sound and Vibration, 1983, 87(2), pp. 339-350.

[138] J.P. Wolf, *Foundation Vibration Analysis Using Simple Physical Models.* Prentice-Hall, 1994.

[139] J.P. Wolf and C. Song, *Finite-Element Modelling of Unbounded Media.* John Wiley & Sons, 1996.

[140] J. Woodhouse, *An introduction to statistical energy analysis of structural vibration.* Applied Acoustics, 1981, 14, pp. 455-469.

[141] Y. Yang and H. Hung, *A parametric study of wave barriers for reduction of train-induced vibrations.* International Journal of Numerical Methods in Engineering, 1997, 40, pp. 3729-3747.

[142] O.C. Zienkiewicz and R.L. Taylor, *The Finite Element Method vol. 1: The Basis* (5th ed.). Butterworth-Heinemann, 2000.

[143] O.C. Zienkiewicz and R.L. Taylor, *The Finite Element Method vol. 2: Solid Mechanics* (5th ed.). Butterworth-Heinemann, 2000.

Appendix A

THE SINGLE-DEGREE-OF-FREEDOM MODEL

The single-degree-of-freedom (SDOF) oscillator, illustrated in Figure A1, is one of the fundamental models of structural dynamics. It may also be regarded as the simplest model of a base-isolated building, where the rigid mass M represents the building and the linear spring k, together with some form of damping element, represents the isolation bearings. This appendix derives the transmissibility across the spring, a quantity that is often used in the context of base-isolated buildings to illustrate isolation performance.

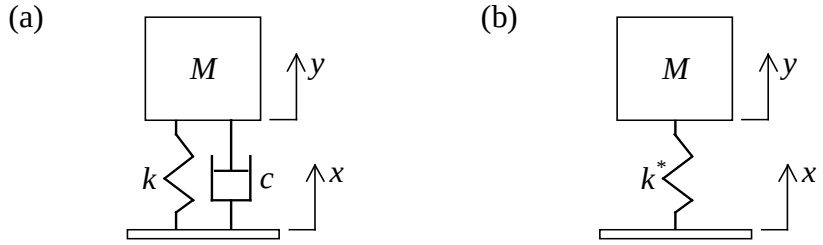

Figure A1: The SDOF oscillator may be regarded as the simplest model of a base-isolated building, where the rigid mass M represents the building and the linear spring k represents the isolation bearing. Damping may be accounted for by (a) a viscous dashpot c or (b) a complex spring stiffness k^*.

The most commonly encountered form of the model, shown in Figure A1(a), accounts for damping by a viscous dashpot. The governing equation for the displacement response y due to displacement excitation x of the rigid base is, from Newton's law:

$$M\frac{d^2y}{dt^2} + c\frac{dy}{dt} + ky = c\left(\frac{dx}{dt}\right) + kx \qquad \text{(A1)}$$

Consider a steady-state excitation, harmonic in time *t* at circular frequency ω, with amplitude *X*, that is, $x = \mathrm{Re}\{Xe^{i\omega t}\}$, where $i = \sqrt{-1}$. The system is linear and the response therefore takes a similar form $y = \mathrm{Re}\{Ye^{i\omega t}\}$, where the complex amplitude *Y* determines both the amplitude and phase of the response. Substitution for *x* and *y* in Equation A1 gives the *transmissibility* of the system:

$$\frac{Y}{X} = \frac{1 + i\eta}{1 - \left(\omega / \omega_n\right)^2 + i\eta} \tag{A2}$$

where $\omega_n = \sqrt{k/M}$ is the resonance frequency, equivalent to the isolation frequency of the building in rad/s, and $\eta = c\omega/k$ is the viscous damping loss factor.

More usually the transmissibility of the viscously damped model is expressed in terms of the damping ratio $\zeta = \eta\omega_n / 2\omega$. In this dissertation the hysteretic damping model is adopted (see Section 3.1.1) and the isolation bearings are represented by a spring of complex stiffness $k^* = k(1 + i\eta_k)$, as in Figure A1(b). In this case the transmissibility is still given by Equation A2 but the viscous loss factor η must be replaced by the frequency-independent hysteretic loss factor η_k.

Transmissibility is plotted against non-dimensional frequency, for both the viscous and hysteretic damping assumptions, in Figure A2. Both ζ and η_k have been set to 0.1 to illustrate the differences between the two models. Bearing manufactures often cite a figure similar to Figure A2 (but usually only the magnitude plot) to illustrate the principles of base isolation. The figure suggests that, above the frequency $\omega \approx \sqrt{2}\omega_n$, the building becomes isolated from its foundation. In the case of the viscously damped model, the level of isolation then increases with frequency at a rate of 20 dB/decade, whereas in the hysteretic case the rate is 40 dB/decade. Such levels of isolation are grossly optimistic for a base-isolated building, primarily due to the fact that a building and its foundation are flexible structures that interact with each other.

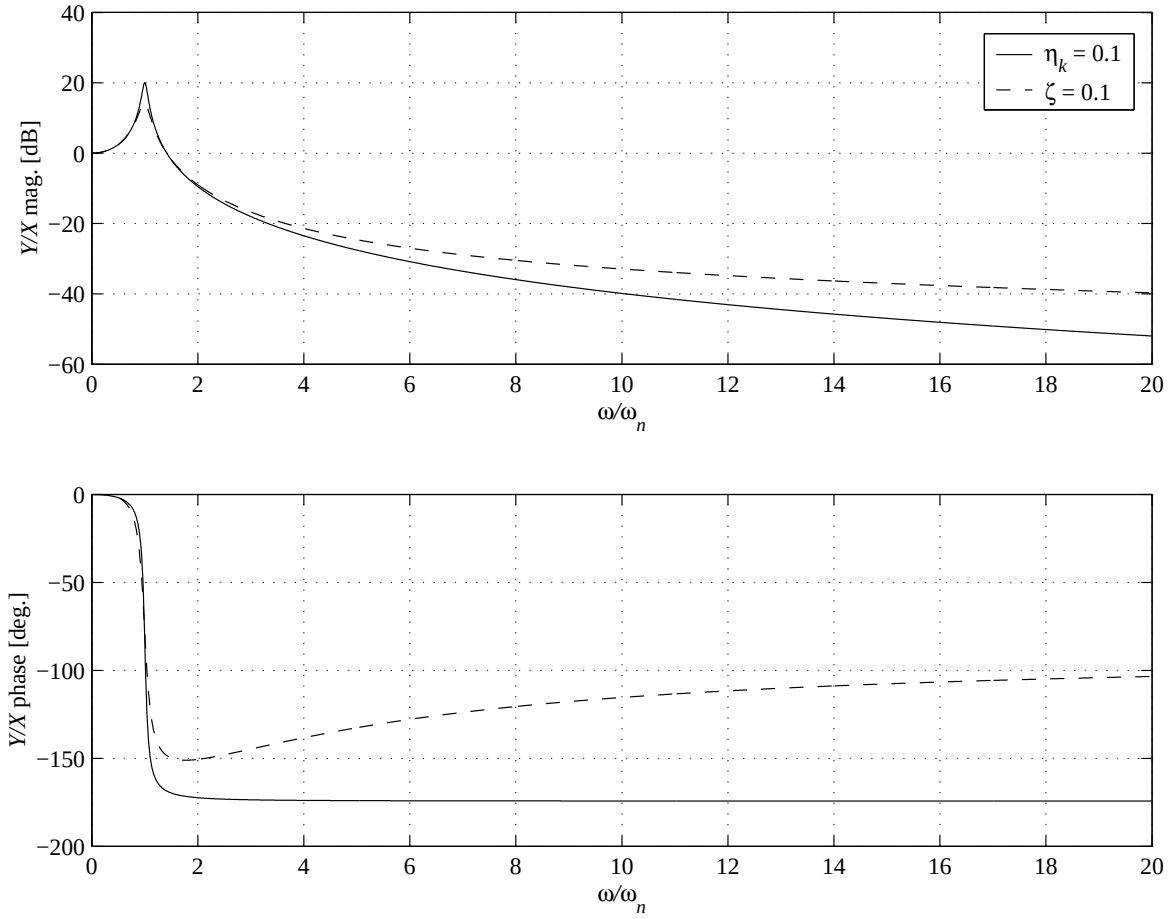

Figure A2: Transmissibility *Y/X* of the SDOF model, plotted against non-dimensional frequency ω/ω_n, for both the viscous and hysteretic damping assumptions. The magnitude plot is often used in the context of base-isolated buildings to illustrate isolation performance.

Appendix B
THE BOUNDARY-ELEMENT METHOD

The boundary-element method (BEM) is the chosen numerical technique for the generic piled-foundation model of this dissertation. This appendix aims to provide a summary of the BEM as used in the field of time-harmonic elastodynamics. A general introduction is given, followed by an outline of the numerical formulation used for this dissertation and two example problems. For further details of the BEM, the reader is referred to the many books on the subject; see for example the introductory texts by Becker [11] and Brebbia and Dominguez [17] and, of particular relevance to this dissertation, the texts by Dominguez [35] and Manolis *et al* [86, 13].

B1. Introduction

In almost every field of engineering analysis, there are many problems for which the governing equations may be represented by a system of boundary integral equations (BIEs). In such equations the unknown field variables appear only in integrals over the boundary of the problem domain.

Following extensive development work throughout the 1970s, the BEM is now the most popular numerical technique for solving BIEs. There are two different but equivalent integral equation formulations: the direct approach and the indirect approach. The latter expresses the equations in terms of non-physical functions from which the physical variables are subsequently derived; the former, which is used in this dissertation, expresses the integral equations directly in terms of the actual field variables of the problem concerned – in this case time-harmonic displacements and tractions.

The BEM may be formulated in either the time or frequency domains. As noted in Section 2.6, the latter is considered to be the most appropriate for use in this dissertation.

B2. Numerical Formulation

Consider a Cartesian coordinate system, denoted by x_j, $j = 1, 2, 3$, in which we define a homogeneous isotropic linear-elastic body Ω, of density ρ, by its boundary surface Γ. The problem of interest concerns a particular elastodynamic state of displacements and tractions, as illustrated in Figure B1(a). One method of deriving the BIEs, relating these two quantities on the surface of the body, is to use the reciprocal theorem of elastodynamics.

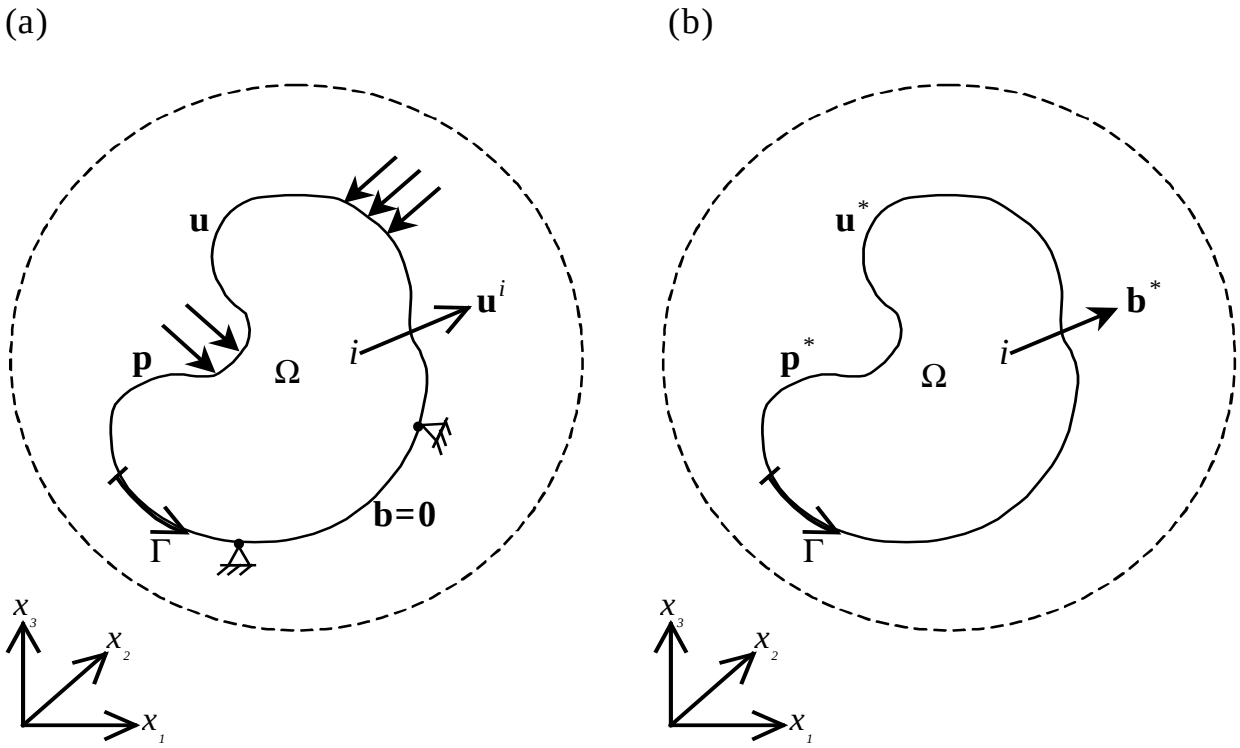

Figure B1: Elastodynamic states of a body illustrating (a) the problem of interest and (b) the fundamental solution corresponding to a point force in an infinite domain. The infinite domain is represented by the dashed circle.

B2.1 The Reciprocal Theorem

The reciprocal theorem of elastodynamics is the dynamic equivalent of Betti's theorem in elastostatics and relates any two elastodynamic states of the body Ω [11, 35].

Consider two elastodynamic states of the body: let the displacements, tractions and body forces per unit mass of the first state be denoted by **u**, **p** and **b** respectively; those of the second

state shall be denoted by $\mathbf{u}^*$, $\mathbf{p}^*$ and $\mathbf{b}^*$. Note that body forces are loads applied to the interior of the body rather than the inertia forces arising naturally due to the body's motion. Here we are concerned with time-harmonic states and all the above field variables take the form of $\mathbf{u} = \mathrm{Re}\{\mathbf{u}(\mathbf{x},\omega)e^{i\omega t}\}$, where t = time, ω = circular frequency and $i = \sqrt{-1}$. For the case of steady-state time-harmonic states of the same frequency, the reciprocal theorem may be expressed as follows:

$$\int_\Gamma p_j u_j^* d\Gamma + \int_\Omega \rho b_j u_j^* d\Omega = \int_\Gamma p_j^* u_j d\Gamma + \int_\Omega \rho b_j^* u_j d\Omega \tag{B1}$$

Now consider the two elastodynamic states to be as follows. The first state corresponds to the problem of interest and here we shall assume zero body forces, $b_k = 0$. Since the problems of interest concern vibration about an equilibrium position, body forces due to gravity may be ignored. The second state, which shall be known as the *fundamental solution*, is chosen to be that due to a point time-harmonic force, of unit amplitude, applied in the direction of the x_l-axis at a point 'i' in an infinite elastic domain; see Figure B1(b). To apply the reciprocal theorem, both states must be defined for the same body and therefore it is assumed that Ω is part of the infinite domain.

The fundamental solution corresponds to a body force of amplitude $\rho b_k^* = \delta(r)\delta_{lk}$, where r is the distance from the point 'i', $\delta(r)$ is the Dirac delta function and δ_{lk} is the Kroneka delta. Given this as the second state, the last domain integral of Equation B1 becomes:

$$\int_\Omega \rho b_k^* u_k d\Omega = \int_\Omega \delta(r) u_k \delta_{lk} d\Omega = u_l^i \tag{B2}$$

where the superscript on u_l^i indicates that the displacement is that of point 'i'. Equation A1 may now be written as:

$$u_l^i + \int_\Gamma p_{lk}^* u_k d\Gamma = \int_\Gamma u_{lk}^* p_k d\Gamma \tag{B3}$$

This expresses the displacement of the state of interest u_l^i, at any point in the body, in terms of the corresponding displacements u_k and tractions p_k on its boundary, and the known

displacements and tractions of the fundamental solution, u_{lk}^* and p_{lk}^*. The latter two functions are often referred to as the Green's functions of the formulation. Their values depend on the locations of point '*i*' – where the point force is applied – and the integration point on the boundary; in other words, they are functions of *r*, as well as ω and the remaining material properties of the body. The latter consist of the shear modulus, Poisson's ratio and damping loss factor.

B2.2 A Note on Green's Functions

In this dissertation the *full-space* Green's functions are used, that is, the fundamental solution is due to a point force in an infinite domain. Analytical expressions exist for these Green's functions and u_{lk}^* and p_{lk}^* may be calculated easily [35]. However, it is worth noting that there exist different formulations of the BEM based on different Green's functions, and a decision must be made on which are the most appropriate for the particular application concerned. One possibility is to use the Green's functions for the case of a point load in an elastic half-space, such as those derived by Banergee and Mamoon [8], or those for a layered half-space derived by Luco and Apsel [78]. None of these alternatives may be expressed explicitly in a simple form and their calculation requires complex numerical integrations that are difficult to evaluate accurately. The use of half-space Green's functions does, however, have its advantages.

Consider the modelling of a structural foundation. By formulating the problem in terms of half-space Green's functions, discretization of the ground's free surface is avoided entirely; only the interface between the soil and the foundation need be discretized. Alternatively, if the full-space Green's functions are used, the free surface around the foundation must also be considered. However, in practice, discretization of the free surface is restricted to a finite portion around the region of interest: for surface foundations excited at moderate frequencies, no free-surface discretization is required at all [35]. In view of this, the complexity of the half-space Green's functions, and the fact that the free surface must be discretized if displacements there are of interest, use of the full-space functions is often preferred.

A final note on Green's functions is worth making. As the point load of the fundamental solution is approached, the displacements and tractions of the elastic body increase without bound

and, in the limit when $r = 0$, the functions become singular. Particular care must therefore be taken when evaluating the integrals in Equation B3. A great deal of work has been done on singular integration techniques for the various types of element used in the BEM; see for example the paper by Huang and Cruse [55]. The method used in this dissertation is described in Section B2.4 below.

B2.3 The Boundary Integral Equation

Equation B3 is valid for all points in the body, including those on the boundary. However, as mentioned above, when $r = 0$, that is, when the integration point coincides with point '*i*', the fundamental solution becomes singular. In order, therefore, to obtain the BIE for the displacements on the boundary, it is necessary to consider '*i*' located on the boundary but augment the domain itself by a small hemisphere centred on '*i*'. The radius of this hemisphere is then reduced and the behaviour of the integrals noted in the limit when the radius equals zero. Details of this limiting process may be found in the books by Brebbia and Dominguez [17, 35]. The final expression for the BIE, when the boundary Γ is smooth, may be written as:

$$\tfrac{1}{2}\delta_{lk}u_k^i + \int_\Gamma p_{lk}^* u_k \, d\Gamma = \int_\Gamma u_{lk}^* p_k \, d\Gamma \tag{B4}$$

or, in vector notation,

$$\tfrac{1}{2}\mathbf{u}^i + \int_\Gamma \mathbf{p}^* \mathbf{u} \, d\Gamma = \int_\Gamma \mathbf{u}^* \mathbf{p} \, d\Gamma \tag{B5}$$

where $\mathbf{u} = [u_1 \quad u_2 \quad u_3]^{\mathrm{T}}$ and $\mathbf{p} = [p_1 \quad p_2 \quad p_3]^{\mathrm{T}}$, 'T' denoting the vector transpose. $\mathbf{u}^*$ and $\mathbf{p}^*$ are 3 x 3 matrices containing the values of the fundamental solution.

B2.4 Numerical Solution

The solution of Equation B5 is undertaken numerically. The boundary surface Γ is divided into *N* planar elements, as illustrated in Figure B2(a), over which the field variables are assumed to be constant.

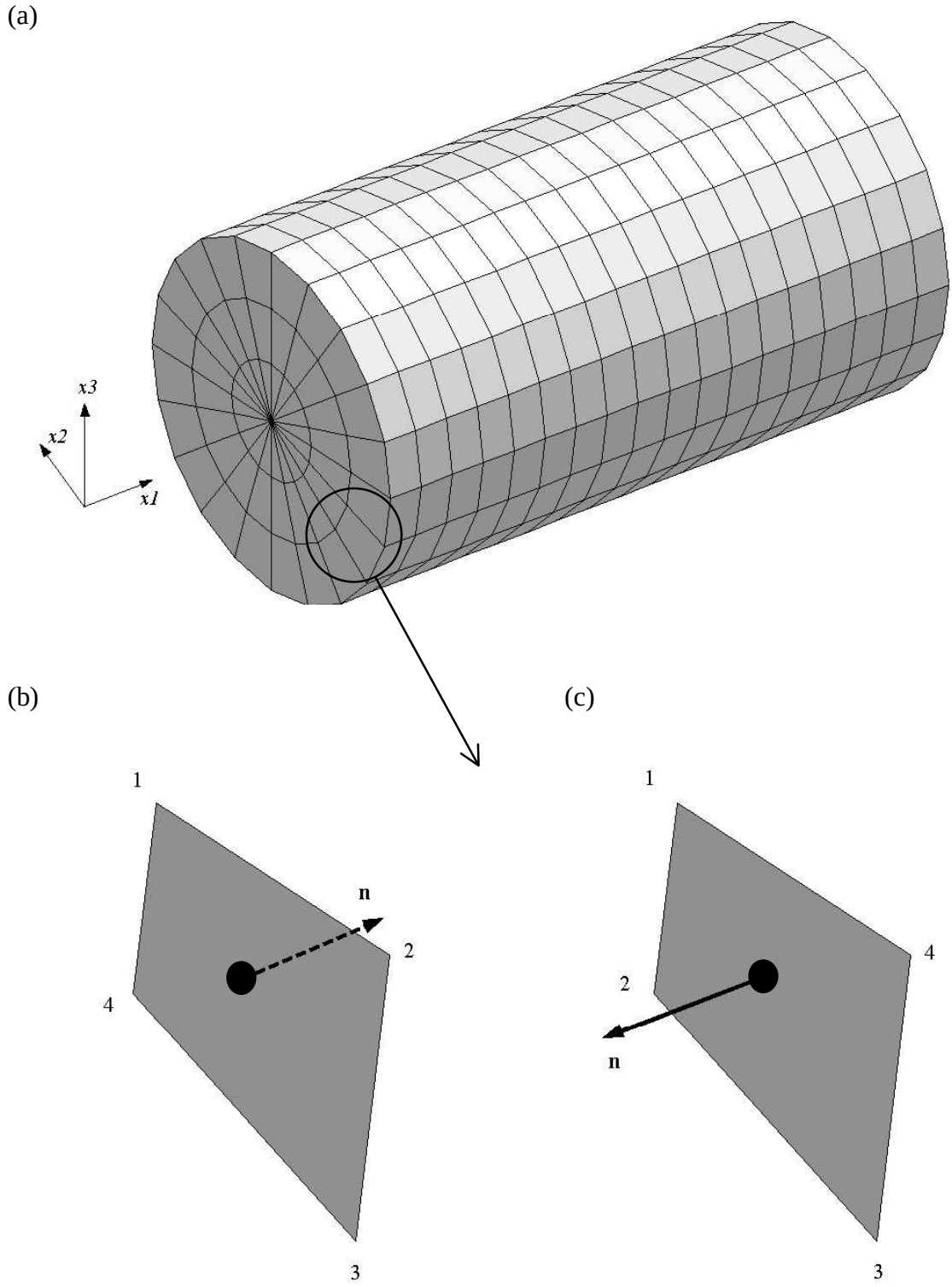

Figure B2: Discretization of a boundary surface into *N* constant elements, illustrating (a) the global mesh geometry, along with the definition of the local normal **n** for elements representing (b) internal domains and (c) external domains.

For element '*j*' the field variables are assumed to take the values $\mathbf{u}^j$ and $\mathbf{p}^j$, which are the values at a *node* in the centre of the element. Such elements are known as constant elements although, just as with the FEM, higher-order elements may be used in which the field variables are assumed to vary either linearly or quadratically over each element.

One of the great advantages of the BEM is the ability to model external as well as internal domains. The elements are always defined such that their outward normals point into the interior of the domain. For example, consider the element mesh shown in Figure B2(a). If the normals are defined as in Figure B2(b) then an internal domain is modelled and the mesh represents a solid cylindrical bar. If, on the other hand, the normals are defined as in Figure B2(c) then the mesh represents a cylindrical cavity in an infinite domain. With the latter, since the method is based on the fundamental solution for an infinite domain, the radiation of waves to infinity is automatically accounted for.

The integrals in Equation B5 are now written as a summation of integrals over each element. Assuming **u** and **p** are constant over each element allows them to be taken outside of the integrals. Equation B5 becomes:

$$\tfrac{1}{2}\mathbf{u}^i + \sum_{j=1}^{N}\left(\int_{\Gamma_j}\mathbf{p}^* d\Gamma\right)\mathbf{u}^j = \sum_{j=1}^{N}\left(\int_{\Gamma_j}\mathbf{u}^* d\Gamma\right)\mathbf{p}^j \tag{B6}$$

Thus two types of integral remain relating node '*i*', where the point force is applied, to any other node '*j*'. The values of these integrals are known as the influence coefficients $\hat{\mathbf{H}}^{ij}$ and $\mathbf{G}^{ij}$; Equation B6 may be written as:

$$\tfrac{1}{2}\mathbf{u}^i + \sum_{j=1}^{N}\hat{\mathbf{H}}^{ij}\mathbf{u}^j = \sum_{j=1}^{N}\mathbf{G}^{ij}\mathbf{p}^j \tag{B7}$$

It is now assumed that the point force of the fundamental solution may be applied at each node of the boundary in turn and '*i*' is allowed to vary from 1 to *N*. This produces a system of *N* independent matrix equations by writing Equation B7 for each node:

$$\sum_{j=1}^{N}\mathbf{H}^{ij}\mathbf{u}^j = \sum_{j=1}^{N}\mathbf{G}^{ij}\mathbf{p}^j \quad \text{for } i = 1,...N \tag{B8}$$

where

$$\mathbf{H}^{ij} = \begin{cases} \hat{\mathbf{H}}^{ij} & \text{when } i \neq j \\ \hat{\mathbf{H}}^{ij} + \mathbf{C} & \text{when } i = j \end{cases}$$

and $\mathbf{C} = \frac{1}{2}\mathbf{I}$, where $\mathbf{I}$ is a 3 x 3 identity matrix.

These N matrix equations may be assembled into one overall matrix equation representing the problem to be solved:

$$\mathbf{HU} = \mathbf{GP} \tag{B9}$$

where $\mathbf{H}$ and $\mathbf{G}$ are two $3N$ x $3N$ matrices and $\mathbf{U}$ and $\mathbf{P}$ are two $3N$ x 1 vectors.

The computation of the influence coefficients, $\mathbf{H}^{ij}$ and $\mathbf{G}^{ij}$, requires numerical integration of the fundamental solution over each element. When the point force of the fundamental solution lies outside the integration element, that is $i \neq j$, and the integrals are computed using standard Gaussian quadrature [67]. This requires a transformation to the homogeneous coordinates ξ_1 and ξ_2 in order to use the standard formulae; see Figure B3.

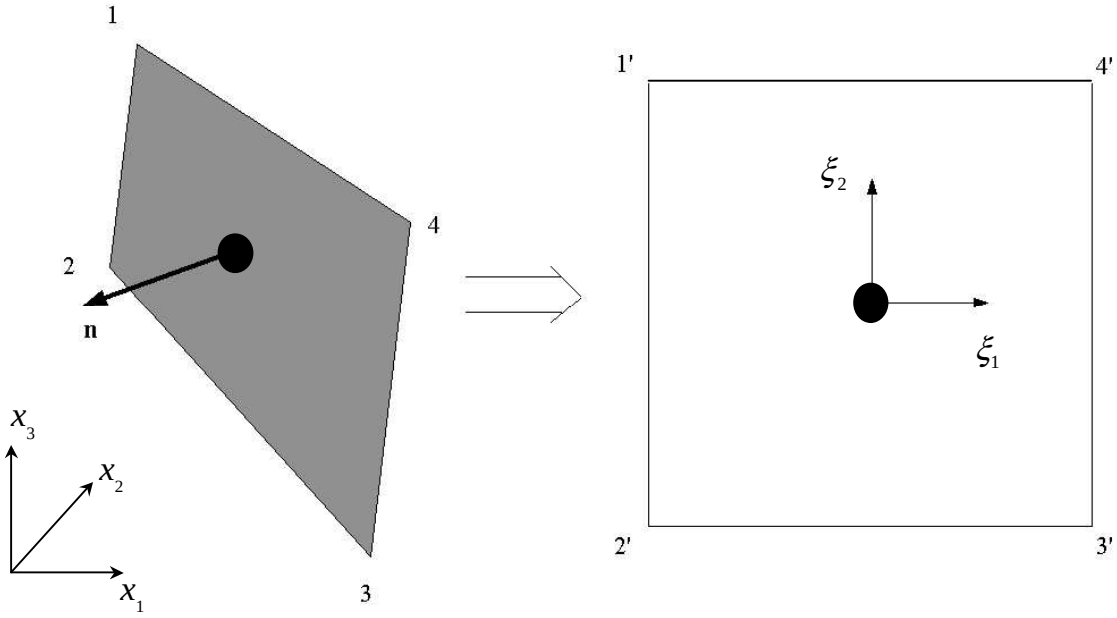

Figure B3: Numerical integration requires a transformation from the global Cartesian coordinates x_j, $j = 1, 2, 3$, to the local homogeneous coordinates ξ_1 and ξ_2.

For example, $\hat{\mathbf{H}}^{ij}$ is computed as follows:

$$\int_{\Gamma_j} \mathbf{p}^* d\Gamma = \int_{-1}^{1}\int_{-1}^{1} \mathbf{p}^* |G| d\xi_1 d\xi_2 = \sum_{l=1}^{n_g}\sum_{k=1}^{n_g} \mathbf{p}^* |G| w_k w_l \tag{B10}$$

where $|G|$ is the determinant of the reduced Jacobian matrix of the transformation and w_k are the weighting factors of the n_g - point quadrature. Six Gauss points have been found to be sufficient for the modelling described in this dissertation.

When $i = j$ the integration element contains the singularity of the fundamental solution and special care must be taken when performing the integration. The computation of $\mathbf{H}^{ii}$ is straightforward when, as in this dissertation, rectangular elements are used: $\mathbf{H}^{ii} = \mathbf{C}$ [35]. For non-rectangular elements the computation of $\mathbf{H}^{ii}$ is more involved and requires consideration of a static rigid-body displacement.

The computation of $\mathbf{G}^{ii}$ is undertaken in this dissertation using the element subdivision method used by Dominguez [35]. This devides the quadrilateral integration element into four triangular sub-elements, as illustrated in Figure B4, which are then treated as quadrilaterals for which two corners coincide at the central node of the element. The important feature of this approach is that the weak '1/*r*' sinularity contained in $\mathbf{u}^*$ is eliminated by the zero in the determinant of the Jacobian $|G|$. The integration may therefore be undertaken over each sub-element using standard Gaussian quadrature.

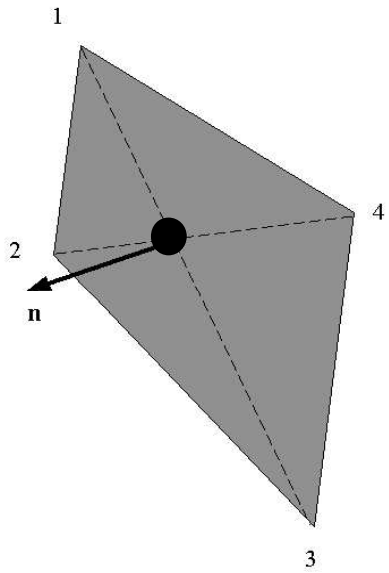

Figure B4: Subdivision of the integration element into four triangular 'quadrilaterals' when it contains the singularity of the fundamental solution.

The final solution of the problem requires the incorporation of the boundary conditions into Equation B9. There are 3*N* unknowns in the system – one per node and direction – and, in general, these will involve both displacements and tractions. As a result, the columns of **H** and **G** must be rearranged such that all the unknowns are passed to the left-hand side to give:

$$\mathbf{AX} = \mathbf{F} \tag{B11}$$

where **X** is the vector of unknown displacements and tractions and **F** is obtained by multiplying all the known values by the appropriate columns of **H** and **G**. Solution of Equation B11 may be achieved by any standard matrix-inversion routine, although it should be noted that the system of equations is fully populated and non-symmetric, and therefore the solution techniques used with the banded matrices of the FEM cannot be employed.

The BEM formulation outlined in this section has been implemented using the Matlab technical computing software [87]. A series of programs have been written which, in summary, perform the following operations:

- define the element mesh geometry, material properties, boundary conditions and frequencies of interest;
- load the Gaussian quadrature data;
- consider the point load of the fundamental solution at each node in turn and assemble the matrices **H** and **G**;
- incorporate the boundary conditions into **H** and **G**;
- compute $\mathbf{X} = [\mathbf{A}]^{-1}\mathbf{F}$;
- separate out the computed displacements and tractions and display the results.

B2.5 A Note on Plane and Anti-Plane Problems

Certain problems may be solved using two-dimensional models, thereby significantly reducing the computation time required. An example is a transverse section through a pile, as considered in Section 4.1.1. If the section is far enough away from either end of the pile, the pile may be considered as infinitely long and the pile-soil interface of the section may be represented by two-dimensional boundary elements in the x_1x_2-plane.

Depending on the direction of the applied load, two-dimensional problems are classed as either plane or anti-plane. In the case of the pile section, transverse loading of the pile leads to a plane problem in which the applied load and the resultant tractions and displacements of the soil lie in the x_1x_2-plane. Alternatively, longitudinal loading leads to an anti-plane problem with the load, tractions and displacements lying perpendicular to the section in the x_3-direction. Anti-plane problems are the simplest kind of elastodynamic problem since the equilibrium equation for the x_3-coordinate is uncoupled from x_1 and x_2.

Both plane and anti-plane problems are still described by Equation B5 but the required fundamental solutions are simpler and the field variables are either the 2 x 1 vectors $\mathbf{u} = [u_1 \quad u_2]^{\mathrm{T}}$ and $\mathbf{p} = [p_1 \quad p_2]^{\mathrm{T}}$ or the scalars u_3 and p_3. The numerical solution is therefore similar to that outlined in Section B2.4 but only line integrals are required and the computation time required is much shorter.

B2.6 A Note on Fictitious Natural Frequencies

As described in Section B2.4, one of the advantages of the BEM is the ability to model external domains. However, it is important to be aware that such models suffer from a spurious numerical difficulty. The BIE describing any exterior problem with boundary Γ has a non-unique solution when the excitation frequency coincides with a natural frequency of the interior problem with the same boundary subject to prescribed displacements. As a result, when modelling the response of an external domain, to either prescribed displacements or tractions, a series of fictitious natural frequencies may be predicted.

A number of special BEM formulations have been proposed that are free of this problem [35], although it is often simplest to obtain results for frequencies near the fictitious ones by

interpolation of the results either side. However, fictitious natural frequencies are not always encountered and, in particular, they do not arise if the full-space Green's functions are used in conjunction with a free-surface discretization [13].

B3. Example Problems

To illustrate the effectiveness of the BEM programs developed for this dissertation, two example problems will now be presented. The first problem has a simple analytical solution with which the BEM results may be compared. The second illustrates the use of the BEM for modelling external domains.

B3.1 Longitudinal Vibration of an Elastic Bar

Consider a homogeneous linear-elastic bar of length L, density ρ, Young's modulus E and cross-sectional area A. The bar is fixed at $x_3 = 0$ and loaded by a longitudinal time-harmonic traction p applied uniformly over the cross-section at $x_3 = L$; see figure B5.

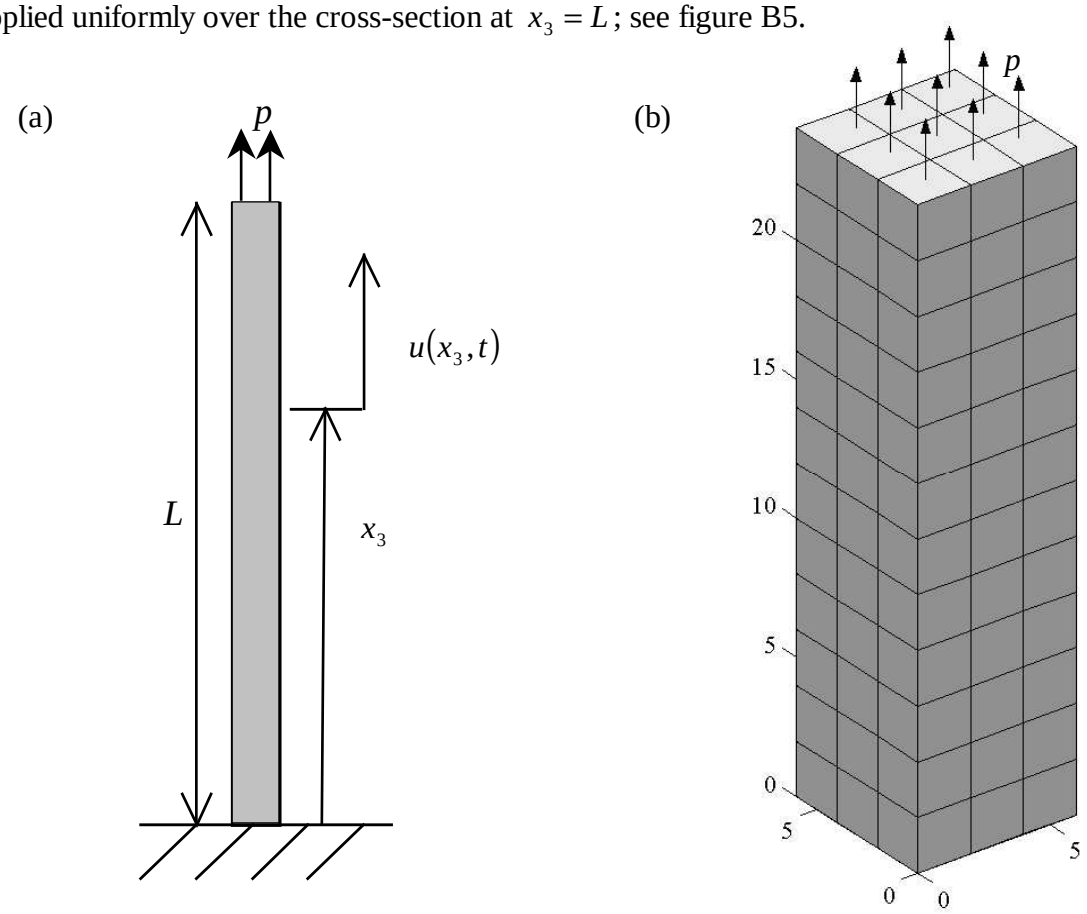

Figure B5: Longitudinal vibration of a linear-elastic bar may be described by (a) a one-dimensional analytical model or (b) a three-dimensional BEM model.

The analytical solution to this problem is straightforward provided that the effects of Poisson's ratio are neglected and the stress-state is assumed to be one-dimensional. Newland [101] derives the following expression for the displacement frequency-response function:

$$H = \frac{1}{k}\frac{\tan \omega a}{\omega a} \tag{B12}$$

where $k = EA/L$ and $a = L\sqrt{\rho/E}$.

The analytical result of Equation B12 may be compared with the results from a three-dimensional BEM model. The model is shown in Figure B5(b) and comprises 162 constant rectangular elements. The base of the bar is constrained in the x_3-direction, with the remainder of the surface specified as traction-free except for the uniform traction over the top face. To compare the results directly, the same complex Young's modulus, with a damping loss factor of 0.05, is specified in both models (see Section 3.1.1 for a discussion on damping models). The BEM model also requires a value for Poisson's ratio, which has been specified as 0.25.

Figure B6 presents the results over a frequency range containing the first two resonances of the system. The two models agree very well for the chosen geometry and frequency range, and in this case the complexity of the BEM model cannot be justified. However, for less slender bars with more complex boundary conditions, and at higher frequencies when deformation becomes more localised, the BEM model is ideal.

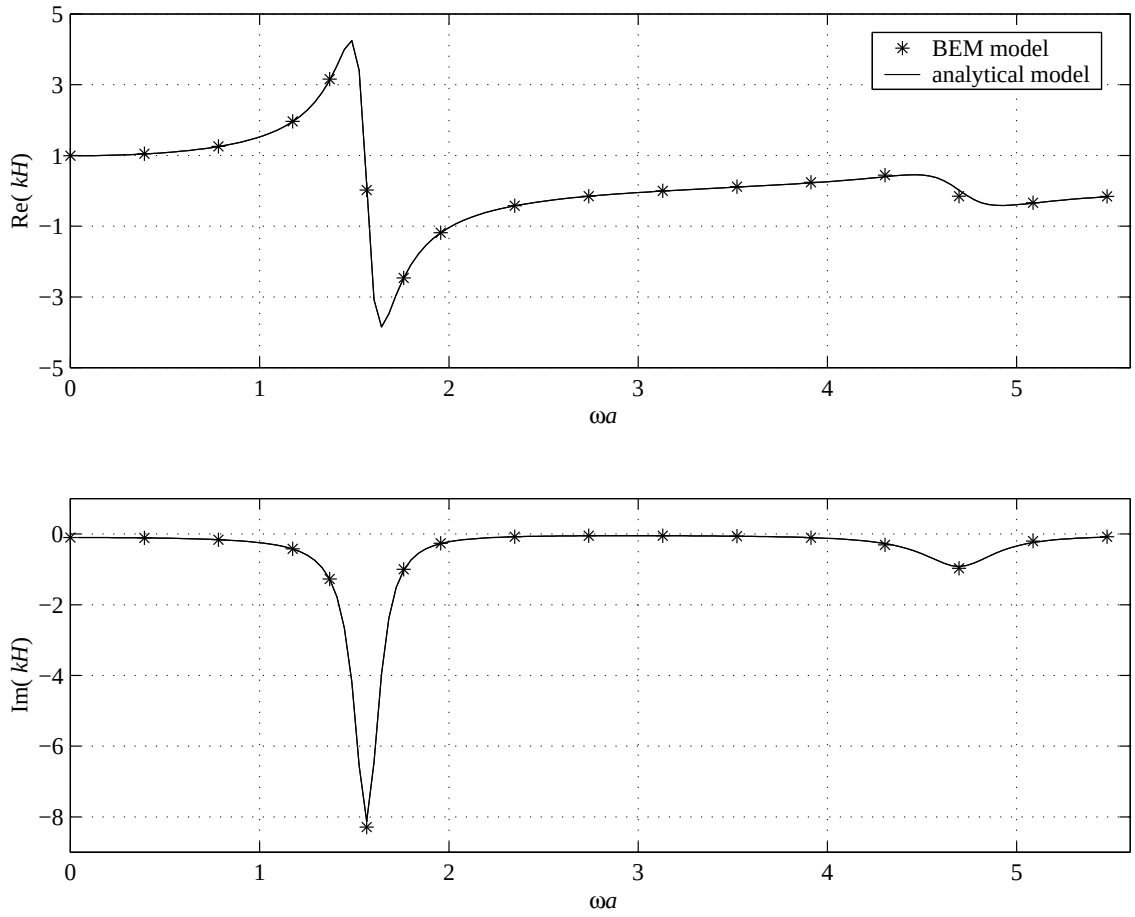

Figure B6: The driving-point displacement frequency response of a homogeneous linear-elastic bar when loaded by a longitudinal time-harmonic traction applied uniformly over one end, with the other end fixed. The frequency-response function H, as calculated using a one-dimensional analytical model and a three-dimensional BEM model, is multiplied by the static stiffness of the bar k and plotted against non-dimensional frequency $a\omega$.

The corresponding mode shapes predicted by the BEM model are given in Figure B7. These illustrate the effect of Poisson's ratio, evident in the cross-sectional expansion and contraction of the bar.

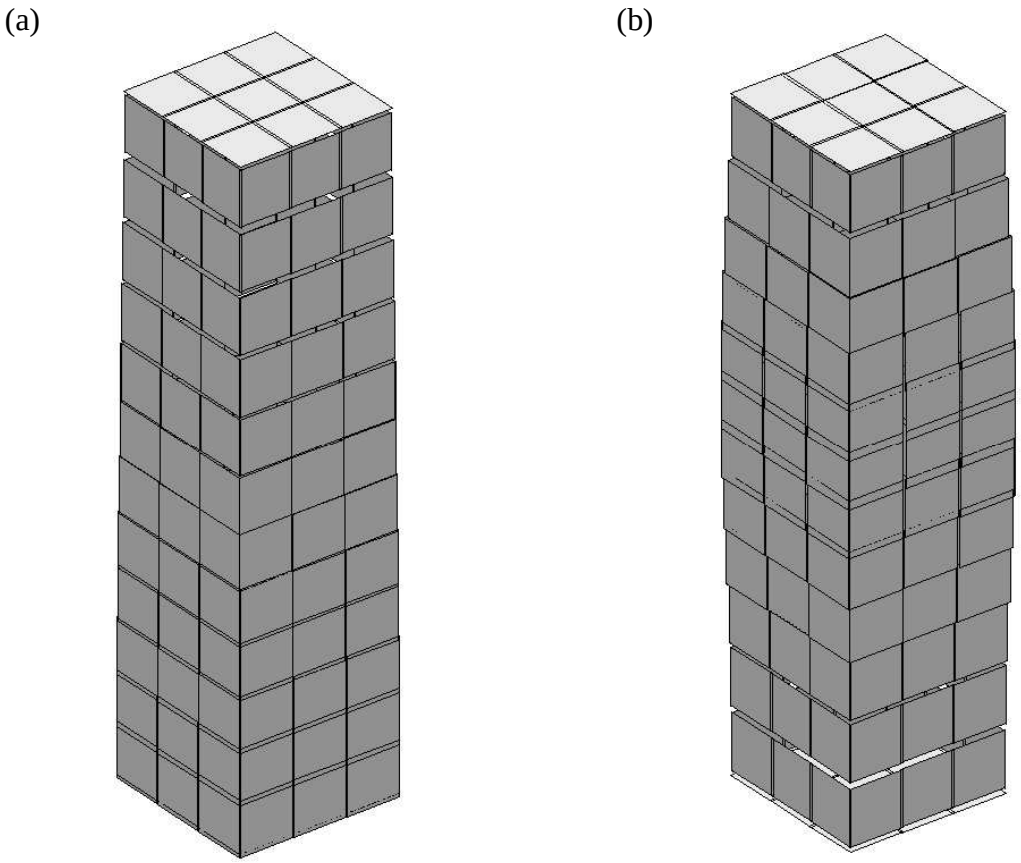

Figure B7: Deformation of a homogeneous linear-elastic bar when loaded by a longitudinal time-harmonic traction applied uniformly over one end, with the other end fixed. The plots correspond to (a) the first and (b) the second resonance as predicted by a three-dimensional BEM model.

B3.2 Wave Propagation from a Cylindrical Cavity

This problem illustrates the use of the BEM for modelling external domains. Before it is considered in detail, it is worth returning to the numerical formulation of the BEM. Once Equation B11 has been solved for a particular problem and all the values of **u** and **p** are known on the boundary, the value of **u** at any internal point may be obtained from Equation B3 (the calculation of internal stresses requires differentiation of these displacements and use of the stress-strain relations). The BEM is therefore efficient at modelling external domains for two reasons: only the boundary of the domain must be discretized and, once the boundary-value problem has been solved, field variables are only calculated at the internal points of interest. A further advantage is that the interior solution is fully continuous and no numerical approximations are involved as on the boundary. This gives particularly accurate results at internal points, given the assumptions of linear-elasticity, and this accuracy increases with distance from the boundary.

Consider a cylindrical cavity, of radius R, in the centre of a homogeneous isotropic linear-elastic solid of density ρ, shear modulus μ and Poisson's ratio υ. The solid will be assumed to be of infinite extent and the cavity of infinite length. The latter assumption greatly simplifies the problem since the solution must be invariant along the cavity's length. The problem may therefore be represented by a two-dimensional model under plane-strain conditions. The BEM model presented here consists of just 16 constant elements representing the surface of the cavity; see Figure B8(a). A uniform radial traction is applied to this surface as if the cavity were subject to a time-harmonic internal pressure.

(a)

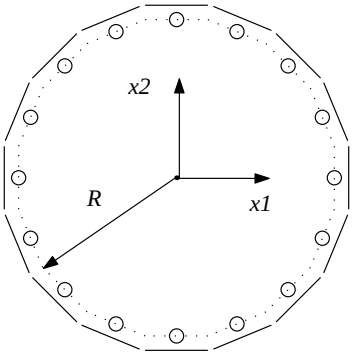

(b)

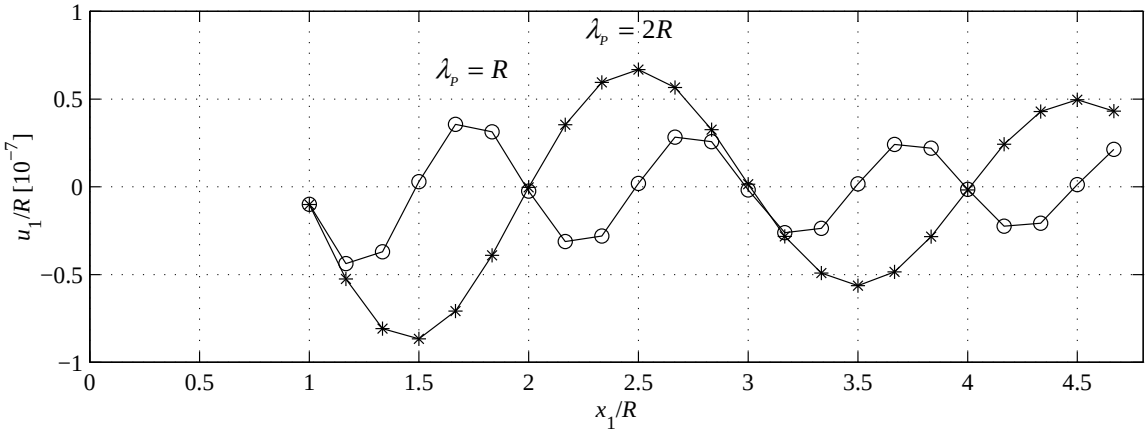

Figure B8: P-wave propagation from an internally pressurised, infinitely long cylindrical cavity in an infinite elastic solid. The elements of the two-dimensional BEM model (a) are shown in their unloaded (dashed) and loaded (solid) configuration, the nodes being represented by 'o'. The predicted radial displacement of the solid is divided by the cavity radius R and plotted (b) against non-dimensional distance x_1/R for frequencies corresponding to P-wavelengths equal to R and $2R$.

As described in Section 2.7.1, the infinite solid can support two types of wave motion: P-waves and S-waves. In this problem, the fluctuating internal pressure of the cavity generates P-

waves, which propagate away from the cavity on cylindrical wavefronts. Nominal values have been specified for the governing parameters of the model ($\mu = 10^6\,\mathrm{N/m^2}$, $\rho = 100\mathrm{kg/m^3}$, $\upsilon = 0.25$, $\beta = 0.05$) and two frequencies have been selected such that the P-wavelength in the solid is equal to *R* and 2*R*.

$$\lambda_p = \frac{2\pi c_p}{\omega} = \frac{2\pi}{\omega}\sqrt{\frac{\lambda + 2\nu}{\rho}} \tag{B13}$$

where $\lambda = \dfrac{2\nu\mu}{1-2\nu}$

Figure B8(b) presents the results for the radial displacement of the solid u_1 calculated at 23 internal points lying along the x_1-axis. It is clear that the resulting motion does indeed consist of P-waves and that their wavelengths are equal to the expected values.

Appendix C

THE DYNAMIC-STIFFNESS METHOD APPLIED TO PORTAL FRAMES

The dynamic-stiffness method (DSM) is used in this dissertation to model the behaviour of a typical building, as represented by a two-dimensional portal frame. This appendix uses the analytical solutions for an elastic bar and Euler beam to derive the dynamic-stiffness matrix that describes the behaviour of one element from such a structure.

A typical element from a two-dimensional portal frame, illustrated in Figure C1, is defined by its length L, cross-sectional area A, second moment of area I, density ρ and Young's modulus E.

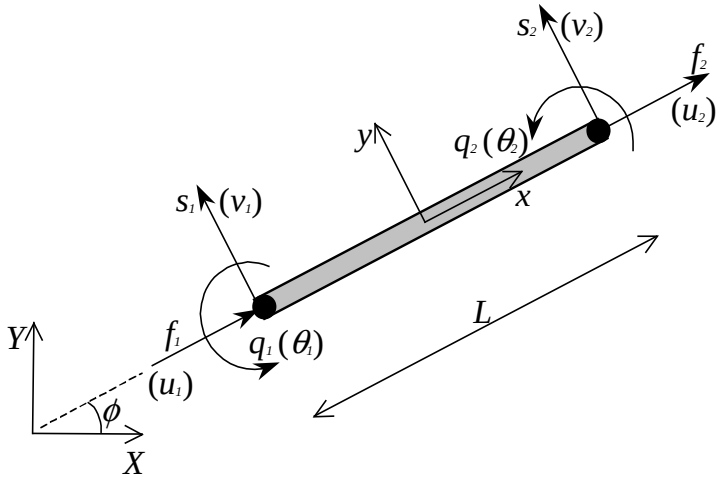

Figure C1: A typical bar-beam element from a two-dimensional portal frame. The generalised forces f, s and q, and the corresponding generalised displacements (u, v and θ) are related through the element's dynamic-stiffness matrix.

The equation of motion governing undamped, longitudinal motion of an elastic bar is given by Newland [101] as:

$$\frac{\partial^2 u}{\partial t^2} - \frac{E}{\rho}\frac{\partial^2 u}{\partial x^2} = 0 \tag{C1}$$

For time-harmonic motion at frequency ω, the general solution for the displacement at point x along the element takes the form:

$$u(x,t) = \mathrm{Re}\left\{u(x,\omega)e^{i\omega t}\right\} \tag{C2}$$

where

$$u(x,\omega) = c_1 e^{\alpha x} + c_2 e^{-\alpha x}, \qquad \alpha = \omega\sqrt{\rho/E}$$

$i = \sqrt{-1}$ and the constants c_1 and c_2 are to be determined. The longitudinal force acting on the cross-section at x is obtained by differentiating Equation C2 to obtain the strain:

$$f = AE\frac{\partial u}{\partial x} \tag{C3}$$

For an Euler beam, the undamped equation of motion is [101]:

$$\frac{\partial^4 v}{\partial t^4} + \frac{EI}{\rho A}\frac{\partial^4 v}{\partial x^4} = 0 \tag{C4}$$

and the general harmonic solution takes the form:

$$v(x,t) = \mathrm{Re}\left\{v(x,\omega)e^{i\omega t}\right\} \tag{C5}$$

where

$$v(x,\omega) = c_3 e^{\beta x} + c_4 e^{i\beta x} + c_5 e^{-\beta x} + c_6 e^{-i\beta x}, \qquad \beta = \left(\frac{\rho A\omega^2}{EI}\right)^{1/4}$$

and the constants c_3 to c_6 are to be determined. Successive differentiation of Equation C5 gives the rotation θ, the bending moment q and the shear force s at point x:

$$\theta = \frac{\partial v}{\partial x}, \qquad q = EI\frac{\partial^2 v}{\partial x^2}, \qquad s = EI\frac{\partial^3 v}{\partial x^3} \tag{C6}$$

The generalised forces and displacements are related through the following boundary conditions at the ends of the element:

$$u = u_1, \quad v = v_1, \quad \theta = \theta_1, \quad f = -f_1, \quad s = s_1, \quad q = -q_1 \quad \text{at } x = -L/2 \tag{C7a}$$

$$u = u_2, \quad v = v_2, \quad \theta = \theta_2, \quad f = f_2, \quad s = -s_2, \quad q = q_2 \quad \text{at } x = L/2 \tag{C7b}$$

By combining the above equations, the following matrix equations may be assembled:

$$\begin{bmatrix} u_1 \\ v_1 \\ \theta_1 \\ u_2 \\ v_2 \\ \theta_2 \end{bmatrix} = \begin{bmatrix} e^{-\alpha L/2} & e^{\alpha L/2} & 0 & 0 & 0 & 0 \\ 0 & 0 & e^{-\beta L/2} & e^{-i\beta L/2} & e^{\beta L/2} & e^{i\beta L/2} \\ 0 & 0 & \beta e^{-\beta L/2} & i\beta e^{-i\beta L/2} & -\beta e^{\beta L/2} & -i\beta e^{i\beta L/2} \\ e^{\alpha L/2} & e^{-\alpha L/2} & 0 & 0 & 0 & 0 \\ 0 & 0 & e^{\beta L/2} & e^{i\beta L/2} & e^{-\beta L/2} & e^{-i\beta L/2} \\ 0 & 0 & \beta e^{\beta L/2} & i\beta e^{\beta L/2} & -\beta e^{-\beta L/2} & -i\beta e^{-\beta L/2} \end{bmatrix} \begin{bmatrix} c_1 \\ c_2 \\ c_3 \\ c_4 \\ c_5 \\ c_6 \end{bmatrix}$$

or $$\mathbf{u_1} = \mathbf{Mc} \tag{C8}$$

and

$$\begin{bmatrix} f_1 \\ s_1 \\ q_1 \\ f_2 \\ s_2 \\ q_2 \end{bmatrix} = \begin{bmatrix} -AE\alpha e^{-\alpha L/2} & AE\alpha e^{\alpha L/2} & 0 & 0 & 0 & 0 \\ 0 & 0 & EI\beta^3 e^{-\beta L/2} & -iEI\beta^3 e^{-i\beta L/2} & -EI\beta^3 e^{\beta L/2} & iEI\beta^3 e^{i\beta L/2} \\ 0 & 0 & -EI\beta^2 e^{-\beta L/2} & EI\beta^2 e^{-i\beta L/2} & -EI\beta^2 e^{\beta L/2} & EI\beta^2 e^{i\beta L/2} \\ AE\alpha e^{\alpha L/2} & -AE\alpha e^{-\alpha L/2} & 0 & 0 & 0 & 0 \\ 0 & 0 & -EI\beta^3 e^{\beta L/2} & iEI\beta^3 e^{i\beta L/2} & EI\beta^3 e^{-\beta L/2} & -iEI\beta^3 e^{-i\beta L/2} \\ 0 & 0 & EI\beta^2 e^{\beta L/2} & -EI\beta^2 \beta e^{\beta L/2} & EI\beta^2 e^{-\beta L/2} & -EI\beta^2 e^{-\beta L/2} \end{bmatrix} \begin{bmatrix} c_1 \\ c_2 \\ c_3 \\ c_4 \\ c_5 \\ c_6 \end{bmatrix}$$

or $$\mathbf{f_1} = \mathbf{Nc} \tag{C9}$$

where the subscript 'l' on the generalised force and displacement vectors indicates that they are defined in the local coordinates (*x*, *y*) of the element. Their component values u_1, f_1, *etc*. are the complex amplitudes $u_1(\omega)$, $f_1(\omega)$, *etc*. at the ends of the element.

Finally, eliminating **c** from Equations C8 and C9 gives the local dynamic-stiffness matrix $\mathbf{K}_\mathbf{l}$ of the element:

$$\mathbf{f}_\mathbf{l} = \mathbf{K}_\mathbf{l}\mathbf{u}_\mathbf{l}, \qquad \mathbf{K}_\mathbf{l} = \mathbf{N}[\mathbf{M}]^{-1} \tag{C10}$$

In general the element will be inclined at some angle ϕ to the global horizontal. A coordinate transformation is therefore required to obtain the global generalised forces and displacements:

$$\mathbf{u}_\mathbf{g} = \mathbf{R}\mathbf{u}_\mathbf{l} \quad \text{and} \quad \mathbf{f}_\mathbf{g} = \mathbf{R}\mathbf{f}_\mathbf{l}, \qquad \mathbf{R} = \begin{bmatrix} \cos\phi & -\sin\phi & 0 & 0 & 0 & 0 \\ \sin\phi & \cos\phi & 0 & 0 & 0 & 0 \\ 0 & 0 & 1 & 0 & 0 & 0 \\ 0 & 0 & 0 & \cos\phi & -\sin\phi & 0 \\ 0 & 0 & 0 & \sin\phi & \cos\phi & 0 \\ 0 & 0 & 0 & 0 & 0 & 1 \end{bmatrix} \tag{C11}$$

which leads to the global dynamic-stiffness matrix $\mathbf{K}_\mathbf{g}$:

$$\mathbf{f}_\mathbf{g} = \mathbf{K}_\mathbf{g}\mathbf{u}_\mathbf{g}, \qquad \begin{aligned} \mathbf{K}_g &= \mathbf{R}\mathbf{K}_\mathbf{l}[\mathbf{R}]^{-1} \\ &= \mathbf{R}\mathbf{K}_\mathbf{l}[\mathbf{R}]^{\mathrm{T}} \end{aligned} \tag{C12}$$

where 'T' denotes the matrix transpose.

Vibration damping may be accounted for in the formulation in a number of ways. In this dissertation the hysteretic damping model is adopted and Young's modulus *E* is replaced with a suitable complex value, as described in Section 3.1.1.

Appendix D

A TWO-DEGREE-OF-FREEDOM BUILDING MODEL

Section 3.2.2 investigates wave interaction between surface footings by considering a two-degree-of-freedom (2-DOF) model of a base-isolated building founded on two, rigid massless footings bonded to the surface of an elastic half-space. The purpose of this appendix is to derive the displacement frequency-response functions (FRFs) of the building model.

The model, illustrated in Figure D1, is a 2-DOF system, comprising a rigid body, of mass *M* and moment of inertia I_G, connected to two springs of stiffness *k*.

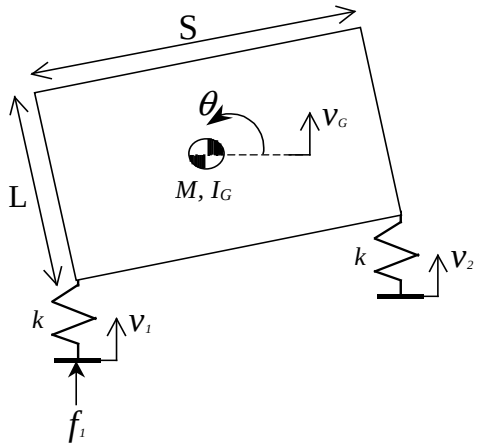

Figure D1: A 2-DOF base-isolated building model, comprising a rigid body, of mass *M* and moment of inertia I_G, connected to two springs of stiffness *k*.

Consider a time-harmonic force of amplitude f_1 and frequency ω applied to footing 1. For small rotation θ, equilibrium of forces implies for the spring that:

$$f_1 = k\left(v_1 - v_G + \frac{S}{2}\theta \right) \tag{D1}$$

and, for the mass, that:

$$f_1 = -\omega^2 M v_G \qquad \text{and} \qquad f_1 \frac{S}{2} = \omega^2 I_G \theta \tag{D2}$$

Eliminating the displacements v_G and θ from Equations D1 and D2 gives:

$$H_{11} = \frac{v_1}{f_1} = \frac{2 - (\omega_1/\omega)^2 - (\omega_2/\omega)^2}{2k} \tag{D3}$$

where $\omega_1 = \sqrt{2k/M}$ is the vertical resonance frequency, equivalent to the isolation frequency of the building in rad/s, and $\omega_2 = S\sqrt{k/2I_G}$ is the rotational resonance frequency. Symmetry implies that $H_{22} = H_{11}$.

Considering the second footing:

$$v_2 = v_G + \frac{S}{2}\theta \tag{D4}$$

Eliminating the displacements v_G and θ from Equations D1 and D4 gives:

$$H_{21} = \frac{v_2}{f_1} = \frac{(\omega_2/\omega)^2 - (\omega_1/\omega)^2}{2k} \tag{D5}$$

Reciprocity implies that $H_{12} = H_{21}$.

If the building is modelled as a uniform mass of width S and height L then:

$$I_G = \frac{M}{12}\left(S^2 + L^2\right) \tag{D6}$$

The relationship between the resonance frequencies may then be expressed as:

$$\omega_2^2 = \frac{S^2 k}{2I_G} = \left(\frac{3S^2}{S^2 + L^2}\right)\omega_1^2 \tag{D7}$$

Appendix E

INSERTION PERFORMANCE OF A SINGLE-INPUT SINGLE-OUTPUT SYSTEM

Insertion performance is one of the categories of measure commonly used to describe the performance of base isolation and represents the benefit of inserting isolation bearings beneath a building; see Section 2.4.3. This appendix considers the special case of a single-input single-output system and shows that two particular measures of insertion performance, insertion gain (IG) and power flow insertion gain (PFIG), are directly equivalent.

E1. Insertion Gain

Figure E1 shows a general linear-elastic body Ω mounted on a linear spring *k*. The spring may also be damped, in which case it may be represented by a complex stiffness k^*. The purpose of the spring is to isolate the body from the displacement *x* of the rigid base, which moves harmonically in time *t*, at circular frequency ω, with amplitude *X*, that is, $x = \mathrm{Re}\{Xe^{i\omega t}\}$, where $i = \sqrt{-1}$. The system is linear and therefore the response at a general point **r** takes a similar form $y(\mathbf{r}) = \mathrm{Re}\{Y(\mathbf{r},\omega)e^{i\omega t}\}$.

Assume that the frequency-response function $H(\mathbf{r},\omega)$, relating *y* to the force $f = \mathrm{Re}\{Fe^{i\omega t}\}$ applied to the body at *O*, is known:

$$Y(\mathbf{r},\omega) = H(\mathbf{r},\omega)F \tag{E1}$$

The force at O is the elastic force in the spring $F = k(X - Y(0))$. Substituting for F in Equation E1, and noting that $Y(0,\omega) = H(0,\omega)F$, gives:

$$\frac{Y(\mathbf{r},\omega)}{X} = \frac{kH(\mathbf{r},\omega)}{1 + kH(0,\omega)} \tag{E2}$$

Equation E2 forms the basis for calculating the IG associated with the spring.

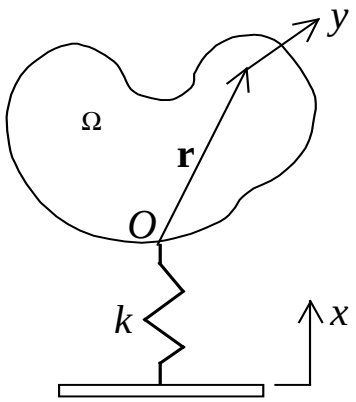

Figure E1: A general linear-elastic body Ω mounted on a linear spring *k* to isolate it from the displacement *x* of the rigid base. The insertion performance describes the reduction in the vibration of the body achieved by inserting the spring.

IG is defined as the ratio of the vibration response of a building with the isolation bearings in position to that with no bearings at all:

$$\mathrm{IG} = 20\log_{10}\left(\frac{Y_{isol}}{Y_{unisol}}\right) \tag{E3}$$

where Y_{isol} and Y_{unisol} are the amplitudes of the building response in the isolated and unisolated condition respectively. It is usual to take the response of the building at its base, directly above the isolation bearings themselves. Here the IG will be calculated for the response at the general point **r**. The response in the isolated condition is given directly by Equation E2:

$$Y_{isol}(\mathbf{r},\omega) = \frac{kH(\mathbf{r},\omega)}{1 + kH(0,\omega)} X \tag{E4}$$

In the unisolated condition the response may be obtained by considering the limit of Equation E2 as $k \to \infty$:

$$Y_{unisol}(\mathbf{r},\omega) = \frac{H(\mathbf{r},\omega)}{H(0,\omega)} X \tag{E5}$$

Combining Equations E3, E4 and E5 gives the IG:

$$\mathrm{IG} = 20\log\left(\frac{kH(0,\omega)}{1+kH(0,\omega)}\right) \tag{E6}$$

The important thing to note about Equation E6 is that the value of IG is independent of the location in the body at which the response is measured. It depends only on the value of the frequency-response function at $\mathbf{r} = 0$, the driving-point response of the body.

E2. Power Flow Insertion Gain

In Section 3.3.3, the concept of PFIG is introduced as an alternative measure of insertion performance for base-isolated buildings. PFIG is based on the mean vibrational power flow entering the building through the isolation bearings:

$$\mathrm{PFIG} = 10\log_{10}\left(\frac{\overline{P}_{isol}}{\overline{P}_{unisol}}\right) \tag{E7}$$

where $\overline{P}_{isol}$ and $\overline{P}_{unisol}$ are the total mean power flows entering a building in the isolated and unisolated cases respectively.

It is instructive to consider PFIG in the case of the general linear-elastic body of Figure E1. The instantaneous power flow into the body is equal to the instantaneous rate at which the force *f* does work at point *O*:

$$P = \mathrm{Re}\left\{i\omega Y(0,\omega)e^{i\omega t}\right\}\mathrm{Re}\left\{Fe^{i\omega t}\right\} \tag{E8}$$

Both *Y* and *F* are complex quantities: $Y(0,\omega) = Y_R + iY_I$ and $F = F_R + iF_I$. *P* may therefore be expressed as:

$$\begin{aligned} P &= \mathrm{Re}\{i\omega(Y_R + iY_I)(\cos\omega t + i\sin\omega t)\}\mathrm{Re}\{(F_R + iF_I)(\cos\omega t + i\sin\omega t)\} \\ &= -\omega Y_I F_R \cos^2\omega t + \omega Y_R F_I \sin^2\omega t - \omega(Y_R F_R - Y_I F_I)\cos\omega t \sin\omega t \end{aligned} \quad \text{(E9)}$$

The first two terms have a positive mean value and represent the power dissipated by the damping of the body. The third term varies in proportion to $\sin(2\omega t)$ and represents the *reactive* power required to balance the fluctuating total energy (potential plus kinetic) of the body. Averaging Equation E9 over one period *T*, gives the mean power flow:

$$\overline{P} = \frac{1}{T}\int_0^T P dt = \frac{1}{2}\omega(Y_R F_I - Y_I F_R) = \frac{1}{2}\mathrm{Re}\{i\omega Y(0,\omega)F^*\} \quad \text{(E10)}$$

where * denotes the complex conjugate.

Defining PFIG in terms of the mean power flow only considers the dissipative power; the reactive power is ignored. This raises the question of whether PFIG is representative of vibration amplitudes, since in a lightly damped structure the dissipative power will be small despite the fact that the structure vibrates. It is shown below that PFIG is indeed representative of vibration amplitudes for the system considered here.

By substituting for *F* from Equation E1, Equation E10 becomes:

$$\overline{P} = \frac{1}{2}\mathrm{Re}\left\{i\omega Y(0,\omega)\left(\frac{Y(0,\omega)}{H(0,\omega)}\right)^*\right\} \quad \text{(E11)}$$

Substituting for *Y* from Equations E4 and E5 gives:

$$\overline{P}_{isol} = \frac{1}{2}\mathrm{Re}\left\{i\omega\frac{kH(0,\omega)X}{1+kH(0,\omega)}\left(\frac{kX}{1+kH(0,\omega)}\right)^*\right\} = \frac{1}{2}\omega\frac{|k|^2 X^2}{|1+kH(0,\omega)|^2}\mathrm{Re}\{iH(0,\omega)\} \quad \text{(E12)}$$

and

$$\overline{P}_{unisol} = \frac{1}{2}\mathrm{Re}\left\{i\omega X\left(\frac{X}{H(0,\omega)}\right)^*\right\} = \frac{1}{2}\omega\frac{X^2}{|H(0,\omega)|^2}\mathrm{Re}\{iH(0,\omega)\} \quad \text{(E13)}$$

Combing Equations E7, E12 and E13 gives the PFIG:

$$\text{PFIG} = 10\log\left(\frac{|k|^2|H(0,\omega)|^2}{|1+kH(0,\omega)|^2}\right) = 20\log\left(\frac{kH(0,\omega)}{1+kH(0,\omega)}\right) \tag{E14}$$

By comparing Equations E6 and E14 it is clear that the IG and PFIG are directly equivalent.

E3. Conclusion

When defining a measure of base-isolation performance for the special case of a single-input single-output system, the IG has been shown to be independent of position and directly equivalent to the PFIG. PFIG therefore provides a direct measure of the reduction in vibration amplitude at any location in the isolated body.

Appendix F

ANTI-PLANE MOTION OF A RIGID CAVITY IN AN INFINITE SOLID

Section 4.1.1 considers a two-dimensional BEM model of an infinitely long, rigid cylindrical cavity in an infinite elastic solid. By solving the model for both the plane and anti-plane cases, that is, for transverse and longitudinal motion of the cavity, the significance of the number of circumferential boundary-elements is investigated. The investigation compares the BEM results with the analytical solution. For the plane case, this is derived by Wolf and Song [139]; the purpose of this appendix is to derive the anti-plane solution. Consider the transverse section through the cavity shown in Figure F1.

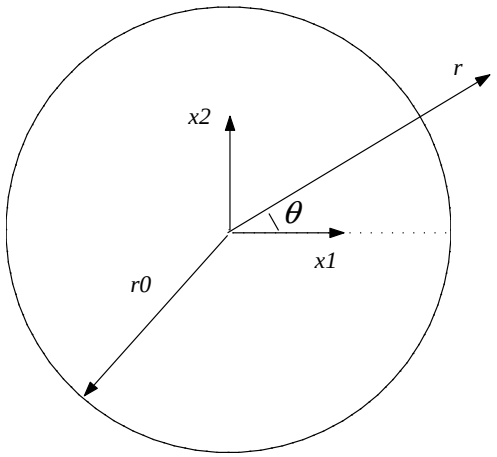

Figure F1: A transverse section through an infinitely long, rigid cylindrical cavity in an infinite elastic solid.

Longitudinal motion of the cavity results in tractions and displacements in the x_3-direction, perpendicular to the x_1x_2-plane. This motion is uncoupled from x_1 and x_2, and the displacement amplitude u_3 in the surrounding solid is described by the wave equation [35]:

$$\frac{\partial^2 u_3}{\partial x_1^2} + \frac{\partial^2 u_3}{\partial x_2^2} + \frac{\omega^2}{c_s^2} u_3 = 0 \tag{F1}$$

Where ω is the circular frequency of the motion and c_s is the S-wave speed in the solid.

Transforming Equation F1 into polar coordinates and noting, from symmetry, that $\frac{\partial u_3}{\partial \theta} = 0$:

$$\frac{1}{r}\left(\frac{du_3}{dr} + r\frac{d^2 u_3}{dr^2}\right) + \frac{\omega^2}{c_s^2} u_3 = 0 \tag{F2}$$

This may be written in the standard form of Bessel's equation [67] by introducing the non-dimensional parameter $a = \omega r / c_s$:

$$\frac{d^2 u_3}{da^2} + \frac{1}{a}\frac{du_3}{da} + u_3 = 0 \tag{F3}$$

For unit-amplitude motion of the cavity, the boundary conditions of the problem are $u_3 = 1$ and 0 at $r = r_0$ and ∞ respectively. These lead to the following solution:

$$u_3 = \frac{H_0^{(2)}(a)}{H_0^{(2)}(a_0)} \tag{F4}$$

where a_0 is the value of a at $r = r_0$ and $H_0^{(2)}$ and $H_1^{(2)}$ are second kind Hankel functions of order zero and one.

The longitudinal dynamic stiffness of the cavity is calculated by integrating the longitudinal stress σ_3 around its circumference:

$$K_l = -\int_0^{2\pi} \sigma_3 r_0 d\theta = -2\pi r_0 \mu \left(\frac{du_3}{dr}\right)_{r=r_0} = 2\pi a_0 \mu \frac{H_1^{(2)}(a_0)}{H_0^{(2)}(a_0)} \tag{F5}$$

where μ is the shear modulus of the solid.

Appendix G

TRANSFORMATION MATRICES FOR COUPLING THE PILE AND SOIL

Section 4.1.4 describes the coupling of the pile and soil of the generic piled-foundation model. This appendix presents the two transformation matrices $\mathbf{Q_1}$ and $\mathbf{Q_2}$ that relate the displacements and tractions of the soil-pile interface with the displacements and forces of the pile centroid.

Equation 4.26 expresses displacement compatibility, in three dimensions, between the N_{sp} nodes of the soil-pile interface and the $N_p + 1$ nodes of the pile, excluding the pile-head node (which is reserved for the application of external loads):

$$\mathbf{u_{sp}} = \mathbf{Q_1 u_p} \tag{G1}$$

The $(12N_p + 3)$ x $(3N_p + 3)$ matrix $\mathbf{Q_1}$ is a banded matrix assembled from 3 x 3 identity matrices **I**:

$$\mathbf{Q_1} = \begin{bmatrix} \mathbf{I} & & \\ \mathbf{I} & & \\ \mathbf{I} & & \\ \mathbf{I} & & \\ & \mathbf{I} & \\ & \mathbf{I} & \\ & \mathbf{I} & \\ & \mathbf{I} & \\ & & \ddots \\ & & \mathbf{I} \end{bmatrix} \tag{G2}$$

In a similar way, $[\mathbf{Q_1}]^T$ relates the tractions of the soil-pile interface with the forces acting on the pile centroid; see Equation 4.28.

The planar building model results in the x_2-displacements being zero along the entire length of the pile centroid and only the components of $\mathbf{u_p}$ in the x_1x_3-plane need to be retained. Equation 4.26 therefore becomes Equation 4.32 with the addition of the matrix $\mathbf{Q_2}$ to complete the transformation from the two-dimensional vectors of the pile to the three-dimensional vectors of the soil-pile interface:

$$\mathbf{u_{sp}} = \mathbf{Q_1 Q_2 u_p} \tag{G3}$$

The $(3N_p + 3)$ x $(2N_p + 2)$ matrix $\mathbf{Q_2}$ is a banded matrix with the following form:

$$\mathbf{Q_2} = \begin{bmatrix} 1 & 0 & 0 & & & & \\ 0 & 0 & 0 & & & & \\ 0 & 1 & 0 & & & & \\ & & 1 & 0 & 0 & & \\ & & 0 & 0 & 0 & & \\ & & 0 & 1 & 0 & & \\ & & & & \ddots & & \\ & & & & & 1 & 0 & 0 \\ & & & & & 0 & 0 & 0 \\ & & & & & 0 & 1 & 0 \end{bmatrix} \tag{G4}$$

In a similar way, $[\mathbf{Q}_2]^T$ is required to complete the transformation between forces and tractions; see Equation 4.33.

Appendix H

A SOLUTION FOR THE STATIC PILE-HEAD COMPLIANCE OF A SINGLE FLOATING PILE

In Section 4.1.5 a check is required on the low-frequency solution of the single-pile BEM model. This appendix calculates an alternative solution by using the results of Poulos and Davis [112] for the static pile-head compliance of a single floating pile in a uniform half-space.

Poulos and Davis consider a cylindrical pile, of length *L*, radius r_0 and Young's modulus E_p, embedded in a homogeneous isotropic linear-elastic half-space with Young's modulus E_s and Poisson's ratio ν. The pile is modelled as an elastic bar-beam and soil displacements are obtained numerically by integrating Mindlin's equations [92] for the static Green's functions of an elastic half-space.

The direct horizontal compliance is given by:

$$C_{11} = \frac{I_{11}}{E_s L} \tag{H1}$$

where I_{11} is the influence factor for the displacement due to a unit horizontal load. Poulos and Davis present I_{11} as a function of the non-dimensional parameters L / r_0 and $E_p I_p / E_s L^4$, where $I_p = \pi r_0^4 / 4$ is the second moment of area of the pile. For the set of parameter values used in Section 4.1.5 ($L / r_0 = 21.2$, $E_p I_p / E_s L^4 = 3.8 \times 10^{-4}$) $I_{11} \approx 7.0$ and Equation H1 gives $C_{11} = 3.3 \times 10^{-9}$ m/N.

The coupling compliance is given by:

$$C_{31} = C_{13} = \frac{I_{31}}{E_s L^2} \tag{H2}$$

where I_{31} is the influence factor for the rotation due to a unit horizontal load or, by reciprocity, for the horizontal displacement due to a unit moment. For the same parameter values, $I_{31} \approx 35$ and Equation H2 gives $C_{31} = 2.2 \text{ x } 10^{-9}$ rad/N. These values of C_{11} and C_{31} are for a soil with $\nu = 0.5$, although ν has little influence on the solution for horizontal loading.

The vertical compliance is given by:

$$C_{22} = \frac{I_{22}}{2E_s r_0} \tag{H3}$$

I_{22} depends on the parameters L/r_0 and E_p/E_s, as well as ν. For the values used in Section 4.1.5 ($L/r_0 = 21.2$, $E_p/E_s = 100$, $\nu = 0.4$) $I_{22} \approx 0.12$ and Equation H3 gives $C_{22} = 8.3 \text{ x } 10^{-10}$ m/N.

Finally, the direct rotational compliance is given by:

$$C_{33} = \frac{I_{33}}{E_s L^3} \tag{H4}$$

I_{33} again depends on L/r_0 and $E_p I_p / E_s L^4$. Here $I_{33} \approx 410$ and Equation H4 gives $C_{33} = 3.5 \text{ x } 10^{-9}$ rad/Nm.